Nonlinear Vibrations of Thin Rectangular Plates: A Numerical Investigation with Application to Wave Turbulence and Sound Synthesis

Michele Ducceschi

Michele Ducceschi. Nonlinear Vibrations of Thin Rectangular Plates: A Numerical Investigation with Application to Wave Turbulence and Sound Synthesis. Vibrations [physics.class-ph]. ENSTA ParisTech, 2014. English. NNT : . pastel-01068284

HAL Id: pastel-01068284
https://pastel.hal.science/pastel-01068284

Submitted on 25 Sep 2014

Nonlinear Vibrations of Thin Rectangular Plates
A Numerical Investigation with Application to Wave Turbulence and Sound Synthesis

---

THÈSE

présentée et soutenue publiquement l'11 février 2014
pour l'obtention du

Doctorat de l'ENSTA

par

Michele Ducceschi

Composition du jury

Directeurs de thèse:	Cyril Touzé (ENSTA-ParisTech, UME, Palaiseau) Olivier Cadot (ENSTA-ParisTech, UME, Palaiseau)
Rapporteurs:	Basile Audoly (IJLRDA, UPMC, Paris 6) Thomas Hélie (IRCAM, Paris)
Examinateurs:	Patrick Joly (ENSTA-ParisTech, UMA, Palaiseau) Arezki Boudaoud (École Normale Supérieure de Lyon) Xavier Boutillon (École Polytechnique) Stefan Bilbao (University of Edinburgh)

Abstract. Thin plate vibrations display a rich and complex dynamics that ranges from linear to strongly nonlinear regimes when increasing the vibration amplitude with respect to the thickness. This thesis is concerned with the development of a numerical code able to simulate without restrictions this large spectrum of dynamical features, described by the von Kármán equations, in the case of flat, homogeneous plates presenting a rectangular geometry. The main application is the synthesis of gong-like sounds, within the larger context of physical modelling. For that, a modal approach is used, in order to reduce the original Partial Differential Equations to a set of coupled Ordinary Differential Equations. An energy-conserving, second-order accurate time integration scheme is developed, including a stability condition. The most appealing features of the modal scheme are its accuracy and the possibility of implementing a rich loss mechanism by selecting an appropriate damping factor for each one of the modes. The sound produced by the numerical code is systematically compared to another numerical technique based on Finite Difference techniques. Fundamental aspects of the physics of nonlinear vibrations are also considered in the course of this work. When a plate vibrates in a weakly nonlinear regime, modal couplings produce amplitude-dependent vibrations, internal resonances, instabilities, jumps and bifurcations. The modal scheme is used to construct and analyse the nonlinear response of the plate in the vicinity of its first eigenfrequencies, both in free and forced-damped vibrations, showing the effect of damping and forcing on the nonlinear normal modes of the underlying Hamiltonian system. When plates vibrate in a strongly nonlinear regime, the most appropriate description of the dynamics is given in terms of the statistical properties of the system, because of the vast number of interacting degrees-of-freedom. Theoretically, this framework is offered by the Wave Turbulence theory. Given the large amount of modes activated in such vibrations, a Finite Difference, energy-conserving code is preferred over the modal scheme. Such a scheme allows to produce a cascade of energy including thousands of modes when the plate is forced sinusoidally around one of its lowest eigenfrequencies. A statistical interpretation of the outcome of the simulation is offered, along with a comparison with experimental data and other numerical results found in the literature. In particular, the effect of the pointwise forcing as well as geometrical imperfections of the plates are analysed.

Contents

Introduction

This thesis is concerned with the numerical reproduction of the nonlinear vibrations of thin rectangular plates. The scientific interest of studying such a system is really broad, and comprises domains that are apparently very different. Many applications are found in common engineering problems, for example: panel flutter in aeronautics [18], energy harvesting of fluttering flexible plates [26], piezoelectric and laminated plates [20, 36], and others.

Unsurprisingly, thin vibrating structures are found very often in music. For example, plates are fundamental components of the piano and the guitar, serving as soundboards; plates have been extensively used as analog reverb units before the advent of digital effects; instruments such as bells, gongs or cymbals are, roughly speaking, curved plates. In old theatres, large metallic plates were used at times to simulate the powerful sounds of thunders and storms.

The examples proposed show that the range of applications of plates in musical acoustics is indeed quite large. A more technical explanation for this can be found by considering the degree of "nonlinearity" involved in such vibrations. In the case of the soundboard and the reverb, the plate is used as a "radiating" unit; the vibrations can be categorised as (almost) linear. Acoustically speaking, a plate is a structure that presents an almost constant density of resonant frequencies covering a large interval, and so it can radiate very efficiently. The soundboard of a piano, for example, is devoted to radiate the vibrations coming from the strings attached to it. When used as a reverb unit, the plate is able to add a somewhat "wet" character and a longer decay to a dry sound. In any case, in these examples the plate is always vibrating at amplitudes much smaller than its thickness, which guarantees that nonlinear phenomena will not come into play.

When a plate vibrates at amplitudes comparable to its thickness (but not larger), nonlinear phenomena of moderate proportions appear. This scenario is typical of some thick chinese gongs. When listening to the sound produced by these instruments in a weakly nonlinear regime, the most salient feature appears to be a "pitch glide" effect. What happens in these cases is that the resonant frequencies of the structure depend on the amplitude of vibration. After the strike, the amplitude grows quickly, and is successively damped by some loss mechanism: during the instants of rapid growth and decay, the nonlinear phenomena account for the perceived pitch glide effect.

Thunder plates, gongs and cymbals undergo strongly nonlinear effects when they vibrate at amplitudes larger than their thickness. In this case, not only the resonant frequencies of the plate are heavily modified, but they also "couple" in order to activate a cascade of energy to higher frequencies. In terms of acoustics, such a cascade is perceived as a bright, shimmering sound, or a crash.

Needless to say, this is one of the most dramatic dynamical features that plate-like structures display, and it is anticipated that the interest of studying its properties lies beyond its applications in musical acoustics.

The main motivation at the origin of this work is to be found precisely in its musical application: at the beginning, the idea was to develop a numerical code able to simulate all types of plate dynamics, from the linear to the strongly nonlinear case. In this sense, this thesis tries to give a contribution to the realm of sound synthesis by physical modelling.

Physical modelling is a very appealing, yet challenging way of synthesising sound: the waveform, in this case, is produced by a computer routine which solves the dynamical equations of a given instrument. The dynamical equations are expressed as Partial Differential Equations (PDEs), because an instrument is often a continuum where the vibrations are a function of time and space. The computer routine depends of a few simulation parameters that control, for example, how the instrument is set into motion, the geometry and material, or what kind of loss mechanism is being simulated. Needless to say, the computational requirements for this type of synthesis are enormous, and in most cases a real time simulation is out of reach. However, the increasing computational power of new generation processors and the use of graphic cards for parallel computing has rendered the computational issues less of a burden and this is why physical modelling has seen a growing amount of research over the recent years [10, 13].

Restricting the attention to thin plates, one may be led to believe that the rich dynamics of their vibrations must be described by complex equations. In actual fact, all types of dynamics of a plate can be simulated within the description given by the von Kármán equations [2, 83, 91]. Such equations constitute a system of two PDEs which are nonlinear. The theoretical derivation of such equations is not extremely difficult as it involves a single second-order correction of the strain tensor in the in-plane direction with respect to the linear model by Kirchhoff. Despite this theoretical simplicity, the equations are unsolvable analytically and thus numerics is really the only tool in the hands of the analyst wishing to simulate without restrictions the large spectrum of dynamical features that such a system can offer.

Note that, at least to a first approximation, a homogeneous, isotropic, flat rectangular plate can simulate quite efficiently the sound of a gong, which is a somewhat different structure that could present inhomogeneities, anisotropy and curvature, other than a circular geometry. Thus, the plate is very attractive to study numerically because, although it is a very simple structure, its dynamics is rich enough to simulate actual percussive instruments.

This said, developing a "good" scheme for sound synthesis is not a straightforward task. There are, at least, two main problems that need to be addressed: accuracy and stability. An inaccurate reproduction of the dynamics could spoil to different degrees the quality of the simulation; on the other hand, an accurate routine might not be necessarily stable, meaning that the numerical simulation could "blow up" unexpectedly even after many steps of a seemingly convergent solution.

Bilbao [8, 7] can be regarded as the first ever reference addressing these kind of problems in the realm of the von Kármán equations. Bilbao solved the plate equations by making use of Finite Difference schemes: in particular, he proposed a second-order accurate scheme whose positive definiteness of discrete energy leads to a stability condition. The same idea of a positive-definite discrete energy is behind the development of the scheme presented in this work. However, rather than adopting a fully discretised space-time grid, as in a Finite Difference environment, the code developed for this work makes use of a modal description.

A plate is a continuous system, and thus, in the language of Mechanical Engineering, it possesses an infinite number of degrees of freedom. Truncating the degrees of freedom from an infinite number to a finite one can lead nonetheless to a faithful reproduction of the dynamics. This is common practice in what is collectively known as "modal method", which is the method developed in the course of this work. In practice, the solution to the dynamical equation is written as a weighted sum of spatial functions, whose time-dependent weights can be obtained by solving a system of Ordinary Differential Equations. Modal methods applied to the solution of PDEs are very common, and they have found applications in many fields, including that of musical acoustics. Entire projects in the realm of sound synthesis, such as MOSAIC [68] and Modalys [33], are based around the idea of modal projection. Their scope, however, is limited to linear systems. In actual fact, the modal decomposition appears as the most natural description of linear dynamical systems, which can be thought of, generally speaking, as a sum of independent contributions vibrating at specific frequencies, and known as the modes of the system. When nonlinear vibrations are in place, however, such contributions stop being independent of each other, and the modes "couple" together. The nature of these couplings depends strictly on the nature of the problem, and even seemingly slight changes of the nature of the system can lead to a completely different set of coupling mechanisms. In the case of a rectangular plate, for example, a "slight change" may be realised by changing the aspect ratio or by changing one boundary condition along one of the edges. In a Finite Difference scheme, the problem of changing the aspect ratio is treated straightforwardly by adopting an appropriate grid; the different boundary conditions can instead be simulated by modifying the matrices defining the difference operators. The very intimate nature of the scheme, however, remains unchanged. This is actually one of the most appealing features of Finite Differences schemes as opposed to modal techniques: they represent a very flexible and general method, that can be applied to many different problems.

Modal methods, on the other hand, suffer a lack of generality. This is somewhat surprising given that such techniques were the first to appear as methods of solution of PDEs [34]. The biggest problem in applying modal methods is to be able to calculate the eigenfunctions and frequencies for arbitrary boundary conditions. This is really an essential task that cannot be circumvented. Although there are some tools at the analyst's disposal, such as the Rayleigh-Ritz method, there is no universal strategy to accomplish this task, and a case-by-case study needs to be enforced. A second problem, which has already surfaced this discussion, has to do with the amount of modes to be retained to simulate the nonlinear dynamics. Such a number is of the order of a few hundreds, and thus an eigenvalue routine capable of calculating that many modes is essential. Ideally, a modal method with application to sound synthesis should avoid all ad-hoc assumptions and reproduce the dynamics faithfully.

Despite this apparently discouraging outline, there are at least two good reasons to try to perform modal synthesis of nonlinear plates. These have to do with the accuracy of the calculated solutions, and the efficiency of the numerical scheme. Modal methods, when properly set up, *are* accurate. Not only the characteristic frequencies of vibrations can be computed with a large precision, but the fact of having decomposed the original, continuous problem onto a series of "building blocks" allows to enrich the global dynamics of the plate by enriching the dynamics of each building block. In this sense, of particular interest is the possibility of adding a damping ratio to each one of the modes. In turn, this allows to simulate an extremely lively loss effect without having to spend any extra analytical or computational effort. Such a perspective is indeed very attractive in view of an application to sound synthesis, namely because loss bears a lot of perceptual information, and it can help in improving the overall perceived "quality" of the generated output. Nonetheless, one may also wish to experiment with unrealistic damping laws, in order to generate sounds which cannot be obtained when striking a real plate. In addition to being very accurate, modal techniques may as well be cheaper than Finite Differences. In actual fact, when a plate is not too thin, a fairly small number of modes suffices to reproduce the dynamics of highly nonlinear phenomena, and thus in a simulation one may just keep the number of degrees of freedom to a bare minimum, leading to fast computations.

These two reasons (accuracy and efficiency) are enough to give the modal approach a try in the realm of nonlinear vibrations. This motivation is further compounded by the fact that, for the von Kármán system, the modal couplings can be quantified quite easily in terms of the eigenfunctions of the associated linear problems [83]. Hence, if one is able to calculate with sufficient precision the eigenmodes of the problem, no ad-hoc assumptions are needed and the dynamics of the plate can be reproduced faithfully.

The applications of the modal scheme are not limited to sound synthesis. The brief discussion on the musical aspects of plates at the beginning of this introduction revealed that their acoustical properties are connected to more fundamental aspect of the science of vibrations and, more generally, physics. Thus, the outline of this thesis will try to incorporate an investigation of these more fundamental aspects. For weakly nonlinear vibrations, the amplitude-frequency dependence and stability of periodic solutions should be analysed within the framework on Nonlinear Normal Modes. The cascade of energy to higher frequencies in a strongly nonlinear regime should instead by studied statistically within the framework of Wave Turbulence.

The Nonlinear Normal Modes (NNMs) are a theoretical extension of the concept of linear modes. In a linear setting, modal decomposition allows for a simplified analysis because the modes are invariant (a solution starting on a given mode will remain indefinitely in the same mode) and they constitute the basis functions for constructing the most general solution to the PDE. In a nonlinear settings, such properties cease to exist. In actual fact, nonlinear systems display jumps, bifurcations, subharmonic and superharmonic internal resonances, modal interactions, chaotic motions and unstable solutions. There is, however, a theoretical framework which allows to extend, with some caution, the concept of linear mode to a nonlinear setting, and thus to help in the analysis of the nonlinear features. This framework is that of the Nonlinear Normal Modes [77, 78, 90]. There are many ways of defining a NNM. In essence (and what is actually of interest here) it is possible to show that, for a conservative system, an invariant manifold still exists, meaning that solutions that start on the manifold will there remain for all times. Such a manifold is tangent to the manifold of the associated linear setting (a flat plane) at each equilibrium point. Being able to compute and characterise the stability of such a manifold corresponds to gaining knowledge of the associated nonlinear system. Basically, a representation of a NNM can help answer questions about the frequency-amplitude relation of the periodic orbits, the type of bifurcations, the quality and ratio of the internal resonances. Unsurprisingly, calculating the NNM for a system cannot, in general, be accomplished analytically. Help comes in this case from continuation analysis, which permits to calculate numerically the periodic orbits as a function of the period of vibration, as well as their stability. Research of NNM is ongoing, especially in view of practical modal analysis of vibrating structures with continuously distributed nonlinearities [72]. Cyril Touzé, the first supervisor of this thesis, has largely contributed to this field with publications, for example, on damped structures [86], shells [87] and general continuous systems [89].

When a very large number of modes (say, thousands) is activated nonlinearly in a plate, a description of the dynamics must be given in terms of the statistical properties of the system. In fact, a plate at large amplitudes of vibrations can be viewed as the container of a set of nonlinear waves of different wavenumbers exchanging energy and producing other waves, and eventually giving rise to a cascade, or flux, of energy through scales. This scenario is typical of turbulent systems in hydrodynamics, and hence one may think, reasonably, that the plate also displays some kind of turbulent behaviour. A proper theoretical framework for such an analysis is offered in this case by Wave Turbulence. Such a framework was developed heavily in the mid-1960s, and was fundamentally contributed to by Zakharov, who showed for the first time that turbulent spectra of systems composed by waves only could be analytically computed by solving the kinetic equations [70, 98]. This is a huge advantage with respect to the traditional framework of hydrodynamics turbulence, where the spectra can be deduced only following dimensional arguments.

Von Kármán plates can then be studied within this framework. The seminal work by Düring *et al.* [32] laid the foundation for a lot of subsequent work by deriving the theoretical spectra of wave turbulence for thin elastic plates vibrations described by the von Kármán equations. Of particular importance are the experimental works carried out by Boudaoud *et al.* [11] and [67], who showed that the experimental spectra were in disagreement with the theoretical predictions. Hence, subsequent papers followed in order to understand, and possibly quantify, the origin of the discrepancy. Of particular importance here is the numerical aspect of such investigation. In their paper, Düring *et al.* [32] show the results coming from early numerical simulations and conclude that they are consistent with the theoretical prediction. Miquel *et al.* [63] also perform numerical simulations and conclude that, when such simulations are run using a setup close to that of the theory, then the spectra are recovered. Similar conculsions are drown by Yokoyama and Takaoka in [97].

One may then wonder why more numerical investigation is required. The answer comes from observing that all the cited works present numerical resolution of the von Kármán equations in Fourier space, not in physical space. Fundamental aspects of real experiments (such as the type of forcing, dissipation, boundary conditions, ...) are oversimplified in such Fourier schemes. In fact, in Fourier space one is free to set injection and dissipation at specific eigenmodes, as the theory assumes, but which can never be the case in a real experiment. In addition, the influence of physical boundary conditions and geometrical imperfections is not considered in such works. Part of this thesis is then concerned with running the Finite Difference scheme by Bilbao [7] in order to construct a numerical setup as close as possible to a real experiment, particularly thanks to the possibility of injecting energy by means of a pointwise, sinusoidal forcing, and to dissipate energy at all scales.

Organisation of the manuscript

The work is structured in two parts. The first part is devoted to present the numerical schemes that have been used for this work. A brief introduction to the von Kármán equations in the framework of elasticity theory is given in Chapter 1. Chapter 2 presents the modal techniques. This chapter corresponds to the core of the work developed in the course of this doctorate studies. The Finite Difference schemes by Bilbao are presented in Chapter 3.

The second part presents the applications of the numerical schemes. Chapter 4 is concerned with the nonlinear modal interactions and NNM, and corresponds to an article publisheds in Acta Mechanica [31]. Chapter 5 presents the results of flexural wave turbulence obtained by running the energy conserving Finite Difference scheme. This chapter corresponds to an article published on Physica D [28]. Finally, Chapter 6 presents the results obtained in the context of sound synthesis of gongs, by comparing the simulations coming from the modal code and the Finite Difference Scheme.

Part 1

Part I: Numerical Methods

CHAPTER 1

Dynamical equations of beams and plates

The aim of this chapter is to introduce the equations of motion of the system of interest, the von Kármán plate. To do so, the Euler-Bernoulli beam and the Kirchhoff plate are first introduced. This is done for two main reasons: firts, the von Kármán plate is, physically speaking, an extension of the Kirchhoff plate, who is itself the 2-dimensional counterpart of the Euler-Bernoulli beam; second, in the following chapter a numerical strategy in terms of modes is outlined for the von Kármán plate, and again, the beam and Kirchhoff plate will serve as the basis to test the goodness and robustness of the numerical method.

In this chapter, the equations of motion will be derived following a strict procedure: Hamilton's principle. This principle is based on the knowledge of the elastic potential energy of the system under consideration. Such a function is easily derived in terms of the strain and stress tensors of the body, and so the elasticity equations are briefly recalled at the beginning of this chapter. The index notation has been preferred over the tensorial notation making use of boldface fonts. The idea is to focus on the kinematics of the systems following very simple physical considerations: hence, a description in terms of the strain vector components will be used instead of the description making use of momenta and forces.

There are many excellent references that cover the topics overlooked in this chapter. Amongst the others, one may refer to [56] for the elasticity equations. Hamilton's principle and the equations of motion for continuous systems are treated in some detail in [37, 42]. The nonlinear von Kármán equations are derived in [69], using the tensorial description.

1.1. Elements of Elasticity Theory

An elastic body subjected to forcing displays a deformation. The effect of the deformation is to displace the body from a reference configuration to a deformed configuration. The reference configuration will be denoted here by unprimed quantities, hence before the deformation the body is assumed to occupy a certain portion of space V, bounded by a surface or contour Ω, and whose points are found at a particular position in space described by cartesian coordinates $\mathbf{x} \equiv x_i$. After the deformation occurs, primed quantities will be used to describe the new configuration, where the body occupies a portion of space V' bounded by Ω' and whose points are described by $\mathbf{x}' \equiv x'_i$. The two reference frames are assumed to share the same origin. A displacement vector $\mathbf{u} \equiv u_i$ can then be defined as the difference between x_i' and x_i, so that

$$x_i' = x_i + u_i. \tag{1.1}$$

For the remainder of the chapter, a Lagrangian description will be adopted, meaning that the coordinates x_i' and the vector u_i are considered functions of the reference configuration coordinates x_i.

1.1.1. Strain. The deformation of a body can be decomposed into a rigid body motion and relative displacements of the material particles composing the body. These displacements can be characterised by an appropriate tensor, called *strain tensor*. There are different ways of measuring the strains in a body. Here finite strains are considered, and the Green-Lagrange tensor u_{ij} is used. This tensor is a measure of the difference between two line elements after and before the deformation occurs and, in the Lagrangian description, is defined as

$$dl'^2 - dl^2 = 2u_{ik} dx_i dx_k. \tag{1.2}$$

Note that, for the remainder of this chapter, the summation rule is used[1]. In addition, partial space derivatives will be denoted by an index following a comma, (so, for example $u_{,i} = \frac{\partial u}{\partial x_i}$). An overdot will instead indicate a time derivative. To derive an explicit expression for u_{ij}, consider the line elements $dl'^2 = dx_i' dx_i'$, $dl^2 = dx_i dx_i$. Differentiating Eq. (1.1) allows to write

$$dx_i' dx_i' = (dx_i + u_{i,k} dx_k)(dx_i + u_{i,k} dx_k). \tag{1.3}$$

This results in

$$dl'^2 - dl^2 = u_{i,k} dx_k dx_i + u_{i,k} dx_k dx_i + u_{i,m} u_{i,k} dx_m dx_k. \tag{1.4}$$

Secondly, in the second term of the right hand side, the indices i and k are exchanged (this is allowed as the indices are summed); in the third term of the right hand side the indices i, m are replaced respectively by l, i so to get

$$u_{ik} = \frac{1}{2}(u_{i,k} + u_{k,i} + u_{l,i} u_{l,k}). \tag{1.5}$$

The Green-Lagrange strain tensor is clearly symmetric and nonlinear, due to the presence of the quadratic term. The nonlinear terms $u_{l,i} u_{l,k}$ can be neglected in the case of small deformations. In this case the strain tensor takes the form

$$u_{ik} = \frac{1}{2}(u_{i,k} + u_{k,i}). \tag{1.6}$$

Small deformations will be considered in the remainder of the chapter, except for section 1.3.3, where a correction to the linear strain tensor will be used.

---

[1] The index summation rule states that a same index repeated twice in a product is assumed to be summed over; hence the expression $dx_i' = Z_{ij} dx_j$ is equivalent to $dx_i' = \sum_{j=1}^{3} Z_{ij} dx_j$

1.1.2. Stress. When a body is deformed, internal forces arise amongst its material points as a reaction to the deformation. In the case of elastic bodies, these forces arise in order to restore the original configuration of the body. Such internal forces are called stresses. The deformation can arise following forces applied to an element of surface $d\Omega$, or by body forces acting on volume elements dV. At equilibrium, the sum of the body forces and surface tractions must be zero. The traction forces per unit surface are denoted here t_i. The stress tensor σ_{ik} is defined as

$$\sigma_{ik}n_k = t_i,$$

where n_k is the unit outward vector of the element of surface dS. The body forces per unit volume are denoted here by f_i.

When the body is subjected to external forcing, the equation of motion can be derived by assuming conservation of momentum, which is expressed as

$$\oint_\Omega t_i \; d\Omega + \int_V f_i \; dV = \frac{d}{dt}\int_V \rho \dot{u}_i \; dV.$$

where ρ is the volumetric density of the body (assumed constant). By making use of the divergence theorem, one can transform the surface integral into a volume integral, to get

$$\int_V \left[\rho \ddot{u}_i - \sigma_{ik,k} - f_i\right] \; dV = 0.$$

Thus, the following equation of motion and boundary conditions are recovered

$$\sigma_{ik}n_k = t_i \quad \text{on the surface of the body,} \tag{1.7a}$$

$$\rho \ddot{u}_i = \sigma_{ik,k} + f_i \quad \text{inside the body.} \tag{1.7b}$$

The stress tensor is symmetric. This is not evident from its definition as it is for the strain tensor. However, this can be obtained by considering the total moment of a body in equilibrium. Hence

$$\int_V \rho(\mathbf{x} \times \ddot{\mathbf{u}}) \; dV = \oint_\Omega \mathbf{x} \times \mathbf{t} \; d\Omega + \int_V \mathbf{x} \times \mathbf{f} \; dV \tag{1.8}$$

The cross product between two vector can be expressed in index form using the permutation symbol

$$e_{ijk} = \begin{cases} 1 & \text{if } i,j,k \text{ even permutation of } 1,2,3; \\ -1 & \text{if } i,j,k \text{ odd permutation of } 1,2,3; \\ 0 & \text{otherwise.} \end{cases}$$

The equilibrium of moment then reads

$$\frac{d}{dt}\int_V e_{ijk}x_j\dot{u}_k \; dV = \oint_\Omega e_{ijk}x_j t_k \; d\Omega + \int_V e_{ijk}x_j f_k \; dV. \tag{1.9}$$

Remembering the equilibrium equations (1.7), and transforming the surface integral into a volume integral using the divergence theorem, one get

$$\int_V e_{ijk}\sigma_{kj} \; dV = 0, \tag{1.10}$$

which is verified if and only if $\sigma_{kj} = \sigma_{jk}$.

1.1.3. Strain Energy and Stress-Strain Relationships. The energy stored in a body undergoing a deformation can be described in terms of an energy density function. This function is derived easily by considering the work of traction and body forces for a virtual displacement δu_i. In the following, the symbol overbar ($\bar{\ }$) will denote quantities per unit volume. The total work for a virtual displacement δu_i is

$$\int_V \delta\bar{W}\ dV = \int_V f_i \delta u_i\ V + \oint_\Omega t_i \delta u_i\ d\Omega.$$

Using the equilibrium equations (in this case $\dot{\mathbf{u}} = 0$ as the displacement is virtual) and the divergence theorem gives

$$\int_V \delta\bar{W}\ dV = \int_V [(\sigma_{ik,k}\delta u_i)_{,k} - \sigma_{ik,k}\delta u_i]\ dV = \int_V \sigma_{ik}\delta u_{i,k}\ dV.$$

Now, the strain component $u_{i,k}$ can be written as the sum of the symmetric tensor u_{ik} plus the antisymmetric tensor $\omega_{ik} = \frac{1}{2}(u_{i,k} - u_{k,i})$. The stress tensor is symmetric, thus $\sigma_{ik}\omega_{ik} = 0$. Plugging this result in the expression for $\delta\bar{W}$ gives

$$\int_V \delta\bar{W}\ dV = \int_V \sigma_{ik}\delta u_{ik}\ dV.$$

The work done on the body corresponds to a change in the potential energy $\bar{U}$ of the system, so that

$$\delta\bar{W} = \delta\bar{U}.$$

Thus, the strain potential energy is defined as

$$\bar{U} = \sigma_{ik}\delta u_{ik}. \tag{1.11}$$

The relation above becomes an exact differential by assuming that the potential energy $\bar{U}$ is actually a function of the strain tensor u_{ik}; in that case

$$\sigma_{ik} = \frac{\partial\bar{U}}{\partial u_{ik}}. \tag{1.12}$$

This is the fundamental relation between stress and strain. The exact form of the function $\bar{U}$ depends on the type of material (homogeneity, isotropy, degree of nonlinearity,...). For a linear, isotropic and homogeneous material it is possible to show that

$$\bar{U} = \frac{1}{2}\lambda(u_{ii})^2 + \mu u_{ik}u_{ik}, \tag{1.13}$$

where λ, μ are known as Lamé constants. These constant are related to the more common Young's modulus E and Poisson's ratio ν by

$$\begin{aligned} E &= \mu(3\lambda + 2\mu)/(\lambda + \mu) && \text{Young's modulus;} \\ \nu &= \frac{1}{2}\lambda/(\lambda + \mu) && \text{Poisson's ratio.} \end{aligned}$$

Now, the expression for $\bar{U}$ is quadratic in the strain tensor; following Euler's theorem then one has $u_{ik}\partial\bar{U}/\partial u_{ik} = 2\bar{U}$; this shows that

$$\bar{U} = \frac{1}{2}\sigma_{ik}u_{ik}. \tag{1.15}$$

This is the fundamental relation that will be used in deriving the expressions for the potential energy in the following sections. The stress strain relationships are obtained easily in terms of Young's modulus and Poisson's ratio as

$$\sigma_{ik} = \frac{E}{1+\nu}\left(u_{ik} + \frac{\nu}{1-2\nu}u_{ll}\delta_{ik}\right); \tag{1.16a}$$

$$u_{ik} = \frac{1}{E}\left((1+\sigma)\sigma_{ik} - \nu\sigma_{ll}\delta_{ik}\right); \tag{1.16b}$$

where δ_{ik} is Kronecker delta.

1.2. Variational Principles

Now that the basic equations of elasticity have been derived, the aim is to be able to determine the equation of an elastic body subjected to forces. The developments will stem from Hamilton's principle.

Newton's basic laws of physics consider the case of material particles acted upon by forces. The extension of Newtonian methods to a body occupying a finite portion of space is done by integrating the effects of the single "material particles" over the volume V. Lagrange generalised this process for a system comprising a finite number of degrees of freedom, and the motion of the system is fully specified once position and velocities of all the components are specified at an instant of time t_0. Hamilton stated the problem somewhat differently, by specifying the position of the system at two instants t_0, t_1, and by proving that the dynamics therein follows a geodesic. The mathematical statement of this principle is

$$\delta\int_{t_0}^{t_1}(T - U + W_e)dt = 0, \qquad \delta u_i(t_1) = \delta u_i(t_2) = 0; \tag{1.17}$$

where T is the kinetic energy of the system, U is the potential energy, and W_e is the work done by the external forces on the system. The symbol δ is intended in the sense of calculus of variations. The equations of motion and boundary conditions can be derived from the integral above. The three terms involving T, U, W_e are now analysed. The symbol $\bar{}$ will denote a quantity per unit volume. The body is assumed to have a constant density ρ. The kinetic energy density is

$$\bar{T} = \frac{\rho}{2}\dot{u}_i\dot{u}_i, \qquad \delta\bar{T} = \rho\dot{u}_i\delta u_i.$$

Integrating by parts in the time variable gives

$$\delta\int_{t_0}^{t_1}\bar{T}\,dt = \underbrace{\int_V [\rho\dot{u}_i\delta u_i]\Big|_{t_0}^{t_1} dV}_{=0} - \int_{t_0}^{t_1}\int_V [\rho\ddot{u}_i\delta u_i]\,dV dt.$$

The potential energy density is

$$d\bar{U} = \frac{\partial U}{\partial u_{ij}} du_{ij}; \qquad \delta\bar{U} = \frac{\partial \bar{U}}{\partial u_{ij}}\delta u_{ij} = \frac{1}{2}\frac{\partial \bar{U}}{\partial u_{ij}}(u_{i,j} + u_{j,i}).$$

Thus

$$\delta \int_{t_0}^{t_1} \bar{U} \; dV = \int_{t_0}^{t_1} \int_V \frac{1}{2}\frac{\partial \bar{U}}{\partial u_{ij}}(\delta u_{i,j} + \delta u_{j,i}) dV.$$

The last expression can be integrated by parts, to give

$$\delta \int_{t_0}^{t_1} \bar{U} \; dV = \frac{1}{2}\int_{t_0}^{t_1} \left\{ \oint_\Omega \left(\frac{\partial \bar{U}}{\partial u_{ij}}\delta u_i n_j + \underbrace{\frac{\partial \bar{U}}{\partial u_{ij}}\delta u_j n_i}_{A.} \right) d\Omega - \int_V \left[\left(\frac{\partial \bar{U}}{\partial u_{ij}}\right)_{,j} \delta u_i + \underbrace{\left(\frac{\partial \bar{U}}{\partial u_{ij}}\right)_{,i} \delta u_j}_{B.} \right] dV \right\} dt$$

In A. and B. the indices (i, j) are swapped; owing to the symmetry of the strain tensor and remembering that $\sigma_{ij} = \partial\bar{U}/\partial u_{ij}$ one gets

$$\delta \int_{t_0}^{t_1} U dt = \int_{t_0}^{t_1} \left\{ \oint_\Omega \sigma_{ij}\delta u_i n_j \; d\Omega - \int_V \sigma_{ij,j}\delta u_i \; dV \right\} \; dt.$$

The last variation to calculate is the external work. This is done easily considering

$$\int_V \delta\bar{W}_e \; dV = \int_V f_i \delta u_i \; dV + \oint_\Omega t_i \delta u_i \; d\Omega.$$

Hence Hamilton's principle reduces to

$$\delta \int_{t_0}^{t_1} (T - U + W_e) \; dt = \int_{t_0}^{t_1} \int_V [-\rho\ddot{u}_i + f_i + \sigma_{ij,j}] \; dV dt - \int_{t_0}^{t_1} \oint_\Omega [\sigma_{ij} n_j - t_i] \; d\Omega dt = 0. \tag{1.18}$$

It is possible then to recognize the following

Equation of Motion	*Boundary Conditions*
$\rho\ddot{u}_i = f_i + \sigma_{ij,j}$	$\sigma_{ij} n_j = t_i$

These equations are formally identical to Eqs. (1.7), and thus it is seen that Hamilton's principle allows to derive the same equation of motion and boundary conditions as the classical approach in terms of equilibrium of forces. In the following sections, the equations of motion will be derived systematically by making use of Hamilton's principle. The strategy to follow is to:

1. list the kinematic hypotheses of the problem in line with physical reasoning;
2. derive either the strain tensor (stress tensor) in accordance with the hypotheses in 1., and use Eq. (1.16) to derive the stress tensor (strain tensor);
3. derive an expression for the potential energy by making use of the general expression (1.15);
4. use the kinetic and potential energy expressions to formulate Hamilton's principle;
5. integrate by parts in order to obtain the equation of motion and the boundary conditions.

1.3. Applications to Beams and Plates

Now that the constitutive equations of elasticity and variational principles have been recalled, it is possible to derive the equations of motion for continuous systems. The cases presented here deal with isotropic materials, for which the linear stress-strain relationships hold. The deformations are supposed to be homogeneous. Nonlinearities will then appear from geometric considerations, due to the large amplitude of vibrations. The cases presented here are those that will be considered in the following chapters: the Euler-Bernoulli beam, the Kirchhoff plate, and the von Kármán plate.

1.3.1. The Euler-Bernoulli Beam. The Euler-Bernoulli beam is the simplest model to describe bending in a slender elastic structure. It is a linear model valid for small vibration amplitudes, and considers the flexural vibrations of a slender beam of cross section $A(x)$ and length L. The following assumptions are considered:

- The material is homogeneous and isotropic, and obeys the linear stress-strain relationships (1.16).
- The bending is small compared to the length l of the beam.
- The motion is planar and takes place in the $x - z$ plane. Thus $u_y = 0$.
- The bending in the z direction is uniform, so that $u_z \equiv w = w(x)$.
- The cross section of the beam remains perpendicular to the neutral axis of the beam after the deformation occurs. This implies that the longitudinal strain u_{xx} can be written as $u_{xx} = z/r_x$, where r_x is the radius of curvature in the $x - z$ plane. Owing to the small deflections assumption, one may write $1/r_x = -w_{,xx}$. Hence $u_{xx} = -zw_{,xx}$. Thus, $u_x \equiv u = -zw_{,x}$

Owing to the hypotheses above, the linear strain tensor can be written as

$$u_{xx} = -zw_{,xx}; \qquad u_{xz} = u_{zz} = 0.$$

The equation of motion may be derived from varying the total energy of the system, as in Eq. (1.17). The potential energy per unit volume can be calculated easily thanks to Eq. (1.15). Thus

$$\bar{U} = \frac{1}{2}\sigma_{ik}u_{ik} = \frac{1}{2}\sigma_{xx}u_{xx}.$$

The stress component σ_{xx} is obtained from the stress-strain relationships (1.16) by setting $\nu = 0$ (the Poisson effect is neglected). Hence

$$\sigma_{xx} = Eu_{xx}.$$

The expression for the total potential energy is then given by

$$U = \frac{1}{2}\int_0^L \int_{A(x)} Ez^2(w_{,xx})^2 \; dxdA.$$

Introducing the geometric moment of inertia $I(x) = \int_{A(x)} z^2 dA$ gives

$$U = \frac{1}{2}\int_0^L EI(x)(w_{,xx})^2 \; dx. \tag{1.19}$$

The kinetic energy is obtained as the sum of two contributions, the motion in the z direction and the rotation of the cross section. Hence

$$T = \frac{\rho}{2}\int_0^L \int_{A(x)} (\dot{u}^2+\dot{w}^2)\ dAdx = \frac{\rho}{2}\int_0^L \int_{A(x)} (z^2(\dot{w}_{,x})^2+\dot{w}^2)\ dAdx = \frac{\rho}{2}\int_0^L I(x)\dot{w}_{,x}^2\ dx+\frac{\rho}{2}\int_0^L A(x)\dot{w}^2\ dx.$$

Upon definitions of the mass per unit length $m = \rho A(x)$ and the cross section gyration radius $r^2 = I(x)/A(x)$, the form for the kinetic energy is

$$T = \frac{1}{2}\int_0^L mr^2\dot{w}_{,x}^2\ dx + \frac{1}{2}\int_0^L m\dot{w}^2\ dx. \tag{1.20}$$

The equation for the free vibrations of the Euler-Bernoulli beam can be easily obtained from the variational principle Eq. (1.17), where it is assumed that no external forces are acting. Thus

$$\delta\int_{t_1}^{t_2}\int_0^L [m\dot{w}^2 + mr^2\dot{w}_{,x}^2 - EI(x)w_{,xx}^2]\ dxdt = 0. \tag{1.21}$$

The integral above contains three terms, the variation of which is given by

$$\delta(m\dot{w}^2) = 2m\dot{w}\delta\dot{w}; \tag{1.22a}$$

$$\delta(mr^2\dot{w}_{,x}^2) = 2mr^2\dot{w}_{,x}\delta\dot{w}_{,x}; \tag{1.22b}$$

$$\delta(EI(x)w_{,xx}^2) = 2EI(x)w_{,xx}\delta w_{,xx}. \tag{1.22c}$$

To obtain the equation of motion, integration by parts is performed. Particularly, Eq. (1.22a) will be integrated by parts once in the time variable; Eq. (1.22b) will be integrated once in the time variable, and once in the space variable; Eq. (1.22c) will be integrated twice in the space variable. This results in

$$\int_{t1}^{t_2}\int_0^L \delta(m\dot{w}^2)\ dxdt = \underbrace{\int_0^L \left[2m\dot{w}\delta w\Big|_{t_1}^{t_2}\right]\ dx}_{=0} - \int_{t1}^{t_2}\int_0^L 2m\ddot{w}\delta w\ dxdt; \tag{1.23a}$$

$$\int_{t1}^{t_2}\int_0^L \delta(mr^2\dot{w}_{,x}^2)\ dxdt =$$

$$\underbrace{\left[2mr^2\dot{w}_{,x}\delta w\Big|_{t_1}^{t_2}\right]\Bigg|_0^L}_{=0} - \underbrace{\int_0^L (2mr^2\dot{w}_{,x})_{,x}\delta w\Big|_{t_1}^{t_2}\ dx}_{=0}$$

$$-\int_{t_1}^{t_2} 2mr^2\ddot{w}_{,x}\delta w\Big|_0^L\ dt + \int_{t1}^{t_2}\int_0^L (2mr^2\ddot{w}_{,x})_{,x}\ dxdt; \tag{1.23b}$$

$$\int_{t1}^{t_2}\int_0^L \delta(EI(x)w_{,xx}^2)\ dxdt =$$

$$\int_{t_0}^{t_1}\left\{\left[2EI(x)w_{,xx}\delta w_{,x}\Big|_0^L\right] - \left[(2EI(x)w_{,xx})_{,x}\delta w\Big|_0^L\right]\right\}\ dt + \int_{t1}^{t_2}\int_0^L (2EI(x)w_{,xx})_{,xx}\ dxdt. \tag{1.23c}$$

Following the assumption of zero virtual displacement δw at t_1, t_2, some boundary integrals vanish in the equations above. Collecting these results together gives

$$\delta \int_{t_1}^{t_2} \int_0^L (T-U)\ dxdt = \int_{t_1}^{t^2} \int_0^L \left[(mr^2 \ddot{w}_{,x})_{,x} - m\ddot{w} - \left(EI(x) w_{,xx}\right)_{,xx} \right] \delta w\ dxdt +$$

$$\int_{t_1}^{t_2} \left\{ \left[\left(EI(x) w_{xx}\right)_{,x} - mr^2 \ddot{w}_{,x} \right] \delta w \Big|_0^L - \left[EI(x) w_{xx}\right] \delta w_{,x} \Big|_0^L \right\} dt = 0. \tag{1.24}$$

This equality permits to state the following

Equation of Motion of Euler-Bernoulli Beam with Rotatory Inertia

$$\rho A \ddot{w} = (\rho A r^2 \ddot{w}_{,x})_{,x} - E\left(I(x) w_{,xx}\right)_{,xx};$$

Boundary Conditions

Simply Supported End	Clamped End	Free End
$w = w_{,xx} = 0.$	$w = w_{,x} = 0.$	$\rho A r^2 \ddot{w}_{,x} = E\left(I(x) w_{,xx}\right)_{,x};$ $w_{,xx} = 0.$

A further simplification can be introduced at this stage. In actual fact, the inertia terms can be neglected at low frequencies, because the rotation of the cross section becomes small with respect to the flexural velocity. When this is done, the Euler-Bernoulli beam equations are obtained as:

Equation of Motion of Euler-Bernoulli Beam without Rotatory Inertia

$$\rho A \ddot{w} = -E\left(I(x) w_{,xx}\right)_{,xx};$$

Boundary Conditions

Simply Supported End	Clamped End	Free End
$w = w_{,xx} = 0.$	$w = w_{,x} = 0.$	$w_{,xx} = w_{,xxx} = 0.$

1.3.2. Small Deflections of Plates: the Kirchhoff Equation. The Kirchhoff plate is the two-dimensional analogue of the Euler-Bernoulli beam. Its dynamics consists of flexural vibrations, with no in-plane motion. The plate occupies a portion of space V, composed of a rectangular surface S and a thickness h, hence $V = [0, L_x] \times [0, L_y] \times [-h/2, h/2]$, with $h \ll L_x$, $h \ll L_y$. The plate is equipped with a neutral surface, which serves as the analogue of the neutral axis of the beam. The same kinematic assumptions apply, except that now the vertical deflection w is a function of the two space coordinates x and y, hence $w \equiv w(x, y)$. In addition

- The material is isotropic, homogeneous with density ρ, Young's modulus E and Poisson's ratio ν, and obeys the linear stress-strain relationships (1.16).
- The bending is small compared to the thickness h of the plate. The small displacement strain tensor is used.
- On the neutral surface the displacement vector is $u_i = (0, 0, w(x, y))$. Away from the surface, given the smallness of the thickness, the displacement vector is defined as $u_i = (u(x, y, z), v(x, y, z), w(x, y))$.
- Plane sections of the plate remain plane and perpendicular to the neutral surface when deformations occur.

The plate is thin, and the amplitude of the flexural waves developing on the surface are small compared to the thickness. Thus, relatively small forces are applied to the surface of the plate in order to bend it. These forces are in magnitude considerably smaller than the stresses developing in the plate, thus they can be neglected in the boundary term of Eq. (1.7). Hence

$$\sigma_{ik} n_k = 0.$$

The plate is only slightly bent, hence $n_k = n_z$ everywhere on the surface. Consequently

$$\sigma_{xz} = \sigma_{yz} = \sigma_{zz} = 0.$$

These relations hold true along the thickness of the plate, because h is small. From the stress-strain relationships (1.16), it is seen that $u_{zx} \propto \sigma_{zx}$, $u_{zy} \propto \sigma_{zy}$, hence

$$u_{zx} = 0 = \frac{1}{2}\left(u_{,z} + w_{,x}\right); \qquad \rightarrow \qquad u = -z w_{,x}$$

$$u_{zy} = 0 = \frac{1}{2}\left(v_{,z} + w_{,y}\right); \qquad \rightarrow \qquad v = -z w_{,y}$$

Note that the constant of integration was chosen to make (u, v) vanish on the neutral surface at $z = 0$. Thus

$$u_{xx} = -z w_{,xx}; \;\; u_{yy} = -z w_{,yy}; \;\; u_{xy} = -z w_{,xy}.$$

The strain component u_{zz} is derived easily by equating to zero the equation for σ_{zz} in the stress-strain relationships, and by using the strain components above. Hence

$$u_{zz} = \frac{\nu}{1-\nu} z (w_{,xx} + w_{,yy}).$$

It is now possible to derive an explicit expression for the strain potential energy density in terms of the displacement $w(x, y)$:

$$\bar{U} = \frac{1}{2}\sigma_{ik} u_{ik} = z^2 \frac{E}{1+\nu}\left\{\frac{1}{2(1-\nu)}(\Delta w)^2 + \left[(w_{,xy})^2 - w_{,xx} w_{,yy}\right]\right\}, \tag{1.26}$$

where the symbol Δ denotes the bi-dimensional Laplacian. Integrating over the volume element $dV = dxdydz$, and introducing the rigidity constant $D = Eh^3/12(1-\nu^2)$ gives

$$U = \frac{D}{2}\int_0^{L_y}\int_0^{L_x} \{(\Delta w)^2 + 2(1-\nu)[(w_{,xy})^2 - w_{,xx} w_{,yy}]\} dxdy. \tag{1.27}$$

The kinetic energy is expressed easily as

$$T = \frac{\rho h}{2} \int_0^{L_y} \int_0^{L_x} (\dot{w})^2 dxdy. \tag{1.28}$$

Note that the in-plane contributions of the kinetic energies have been neglected. As for the case of the beam, this will pose limitations to the validity of the plate model at high frequencies. The equation of motion with the boundary conditions can be derived by considering variations of the Lagrangian of the system

$$\delta \int_{t_1}^{t_2} (T - U) dt = 0; \qquad \delta w(t_1) = \delta w(t_2) = 0. \tag{1.29}$$

Now

$$\delta U = D \int_0^{L_y} \int_0^{L_x} \{(\Delta w)\delta(\Delta w) + (1-\nu)[2w_{,xy}\delta w_{,xy} - w_{,xx}\delta w_{,yy} - w_{,yy}\delta w_{,xx}]\} dxdy;$$

$$\delta T = \rho h \int_0^{L_y} \int_0^{L_x} \dot{w}\delta\dot{w} \ dxdy.$$

These variations are inserted into Eq. (1.29); the kinetic term is integrated by parts once in the time variable, whereas the potential term is integrated by parts twice in the space variables. The final result is

$$\delta \int_{t_1}^{t_2} T dt = - \int_{t_1}^{t_2} \int_0^{L_y} \int_0^{L_x} \rho h \ddot{w} \delta w \ dxdydt. \tag{1.31a}$$

$$\begin{aligned} \delta \int_{t_1}^{t_2} U dt = \int_{t_1}^{t_2} \Bigg\{ & \int_0^{L_y} \int_0^{L_x} D\Delta\Delta w \delta w \ dxdy \\ & + \int_0^{L_y} (w_{,xx} + \nu w_{,yy}) \Big|_0^{L_x} \delta w_{,x} dy - \int_0^{L_y} (w_{,xxx} + (2-\nu) w_{,xyy}) \Big|_0^{L_x} \delta w \ dy \\ & + \int_0^{L_x} (w_{,yy} + \nu w_{,xx}) \Big|_0^{L_y} \delta w_{,y} dx - \int_0^{L_x} (w_{,yyy} + (2-\nu) w_{,xxy}) \Big|_0^{L_y} \delta w \ dx + w_{,xy}\delta w \Big|_{\text{at corners}} \Bigg\} dt. \end{aligned} \tag{1.31b}$$

It is evident that the application of Hamilton's principle allowed to write

$$\delta U = \delta \mathrm{S} + \delta \mathrm{B},$$

so that the contribution is split between a surface integral and boundary integrals; in other words, part of the potential energy contributes to the inertial forces that appear in the equation of motion through $\delta \mathrm{S}$, and the other part has to be compensated by the boundary conditions, so that $\delta \mathrm{B}$ disappears along the contour. The results are summarised as follows (the indices n, t refer to a direction normal and tangential to the boundary, respectively):

Equation of Motion

$$\rho h \ddot{w} = -D\Delta\Delta w$$

Boundary Conditions

Simply Supported Edge	Clamped Edge	Free Edge
$w = w_{,nn} = 0.$	$w = w_{,n} = 0.$	$w_{,nnn} + (2-\nu)w_{,ntt} =$ $w_{,nn} + \nu w_{,tt} = 0;$ $w_{,nt} = 0$ at corners.

1.3.3. Large Deflections of Plates: the von Kármán Equations. The results derived in the previous section are valid in the limit of small vibrations/small frequencies. When large-amplitude vibrations are considered, stretching arises in the in-plane directions as a consequence of bending. For example, let a circular plate be bent by applying a force at is centre: if the circumference stays constant, the diameter must increase; if the diameter remains constant, then the circumference gets smaller. Again, the plate considered is thin, and occupies a portion of space V, composed of a rectangular surface S and a thickness h, hence $V = [0, L_x] \times [0, L_y] \times [-h/2, h/2]$, with $h \ll L_x$, $h \ll L_y$. Then

- The material is isotropic, homogeneous with density ρ, Young's modulus E and Poisson's ratio ν, and obeys the elasticity equations (1.16).
- The bending is the same order as the thickness h of the plate. However, nonlinear terms deriving form the x, y components of the in-plane strain tensor are neglected.
- In-plane inertia terms are neglected.

For small flexural vibrations the stretching can be neglected. Thus the contribution to the potential energy comes entirely from flexural deformations. For a plate undergoing large deflections, a second contribution to the potential energy arises as a consequence of stretching due to bending and hence the total strain energy density becomes

$$\bar{U} = \bar{U}_b + \bar{U}_s,$$

where $\bar{U}_b$ is the energy due to pure bending (see Eq. (1.26)) and $\bar{U}_s$ is the contribution coming from the stretching. This contribution is calculated easily once a corrected form for the in-plane strain tensor is derived. For that, consider two points on the surface of the plate before the deformation, separated by an infinitesimal distance dl. Greek indices will be used to denote the coordinates (x, y) of the plate surface. Hence

$$dl^2 = dx_\alpha dx_\alpha.$$

After the deformation, the infinitesimal distance becomes dl' and is

$$dl'^2 = (dx_\alpha + du_\alpha)(dx_\alpha + du_\alpha) + dw^2,$$

where the strain vector has been denoted $u_i = (u(x,y), v(x,y), w(x,y))$. The expression above can rewritten as

$$dl'^2 = (dx_\alpha + u_{\alpha,\beta} dx_\beta)\,(dx_\alpha + u_{\alpha,\gamma} dx_\gamma) + w_{,\alpha} dx_\alpha\; w_{,\beta} dx_\beta,$$

and thus

$$dl'^2 - dl^2 = (u_{\alpha,\beta} + u_{\beta,\alpha})\, dx_\alpha dx_\beta + w_{\alpha,\beta} w_{\beta,\alpha} dx_\alpha dx_\beta = 2u_{\alpha\beta} dx_\alpha dx_\beta, \tag{1.32}$$

where the term proportional to $u_{\alpha,\beta} u_{\alpha,\gamma}$ (higher order in u_α) has been neglected. Then

$$\bar{U}_s = \frac{1}{2}\sigma_{\alpha\beta} u_{\alpha\beta},$$

where $\sigma_{\alpha\beta}$ is given by the strain-stress relationships (1.16). The total potential energy due to stretching is obtained by integrating the expression above over the volume of the plate. Hence

$$\bar{U}_s = \frac{h}{2}\int_0^{L_y}\int_0^{L_x} u_{\alpha\beta}\sigma_{\alpha\beta} dxdy.$$

Owing to the symmetry of the stress and strain tensors, the variation of the potential energy becomes

$$\delta U_s = h\int_0^{L_y}\int_0^{L_x} \sigma_{\alpha\beta}(\delta u_{\alpha,\beta} + w_\alpha \delta w_{,\beta}) dxdy.$$

Integrating by parts the expression above gives

$$\delta U_s/h = \int_0^{L_y} (\sigma_{xx}\delta u + \sigma_{xx} w_{,x}\delta w)\Big|_0^{L_x} dy - \int_0^{L_y}\int_0^{L_x} \sigma_{xx,x}\delta u_x + (\sigma_{xx} w_{,x})_{,x}\delta w dxdy \tag{1.33}$$

$$+ \int_0^{L_y} (\sigma_{yx}\delta v + \sigma_{yx} w_{,y}\delta w)\Big|_0^{L_x} dy - \int_0^{L_y}\int_0^{L_x} \sigma_{yx,x}\delta u_y + (\sigma_{yx} w_{,y})_{,x}\delta w dxdy \tag{1.33}$$

$$+ \int_0^{L_x} (\sigma_{xy}\delta u + \sigma_{xy} w_{,x}\delta w)\Big|_0^{L_y} dx - \int_0^{L_y}\int_0^{L_x} \sigma_{xy,y}\delta u_x + (\sigma_{xy} w_{,x})_{,y}\delta w dxdy \tag{1.33}$$

$$+ \int_0^{L_x} (\sigma_{yy}\delta v + \sigma_{yy} w_{,y}\delta w)\Big|_0^{L_y} dx - \int_0^{L_y}\int_0^{L_x} \sigma_{yy,y}\delta u_y + (\sigma_{yy} w_{,y})_{,y}\delta w dxdy \tag{1.33}$$

Again, the variation of the potential energy is the sum of boundary terms and surface terms, in other words

$$\delta U_s/h = \delta \mathrm{B} + \delta \mathrm{S}. \tag{1.34}$$

The surface terms can be collected together in the following way

$$\delta \mathrm{S} = -\int_0^{L_y}\int_0^{L_x} \{(\sigma_{xx,x} + \sigma_{xy,x})\,\delta u + (\sigma_{yy,y} + \sigma_{yx,x})\,\delta v +$$
$$\Big[(\sigma_{xx} w_{,x} + \sigma_{xy} w_{,y})_{,x} + (\sigma_{yy} w_{,y} + \sigma_{yx} w_{,x})_{,y}\Big]\,\delta w\Big\}\, dxdy.$$

A simplified expression can be found by considering Airy's stress function χ defined implicitly as

$$\chi_{,xx} = \sigma_{yy}; \;\; \chi_{,xy} = -\sigma_{xy}; \;\; \chi_{,yy} = \sigma_{xx}. \tag{1.36}$$

Owing to this definition, one gets immediately

$$\sigma_{xx,x} + \sigma_{xy,y} = \sigma_{yy,y} + \sigma_{yx,x} = 0,$$

and hence the integral for $\delta \mathrm{S}$ above simplifies to

$$\delta \mathrm{S} = -\int_0^{L_y}\int_0^{L_x} \mathcal{L}(\chi, w)dxdy, \tag{1.37}$$

where $\mathcal{L}(\cdot,\cdot)$ is a bilinear operator known as von Kármán operator, who reads

$$\mathcal{L}(\chi, w) = \chi_{,xx}w_{,yy} + \chi_{,yy}w_{,xx} - 2\chi_{,xy}w_{,xy}. \tag{1.38}$$

The variation of the pure bending energy δU_b was calculated in the previous section. Hence, the variation of the potential energy for a plate undergoing large deflections can be written as

$$\delta U = \delta U_b + \delta U_s = \int_0^{L_y}\int_0^{L_x} \left(D\Delta\Delta w - h\mathcal{L}(\chi, w)\right)\delta w \; dxdy = 0. \tag{1.39}$$

It is seen that the problem of flexural vibrations is now coupled to in-plane motion in a way described by the stress function χ. Thus, a second constitutive equation is needed, as the unknowns are now the vertical displacement $w(x, y)$ and the stress function $\chi(x, y)$. This equation is obtained from the stress-strain relationships for the in-plane motion. The strains are

$$u_{xx} = (\sigma_{xx} - \nu\sigma_{yy})/E; \;\; u_{yy} = (\sigma_{yy} - \nu\sigma_{xx})/E; \;\; u_{xy} = (1+\nu)\sigma_{xy}/E. \tag{1.40}$$

Hence, inserting (1.36) into (1.40) and remembering the defintion of the in-plane strain tensor $u_{\alpha,\beta}$ in (1.32) one gets

$$u_{,x} + \frac{1}{2}(w_{,x})^2 = \frac{1}{E}(\chi_{,yy} - \nu\chi_{,xx}); \tag{1.41a}$$

$$v_{,y} + \frac{1}{2}(w_{,y})^2 = \frac{1}{E}(\chi_{,xx} - \nu\chi_{,yy}); \tag{1.41b}$$

$$u_{,y} + v_{,x} + w_{,x}w_{,y} = -\frac{2(1+\nu)}{E}\chi_{,xy}. \tag{1.41c}$$

Taking $\partial^2/\partial y^2$ of the first, $\partial^2/\partial x^2$ of the second, $-\partial^2/\partial y\partial x$ of the third and summing gives

$$\Delta\Delta\chi = -\frac{E}{2}\mathcal{L}(w, w). \tag{1.42}$$

This is the second constitutive equation that must be used in conjunction with Eq. (1.39). These equations have to be supplied with boundary conditions. These come from the boundary terms of the variation of the total potential energy. The variation for pure bending was calculated previously for the case of the Kirchhoff plate. The contribution to the boundary conditions coming from the stretching energy is obtained by exploiting the term $\delta\mathrm{B}$ of Eq. (1.34). The boundary term can be expressed as

$$\delta\mathrm{B} = \int_0^{L_y} [\sigma_{xx}\delta u + \sigma_{xy}\delta v + (\sigma_{xx}w_{,x} + \sigma_{xy}w_{,y})\delta w]\Big|_0^{L_x} dy + \int_0^{L_x} [...]\Big|_0^{L_y} dx, \tag{1.43}$$

where the second integral is obtained form the first by swapping x and y. For starters, consider the term

$$\int_0^{L_y} [\sigma_{xx}\delta u + \sigma_{xy}\delta v]\Big|_0^{L_x} dy.$$

Two situations are possible:

(1) the edge is movable ($\delta u \neq 0$, $\delta v \neq 0$);
(2) the edge is immovable ($\delta u = \delta v = \delta w = 0$).

Case 1. is solved easily by imposing $\sigma_{xx} = \sigma_{xy} = 0$. In terms of the stress function

$$\chi_{,yy} = \chi_{,xy} = 0.$$

In terms of the normal and tangential indices n, t this conditions is

$$\chi_{,tt} = \chi_{,nt} = 0. \tag{1.44}$$

Case 2. is solved by imposing $\delta u = \delta v = 0$. This form of the boundary conditions is not very useful as it involves the strain components u, v that should be eliminated in favour of the stress function. Hence

$$\int_0^{L_y} [\sigma_{xx}\delta u + \sigma_{xy}\delta v]\Big|_0^{L_x} dy = \underbrace{\int_0^{L_y} [\chi_{,yy}\delta u]\Big|_0^{L_x} dy}_{A} - \underbrace{\int_0^{L_y} [\chi_{,xy}\delta v]\Big|_0^{L_x} dy}_{B}.$$

Obviously one must impose $A = B = 0$. Integral A is calculated by parts to give

$$A = \underbrace{\chi_{,y}\delta u\Big|_{\text{corners}}}_{=0} - \int_0^{L_y} \chi_{,y}\delta u_{,y}\Big|_0^{L_x} dy = 0.$$

The first integral disappears as, by hypothesis, $\delta u = 0$. In the second integral, the expression for $\delta u_{,y}$ is derived from identities (1.41), and considering that $\delta w = 0$. Hence

$$\delta u_{,y} = -\left(\frac{2(1+\nu)}{E}\delta\chi_{,y} + \delta v\right)_{,x}.$$

Thus

$$A = \int_0^{L_y} \left[\frac{2(1+\nu)}{E}\delta\chi_{,y} + \delta v\right]_{,x} \chi_{,y}\Big|_0^{L_x} dy = 0.$$

Integrating a second time by parts results in

$$A = \chi \underbrace{\left[\frac{2(1+\nu)}{E}\delta\chi_{,xy} + \delta v_{,x}\right]}_{=\delta u_{,y}=0}\Big|_{\text{corners}} - \int_0^{L_y} \left[\frac{2(1+\nu)}{E}\delta\chi_{,yy} + \delta v_{,y}\right]_{,x} \chi\Big|_0^{L_x} dy = 0.$$

The expression for $\delta v_{,y}$ is again derived from identities (1.41). Substituting in the integral above gives

$$-\int_0^{L_y} \frac{\delta}{E}\left[(2+\nu)\chi_{,xyy} + \chi_{,xxx}\right]\chi\Big|_0^{L_x} dy = 0,$$

or

$$(2+\nu)\chi_{,xyy} + \chi_{,xxx} = 0,$$

or

$$(2+\nu)\chi_{,ntt} + \chi_{,nnn} = 0, \tag{1.45}$$

The integral B is easily solved. Integration by parts gives

$$B = \underbrace{\chi_{,x}\delta v}_{=0}\Big|_0^{L_x} - \int_0^{L_y} \chi_{,x}\delta v_{,y} dy = 0.$$

Substituting the expression for $\delta v_{,y}$ from identities (1.41) gives immediately

$$B = -\int_0^{L_y} \chi_{,x}\frac{\delta}{E}(\chi_{,xx} - \nu\chi_{,yy})dy = 0,$$

or

$$\chi_{,xx} - \nu\chi_{,yy} = 0,$$

or

$$\chi_{,nn} - \nu\chi_{,tt} = 0, \tag{1.46}$$

Summarising, conditions (1.44) must be imposed for a movable edge in the in-plane direction, whereas conditions (1.45) and (1.46) must be imposed in the case of an immovable edge. The last part of the boundary integral (1.43) involves a factor proportional to δw. This part has to be added to the boundary integrals coming from the pure bending contributions, that are also proportional to δw (see Eq. (1.31)). These terms describe the conditions of the edge rotation. Summarising

(1) Transversely immovable edge

$$w = 0; \tag{1.47}$$

(2) Transversely movable edge

$$w_{,nnn} + (2-\nu)w_{,ntt} - \frac{h}{D}\left(\chi_{,tt}w_{,n} - \chi_{,nt}w_{,t}\right) = 0. \tag{1.48}$$

In order to obtain the equations of motion, the variation of the kinetic energy has to be derived. This is was done already in Eq. (1.31). Introducing the function $F = h\chi$, the von Kármán equations take the following form

Equation of Motion

$$\rho h\ddot{w} = -D\Delta\Delta w + \mathcal{L}(w,F);$$

$$\Delta\Delta F = -\frac{Eh}{2}\mathcal{L}(w,w).$$

Boundary Conditions

In-plane direction	Edge Rotation	Edge Vertical Translation
• Movable	• Rotationally Free	• Transversely Movable
$F_{,nt} = F_{,tt} = 0.$	$w_{,nn} + \nu w_{,tt} = 0.$	$w_{,nn} + (2-\nu) w_{,ntt}$ $-\frac{1}{D}(F_{,tt}w_{,n} - F_{,nt}w_{,t}) = 0;$ $w_{,nt} = 0$ at corners.
• Immovable (with $w = 0$)	• Rotationally Immovable	• Transversely Immovable
$F_{,nn} - \nu F_{,tt} =$ $F_{,nnn} + (2+\nu)F_{,ntt} = 0.$	$w_{,n} = 0.$	$w = 0.$

1.3.3.1. *Properties of the L operator and energy expressions.* A useful property of the von Kármán operator $\mathcal{L}(\cdot,\cdot)$ can be recovered by considering the following integral

$$\mathcal{I} = \int_0^{L_y}\int_0^{L_x} \alpha\mathcal{L}(\beta,\gamma)\ dxdy,$$

for generic functions α, β, γ. Integrating by parts results in

$$\mathcal{I} = \int_0^{L_y}\int_0^{L_x} \gamma\mathcal{L}(\alpha,\beta)\ dxdy + \oint_\Omega \left[\beta_{,tt}(\alpha\gamma_{,n} - \gamma\alpha_{,n}) - \beta_{,nt}(\alpha\gamma_{,t} - \gamma\alpha_{,t})\right]\, d\Omega, \tag{1.49}$$

which has been called "triple self-adjointess" property [8, 83].

Consider now the first of the two equations of motion of the von Kármán system. Multiplying both terms by $\dot{w}$ and integrating over the surface of the plate gives

$$\rho h \int_0^{L_y}\int_0^{L_x} \ddot{w}\dot{w}\ dxdy + D\int_0^{L_y}\int_0^{L_x} \Delta\Delta w\dot{w}\ dxdy = \int_0^{L_y}\int_0^{L_x} \mathcal{L}(w,F)\dot{w}\ dxdy.$$

Integration by parts is now performed. Owing to property (1.49), and remembering that $L(w,w) = -2/Eh\Delta\Delta F$, one can effortlessly see that the expression above reduces to

$$\frac{d}{dt}\left[\frac{\rho h}{2}\int_0^{L_y}\int_0^{L_x} \dot{w}^2\ dxdy + \frac{D}{2}\int_0^{L_y}\int_0^{L_x} (\Delta w)^2\ dxdy + \frac{1}{2Eh}\int_0^{L_y}\int_0^{L_x} (\Delta F)^2\ dxdy\right] = \mathrm{B} = 0, \tag{1.50}$$

where B is a boundary integral that vanished under the prescribed boundary conditions. The left hand side can be then interpreted as $d\mathfrak{E}/dt = 0$, where $\mathfrak{E}$ is the total energy of the plate, composed of

$$T = \int_0^{L_y}\int_0^{L_x} \frac{\rho h}{2}\,\dot{w}^2\ dxdy \qquad \text{Kinetic Energy} \tag{1.51a}$$

$$U_l = \int_0^{L_y}\int_0^{L_x} \frac{D}{2}\,(\Delta w)^2\ dxdy \qquad \text{Linear Potential Energy} \tag{1.51b}$$

$$U_{nl} = \int_0^{L_y}\int_0^{L_x} \frac{1}{2Eh}\,(\Delta F)^2\ dxdy \qquad \text{Nonlinear Potential Energy} \tag{1.51c}$$

These are the expressions for the energy of the plate once the boundary contribution has been removed.

CHAPTER 2

Numerical Methods I: Modal Techniques

The aim of this chapter is to introduce the modal techniques adopted for the von Kármán equation. The techniques are developed starting from the case of a linear beam, that serves as the basis for a more complex strategy for plates. The von Kármán equations will be then projected on the eigenfunctions of the corresponding linear plate problems.

In this chapter, the literature review and the numerical applications will be considered within the domain of "semi-analytical" techniques. By the expression "semi-analytical" it is intended an approach where the eigenfunction is assumed to be an averaged sum of carefully selected expansion functions, and where the weights and eigenfrequencies are determined by a numerical approach involving either an infinite determinant or an algebraic eigenvalue problem. Methodologies such as the Rayleigh-Ritz method (and analogous energy methods) fall into this category. Purely numerical approaches, such as the Finite Difference and Finite Element methods are instead not considered in this chapter. Finite Difference schemes will be however briefly treated in the next chapter.

Modal techniques for nonlinear plates have been used for decades. Pioneering analytical work in the analysis of rectangular thin plate vibrations with geometrical nonlinearities was carried out in the 1950s by Chu and Herrmann [21], demonstrating for the first time the hardening-type nonlinearity that has been confirmed by numerous experiments; see *e.g.* [53, 2, 71]. Amongst the others, one may cite the works by Yamaki [95], Chang *et al.* [19], Seo *et al.* [80], Anlas and Elbeyli [4]: all of these works make use of modal analysis for investigating the nonlinear behaviour of plates in the vicinity of a particular eigenfrequency.

Hence, to a certain extent, modal techniques are certainly not innovative as compared to more modern techniques (namely, Finite Elements and Finite Differences), and their use in a numerical context may rise, so to speak, a few questions. There are, however, at least two good reasons to exploit a modal approach for nonlinear plates vibration

(1) accuracy of the calculated solution;
(2) possibility of adding damping and forcing factors to each one of the modes.

Point 1. is the pillar of modal the modal approach. The great accuracy of the modal techniques permits to perform a precise dynamical analysis of the nonlinear system (*i.e.* calculating the amplitude-dependent responses, drawing bifurcation diagrams, analysing the stability of periodic solutions, ...). This is, in actual fact, the classical application of the modal description and good amount of research work is still being done (see, for instance [1] for the case of plates). However, all the cited works restrict their attention to specific resonances and/or frequency intervals, introducing ad-hoc assumptions with respect to the coupling rules amongst the modes. Little or no attention is given to global dynamical features arising when tens or hundreds of modes are activated.

Point 2. is now discussed. Metallic plates are vibrating structures presenting a very rich damping mechanism, which is originated by at least three contributions: material damping (*i.e.* arising from friction amongst the material particles composing the body, due mainly to thermoelastic and viscoelastic effects); damping due to junctions/clamps at the edges and supports; acoustic radiation in the surrounding medium (for a detailed discussion, see [94]). These contributions are notoriously hard to be separated and studied independently. However, metallic plates are usually only slightly damped, meaning that an accurate description of energy loss per mode can be given in terms of a single viscous modal damping coefficient. In such a description, each one of the modal equations presents a damping factor proportional to the velocity of the mode, where the constant of proportionality can be obtained experimentally (see, for instance, [54, 73]). Numerically, these coefficients can be inserted directly in a modal scheme, without requiring any extra effort. On the other hand, such an implementation is basically impossible in a Finite Difference scheme. In view a possible application for sound synthesis, the ease of implementation of loss factors in the modal scheme is very appealing, because loss bears a great deal of perceptual information. On the other hand, sound synthesis is possible only when hundreds of modes are considered numerically and, as noted for point 1., this large number of degrees of freedom has never been comprised in a modal scheme.

Hence, this work is oriented towards constructing a precise modal scheme allowing to comprise hundreds of modes. Ideally, the scheme should preserve the benefits of the modal description (accuracy) and to overcome its limitations (small amount of degrees of freedom, ad-hoc assumptions). To this extent, the solution of the von Kármán equations will be projected on the eigenfunctions of the associated linear problems. This will be explained in section 2.6. A theoretical derivation of this approach is offered in [83]: in this work, it is seen that the modes couple in order to yield a cubic-type nonlinearity, where the coupling coefficients are expressed in terms of the eigenfunctions. Hence, no ad-hoc assumptions are needed, as the coupling is automatically quantified by the tensor of coupling coefficients. So, a numerical scheme based on this approach can comprise, in theory, an infinite amount of degrees of freedom, as no limitations are imposed by the model when the tensor of coupling coefficients is known. Clearly, the goodness of the modal scheme depends on the accuracy of the coupling coefficients, which, in turn, depend on the accuracy of the numerically calculated eigenfunctions. Thus, a reliable solution of the nonlinear problem depends strictly on the quality of the solutions of the associated linear problems.

This chapter presents a solid numerical strategy to calculate the eigenfrequencies and functions a linear plate under various boundary conditions. The case of the beam is presented first, as it will serve as a basis for the case of plates.

The elastically restrained beam has been treated in some detail by various authors. Early works focused on some special cases: Rao *et al.* [74] show the solution for beams presenting asymmetric translations and rotations at the end points; Maurizi *et al.* [60] take into account the case of one hinged end and a translational restraint at the other end; Goel *et al.* [39] studied the free vibration of a cantilever beam carrying a concentrated mass at an arbitrary intermediate location, and Kounandis [52] studied the free and forced vibrations of a restrained cantilever beam with attached masses. Wang *et al.* [92] make use of a sine Fourier series to study the vibrations of beams presenting zero displacement at the ends. Ding [25] presents the case of a modified sine series in order to comply with cases where the displacement at the ends does not vanish. Finally, Li [58] presents the case of a modified cosine Fourier series to study the cases of beams under all boundary conditions. This methodology will be treated in some detail in section 2.2.1.

The plate problem has been extensively studied by many authors over the years. A summary of early published papers can be found in the excellent book by Leissa [57]. This book is an extended compendium of the main works on plate vibrations up to the mid 1960s. Many more papers have been published ever since, and although Leissa is still regarded as a main source in the field of plate vibrations, his book has become somehow outdated. Given the large amount of available literature, one may erroneously led to believe that a general solution exists for plates under general boundary conditions. Although this is partly true, the vast majority of the available papers focus on very specific cases, hardly generalisable to other boundary conditions. In addition, many works consider only the very first few frequencies, with little or no care for high-range eigenfrequencies. Many authors have found solutions to particular boundary conditions by making use of the beam functions as expansion functions in the Rayleigh-Ritz method, see for instance [24, 12]. The beam function approach gives consistent results in some specific cases; however, this strategy is very tedious as the beam functions change case by case and they depend on frequency parameters that must be determined numerically for each particular set of boundary conditions. In addition, not all cases can be treated by such a method. Some authors have tried to use expansion functions different from the beam functions. Polynomials have been used, amongst the others, by Kim *et al.* [51], Bhat [6], Grossi *et al.* [43]. The problem with polynomials is that they are tend to give slow convergence and to generate unstable algorithms [59, 46]. Fourier series have been used by Hurlebaus *et al.* [48] for the case of an orthotropic plate with free boundaries, as an extension of an analogous strategy developed for beams [92]. The case of the completely clamped plate has been successfully treated by Mochida [65] using Gorman's ”superposition method” [41]: the eigenfunctions are sought as combinations of building blocks satisfying particular symmetry properties. The idea is to divide the modal shapes in four groups, according to the symmetry with respect to a cartesian coordinate system having the origin at the centre of the plate. The four groups are: doubly-symmetric, doubly-antisymmetric, symmetric-asymmetric, asymmetric-symmetric. The plate is then divided into four quarters and the solution on each quarter is constructed by summing up two building blocks that satisfy the symmetry conditions. Implementation of the boundary conditions results in an infinite characteristic determinant that depends on one free parameter. The eigenfrequencies and shapes are given by the values of the free parameter that nullify the determinant, searched by trial and error. An extensive solution for the elastically restrained plate has been developed by Li [59]. This methodology will be explained in some detail in section 2.3.1, as an extension of the corresponding strategy for beams in section 2.2.1. In this work, the case of an elastically restrained plate is solved by making use of a modified double cosine Fourier series, showing very good convergence and stability properties. Some cases, however, cannot be treated under the presented framework, namely the cases of plates presenting at least two free adjacent edges, and hence the problem of the completely free plate.

The problem of the completely free plate is perhaps the hardest amongst all possible combinations of classical boundary conditions. This has much to do with the fact that none of the boundary conditions for a free edge are geometrical, and thus less straightforwardly treated in energy methods such as the Rayleigh-Ritz method. The problem of the free plate has a rich history. The first systematic attempts at finding modal frequencies and patterns trace back to Ritz [76], who extended Rayleigh results to compute upper bounds for the eigenfrequencies. Ritz made use of the beam functions as expansion functions for the plate. This seems a reasonable idea since the plate is a 2-dimensional extension of the beam. However, due to the added dimension the edge of a free plate behaves somehow differently from the free end of a beam, mainly because of the presence of a twisting moment parallel to the edge that causes it to curve. In turn, using beam functions in the Rayleigh-Ritz method results in slow convergent results for higher modes; moreover some modes are completely left out [57]. Iguchi [49] wrote an approximate solution in a somewhat different way, by considering

$$\bar{\Phi}(x,y) = \sum_m Y_m(y)\cos\left(m\pi\left(\frac{1}{2}+\frac{x}{L_x}\right)\right) + \sum_n X_n(x)\cos\left(n\pi\left(\frac{1}{2}+\frac{y}{L_y}\right)\right),$$

where the coordinate system is chosen so to have the origin at the centre of the plate. In this way, the corner conditions is automatically satisfied. The functions X_n, Y_n are chosen in order to satisfy the other boundary conditions, and they expressed as a complicated combination of hyperbolic functions and four unknown constants to be determined. Convergence for the first few eigenfrequencies is fast, although the method somehow fails to detect larger eigenfrequencies [57]. Gorman [40] proposed a solution to free rectangular plate problems by applying the superposition method in the case of free boundary conditions. Filipich *et al.* [35] proposed a "Whole Element Method" (WEM) based on the construction of a generating sequence forming a complete set in the sense of L^2 functions over the plate domain. The generating sequence depends on unknown coefficients that are determined through an algebraic process considering the boundary conditions and the symmetry of the modal shape.

In this chapter, the modal techniques will be presented step by step, starting from the case of a linear beam. To do so, a quick review of modal decomposition for linear, self-adjoint system is offered at the beginning of the chapter. This will serve to introduce some notation, and to recall the importance of modal analysis in vibration problems. The case of an elastically restrained beam is treated thereafter. It will be shown that an appropriate modification of the Fourier series will allow to solve the equation under all possible boundary conditions. This is the strategy adopted by Li in [58]. The Kirchhoff plate is presented next. The idea is to extend the strategy for beams to its 2-dimensional counterpart

[59]. It will be seen that, to some extent, the extension is almost straightforward; however, the added dimensionality creates problems when the plate presents two adjacent free edges. Hence, care will be taken in order to show a particular solution for the completely free plate. This will serve as the basis to present a solution to the plate under uncommon boundary conditions (i.e. a completely free plate supported at its centre). The case of the completely clamped plate will also be treated in some detail, as it will become useful for the second part of this work.

2.1. Generalities on Linear, Self-Adjoint Systems

Modal techniques have been amongst the first to appear as standard resolution strategies for linear PDEs (Partial Differential Equations).

The idea is to recall the concept of eigemode and eigenfrequency, and to see how modal techniques help in the analysis of vibrating systems, in the cases where the system is free from external forcing, or subjected to general nonconservative forcing.

Let a system be continuous, conservative, homogeneous, self-adjoint and linear; its dynamics can be described by

$$\rho(\mathbf{x})\ddot{w}(\mathbf{x},t) + \mathcal{G}(w(\mathbf{x},t)) = 0, \qquad \forall \mathbf{x} \in V,\ \forall t. \tag{2.1}$$

Here w is a scalar displacement field, V is the domain of the problem, bounded by a surface or contour Ω. The function $\rho(\mathbf{x})$ represents the volumetric density which is a constant for homogeneous materials, for which then $\rho(\mathbf{x}) \equiv \rho$. The equation above is a PDE, second order in time and p^{th} order in space, where p is given by the linear differential operator $\mathcal{G}(w(\mathbf{x},t))$ (acting exclusively on the space variables). The equation does not include damping or forcing terms. The problem is fully specified once the boundary conditions on Ω are given,

$$\mathcal{B}_i(w(\mathbf{x},t)) = 0, \qquad \forall \mathbf{x} \in S,\ \forall t,\ \ i = 1, ..., p. \tag{2.2}$$

A solution to Eq. (2.1) is obtained by expanding the displacement field in the following way

$$w(\mathbf{x},t) = \sum_{n=1}^{N_\Phi} e^{i\omega_n t}\Phi_n(\mathbf{x}), \tag{2.3}$$

where ω_n are the *eigenfrequencies* and $\Phi_n(\mathbf{x})$ the *eigenfunctions*. This is known as *expansion theorem*. The number N_Φ is, in theory, infinite. However, in all numerical implementations this number is understood to be a finite integer.

The eigenfunctions clearly satisfy the boundary conditions (2.2), and the following differential eigenvalue problem

$$\mathcal{G}(\Phi_n(\mathbf{x})) = \omega_n^2 \rho \Phi_n(\mathbf{x}). \tag{2.4}$$

It is possible to show [61] that the eigenfunctions form a complete vectorial basis over the domain V of the problem, in the sense of L^2 function spaces. In other words, any function that satisfies the same boundary conditions can be expressed as a linear sum of eigenfunctions. These are then naturally orthogonal with respect to a suitable inner product; for two eigenfunctions $\Phi_a(\mathbf{x})$, $\Phi_b(\mathbf{x})$ the orthogonality is expressed as

$$\int_V \Phi_a(\mathbf{x})\Phi_b(\mathbf{x})dV = \|\Phi_a\|^2\delta_{a,b}. \tag{2.5}$$

where δ is Kronecker's delta, and the symbol $\|\ \|$ indicates the norm. Hence, the inner product between two functions $\Psi_a(\mathbf{x})$, $\Psi_b(\mathbf{x})$ (not necessarily eigenfunctions) reads

$$< \Psi_a, \Psi_b >_V = < \Psi_b, \Psi_a >_V = \int_V \Psi_a(\mathbf{x})\Psi_b(\mathbf{x})\ dV. \tag{2.6}$$

It is seen than that the free vibrations of a conservative linear systems can be described in terms of a sum of uncoupled harmonic oscillators. The extension to forced-damped vibrations is straightforward. Consider the following system

$$\rho\ddot{w}(\mathbf{x},t) + \mathcal{G}(w(\mathbf{x},t)) = P(\mathbf{x},t) - C\dot{w}(\mathbf{x},t). \tag{2.7}$$

In this system, a general forcing term $P(\mathbf{x},t)$ and a viscous-type damping $C\dot{w}(\mathbf{x},t)$ were added to the original PDE (2.1). In this case, the displacement can be sought as

$$w(\mathbf{x},t) = \sum_{n=1}^{N_\Phi} q_n(t)\Phi_n(\mathbf{x}), \tag{2.8}$$

where $q_n(t)$ are unknown modal coordinates. Assuming that the forcing is also separable in space and time (which is the case for many time dependent loads encountered in practical situations), then taking the inner product with the eigenfunction Φ_k gives the following modal equation

$$\ddot{q}_k + \frac{C}{\rho}\dot{q}_k + \omega_k^2 q_k = \frac{p_k(t)}{\|\Phi_k\|^2\rho}; \qquad p_k(t) = \int_V \Phi_k P(\mathbf{x},t)dV, \tag{2.9}$$

which shows that the modal coordinates satisfy a system of uncoupled forced-damped oscillator equations. In conclusion, once the modal shapes and frequencies are known, the system can be decomposed onto a series of uncoupled oscillators, each one describing the behaviour of the system around a particular frequency.

The main problem when using modal techniques applied to continuous system resides in being able to calculate the eigenfunctions and associated frequencies for nontrivial boundary conditions. In the case of Kirchhoff plates, algebraic solutions exist only for the cases of plates presenting two opposite simply-supported edges. Important cases such as the completely clamped plate and the completely free plate must be solved numerically. Energy methods, such as the Rayleigh-Ritz method, are the most widely used for this category of problems. The next subsection will serve as a review of such a technique.

After that, the discussion will continue by considering the Euler-Bernoulli beam subjected to general boundary conditions. A global strategy based on the Rayleigh-Ritz method will be detailed and results shown. The Kirchhoff plate problem will then be approached by extending the results for beams, and finally the von Kármán plate problem will be solved by making use of the results coming from the linear case.

2.1.1. Calculating eigenfunctions and frequencies: the Rayleigh-Ritz method. The Rayleigh-Ritz method is based around the idea that a particular eigenfunction $\tilde{\Phi}(\mathbf{x})$ can be sought as a linear sum of expansion function $\Lambda_m(\mathbf{x})$. The expansion coefficients are calculated by an algebraic eigenvalue problem, whose eigenvalues are approximate values for the eigenfrequencies ω_n of Eq. (2.3). The steps leading to the definition of the algebraic eigenvalue problem are here recalled. Let now $\Psi(\mathbf{x})$ be a generic function (not necessarily an eigenfunction) defined over V in the following way

$$\Psi(\mathbf{x}) = \sum_{m=1}^{N_\Psi} a_m \Lambda_m(\mathbf{x}), \tag{2.10}$$

where N_Ψ is a finite integer. The functions $\Lambda_m(\mathbf{x})$ are understood to come from the set of the *admissible functions*, i.e. those functions that satisfy the *geometric* boundary conditions [62, 38, 3] of a particular PDE. Such functions, in fact, are expressible as linear combinations of eigenfunctions. Let then be $\Lambda(\mathbf{x})$ a generic admissible function. Then one has

$$\Lambda(\mathbf{x}) = \sum_{m=1}^{N_\Lambda} b_m \Phi_m(\mathbf{x}).$$

Owing to this definition, one may consider Λ as a particular state of the system; in this way, one can write the potential and kinetic energy functionals associated to that particular state. Let these functionals be called $U[\Lambda]$, $T[\Lambda]$ respectively. They are defined as

$$T[\Lambda] = \frac{1}{2}\int_V \rho \Lambda(\mathbf{x})^2 \, dV \tag{2.11a}$$

$$U[\Lambda] = \int_V \bar{U}[\Lambda] \, dV, \tag{2.11b}$$

where $\bar{U}[\Lambda]$ is the potential energy density of the system in the configuration Λ. Now, the kinetic and potential energy functionals are calculated for the function $\Psi(\mathbf{x})$ in Eq. (2.10). Because these functionals are scalars, and they are quadratic functions of their arguments, then one may write them as

$$T[\Psi] = \mathbf{a}^T \, \mathbf{M} \, \mathbf{a} \tag{2.12a}$$

$$U[\Psi] = \mathbf{a}^T \, \mathbf{K} \, \mathbf{a}. \tag{2.12b}$$

where the matrices $\mathbf{M}$, $\mathbf{K}$ are known respectively as mass and stiffness matrices, and $\mathbf{a} = [a_1, a_2, ..., a_{N\Psi}]$ is the vector of expansion coefficients of Eq. (2.10). If one considers the following algebraic eigenvalue problem

$$\mathbf{K} \, \mathbf{a} = \sigma^2 \, \mathbf{M} \, \mathbf{a}, \tag{2.13}$$

then it is possible to show that the eigenvector $\mathbf{a}$ renders the function Ψ of Eq. (2.10) an eigenfunction of the associated PDE, in the limit of $N_\Psi \to \infty$. In the same way, the eigenvalue σ^2 will tend to the associated eigenfrequency ω^2, in the same limit. In actual fact, it is possible to show that the convergence of the eigenfrequencies is monotonic and from above. This is, in essence, the core of the Rayleigh-Ritz method.

The choice of the expansion function is crucial. In fact, a badly selected expansion set may result in slow convergence, instability issues, or wrong results. Although the Rayleigh-Ritz method has been known for decades, the literature is vague when it comes to give a precise rule on how to pick the expansion functions (except of course the fact that they must be admissible functions).

In the following sections, the Rayleigh-Ritz method will be applied constantly, and the choice of the expansion functions justified case by case.

2.2. Modes of the Euler-Bernoulli beam

In this section the free vibrations of an Euler-Bernoulli beam are solved in terms of modes. The aim of this section is to outline a procedure that will be adopted in the more complex case of a Kirchhoff plate under general boundary conditions. Consider a beam of length L with homogeneous density ρ, constant cross section A, constant moment of inertia I, Young's modulus E. The equation of motion and boundary conditions have been derived in section 1.3.1. For clarity they are here recalled

Equation of Motion

$$\rho A \ddot{w} = -EI w_{,xxxx}.$$

Boundary Conditions

- Simply Supported End
$$w = w_{,xx} = 0.$$
- Clamped End
$$w = w_{,x} = 0.$$
- Free End
$$w_{,xxx} = w_{,xx} = 0.$$

In the literature, the beam equation has been extensively studied (for a quick review, see [37, 44]), and the solutions are given in terms of semi-analytical functions and frequencies. However, this classical approach is affected by at least 2 issues:

(1) the semi-analytical eigenfunctions, expressed as linear combinations of hyperbolic and trigonometric functions, change from case to case according to the boundary conditions;
(2) the eigenfrequencies are found as the roots of a particular transcendental equation, and hence an extra numerical effort is needed in order to calculate them.

It is evident that the classical approach is unsatisfactory for anyone wishing to approach the beam equations under general boundary conditions, including elastically restrained ends. This is why a numerical method will be presented in the next section. The proposed method will provide the analyst with a global solution, adaptable to an infinity of different cases, making use of only one algebraic eigenvalue problem.

Boundary Condition	ζ_1/π	ζ_2/π	ζ_3/π	$\zeta_n/\pi (n>3)$
F - F	1.5056	2.4997	3.5000	$\frac{1}{2}(2n+1)$
SS - F	1.2499	2.2500	3.2500	$\frac{1}{4}(4n+1)$
C - F	1.4942	2.5002	3.5000	$\frac{1}{2}(2n+1)$
SS - SS∗	1.0000	2.0000	3.0000	n
C - SS	1.2499	2.2500	3.2500	$\frac{1}{4}(4n+1)$
C - C	1.5056	2.4997	3.5000	$\frac{1}{2}(2n+1)$

TABLE 1. Dimensionless eigenfrequencies ζ_n/π for the Euler-Bernoulli beam under classical boundary conditions. The radian frequencies are given by $\omega_n = \zeta_n^2/L^2\sqrt{EI/\rho A}$. $*$ denotes exact solution; all other solutions are approximated. Note that the F-F case presents two rigid body motions at zero frequency (not reported).

The classical approach and related issues are now quickly reviewed. Consider the free vibrations of a particular solution, i.e.

$$\tilde{w}(x,t) = e^{i\tilde{\omega}t}\tilde{\Phi}(x).$$

In the classical approach a form for the eigenfunction $\tilde{\Phi}(x)$ is expressed as a combination of trigonometric and hyperbolic functions, in the following way

$$\tilde{\Phi}(x) = A\cos\left(\frac{\tilde{\zeta}x}{L}\right) + B\sin\left(\frac{\tilde{\zeta}x}{L}\right) + C\cosh\left(\frac{\tilde{\zeta}x}{L}\right) + D\sinh\left(\frac{\tilde{\zeta}x}{L}\right). \tag{2.14}$$

This form yields a semi-analytical solution for the beam problem. The useful aspect of this function is that it is biharmonic in the space variable x, in other words $\tilde{\Phi}(x)_{,xxxx} = \left(\frac{\tilde{\zeta}}{L}\right)^4\tilde{\Phi}(x)$. Hence, the eigenfrequencies are recovered by considering $\tilde{\zeta}^4 = \frac{\rho A\tilde{\omega}^2}{EI}L^4$. Thus, if the combination of hyperbolic and trigonometric functions is able to satisfy the supplied boundary conditions, one obtains immediately a solution to the problem.

The simplest case is represented by a beam simply supported at both ends: a solution is derived effortlessly by setting $A = C = D = 0$, $\zeta_m = m\pi$ for any positive integer m. Aside from this case, more elaborate solutions are needed for other end types. Note that the eigenvalues ζ must be calculated using numerical methods, for example Newton's method.

The interested reader can find more examples in [42, 37, 44]. Table 1 presents the formulae for the eigenvalues for all possible classical boundary conditions. It is seen that, in the classical approach, looking for solutions of a particular combination of boundary conditions corresponds to finding the right coefficients in Eq. (2.14) and solving a transcendental equation. In addition, the classical approach does not permit to solve the beam equation when the ends are elastically restrained. The next subsection is then devoted to outline a numerical strategy to overcome the limitations of the classical approach.

2.2.1. A general numerical strategy for beams.

In this subsection, an elastically restrained beam is considered. The elastic constraints are represented by springs attached at the beam ends: basically, each end is attached to one rotational spring and one linear spring. The added springs contribute in a local sense to the potential energy of the beam. For an unconstrained beam, the potential energy takes the form of Eq. (1.19). When the springs are attached, the potential energy reads

$$U = \frac{EI}{2}\int_0^L (w_{,xx})^2 \, dx + \frac{1}{2}\left[k_0 w^2 + K_0 w_{,x}^2\right]\Bigg|_{x=0} + \frac{1}{2}\left[k_L w^2 + K_L w_{,x}^2\right]\Bigg|_{x=L}.$$

In this equation, the symbol k denotes a flexural spring, and the symbol K denotes a rotational spring. Note that a free end corresponds formally to setting the stiffness of all the springs equal to zero; a clamped end is recovered when the springs stiffness is infinite; a simply supported end has zero rotational stiffness and infinite flexural stiffness. The kinetic energy has the same form as Eq. (1.20) (where the rotatory inertia term is dropped). By making use of Hamilton's principle in conjunction with the eigenfunction expansion, one obtains the following eigenvalue problem and boundary conditions for a particular eigenfunction $\tilde{\Phi}(x)$

$$\begin{aligned} \tilde{\Phi}_{,xxxx} &= \left(\frac{\tilde{\zeta}}{L}\right)^4 \tilde{\Phi}; \\ \tilde{\zeta}^4 &= \frac{\rho A \tilde{\omega}^2}{EI} L^4. \end{aligned} \tag{2.15}$$

$$k_0 \tilde{\Phi} = -EI\tilde{\Phi}_{,xxx}, \;\; K_0 \tilde{\Phi}_{,x} = EI\tilde{\Phi}_{,xx} \qquad \text{at } x = 0; \tag{2.16a}$$

$$k_L \tilde{\Phi} = EI\tilde{\Phi}_{,xxx}, \;\; K_L \tilde{\Phi}_{,x} = -EI\tilde{\Phi}_{,xx} \qquad \text{at } x = L. \tag{2.16b}$$

A general solution to the elastically restrained beam problem has been proposed by Li in [58]; this strategy is now outlined.

The idea is to make use of the Rayleigh-Ritz method with carefully selected expansion functions. Let the expansion function be $X_m(x)$. Hence the generic eigenfunction $\tilde{\Phi}$ is expressed as

$$\tilde{\Phi}(x) = \sum_{m=0}^{N_\Phi - 1} \tilde{a}_m X_m(x), \tag{2.17}$$

for a set of expansion coefficients $\tilde{a}_m$ and a (practically finite) integer N_Φ In order to apply the Rayleigh-Ritz method, $X_m(x)$ must be chosen within the set of the admissible functions. However, not all admissible functions can guarantee a fast convergence, or correct results.

An equation such as (2.17) is the generic expression that defines an approximation to the function $\tilde{\Phi}$. Function approximation represents a fundamental branch of applied mathematics and computer science [46]. It is clear that the set of functions $X_m(x)$ must form a *complete* set over the domain of the problem. In general, one resorts to class of functions which are proven to be complete: Legendre polynomials, Chebyschev polynomials, Bessel functions, trigonometric functions. Bessel functions, or

combinations thereof, are indeed useful but find an application in problems whose geometry shows a spherical or cylindrical symmetry [34, 50]. Polynomials are also useful, but in practice they tend to show unstable behaviour for large values of the argument x, or slow convergence when the function to approximate presents a large number of critical values [46]. The high-frequency modes of a beam belong to this category. Given the biharmonic nature of the beam equation, it seems almost natural to seek an expansion (2.17) in terms of trigonometric functions and, in particular, Fourier series.
Fourier series represent an excellent function basis for vibration problems; in the case of the beam, for example, an eigenfunction $\tilde{\Phi}(x)$ is a function that has at least four continuous derivatives, and that is bounded over the interval $[0, L]$. Thus, $\tilde{\Phi}(x)$ is square-integrable and its Fourier series converges at almost every point. The Fourier series for the function $\tilde{\Phi}(x)$ defined on $[0, L]$ is defined as

$$\tilde{\Phi}(x) = \sum_{m=0}^{\infty} \left(\tilde{d}_m \cos\left(\frac{m\pi x}{L}\right) + \tilde{g}_m \sin\left(\frac{m\pi x}{L}\right) \right).$$

From the definition above, one can extract the Fourier *cosine* series and Fourier *sine* series (denoted respectively by the indices c, s). The cosine series expansion is defined as

$$\tilde{\Phi}_c(x) = \sum_{m=0}^{\infty} \tilde{d}_m \cos\left(\frac{m\pi x}{L}\right); \tag{2.18}$$

and the sine series expansion is defined as

$$\tilde{\Phi}_s(x) = \sum_{m=0}^{\infty} \tilde{g}_m \sin\left(\frac{m\pi x}{L}\right). \tag{2.19}$$

It is evident that the expansion functions in the Fourier series are orthogonal in the sense of Eq. (2.5). In fact

$$\int_0^L \cos\left(\frac{m\pi x}{L}\right) \cos\left(\frac{n\pi x}{L}\right) \, dx = \begin{cases} 0 & m \neq n \\ L/2 & m = n \neq 0 \\ L & m = n = 0 \end{cases} \tag{2.20a}$$

$$\int_0^L \sin\left(\frac{m\pi x}{L}\right) \cos\left(\frac{n\pi x}{L}\right) \, dx = \begin{cases} 0 & m \neq n \\ L/2 & m = n \neq 0 \end{cases}$$

$$\int_0^L \cos\left(\frac{m\pi x}{L}\right) \sin\left(\frac{n\pi x}{L}\right) \, dx = 0.$$

Given the orthogonality properties, the coefficients of the expansions are

$$\tilde{d}_0 = \frac{1}{L} \int_0^L \tilde{\Phi}(x) \, dx, \qquad \tilde{d}_{m\neq 0} = \frac{2}{L} \int_0^L \tilde{\Phi}(x) \cos\left(\frac{m\pi x}{L}\right) \, dx, \qquad \tilde{g}_m = \frac{2}{L} \int_0^L \tilde{\Phi}(x) \sin\left(\frac{m\pi x}{L}\right).$$

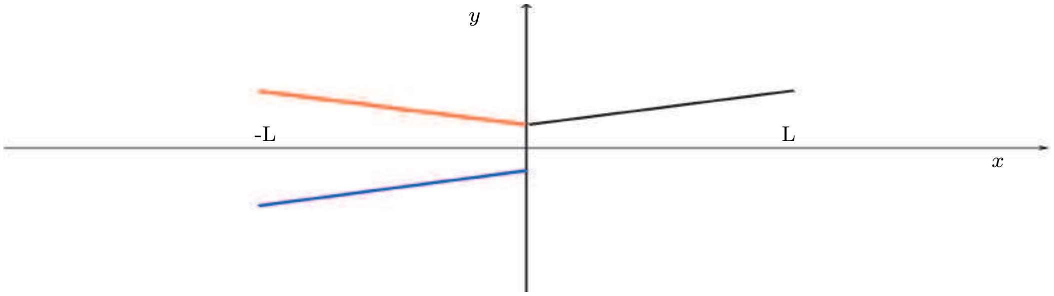

FIGURE 1. Graph of the function $y = ax + b$ (black) defined over [0,L] with odd extension (blue) and even extension (red).

The derivatives of the cosine and sine Fourier series are obtained using the following identities [84]

$$\tilde{\Phi}_c(x)_{,x} = -\sum_{m=1}^{\infty}\left(\frac{m\pi}{L}\right)\tilde{d}_m \sin\left(\frac{m\pi x}{L}\right)$$

$$\tilde{\Phi}_s(x)_{,x} = \frac{\tilde{\Phi}_s(L) - \tilde{\Phi}_s(0)}{L} + \sum_{m=1}^{\infty}\left(\frac{2}{L}\left[(-1)^m\tilde{\Phi}_s(L) - \tilde{\Phi}_s(0)\right] + \left(\frac{m\pi}{L}\right)\tilde{g}_m\right)\cos\left(\frac{m\pi x}{L}\right)$$

Thus, the sine Fourier series can be differentiated term by term if and only if $\tilde{\Phi}_s(0) = \tilde{\Phi}_s(L) = 0$. This fact is only apparently peculiar, and can be easily understood by considering Fig. 1. This is the graph of a simple affine function $y(x) = a + bx$ for $a \neq 0$. The function is defined over the interval $[0, L]$, and its odd and even extensions ($y_o(x)$ and $y_e(x)$) are also represented over $[-L, 0]$. Because the sine Fourier series is an odd function, it converges to $y(x)$ over $[0, L]$ and to $y_o(x)$ over $[-L, 0]$. The function of period $2L$ to which the sine Fourier series converges is thus only piecewise smooth. From the Fourier theorem, then, the sine series will converge at *almost* every point; at the discontinuities the series will converge to zero, regardless the actual value of the original function there. Consider now the displacement of an elastically restrained beam at one end point: when the stiffness of the linear spring is not infinite, the end point is free to move and the odd extension creates a discontinuity. Thus, the sine series cannot be differentiated term by term. In addition, the displacement at the end points is formulated in terms of the first three derivatives, as seen from the boundary conditions (2.16). In conclusion, the convergence of the Fourier series might be greatly affected by the discontinuity of the eigenfunction $\tilde{\Phi}(x)$ and its derivatives at the end points.

To overcome this problem, here a modified cosine Fourier series is used. This is the strategy adopted by Li in [58]. Basically, the displacement function $\tilde{\Phi}(x)$ is sought in the following form

$$\tilde{\Phi}(x) = \tilde{\phi}(x) + p(x). \tag{2.22}$$

The function $\phi(x)$ is a *residual* displacement whose values at the end points is zero, along with its first and third derivatives. The other function $p(x)$ is an auxiliary function that compensates for the difference between the original and residual displacements at the end points. If the residual displacement is expanded onto a cosine Fourier series (truncated to the integer N_Φ),

$$\tilde{\phi}(x) = \sum_{m=0}^{N_\Phi - 1} d_m \cos\left(\frac{m\pi x}{L}\right), \tag{2.23}$$

then its first three derivatives can be taken on a term-by-term basis (following the fact that $\tilde{\phi}_{,x} = \tilde{\phi}_{,xxx} = 0$ at the boundaries). For that to be accomplished, one must impose the following conditions on $p(x)$

$$\tilde{\Phi}_{,xxx}(0) = p_{,xxx}(0) = A_0, \qquad \tilde{\Phi}_{,xxx}(L) = p_{,xxx}(L) = A_L, \tag{2.24a}$$

$$\tilde{\Phi}_{,x}(0) = p_{,x}(0) = B_0, \qquad \tilde{\Phi}_{,x}(L) = p_{,x}(L) = B_L. \tag{2.24b}$$

The constants $(A_0, A_L, B_0, B_L) \equiv \mathbf{A}^T$ need to be determined from (2.16). In practice this corresponds to solving a linear system of four equations, expressed as

$$\mathbf{H}\mathbf{A} = \sum_{m=0}^{N_\Phi - 1} \mathbf{Q}_m \tilde{d}_m;$$

The matrix $\mathbf{H}$ is four by four and depends on the particular form of $p(x)$. $\mathbf{Q}_m$ is instead a column vector with four entries; $\tilde{d}_m$ are the coefficients of the cosine series in (2.23). Hence

$$\mathbf{A} = \mathbf{H}^{-1} \sum_{m=0}^{N_\Phi - 1} \mathbf{Q}_m \tilde{d}_m. \tag{2.25}$$

From the last equation it is clear that the matrix $\mathbf{H}$ has to be invertible in order to yield a form for $\mathbf{A}$.

According to Li, $p(x)$ can be selected to be any well-behaved function satisfying conditions (2.24). Li chooses a polynomial of order four; this form will be denoted by $p_\alpha(x)$. However, if Li's assumptions are correct, then the choice of $p(x)$ should not affect the final results, as long as the boundary conditions above are satisfied. This is why a second form for $p(x)$ will be used here; this will be denoted by $p_\beta(x)$ and it is a sum of sine functions. Hence

$$p_\alpha(x) = \sum_{n=0}^{4} r_{\alpha n} x^n \equiv \sum_{n=0}^{4} r_{\alpha n} p_{\alpha n}(x); \tag{2.26a}$$

$$p_\beta(x) = \sum_{n=0}^{4} r_{\beta n} \sin\left(\frac{n\pi x}{L}\right) \equiv \sum_{n=0}^{4} r_{\beta n} p_{\beta n}(x). \tag{2.26b}$$

The $r_{(\alpha,\beta)n}$ coefficients are obtained so that the boundary conditions (2.24) are satisfied. Hence

$$\begin{pmatrix} r_{\alpha 0} \\ r_{\alpha 1} \\ r_{\alpha 2} \\ r_{\alpha 3} \\ r_{\alpha 4} \end{pmatrix} = \begin{pmatrix} \frac{L^3(8a_0+7a_L)}{360} - \frac{Lb_L}{6} + \frac{Lb_0}{3} \\ -b_0 \\ -\frac{a_L}{12} - \frac{La_0}{6} + \frac{b_L}{2L} + \frac{b_0}{2L} \\ \frac{a_0}{6} \\ \frac{a_L}{24L} - \frac{a_0}{24L} \end{pmatrix}; \qquad \begin{pmatrix} r_{\beta 0} \\ r_{\beta 1} \\ r_{\beta 2} \\ r_{\beta 3} \\ r_{\beta 4} \end{pmatrix} = \begin{pmatrix} 0 \\ \frac{(a_0-a_1)L^3}{16\pi^3} + \frac{9(b_0-b_1)L}{16\pi} \\ \frac{(a_0+a_1)L^3}{48\pi^3} + \frac{(b_0+b_1)L}{3\pi} \\ -\frac{(a_0-a_1)L^3}{48\pi^3} - \frac{(b_0-b_1)L}{48\pi} \\ -\frac{(a_0+a_1)L^3}{96\pi^3} - \frac{(b_0+b_1)L}{24\pi} \end{pmatrix}. \tag{2.27}$$

In other words, the vector $\mathbf{r}_{(\alpha,\beta)}$ can be written as the product of a four-by-four matrix times the vector $\mathbf{A}$, thus

$$\mathbf{r}_{(\alpha,\beta)} = \mathbf{S}_{(\alpha,\beta)}\mathbf{A}. \tag{2.28}$$

Once the vector $\mathbf{A}$ has been determined, the coefficients $r_{(\alpha,\beta)n}$, for the auxiliary functions $p_\alpha(x)$, $p_\beta(x)$ are obtained by combining Eqs. (2.25) and (2.28), and thus

$$\mathbf{r}_{(\alpha,\beta)} = \sum_{m=0}^{N_\Phi-1} \mathbf{S}_{(\alpha,\beta)}\mathbf{H}^{-1}\mathbf{Q}_m\tilde{d}_m \equiv \sum_{m=0}^{N_\Phi-1} \mathbf{R}^m_{(\alpha,\beta)}\tilde{d}_m.$$

In this way, the eigenfunction (2.22) is written as

$$\tilde{\Phi}(x) = \sum_{m=0}^{N_\Phi-1} \tilde{d}_m X_m(x) = \sum_{m=0}^{N_\Phi-1} d_m \left[\cos\left(\frac{m\pi x}{L}\right) + \sum_{n=0}^{4} R^m_{(\alpha,\beta)n} p_{(\alpha,\beta)n}(x)\right], \tag{2.29}$$

and the derivatives of $\tilde{\Phi}(x)$ can be taken term-by-term. Now that a form for the expansion function has been derived, it is possible to build the stiffness and mass matrix in accordance to the Rayleigh-Ritz method. The mass and stiffness matrices read

$$\begin{aligned} M_{mp} =& \frac{\rho A}{2EI}\int_0^L X_m X_p \, dx, \\ K_{mp} =& \frac{1}{2}\int_0^L X_{m,xx}X_{p,xx} \, dx \\ &+ \frac{1}{2EI}\left[k_0 X_m X_p + K_0 X_{m,x}X_{p,x}\right]\Big|_{x=0} + \frac{1}{2EI}\left[k_L X_m X_p + K_L X_{m,x}X_{p,x}\right]\Big|_{x=L}. \end{aligned}$$

The algebraic eigenvalue problem is then

$$(\mathbf{K} - (\tilde{\zeta}/L)^4\mathbf{M})\tilde{\mathbf{d}} = 0.$$

where $\mathbf{K}$, $\mathbf{M}$ are $N_\Phi \times N_\Phi$ matrices. Their explicit form (for the function $p_\alpha(x)$) is given in the paper by Li [58]. In this way the expansion coefficients $\tilde{d}_m$ can be calculated along with the eigenfrequencies.

2.2.2. Results and discussions. Numerical results for the beam are now considered. Table 2 presents the standard cases of a clamped, simply-supported, free beam at both ends. In each subtable, the values of the normalised frequencies ζ_i/π are reported. These are systematically compared with the values reported in the literature, namely those of Table 1. The results are reported for the two choices of the auxiliary function $p(x)$. It is seen that the choice of the auxiliary function does not affect convergence, thus supporting Li's idea that the choice of the auxiliary function is not crucial. The total number of expansion terms N_Φ is reported at the top of each sub-table. It is seen that the clamped case is the case that converges the fastest: $N_\Phi = 30$ expansion terms are sufficient to guarantee the convergence of the first five frequencies up to the sixth significant digit. For the simply-supported and free cases, the number of expansion terms must be increased significantly. Note, however, that the calculation time in MATLAB for $N_\Phi = 100$ is about 1s, and thus the convergence of the eigenfunctions can be considered "fast". In order to simulate the different end types, the stiffness

C-C beam

N_Φ=5

Mode	$p_\alpha(x)$	$p_\beta(x)$
1	1.5046	1.5047
2	2.4839	2.4495
3	3.4900	3.4917
4	4.9128	4.3589
5	6.4257	6.4147

N_Φ=10

Mode	$p_\alpha(x)$	$p_\beta(x)$
1	1.5056	1.5056
2	2.4998	2.4995
3	3.5001	3.4995
4	4.5002	4.4986
5	5.5018	5.4995

N_Φ=20

Mode	$p_\alpha(x)$	$p_\beta(x)$
1	1.5056	1.5056
2	2.4997	2.4997
3	3.5000	3.5000
4	4.5000	4.4999
5	5.5000	5.4999

N_Φ=30

Mode	$p_\alpha(x)$	$p_\beta(x)$
1	1.5056	1.5056
2	2.4997	2.4997
3	3.5000	3.5000
4	4.5000	4.5000
5	5.5000	5.5000

Mode	*Literature*
1	1.5056
2	2.4997
3	3.5000
4	4.5000
5	5.5000

SS-SS beam

N_Φ=10

Mode	$p_\alpha(x)$	$p_\beta(x)$
1	1.0005	1.0000
2	2.0099	2.0000
3	3.0206	3.0000
4	4.4255	4.0000
5	5.5598	5.4048

N_Φ=40

Mode	$p_\alpha(x)$	$p_\beta(x)$
1	1.0001	1.0000
2	2.0006	2.0000
3	3.0028	3.0000
4	4.0051	4.0000
5	5.0164	5.0109

N_Φ=70

Mode	$p_\alpha(x)$	$p_\beta(x)$
1	1.0000	1.0000
2	2.0001	2.0000
3	3.0003	3.0000
4	4.0006	4.0000
5	5.0013	5.0008

N_Φ=100

Mode	$p_\alpha(x)$	$p_\beta(x)$
1	1.0000	1.0000
2	2.0000	2.0000
3	3.0001	3.0000
4	4.0002	4.0000
5	5.0004	5.0002

Mode	*Literature*
1	1.0000
2	2.0000
3	3.0000
4	4.0000
5	5.0000

F-F beam

N_Φ=10

Mode	$p_\alpha(x)$	$p_\beta(x)$
1	1.5059	1.5073
2	2.5018	2.5056
3	3.5043	3.5083
4	4.5121	4.5142
5	5.5168	5.5312

N_Φ=40

Mode	$p_\alpha(x)$	$p_\beta(x)$
1	1.5056	1.5056
2	2.4998	2.4998
3	3.5001	3.5001
4	4.5002	4.5002
5	5.5003	5.5004

N_Φ=70

Mode	$p_\alpha(x)$	$p_\beta(x)$
1	1.5056	1.5056
2	2.4998	2.4998
3	3.5000	3.5000
4	4.5000	4.5000
5	5.5001	5.0001

N_Φ=100

Mode	$p_\alpha(x)$	$p_\beta(x)$
1	1.5056	1.5056
2	2.4998	2.4998
3	3.5000	3.5000
4	4.5000	4.5000
5	5.5000	5.5000

Mode	*Literature*
1	1.5056
2	2.4997
3	3.5000
4	4.5000
5	5.5000

TABLE 2. Tables representing the numerical values for the normalised eigenfrequencies ζ_i/π for a beam under classical boundary conditions. Bottom tables presents reference values from the literature. The number of expansion functions N_Φ is indicated for each subtable.

values have been set to very large and small values. A clamped end presents $K/EI = k/EI = 10^8$; a simply-supported end presents $K/EI = 10^8, k/EI = 10^{-7}$; a free end presents $K/EI = k/EI = 10^{-7}$. A convergence test for the stiffness is presented in Table 3. It is seen that the selected stiffness values are indeed a sensible choice to simulate an infinite (zero) stiffness spring.

Li's method allows to calculate the eigenfrequencies of nonclassical cases, i.e. when the value of the springs is not infinite or zero. As an example, consider a beam simply-supported at $x = 0$, and presenting a infinite linear stiffness at $x = L$. Changing the value of the rotational spring from a very large to a very small value allows to obtain the eigenfrequencies of a beam ranging from the SS-SS to the SS-C configuration. Table 4 presents the values for the first five eigenfrequencies for different values of K_L, when $N_\Phi = 100$ and using the auxiliary function $p_\alpha(x)$. This example shows the advantage of Li's method with respect to the classical approach presented in the previous section: nonclassical boundary conditions can be calculated with the same precision as the classical ones, without having to change the form of the expansion functions. In other words, Li's method is extremely versatile.

Despite the great ease of application, Li's method is not completely free from numerical issues, mainly when it comes to the completely free beam. Consider the second eigenfrequency of the F-F case in Table 2: the converged value differs from the one reported in the literature (by a very small amount, however). This is explained by the fact that the springs are still a bit "too" stiff, so that the second mode behaves anomalously. The problem here is that reducing the stiffness value of the springs generates an unstable eigenvalue problem. In addition, the springs cannot be set to be exactly zero because in this case the matrix $\mathbf{H}$ becomes singular. This does not represent a problem when the very first few eigenfrequencies are looked for: in actual fact the results shown in Table 2 are still very precise. However, when many modes are needed (say, a few hundred), the stability issue becomes evident. In reference [58] the results are shown for the first few eigenfrequencies. Here, however, the robustness of the algorithm is tested when many modes are needed. For example, mode number 200 is calculated here using 500 expansion terms, and using the auxiliary function $p_\alpha(x)$. The calculation time in MATLAB is of the order of 5s. In Table 5, the present results are compared with the literature values for the 3 classical boundary conditions. It is seen that convergence is obtained up to the fourth significant digit for the simply-supported and clamped case. The free beam case, instead, leads to an ill-conditioned algorithm; this happens because, as previously remarked, the matrix $\mathbf{H}$ becomes singular for very small values of the stiffness, and although the first few frequencies can be calculated with sufficient precision, the stability of the algorithm is not guaranteed for high-frequency modes. Hence, although the first few eigenfrequencies for the F-F beam can still be calculated with great precision, it is seen that Li's method is not the most appropriate method to treat this problem.

The stability problem is not going to be investigated any further in this section. However, it will be considered in some detail in the next section, where the Kirchhoff plate is considered and solved using an extension of the Li's method for beams. It is anticipated that Li's method fails at calculating the solution for the completely free plate, and hence a new strategy will be outlined.

$\log_{10} K/EI$	*mode 1*	$\log_{10} k/EI$	*mode 1*	$\log_{10} K/EI$	*mode 1*	$\log_{10} k/EI$	*mode 1*
0	1.2872	**0**	0.7675	**0**	1.5574	**0**	1.5574
1	1.4104	**1**	0.8700	**-1**	1.5120	**-1**	1.5120
2	1.4914	**2**	1.2250	**-2**	1.5063	**-2**	1.5063
3	1.5041	**3**	1.4721	**-3**	1.5057	**-3**	1.5057
4	1.5055	**4**	1.5024	**-4**	1.5056	**-4**	1.5056
5	1.5056	**5**	1.5053	**-5**	1.5056	**-5**	1.5056
6	1.5056	**6**	1.5056	**-6**	1.5056	**-6**	1.5056
7	1.5056	**7**	1.5056	**-7**	1.5056	**-7**	1.5056
8	1.5056	**8**	1.5056	**-8**	1.5056	**-8**	1.5056

TABLE 3. Convergence test for rotational and linear springs in order to simulate infinite and zero stiffness. The reference value from the literature is ζ_1/π =1.5056.

N_Φ=100

Mode	$K_L/EI = 10^{-7}$	$K_L/EI = 10^{0}$	$K_L/EI = 10^{3}$	$K_L/EI = 10^{8}$
1	1.0000	1.0419	1.2486	1.2499
2	2.0000	2.0232	2.2478	2.2500
3	3.0000	3.0159	3.2468	3.2500
4	4.0000	4.0121	4.2458	4.2500
5	5.0000	5.0098	5.2448	5.2500

TABLE 4. Transition from the SS-SS to the SS-C beam, obtained by changing the value of K_L.

	C-C	SS-SS	F-F
present	200.48	200.00	-
literature	200.50	200.00	200.50

TABLE 5. Values for the 200^{th} normalised eigenfrequency ζ_{200}/π for the present method, compared to the reference values from the literature.

In conclusion, Li's method was tested to check the its robustness and convergence properties. It was seen that the first few eigenfrequencies of an elastically restrained beam can be calculated for all end types, giving excellent agreement with the literature in the case of classical boundary conditions. It was checked that the auxiliary function does not affect the stability or convergence properties. Li's method was also tested in order to obtain high-frequency modes, and it was seen that the algorithm remain robust for the cases of a clamped and simply-supported beam. The algorithm for the completely free beam, instead, was seen to be ill-conditioned and thus high-frequency modes cannot be computed within this framework.

2.3. Extension to the Kirchhoff plate

In the previous section the case of a beam under general boundary conditions was investigated. This section is devoted to extending the proposed method to the 2-dimensional problem of a Kirchhoff plate. For clarity, the eigenvalue problem and boundary conditions for a particular eigenfunction $\tilde{\Phi}(x, y)$ are here recalled

Equation of Motion

$$\Delta\Delta\tilde{\Phi} = \frac{\tilde{\zeta}^4}{L_x^4}\tilde{\Phi};$$

$$(\tilde{\zeta}^4 = L_x^4\tilde{\omega}^2\rho h/D).$$

Boundary Conditions

- Simply Supported Edge

$$\tilde{\Phi} = \tilde{\Phi}_{,nn} = 0.$$

- Clamped Edge

$$\tilde{\Phi} = \tilde{\Phi}_{,n} = 0.$$

- Free Edge

$$\tilde{\Phi}_{,nnn} + (2-\nu)\tilde{\Phi}_{,ntt} = \tilde{\Phi}_{,nn} + \nu\tilde{\Phi}_{,tt} = 0;$$

$$\tilde{\Phi}_{,nt} = 0 \text{ at corners.}$$

Note that the eigenvalue $\tilde{\zeta}$ is an nondimensional parameter, proportional to L_x^4. In actual fact, adimensionalisation could be performed by considering any other parameter having dimensions of $(length)^4$ (for example, $L_x^2L_x^2$, $L_x^3L_y$,...). The choice of L_x^4 is due to consistency with the literature. Opposite to what happens for beams, the plate equation cannot be solved semi-analytically for all boundary conditions. In a few cases, however, analytical solutions are available. The simplest case is represented by the SS-SS-SS-SS plate. In this case the particular eigenfunction reads

$$\tilde{\Phi}(x, y) = \sin\left(\frac{m\pi x}{L_x}\right)\sin\left(\frac{n\pi y}{L_y}\right), \quad \tilde{\zeta}^2 = (m\pi)^2 + (L_x/L_y n\pi)^2, \tag{2.31}$$

where m, n are positive integers. It is seen that, in this case, the form for $\tilde{\Phi}(x, y)$ is the product of two functions, each one being the beam function with the same boundary conditions in the x and y directions. In the case of other boundary conditions, the product of two beam functions does not yield a solution to the eigenvalue problem: this happens because a single beam function $\tilde{\Phi}(x)$ is biharmonic in the x coordinate; however, the product of two beam functions in the x and y direction is not, in general, biharmonic in a 2-dimensional sense, i.e. $\Delta\Delta\left(\tilde{\Phi}(x)\tilde{\Phi}(y)\right) \neq \frac{\tilde{\zeta}^4}{L_x^4}\tilde{\Phi}(x)\tilde{\Phi}(y)$. In fact, the expression for the 2-dimensional Laplacian involves not only derivatives of order 4, but also derivatives of order 2 in the x and y directions, $\Delta\Delta f(x, y) = f_{,xxxx} + 2f_{,xxyy} + f_{,yyyy}$.

The particular case of the plate edges all simply-supported represents an exception as the 2-dimensional beam function is also harmonic. Other analytical solutions are possible, namely for plates presenting two opposite sides simply-supported (see [44]for details). All other combinations of boundary conditions cannot be treated analytically, and so it is necessary to develop a numerical strategy in order to obtain approximate solutions. The next subsection is then devoted to develop a numerical strategy to solve the plate equation under general boundary conditions.

2.3.1. A general solution for the Kirchhoff plate: Li's method. Let a plate be supported on all edges by rotational and flexural springs. The potential energy for such a plate is now derived. The potential energy of an unconstrained plate takes the form of Eq. (1.27). When the springs are attached, the potential energy becomes

$$
\begin{aligned}
U = {} & \frac{D}{2}\int_0^{L_y}\int_0^{L_x}\left[(\Delta w)^2-(1-\nu)L(w,w)\right]\,dxdy \\
& +\frac{1}{2}\left\{\int_0^{L_y}\left[K_{0x}w_{,x}^2\Big|_{x=0}+K_{Lx}w_{,x}^2\Big|_{x=L_x}\right]dy+\int_0^{L_x}\left[K_{0y}w_{,y}^2\Big|_{y=0}+K_{Ly}w_{,y}^2\Big|_{y=L_y}\right]dx\right\} \\
& +\frac{1}{2}\left\{\int_0^{L_y}\left[k_{0x}w^2\Big|_{x=0}+k_{Lx}w^2\Big|_{x=L_x}\right]dy+\int_0^{L_x}\left[k_{0y}w^2\Big|_{y=0}+k_{Ly}w^2\Big|_{y=L_y}\right]dx\right\}.
\end{aligned}
$$

The symbol K denotes a rotational spring, and the symbol k a flexural one. As for the case of the beam, a clamped, free or simply supported edge is obtained when $(k = K = 0)$, $(k = K \to \infty)$, $(k \to \infty, K = 0)$ respectively. To derive an eigenvalue problem for the particular eigenfunction $\tilde{\Phi}(x,y)$, the above expression is inserted in Hamilton's principle along with the kinetic energy expression Eq. (1.28). The particular solution $\tilde{w}(x,y,t)$ is then separated in space and time, and harmonic time dependence is assumed with radian frequency $\tilde{\omega}$: $\tilde{w}(x,y,t) = e^{i\tilde{\omega}t}\tilde{\Phi}(x,y)$. This gives rise to the following eigenvalue problem and boundary conditions

$$\Delta\Delta\tilde{\Phi} = \frac{\tilde{\zeta}^4}{L_x^4}\tilde{\Phi}; \tag{2.33a}$$

$$k_{0x}\tilde{\Phi} = Q_x, \qquad K_{0x}\tilde{\Phi}_{,x} = -M_x \qquad \text{at } x = 0; \tag{2.33b}$$

$$k_{Lx}\tilde{\Phi} = -Q_x, \qquad K_{Lx}\tilde{\Phi}_{,x} = M_x \qquad \text{at } x = L_x; \tag{2.33c}$$

$$k_{0y}\tilde{\Phi} = Q_y, \qquad K_{0y}\tilde{\Phi}_{,y} = -M_y \qquad \text{at } y = 0; \tag{2.33d}$$

$$k_{Ly}\tilde{\Phi} = -Q_y, \qquad K_{Ly}\tilde{\Phi}_{,y} = M_y \qquad \text{at } y = L_y; \tag{2.33e}$$

where $\tilde{\zeta}^4 = L_x^4\tilde{\omega}^2\rho h/D$, $Q_x = -D(\tilde{\Phi}_{,yyy} + (2-\nu)\tilde{\Phi}_{,xxy})$, $M_x = -D(\tilde{\Phi}_{,xx} + \nu\tilde{\Phi}_{,yy})$ (and similarly for Q_y, M_y).

Elastically restrained plates have been studied in [59]. The idea is to extend the method proposed for beams to the case of the plate. This method will be referred to as *Li's method*. It will be seen that Li's method is extremely versatile and allows to calculate the first few eigenfrequencies for a variety of cases, including mixed and nonclassical boundary conditions. The results are discussed in the next subsection. However, Li's method has two major drawbacks: it cannot calculate the case of the completely free plate and it becomes somehow unreliable when hundreds of modes are looked for. More on this will be discussed in sec. 2.3.3 onwards.

Li's method is now presented. The eigenfunction $\tilde{\Phi}$ is now assumed to be written as a weighted sum of separable functions

$$\tilde{\Phi} = \sum_{m,n=0}^{N_\Phi} \tilde{a}_{mn} X_m(x) Y_n(y). \tag{2.34}$$

This is analogous to the assumption made for the beam, Eq. (2.17). Given that the Kirchhoff plate is the 2-dimensional extension of the beam, it is plausible to assume that $X_m(x)$ will maintain the same form as Eq. (2.22): in practice, Li's hypothesis is to write the eigenfunction $\tilde{\Phi}(x, y)$ for the Kirchhoff plate as the product of independent beam functions. Hence, the forms for $X_m(x)$ and $Y_n(y)$ are derived following the steps from Eq. (2.17) to Eq. (2.29). This allows to write

$$\begin{aligned} X_m(x) &= \sum_{m=0}^{N_\Phi - 1} \tilde{d}_m \left[\cos\left(\frac{m\pi x}{L_x}\right) + \sum_{s=0}^{4} R_s^m p_s(x) \right]; \\ Y_n(y) &= \sum_{n=0}^{N_\Phi - 1} \tilde{d}_n \left[\cos\left(\frac{n\pi y}{L_y}\right) + \sum_{s=0}^{4} R_s^n p_s(y) \right]; \end{aligned}$$

where $p_s(x)$ is a fourth order polynomial with the same properties as $p_{\alpha n}(x)$ in Eq. (2.26), and $p_s(y)$ is obtained accordingly. Application of the Rayleigh-Ritz method gives rise to the following mass and stiffness matrices

$$\begin{aligned} M_{mn,pq} =& \frac{\rho h}{2D} \int_0^{L_y} \int_0^{L_x} X_m Y_n X_p Y_q \; dx dy, \\ K_{mn,pq} =& \frac{1}{2} \int_0^{L_y} \int_0^{L_x} \left(\Delta(X_m Y_n) \Delta(X_p Y_q) - (1-\nu) L(X_m Y_n, X_p Y_q) \right) \; dx dy \\ &+ \frac{1}{2D} \left\{ \int_0^{L_y} \left[K_{0x} X_{m,x} Y_n X_{p,x} Y_q \Big|_{x=0} + K_{Lx} X_{m,x} Y_n X_{p,x} Y_q \Big|_{x=L_x} \right] dy \right. \\ &+ \left. \int_0^{L_x} \left[K_{0y} X_m Y_{n,y} X_p Y_{q,y} \Big|_{y=0} + K_{Ly} X_m Y_{n,y} X_p Y_{q,y} \Big|_{y=L_y} \right] dx \right\} \\ &+ \frac{1}{2D} \left\{ \int_0^{L_y} \left[k_{0x} X_m Y_n X_p Y_q \Big|_{x=0} + k_{Lx} X_m Y_n X_p Y_q \Big|_{x=L_x} \right] dy \right. \\ &+ \left. \int_0^{L_x} \left[k_{0y} X_m Y_n X_p Y_q \Big|_{y=0} + k_{Ly} X_m Y_n X_p Y_q \Big|_{y=L_y} \right] dx \right\}. \end{aligned}$$

The matrices are then used to define the following eigenvalue problem

$$(\mathbf{K} - (\tilde{\zeta}/L_x)^4 \mathbf{M}) \tilde{\mathbf{a}} = 0. \tag{2.37}$$

where $\mathbf{K}$, $\mathbf{M}$ are matrices of dimension $N_\Phi^2 \times N_\Phi^2$, and $\mathbf{a}$ is the vector of expansion coefficients of length N_Φ^2 defined as $\tilde{a}_{mn} = \tilde{d}_m \cdot \tilde{d}_n$. The explicit form of the matrices are presented in the paper by Li [59].

N_Φ=10			Mode			
	1	**2**	**3**	**4**	**5**	Method
η =1.0	2.000	5.000	5.000	8.000	10.000	Li
	2.000	5.000	5.000	8.000	10.000	Exact
η =1.5	1.444	2.778	4.444	5.000	5.778	Li
	1.444	2.778	4.444	5.000	5.778	Exact
η =2.0	1.250	2.000	3.250	4.250	5.000	Li
	1.250	2.000	3.250	4.250	5.00 0	Exact
η =2.5	1.160	1.640	2.440	3.560	4.160	Li
	1.160	1.640	2.440	3.560	4.160	Exact

TABLE 6. Normalised eigenfrequencies ζ_i^2/π^2 for the SS-SS-SS-SS plate under different aspect ratios $\eta = L_y/L_x$. The exact values from Eq. (2.31) are also reported.

2.3.2. Preliminary results and discussion. To test the goodness of the proposed model, a simply-supported plate is first analysed. For that, the flexural springs stiffness have been set to a very large value, namely $k/D = 10^8$ (see section 2.2.2 for a discussion on this). The analytic frequencies ζ_i are given in Eq. (2.31) for different aspect rations $\eta = L_y/L_x$. It is seen that the first few eigenfrequencies can be calculated with excellent precision. As a second case, Table 7 considers the fully-clamped plate. For this, the springs are set as $k/D = K/D = 10^8$. In this case Li's method is compared to the results obtained by applying Gorman's superposition method, which represents one of the main references for this particular problem [40, 41, 65]. It is seen that the two methods yield the same results. As an application of Li's method, the C-SS-C-F plate is now considered. For this problem, there is no analytical solution. Table 8 presents the first five converged eigenfrequencies for different aspect ratios. Finally, the transition from the C-SS-C-F to the C-SS-C-SS plate is presented in Table 9. The transition is observed by changing the value of the linear spring at $y = L_y$. This is an application of Li's versatile method, which allows to consider nonclassical boundary conditions. The examples provided allow to conclude that Li's method is extremely versatile when it comes to calculate the first few eigenfrequencies for plates under mixed and nonclassical boundary conditions. There are, however, two issues that must be discussed: these are the stability of the algorithm for high-frequency modes, and the problem of plates presenting at least two adjacent free edges. These issues are considered in the next subsection.

2.3.3. Issues related to Li's method. The results presented in the previous section are, in some respect, very convincing. The first eigenfrequencies for the simply supported plate converge quickly to the fifth significant digit of the exact values. In addition, the fully clamped plate frequencies are in exact agreement with [65], which shows the results obtained from Gorman's superposition

N_Φ=10	Mode					
	1	**2**	**3**	**4**	**5**	Method
η =1.0	3.645	7.436	7.436	10.965	13.328	Li
	3.65	7.44	7.44	10.96	13.33	Gorman
η =1.5	2.736	4.225	6.700	6.740	8.112	Li
	2.74	4.23	6.70	6.74	8.11	Gorman
η =2.0	2.490	3.225	4.536	6.417	6.483	Li
	2.49	3.22	4.54	6.48	7.20	Gorman
η =2.5	2.396	2.817	3.589	4.729	6.231	Li
	2.39	2.82	3.59	4.73	6.23	Gorman

TABLE 7. Normalised eigenfrequencies ζ_i^2/π^2 for the C-C-C-C plate under different aspect ratios $\eta = L_y/L_x$. Literature values are taken from [65] which uses Gorman's superposition method.

N_Φ=10	Mode				
	1	**2**	**3**	**4**	**5**
η =1.0	2.376	3.607	6.392	6.766	7.852
η =1.5	2.315	2.834	4.121	6.311	6.348
η =2.0	2.293	2.577	3.251	4.426	6.144
η =2.5	2.283	2.462	2.87	3.578	4.625

TABLE 8. Normalised eigenfrequencies ζ_i^2/π^2 for C-SS-C-F plate under different aspect ratios $\eta = L_y/L_x$.

method. Li's method has been applied to the case of a C-SS-C-F plate, showing the same rate of convergence.

However, Li's method presents two major drawbacks: first, the problem of a plate with at least two adjacent free edges cannot be treated with such a method; second, the stability of the algorithm is questionable when a large number of modes (say, a few hundred) is needed.

The stability issue rears its head when high-frequency modes are looked for. As an example, consider again the fully clamped plate problem. When $N_\Phi = 10$, application of the eigenvalue problem should return, in theory, 100 positive real eigenvalues. However, the algorithm returns only 86 positive real eigenvalues (i.e. 86% of the total); the other 14 are either complex or negative real numbers. When N_Φ gets larger, the number of complex or negative real eigenvalues grows in proportion. For

N_Φ=10			Mode			
	1	**2**	**3**	**4**	**5**	k_{Ly}
η =1.0	2.376	3.608	6.392	6.766	7.852	10^{-7}
	2.378	3.609	6.376	6.768	7.829	10^{0}
	2.976	5.667	5.820	7.015	10.118	10^{4}
	2.933	5.547	7.024	9.583	10.357	10^{8}
η =1.5	2.315	2.834	4.121	6.311	6.348	10^{-7}
	2.316	2.835	4.122	6.305	6.350	10^{0}
	2.536	3.548	5.532	6.584	7.266	10^{4}
	2.537	3.557	5.547	6.587	7.660	10^{8}
η =2.0	2.293	2.577	3.251	4.426	6.144	10^{-7}
	2.294	2.578	3.252	4.427	6.145	10^{0}
	2.413	2.932	3.954	5.524	6.437	10^{4}
	2.413	2.933	3.961	5.547	6.437	10^{8}
η =2.5	2.283	2.462	2.871	3.578	4.625	10^{-7}
	2.284	2.462	2.872	3.579	4.626	10^{0}
	2.358	2.670	3.276	4.226	5.533	10^{4}
	2.358	2.671	3.278	4.233	5.547	10^{8}

TABLE 9. Normalised eigenfrequencies ζ_i^2/π^2 for the transition from the C-SS-C-F plate to the C-SS-C-SS plate under different aspect ratios $\eta = L_y/L_x$, for different values of the spring k_{Ly}.

$N_\Phi = 15$, 175 real positive eigenvalues are returned from a total 225 (i.e. 78%). In turn, this issue has two major consequences: first, some eigenvalues are missed; second, some unwanted values are returned. The unwanted values are not actual eigenvalues of the problem, and the corresponding vector coefficient **a** does not give rise to an eigenfunction. So, Li's method may pose problems if one wishes to calculate a few hundred actual modes. Note that the instability issue affects all ranges of the eigenvalue vector returned by the algorithm; hence a few low-frequency eigenvalues disappear when N_Φ is made larger, and complex or negative eigenvalues are returned. In turn, the results are unreliable when instability turns up, because it is not possible to know which eigenvalues have disappeared and where the unwanted eigenvalues are.

The issue of two adjacent free sides is now discussed. The first problem (which was already mentioned in the case of the beam) is that setting the springs to very small values renders the matrix **H** singular, and thus the eigenvalue problem becomes ill-conditioned. In the case of the beam, however, the first eigenfrequencies can still be calculated with precision. However, this is not possible for the free plate. This happens because the boundary conditions for a free beam are not the same as those for a free plate. Li's method for the plate problem is based around the assumption that the beam functions

(2.29) can be used as expansion functions for the plate; this works out for the simply-supported and clamped plate, because the boundary conditions are the same for the plate and for the beam. However, the edge of the completely free plate is substantially different from the end of a free beam, because of the presence of a twisting moment that tends to bend the free edge in a direction parallel to it. In addition, the free plate has a corner condition that is not taken into account by the beam functions.

In conclusion, Li's method is a versatile method that allows to calculate a few modes with very high precision, at least for the plates which do not present at least two adjacent free sides. In the next sections, the clamped plate problem will be solved instead by modifying Li's method in order to yield a more stable eigenvalue algorithm. Next, the problem of the fully free plate will be considered in some detail, and a so far unavailable solution will be presented.

2.4. An adapted strategy for the clamped plate problem

The clamped plate problem presents two geometrical boundary conditions, namely the vanishing of the displacement and its slope along the boundary. Solving this problem using Rayleigh-Ritz method requires then a set of expansion functions that satisfy the prescribed boundary conditions. The idea is to follow Li's method, so to write the particular eigenfunction $\tilde{\Phi}(x,y)$ as

$$\tilde{\Phi}(x,y) = \sum_{m,n=0}^{N_\Phi-1} \tilde{a}_{mn} X_m(x) Y_n(y) = \sum_{m,n=0}^{N_\Phi} \tilde{a}_{mn} \left[\cos\left(\frac{m\pi x}{L_x}\right) + p(x)\right]\left[\cos\left(\frac{n\pi y}{L_y}\right) + p(y)\right].$$

The functions $p(x)$, $p(y)$ will be looked as polynomials of order four to make $X_m(x)$, $Y_n(y)$ satisfy the boundary conditions. Note that this is a slight, yet substantial variation with respect to Li's approach: in fact, it was seen in section 2.3.1 that the added polynomial was selected so to satisfy conditions (2.24), and the values for the vector $\tilde{\mathbf{a}}$ had to be determined through matrix inversion in order to comply with the different forms of boundary conditions. Here, instead, the clamped plate boundary conditions are satisfied *a priori* by the expansion functions. It can be seen effortlessly that the following function $X_m(x)$ satisfies the boundary conditions for the clamped plate problem

$$X_m(x) = \cos\left(\frac{m\pi x}{L_x}\right) + \frac{15(1+(-1)^m)}{L_x^4}x^4 - \frac{4(8+7(-1)^m)}{L_x^3}x^3 + \frac{6(3+2(-1)^m)}{L_x^2}x^2 - 1. \tag{2.38}$$

Note that the form for $X_m(x)$ is obtainable from Li's method in the limit of infinite stiffness in the matrix $\mathbf{H}^{-1}$. Thus, the same results and convergence rate are expected when comparing Li's method for the clamped plate and the present method. However, having taken the infinite stiffness limit allows to get rid of the spring parameters in the algorithm, resulting in a simplified form for the stiffness and mass matrices and more stable results, as it will be seen in the next subsection.

To apply the Rayleigh-Ritz method, the stiffness and mass matrices are built as follows

$$\begin{aligned} M_{mn,pq} =& \frac{\rho h}{2D} \int_0^{L_y} \int_0^{L_x} X_m Y_n X_p Y_q \; dxdy, \\ K_{mn,pq} =& \frac{1}{2} \int_0^{L_y} \int_0^{L_x} \Delta(X_m Y_n) \Delta(X_p Y_q) \; dxdy \end{aligned}$$

Note the simplified expression of the stiffness matrix with respect to Li's method: in this case, the factor proportional to $\mathcal{L}(\tilde{\Phi}, \tilde{\Phi})$ has been neglected in the expression for the potential energy, as well as the spring integrals. This is allowed as all these terms are boundary terms that are obviously zero along the boundary, given that the clamped boundary conditions are implemented directly in the expansion function. The matrices are then used to define the following eigenvalue problem

$$(\mathbf{K} - (\tilde{\zeta}/L_x)^4 \mathbf{M}) \tilde{\mathbf{a}} = 0. \tag{2.40}$$

The form of these matrices is presented in Appendix A.

2.4.1. Results for the clamped plate problem. The aim of this section is to present the results for the clamped plate problem using the presented approach as compared to Li's method. First, the clamped plate eigenfrequencies are calculated using $N_\Phi = 10$ for both methods. The results are shown in Table 10. It is seen that the two methods yield the same results. In Table 11 the results for $N_\Phi = 20$ are reported. When the number N_Φ is made larger, the results for the square plate show a discrepancy for the fourth eigenfrequency: Li's method gives a value that is larger than the value calculated with $N_\Phi = 10$. This represents an anomaly as the convergence of the Rayleigh-Ritz method should be from above, and thus the eigenvalues should get smaller as N_Φ increases (see comments on the Rayleigh-Ritz method in section 2.1.1). The present method, instead, is not affected by this unwanted instability effect. Examples of eigenfunctions calculated with the present method are shown in Fig. 2. The high-frequency modes are now investigated. Results from the present method are now shown for $N_\Phi = 20, 25, 30$ in Table 12, taking into account the case of the square plate. Note that the present method shows an actual convergence, whereas Li's method gives inconsistent results due to the instability of the algorithm. In conclusion, the present method, adapted for the fully clamped plate case, returns a stable algorithm capable of calculating hundreds of modes without occurring in instability problems. Note that, when $N_\Phi = 30$, the present method returns 899 modes out of 900. As a rule of thumb [62], the total number of "reliable" modes returned by the eigenvalue problem corresponds to one half of the total results. The present method is stable until $N_\Phi = 30$, and thus the total number of modes that one can calculate using the present method is about 450. To the knowledge of the author, this result is unprecedented in the literature and should thus be regarded as an important result from this work.

N_Φ=10			Mode			
	1	**2**	**3**	**4**	**5**	Method
η =1.0	3.646	7.436	7.436	10.965	13.332	Li
	3.646	7.436	7.436	10.965	13.332	Present
η =1.5	2.736	4.225	6.700	6.740	8.086	Li
	2.736	4.225	6.700	6.740	8.086	Present
η =2.0	2.490	3.225	4.536	6.417	6.483	Li
	2.490	3.225	4.536	6.417	6.483	Present
η =2.5	2.396	2.818	3.589	4.729	6.231	Li
	2.396	2.817	3.589	4.729	6.231	Present

TABLE 10. Normalised eigenfrequencies ζ_i^2/π^2 for the C-C-C-C plate under different aspect ratios $\eta = L_y/L_x$. Comparison between Li's method and present method, for $N_\Phi = 10$.

N_Φ=20			Mode			
	1	**2**	**3**	**4**	**5**	Method
η =1.0	3.646	7.436	7.436	11.10	13.33	Li
	3.646	7.436	7.436	10.96	13.33	Present
η =1.5	2.736	4.225	6.700	6.740	8.088	Li
	2.736	4.225	6.700	6.740	8.086	Present
η =2.0	2.490	3.225	4.536	6.417	6.483	Li
	2.490	3.225	4.536	6.417	6.483	Present
η =2.5	2.396	2.817	3.588	4.729	6.231	Li
	2.396	2.817	3.588	4.729	6.231	Present

TABLE 11. Normalised eigenfrequencies ζ_i^2/π^2 for the C-C-C-C plate under different aspect ratios $\eta = L_y/L_x$. Comparison between Li's method and present method, for $N_\Phi = 20$. Value in red represents an anomaly due to Li's algorithm instability.

	Mode			
	100	**150**	**200**	Method
$N_\Phi = 20$	156.6	221.4	302.3	Li
	156.6	219.4	290.3	Present
$N_\Phi = 25$	143.4	NaN	NaN	Li
	156.6	219.4	288.6	Present
$N_\Phi = 30$	NaN	NaN	NaN	Li
	156.6	219.1	288.5	Present

Table 12. High-range normalised eigenfrequencies ζ_i^2/π^2 for the square C-C-C-C plate. Comparison between Li's method and present method, for $N_\Phi = 20, 25, 30$.

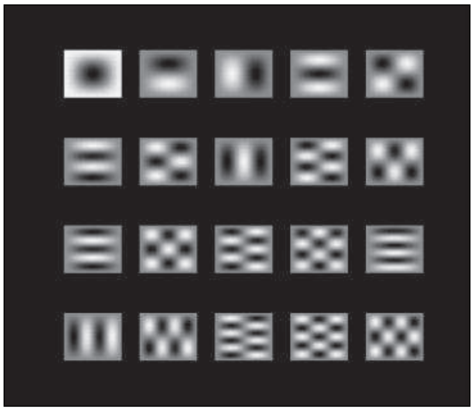

Figure 2. First 20 eigenfunctions for a clamped plate of aspect ratio $\eta = 1.5$ using the present method.

2.5. A simple series solution for the free plate

The plate with completely free edges represents a difficult problem, following the form of the boundary conditions which depend on Poisson's ratio ν and involve third order derivatives of the displacement at boundaries. For clarity, the eigenvalue equation and boundary conditions are here recalled, for a particular eigenfunction $\tilde{\Phi}(\mathbf{x})$

Equation of Motion *Boundary Conditions*

$$\Delta\Delta\tilde{\Phi} = \frac{\tilde{\zeta}^4}{L_x^4}\tilde{\Phi}, \qquad \tilde{\Phi}_{,nnn} + (2-\nu)\tilde{\Phi}_{,ntt} = \tilde{\Phi}_{,nn} + \nu\tilde{\Phi}_{,tt} = 0,$$

$$(\tilde{\zeta}^4 = L_x^4\tilde{\omega}^2\rho h/D). \qquad \tilde{\Phi}_{,nt} = 0 \text{ at corners.}$$

These equations arose quite easily when Hamilton's principle was used in section 1.3.2: the boundary integrals are written as a product of a certain function of the displacement and its derivatives times the variation of either the displacement or its normal derivative. The former conditions are said "natural", whereas the latter are said "geometrical". For the plate problem, the boundary conditions are all natural, including the corner condition. The physical quantities associated with the boundary conditions are the normal bending moment and Kirchhoff shear force [37].

In this section, the free plate problem is solved by making use of a modified double cosine series, and the Rayleigh-Ritz method. The idea is to find a new simple solution, with the same convergence properties as the complicated solutions by the superposition method [40] and WEM [35]. To this extent, let the generic eigenfunction $\tilde{\Phi}(x,y)$ be written as a modified double cosine series

$$\tilde{\Phi}(x,y) = \sum_{m,n=0}^{N_\Phi-1} \tilde{a}_{mn}X_m(x)Y_n(y) = \sum_{m,n=0}^{N_\Phi-1} \tilde{a}_{mn}\left(\cos\left(\frac{m\pi x}{L_x}\right) + p(x)\right)\left(\cos\left(\frac{n\pi y}{L_y}\right) + p(y)\right),$$

where $p(x)$ is, as usual, an auxiliary function of some kind. As noted in section 2.1.1, the expansion functions for the Rayleigh-Ritz method need not satisfy *all* boundary conditions, but only the geometrical ones. The free plate problem does not present any such conditions; in fact, the boundary conditions in this case are all natural.

Here the auxiliary function $p(x)$ is chosen again as a fourth-order polynomial such that

(1) $X_{m,xxx}(x) = 0$ for $x = 0, x = L_x$;
(2) $X_{m,xx}(x) = X_m(x)$ for $x = 0, x = L_x$.

When these conditions are fulfilled by the expansion functions, then the boundary conditions for the free plate problem reduce to $\tilde{\Phi}_{,tt} = 0$, plus the corner condition. This conditions will be satisfied in the limit of $N_\Phi \to \infty$ when using the Rayleigh-Ritz method. It is important to notice that the expansion function must not satisfy any geometric boundary conditions, otherwise the Rayleigh-Ritz method will produce wrong solutions. Note that, contrary to what is done in [40, 35], there is no need to impose particular symmetry conditions on the eigenfunctions. It is easy to see that

$$X_m(x) = \cos\left(\frac{\pi\, m\, x}{L_x}\right) - \frac{\left(L_x^2+\pi^2\,m^2\right)\,\left(L_x^2+6\,(-1)^m-6\right)}{L_x^2\,\left(L_x^2-12\right)}$$

$$+\frac{2\,x\,\left(L_x^2+\pi^2\,m^2\right)\,\left(2\,L_x^2+6\,(-1)^m+(-1)^m\,L_x^2-6\right)}{L_x^3\,\left(L_x^2-12\right)} - \frac{3\,x^2\,\left((-1)^m+1\right)\,\left(L_x^2+\pi^2\,m^2\right)}{L_x^2\,\left(L_x^2-12\right)} \tag{2.41}$$

satisfies the conditions 1.,2., above. An analogous form is selected for $Y_n(y)$. The eigenvalue problem is obtained by considering the stiffness and mass matrices as follows

$$K_{mn,pq} = \frac{1}{2}\int_S \left(\Delta(X_mY_n)\Delta(X_pY_q) - (1-\nu)L(X_mY_n, X_pY_q)\right)\ dxdy; \tag{2.42a}$$

$$M_{mn,pq} = \frac{\rho h}{2D}\int_S \left(X_mY_nX_pY_q\right)\ dxdy. \tag{2.42b}$$

In this way, the eigenvalue algebraic eigenvalue problem reads

$$(\mathbf{K} - (\tilde{\zeta}/L_x)^4\mathbf{M})\tilde{\mathbf{a}} = 0. \tag{2.43}$$

Note that, as opposed to what happens for the completely clamped plate, in this case the eigenfrequencies and functions depend on Poisson's ratio ν; in the stiffness matrix expression, in fact, the boundary term proportional to the von Kármán operator cannot be neglected, as in this case the expansion function do not satisfy the boundary conditions. The explicit forms of the stiffness and mass matrices are presented in Appendix B.

2.5.1. Results and Discussion.

2.5.1. Results and Discussion. The eigenfrequencies calculated with the present method are compared with Gorman's method [65], and WEM [35] in Table 13. Both Gorman's method and WEM are considered "exact" methods by their respective authors. They give, in fact, comparable results, although Gorman's method returns, in general, smaller values then WEM's. The present method gives results that are within the range of 1-2% difference with Gorman's, and that are, in general, larger.

It has been pointed out in [66] that Gorman's method, although fast converging, is affected by an instability problem which bears two major consequences: missed frequencies and unwanted results (similar remarks have been made for the clamped plate problem in section 2.3.3). In actual fact, the cited literature works do not show any results past the 12th eigenfrequency, suggesting that it might be difficult to obtain converged results for higher frequency ranges. On the other hand, the concluding section in [35] mentions that WEM method is not affected by the "lost frequencies" issue. However, this statement is not supported by further evidence: in the paper, no results past the 6th eigenfrequency appear. The present method gives consistent results when compared to WEM and Gorman's. For the first time, high-range frequencies are shown for the completely free plate: the results are summarised in Table 14, where it is seen that the present method allows to produce about 100th eigenfrequencies converging up the third significant digit. Note that the instability issue appears in the current method as well: when $N_\Phi \geq 17$, the results returned by the eigenvalue algorithm are unreliable, as some frequencies are missed and others appear, in a completely unpredictable way (see

N_Φ=15, $\nu = 0.3$	Mode					
	1	**2**	**3**	**4**	**5**	Method
η =1.0	1.364	1.983	2.456	3.521	3.521	Gorman
	1.365	1.987	2.460	3.528	3.528	WEM
	1.366	1.988	2.467	3.533	3.533	Present
η =1.5	0.9044	0.9629	2.084	2.244	2.592	Gorman
	0.9050	0.9650	2.088	2.248	2.601	WEM
	0.9061	0.9667	2.090	2.254	2.604	Present
η =2.0	0.5429	0.6728	1.479	1.505	2.226	Gorman
	-	-	-	-	-	WEM
	0.5464	0.6748	1.483	1.513	2.235	Present
η =2.5	0.3473	0.5345	0.9637	1.146	1.877	Gorman
	0.3480	0.5348	0.9673	1.148	1.887	WEM
	0.3517	0.5371	0.9689	1.149	1.891	Present

TABLE 13. Normalised eigenfrequencies ζ_i^2/π^2 for the F-F-F-F plate under different aspect ratios $\eta = L_y/L_x$. Comparison between Li's method and present method, for $N_\Phi = 15$. Values for Gorman are taken from reference [65]; values for WEM are taken from reference [35].

remarks about Li's method for the clamped plate problem, sec. 2.3.3). Hence, no results are shown in the table for higher values of N_Φ. In conclusion, this section shows that the present method gives results that are close to the "exact" solutions proposed by [40, 35], where close is to be intended within a 1-2% range. Plots of the first twenty eigenfunctions, excluding rigid body motions, are shown in Fig. 3(a). The present method allows to calculate high-range frequencies that have never appeared in the literature before. These high-range frequencies have been shown to converge to the third significant digit. With respect to Gorman's method and WEM, the present method has the advantage of presenting a really simple implementation: in fact, only one algebraic eigenvalue problem is required instead of four.

2.5.2. Modes of the completely free plate supported at the centre. As an application, the presented method has been modified in order to produce results for a completely free plate supported at the centre. The support has been created by adding a linear spring at the plate centre, in the limit of infinite stiffness. The potential energy is thus modified with respect that giving rise to Eq. (2.42a). The modified stiffness matrix is

$$K_{mn,pq} = ... + \frac{1}{2D} k_c \int_0^{L_y} \int_0^{L_x} \delta(\mathbf{x} - \mathbf{x_c}) w^2 \; dxdy, \tag{2.44}$$

	Mode				
$\nu = 0.3$	**25**	**50**	**75**	**100**	N_Φ
η=1.0	20.82	46.57	74.19	106.8	11
	20.81	46.54	73.83	106.5	13
	20.80	46.52	73.75	106.4	15
	20.79	46.51	73.72	106.3	17
η=1.5	13.37	32.28	50.49	80.44	11
	13.36	32.12	49.68	72.30	13
	13.36	32.07	49.65	70.00	15
	13.35	32.05	49.63	69.61	17
η=2.0	10.51	22.91	43.40	73.97	11
	10.49	22.90	37.36	57.65	13
	10.48	22.88	37.32	52.25	15
	10.48	22.87	37.30	52.18	17
η=2.5	7.675	20.10	41.95	73.00	11
	7.670	18.63	31.89	55.34	13
	7.667	18.53	29.91	41.76	15
	7.665	18.50	29.90	41.74	17

TABLE 14. Normalised high-range eigenfrequencies ζ_i^2/π^2 for the F-F-F-F plate under different aspect ratios $\eta = L_y/L_x$, and different values of expansion functions N_Φ, for $\nu = 0.3$.

where ... is the right hand side of Eq. (2.42a), k_c is the linear stiffness and $\mathbf{x_c}$ is the coordinate of the plate centre. The results are summarised in Table 15, where the stiffness value k_x/D has been set to a very large value, namely 10^8. These results are calculated here for the first time, to the knowledge of the author. Note that some unwanted oscillations appear in the results, meaning that the frequencies stop converging from above, as opposed to what is expected when applying the Rayleigh-Ritz method. This is similar to what happens when using Li's method in the case of the clamped plate (see remarks in section 2.4.1). This unwanted behaviour has to be attributed to the presence of the springs whose stiffness is not large enough when N_Φ is large. Note that, for the present case, this issue can be simply resolved by modifying the expansion function (2.41) so that the geometrical boundary condition $w(x, y) = 0$ at the plate centre is automatically satisfied. However, this has not been done for the present work. Examples of eigenfunctions are given in Fig. 3(b).

	Mode									
$\nu = 0.3$	**1**	**2**	**3**	**4**	**5**	**25**	**50**	**75**	**100**	N_Φ
η=1.0	1.147	1.367	1.990	3.538	3.538	21.79	46.60	76.84	106.8	11
	1.146	1.366	1.989	3.536	3.536	21.78	46.54	76.47	106.5	13
	1.143	1.366	1.989	3.535	3.535	21.77	46.52	76.39	106.4	15
	1.140	1.365	1.988	3.533	3.534	21.65	46.51	76.36	106.3	17
η=1.5	0.6136	0.9082	1.587	2.092	2.607	13.50	32.32	53.28	84.29	11
	0.6131	0.9072	1.585	2.091	2.606	13.49	32.12	50.31	72.30	13
	0.6095	0.9067	1.583	2.090	2.672	13.50	32.07	50.02	70.03	15
	0.5889	0.9063	1.579	2.090	2.789	13.50	32.09	49.94	69.76	17
η=2.0	0.3554	0.6775	1.379	1.486	1.514	10.51	22.92	44.05	75.23	11
	0.3537	0.6763	1.376	1.484	1.514	10.49	22.92	37.75	58.74	13
	0.3507	0.6756	1.374	1.483	2.131	10.48	22.91	37.66	52.27	15
	0.3507	0.6752	1.373	1.483	1.863	10.96	22.99	37.52	52.26	17
η=2.5	0.2341	0.5404	0.9701	1.126	1.152	7.674	20.25	42.30	73.14	11
	0.2233	0.5389	0.9697	1.123	1.151	7.670	18.85	31.93	55.88	13
	0.2287	0.5381	0.9696	1.120	1.150	7.667	18.83	30.08	45.04	15
	0.2333	0.5375	0.9692	1.119	1.150	7.664	18.79	29.84	42.01	17

TABLE 15. Eigenfrequencies ζ_i^2/π^2 for the F-F-F-F plate supported at the centre for $k_c/D = 10^8$, under different aspect ratios $\eta = L_y/L_x$, and different values of expansion functions N_Φ, in the case of $\nu = 0.3$. Values in red correspond to instability of the algorithm.

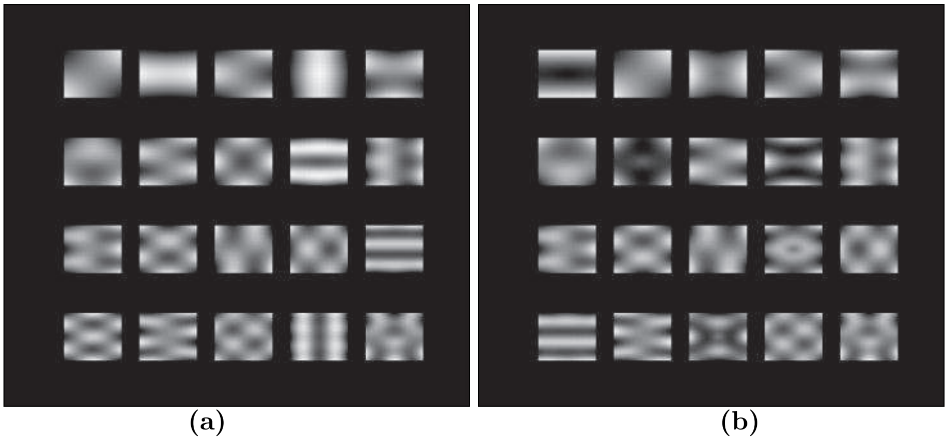

Figure 3. Examples of eigenfunctions plotted using the present method. **(a)**: First 20 eigenfunctions for a free plate of aspect ratio $\eta = 1.5$ and Poisson's ratio $\nu = 0.3$. Note that the three modes at zero frequency corresponding to rigid motions and rotations are not shown. **(b)**: First 20 eigenfunctions for a free plate supported at its centre of aspect ratio $\eta = 1.5$ and Poisson's ratio $\nu = 0.3$. Note that the two modes at zero frequency corresponding to rigid rotations are not shown.

2.6. Extension of the modal techniques to the case of the von Kármán plate

In section 2.1 it was shown that modal techniques can be applied in a quite general manner to the case of linear, self-adjoint systems. These properties allow to represent the general state of the system at a particular time t as a superposition of independent contributions, i.e. the eigenfunctions, which can be proved to be orthogonal in the sense of L^2 function spaces and thus constitute a suitable vector basis for the domain in which they are defined.

When the system is nonlinear, such properties cease to exist. In fact, the nonlinearities tend to couple the modes in some manner, and thus the response of the system cannot be obtained by summing up the single modal responses, as now each one of them may affect the others. In the case of the von Kármán plate the nonlinearities are purely geometrical, as pointed out is section 1.3.3, meaning that they are expected to come into play when the amplitude of motion is large (i.e. of the order of the plate thickness). The von Kármán equations are here recalled for the sake of clarity.

Consider a rectangular plate of dimensions L_x, L_y and thickness h (with $h \ll L_x$, L_y). The plate material is homogeneous, of volume density ρ, Young's modulus E and Poisson's ratio ν. Its flexural rigidity is then defined as $D = Eh^3/12(1-\nu^2)$. The von Kármán system then reads (see section 1.3.3)

$$D\Delta\Delta w + \rho h \ddot{w} = \mathcal{L}(w, F), \tag{2.45a}$$

$$\Delta\Delta F = -\frac{Eh}{2}\mathcal{L}(w, w), \tag{2.45b}$$

where Δ is the Laplacian operator, $w = w(x, y, t)$ is the transverse displacement and $F = F(x, y, t)$ is the Airy stress function.

The strategy adopted here to solve the von Kármán system makes use of the linear modes for the displacement w and Airy stress function F. This strategy is particularly useful for investigating the free and forced vibrations of the system, in the sense that it allows for the reduction of the dynamics of the problem from an infinite number of degrees of freedom to a finite one. The eigenfunctions for the displacement w will be denoted by the symbol $\Phi_k(x, y)$ and thus $w(x, y, t)$ is written as

$$w(x, y, t) = S_w \sum_{k=1}^{N_\Phi} \frac{\Phi_k(x, y)}{\|\Phi_k\|} q_k(t), \tag{2.46a}$$

where Φ_k is such that

$$\Delta\Delta\Phi_k(x, y) = \frac{\rho h}{D}\omega_k^2 \Phi_k(x, y). \tag{2.46b}$$

Note that the sum in Eq. (2.46a) is terminated at N_Φ in practice. The linear modes can be defined up to a constant of normalisation that can be chosen arbitrarily. For the sake of generality, S_w here denotes the constant of normalisation of the function $\bar{\Phi} = S_w \frac{\Phi_k(x,y)}{\|\Phi_k\|}$. The norm is obtained from a scalar product $< \alpha, \beta >$ between two functions $\alpha(x, y)$ and $\beta(x, y)$, defined as

$$< \alpha, \beta >= \int_S \alpha\, \beta\, dS \qquad \longrightarrow \qquad \|\Phi_k\|^2 =< \Phi_k, \Phi_k > . \tag{2.47}$$

Eq. (2.46b) is the eigenvalue problem definition, and it is a Kirchhoff-like equation for linear plates. The Airy stress function is expanded along an analogue series

$$F(x,y,t) = S_F \sum_{k=1}^{N_\Psi} \frac{\Psi_k(x,y)}{\|\Psi_k\|}\eta_k(t), \tag{2.48a}$$

$$\Delta\Delta\Psi_k(x,y) = \zeta_k^4 \Psi_k(x,y). \tag{2.48b}$$

The linear modes so defined are orthogonal with respect to the scalar product, and are therefore a suitable function basis [44]. Orthogonality between two functions $\Lambda_m(x,y), \Lambda_n(x,y)$ is expressed as (see section 2.1)

$$< \Lambda_m, \Lambda_n >= \delta_{m,n}\|\Lambda_m\|^2, \tag{2.49}$$

where $\delta_{m,n}$ is Kronecker's delta.

Once the linear modal shapes are known, system (2.45) may then be reduced to a set of ordinary differential equations, each referring to the $k-$th modal coordinate $q_k(t), \quad k = 1, ..., N_\Phi$. N_Φ represents the order of the system of ODEs.

The introduction of the expansion series (2.46a) and (2.48a) allows for the decomposition of the original von Kármán problem onto a set of coupled, nonlinear ordinary differential equations (ODEs). As a starting point, Eq. (2.48a) is substituted into Eq. (2.45b) to obtain

$$\eta_k = -\frac{Eh}{2\zeta_k^4}\frac{S_w^2}{S_F}\sum_{p,q} q_p q_q \frac{\int_S \Psi_k L(\Phi_p,\Phi_q)\mathrm{d}S}{\|\Psi_k\|\|\Phi_p\|\|\Phi_q\|}. \tag{2.50}$$

Integration is performed over the area of the plate, and the orthogonality relation is used. Injecting Eq. (2.46) and (2.50) into Eq. (2.45a) gives

$$\begin{aligned}\rho h S_w \sum_k \frac{\omega_k^2 \Phi_k}{\|\Phi_k\|} q_k + \rho h S_w \sum_k \frac{\Phi_k}{\|\Phi_k\|}\ddot{q}_k \\ = -\frac{EhS_w^3}{2}\sum_{n,p,q,r}\frac{1}{\zeta_n^4}\frac{L(\Phi_p,\Psi_n)}{\|\Psi_p\|\|\Phi_n\|}\frac{\int_S \Psi_n L(\Phi_q,\Phi_r)\mathrm{d}S}{\|\Phi_q\|\|\Phi_r\|\|\Psi_n\|} q_p q_q q_r.\end{aligned} \tag{2.51}$$

Then the equation is multiplied on both sides by Φ_s and integrated over the surface of the plate. The result is

$$\ddot{q}_s + \omega_s^2 q_s = -\frac{ES_w^2}{2\rho}\sum_{p,q,r}^{n}\frac{H_{q,r}^n E_{p,n}^s}{\zeta_n^4} q_p q_q q_r. \tag{2.52}$$

Two third order tensors, $H_{q,r}^n$ and $E_{p,n}^s$ appear in Eq. (2.52). These are defined as

$$H_{p,q}^n = \frac{\int_S \Psi_n L(\Phi_p,\Phi_q)\mathrm{d}S}{\|\Psi_n\|\|\Phi_p\|\|\Phi_q\|}, \qquad E_{r,n}^s = \frac{\int_S \Phi_s L(\Phi_r,\Psi_n)\mathrm{d}S}{\|\Phi_r\|\|\Phi_s\|\|\Psi_n\|}. \tag{2.53}$$

It is seen that the ODEs are cubic with respect to the variables q_s, so a fourth order tensor Γ can conveniently be introduced in the equations, as

$$\Gamma^s_{p,q,r} = \sum_{n=1}^{N_\Psi} \frac{H^n_{p,q} E^s_{r,n}}{2\zeta_n^4}. \tag{2.54}$$

A stable, energy-conserving scheme will be presented in section 2.7. Such a scheme will be used to solve the von Kármán equations over time in order to reproduce the sound of gongs and cymbals. The results will be presented in Chapter 6. In addition, the modal equations (2.52) will be used to perform bifurcation analysis of free and forced vibrations of a reduced-order system comprising a few modes, in order to study the nonlinear behaviour of the plate around a particular eigenfrequency. Such a study will be carried out by means of continuation techniques, and the results will be shown in Chapter 4.

2.6.1. A discussion on the von Kármán boundary conditions. In the previous section, it was seen that the solution to the von Kármán system can be sought in terms of functions that satisfy the linear plate equation, Eqs. (2.46a) and (2.48a). Such equations must satisfy a particular set of boundary conditions, chosen amongst those presented in the table at the end of sec. 1.3.3. For clarity, the possible choices are here recalled in terms of the particular eigenfunctions $\tilde{\Phi}$, $\tilde{\Psi}$

In-plane direction	Edge Rotation	Edge Vertical Translation
• Movable	• Rotationally Free	• Transversely Movable
$\tilde{\Psi}_{,nt} = \tilde{\Psi}_{,tt} = 0$	$\tilde{\Phi}_{,nn} + \nu\tilde{\Phi}_{,tt} = 0$	$\tilde{\Phi}_{,nn} + (2-\nu)\tilde{\Phi}_{,ntt}$
• Immovable (with $w = 0$)	• Rotationally Immovable	$-\frac{1}{D}(\tilde{\Psi}_{,tt}\tilde{\Phi}_{,n} - \tilde{\Psi}_{,nt}\tilde{\Phi}_{,t}) = 0$
$\tilde{\Psi}_{,nn} - \nu\tilde{\Psi}_{,tt} =$	$\tilde{\Phi}_{,n} = 0$	$\tilde{\Phi}_{,nt} = 0$ at corners.
$\tilde{\Psi}_{,nnn} + (2+\nu)\tilde{\Psi}_{,ntt} = 0$		• Transversely Immovable
		$\tilde{\Phi} = 0$

As a start, consider the in-plane movable conditions for $\tilde{\Psi}$; these can be replaced by

$$\tilde{\Psi}_{,n} = \tilde{\Psi} = 0. \tag{2.55}$$

It is clear that such conditions are sufficient to satisfy the original conditions (if a function is constant along one edge, then all derivatives taken along the edge direction are zero). When Eq. (2.48b) is used in combination with Eq. (2.55), then the problem for the Airy stress function is expressed mathematically as the problem of the clamped Kirchhoff plate. For that, the modal techniques of sec. 2.4 can be used to find the eigenfunctions and frequencies and thus to calculate the tensor of coupling coefficients. When the edges are movable in the in-plane directions, then the conditions for a transversely movable edge reduce to the conditions of a free Kirchhoff plate, which was solved in sec. 2.5. The results from that section can be used as well to calculate the in-plane immovable conditions of $\tilde{\Psi}$ by replacing ν with $-\nu$. In turn, all the combinations of boundary conditions for

the von Kármán plate can be solved using the techniques presented in the previous section, with the sole exception of the in-plane immovable/transversely movable conditions (the latter becoming a nonlinear condition in this case).
For the rest of this work, a *simply supported plate with in-plane movable edges* is considered. Hence

$$w = w_{,nn} = 0; \tag{2.56a}$$

$$F = F_{,n} = 0. \tag{2.56b}$$

Such conditions were chosen before by Touzé *et al.* [88], who investigated the transition scenario to turbulence in a rectangular plate by making use of a Finite Difference Scheme. This scheme will be presented in the next chapter and will be used consistently to test the goodness of the present model.

2.6.2. Von Kármán equations with damping and forcing terms. So far damping and forcing have not been taken into account in the discussion. For linear systems, it was shown in sec. 2.1 that these terms are treated straightforwardly in terms of the modes, as it suffices to project them on the particular eigenfunction $\tilde{\Phi}$. Such an extension can be done for the von Kármán system as well. For that, consider a modification of Eq. (2.45a)

$$D\Delta\Delta w(\mathbf{x},t) + \rho h \ddot{w}(\mathbf{x},t) = \mathcal{L}(w(\mathbf{x},t), F(\mathbf{x},t)) - C\dot{w}(\mathbf{x},t) + \delta(\mathbf{x}-\mathbf{x}_0)P(t).$$

In this equation, a viscous-type damping term appears proportional to the velocity field, as well as a forcing term (which is supposed to be localised in space and having a time-dependent amplitude $P(t)$). Projecting this equation onto a the mode s results in

$$\ddot{q}_s + \omega_s^2 q_s + 2\chi_s\omega_s\dot{q}_s = -\frac{ES_w^2}{\rho}\sum_{p,q,r}\Gamma^s_{p,q,r}\, q_p q_q q_r + \frac{\Phi_s(\mathbf{x}_0)}{\|\Phi_s\|\rho h S_w}P(t), \tag{2.57}$$

where the modal viscous damping (a dimensionless quantity) was introduced for each mode as $\chi_s = C/(2\rho h\omega_s)$. Such a definition for damping is most definitely appropriate, as metallic plates are usually slightly damped structures and thus the damping coefficient matrix can be thought as being composed by diagonal elements only (see [94]). Hence, the modal equations (2.57) allow the inclusion of a damping mechanisms which can be, in theory, very close to reality, when the damping coefficients are known (for instance, by measuring them experimentally [54]).
In view of a comparison with a previously developed finite difference scheme [7, 88], a different version of the damping mechanism is now presented. In a finite difference domain, damping can only be inserted in the global dynamical equations via an ad-hoc time domain representation. This can be done as

$$D\Delta\Delta w(\mathbf{x},t) + \rho h\ddot{w}(\mathbf{x},t) = L(w(\mathbf{x},t), F(\mathbf{x},t)) + R_0(\dot{w}) + R_1(\Delta\dot{w}) + \delta(\mathbf{x}-\mathbf{x}_0)P(t), \tag{2.58}$$

where the loss terms are

$$R_0(\dot{w}) = -2\sigma_0\dot{w}(\mathbf{x},t); \qquad R_1(\Delta\dot{w}) = 2\sigma_1\Delta\dot{w}(\mathbf{x},t),$$

where σ_0, σ_1 have the dimensions of, respectively, $[ML^{-2}T^{-1}]$ and $[MT^{-1}]$. Taking Fourier transforms of the damping laws results in

$$\tilde{R}_0(\tilde{w}) = \gamma_0(f)\tilde{w}(\mathbf{k},t); \qquad \tilde{R}_1(\tilde{w}) = \gamma_1(f)\tilde{w}(\mathbf{k},t),$$

where

$$\gamma_0(f) = -2\sigma_0; \qquad \gamma_1(f) = -2\sigma_1 \frac{2\pi}{hc_b} f. \tag{2.59}$$

For the last equality, the linear dispersion equations for flexural waves in plates was used

$$\omega = hc_b|\mathbf{k}|^2,$$

with $c_b = \sqrt{E/12(1-\nu^2)\rho}$ indicating the bulk velocity. The meaning of Eq. (2.59) is that R_0 dissipates energy at equal rates at all frequencies, whereas R_1 is proportional to the frequency. A frequency-dependent loss factor is desirable as, in plates, frequencies past the "critical frequency" are dissipated at higher rates, mainly due to radiation in air. Physically speaking, R_0 is a common viscous-type law; R_1, however, does not correspond to a physical loss mechanism. Bilbao [8] points out that R_1 appears as an easier-to-implement modification of a damping law proposed by Ruiz [79] for piano strings. Regardless the introduction of a frequency-dependent loss, the capability of simulating an accurate damping model in a Finite Difference scheme should be regarded as very limited when compared to the modal equations. This topic will be discussed further when comparing sound-synthesis results in Chapter 6.

2.6.3. Adjointness and symmetry properties.

In section 1.3.3 a "triple self-adjointness" was shown. In the general case, this is [83]

$$\int_0^{L_y}\int_0^{L_x} \alpha\mathcal{L}(\beta,\gamma)\; dxdy = \int_0^{L_y}\int_0^{L_x} \gamma\mathcal{L}(\alpha,\beta)\; dxdy + \oint_\Omega [\beta_{,tt}(\alpha\gamma_{,n} - \gamma\alpha_{,n}) - \beta_{,nt}(\alpha\gamma_{,t} - \gamma\alpha_{,t})]\; d\Omega.$$

where Ω is the contour of the plate. The triple self-adjointness property has a direct consequence on the tensors H, E. In fact, integrating by parts the integral in the definition of E in Eq. (2.53) gives

$$\|\Psi_q\|\|\Phi_n\|\|\Phi_p\| E^n_{p,q} = \oint_\Omega \left[\Phi_n\Psi_{q,y}\Phi_{p,xx} - 2\Phi_n\Psi_{q,x}\Phi_{p,xy} - \Psi_q\frac{\partial}{\partial y}\left(\Phi_n\Phi_{p,xx}\right)\right]\; \hat{\mathbf{y}}\cdot\mathbf{n}\; d\Omega +$$

$$+ \oint_\Omega \left[\Phi_n\Psi_{q,x}\Phi_{p,yy} + 2\Psi_q\frac{\partial}{\partial y}\left(\Phi_n\Phi_{p,xy}\right) - \Psi_q\frac{\partial}{\partial x}\left(\Phi_n\Phi_{p,yy}\right)\right]\; \hat{\mathbf{x}}\cdot\mathbf{n}\; d\Omega + \int_0^{L_y}\int_0^{L_x} \Psi_q L(\Phi_p,\Phi_n)\; dxdy,$$

where $\hat{\mathbf{x}}$, $\hat{\mathbf{y}}$ are unit vectors in the x, y directions, and $\mathbf{n}$ is the unit vector normal to the boundary Ω. This property is useful when the boundary integrals vanishes. For that, the eigenfunctions Φ_k, Ψ_k need to satisfy particular combinations of boundary conditions. The case that will be mostly used in this work, *i.e.* a simply supported plate with in-plane movable edges, conditions (2.56) render the boundary integral null. Hence

$$E^n_{p,q} = H^q_{p,n}. \tag{2.60}$$

Owing to this property, the tensor Γ may then be conveniently written as

$$\Gamma^s_{p,q,r} = \sum_{n=1}^{N_F} \frac{H^n_{p,q} H^n_{r,s}}{2\zeta_n^4}. \tag{2.61}$$

Note that the tensor H as defined in Eq. (2.53) is divided by the norms of the modes, so the value of Γ is independent of the particular choice for the constants S_w, S_F in Eqs. (2.46b), (2.48b). Note also that the tensor H possess a straightforward symmetry property stemming from its definition

$$H^i_{p,q} = H^i_{q,p}.$$

This property means that a few permutations of the Γ tensor indices will produce the same numerical value. These permutations are

$$(s,p,q,r),\ (r,p,q,s),\ (s,q,p,r),\ (r,q,p,s),\ (q,r,s,p),\ (p,r,s,q),\ (q,s,r,p),\ (p,s,r,q).$$

2.6.4. Energy components in terms of the modes. Eqs. (1.51) are the energy expressions for the von Kármán plate. When the eigenmode expansions (2.46a),(2.48a) are inserted in the energy expressions, one obtains

$$T = \frac{\rho h}{2} S_w^2 \sum_{k,l=1}^{N_\Phi} \int_0^{L_y}\int_0^{L_x} \frac{\Phi_k \Phi_l}{\|\Phi_k\|\|\Phi_l\|}\ dxdy\ \ \dot{q}_k(t)\dot{q}_l(t); \tag{2.62a}$$

$$U_l = \frac{D}{2} S_w^2 \sum_{k,l=1}^{N_\Phi} \int_0^{L_y}\int_0^{L_x} \frac{\Delta\Phi_k \Delta\Phi_l}{\|\Phi_k\|\|\Phi_l\|}\ dxdy\ \ q_k(t)q_l(t); \tag{2.62b}$$

$$U_{nl} = \frac{S_F^2}{2Eh} \sum_{k,l=1}^{N_\Psi} \int_0^{L_y}\int_0^{L_x} \frac{\Delta\Psi_k \Delta\Psi_l}{\|\Psi_k\|\|\Psi_l\|}\ dxdy\ \ \eta_k(t)\eta_l(t); \tag{2.62c}$$

The integrals in Eqs. (2.62b), (2.62c) are calculated by parts. Owing to the selected boundary conditions,Eq. (2.56), the boundary integrals vanish and one is left with

$$\int_0^{L_y}\int_0^{L_x} \frac{\Delta\Phi_k \Delta\Phi_l}{\|\Phi_k\|\|\Phi_l\|}\ dxdy = \int_0^{L_y}\int_0^{L_x} \frac{\Delta\Delta\Phi_k\ \Phi_l}{\|\Phi_k\|\|\Phi_l\|}\ dxdy; \tag{2.63a}$$

$$\int_0^{L_y}\int_0^{L_x} \frac{\Delta\Psi_k \Delta\Psi_l}{\|\Psi_k\|\|\Psi_l\|}\ dxdy = \int_0^{L_y}\int_0^{L_x} \frac{\Delta\Delta\Psi_k\ \Psi_l}{\|\Psi_k\|\|\Psi_l\|}\ dxdy. \tag{2.63b}$$

Making use of Eqs. (2.46b), (2.48b) and of the orthogonality relationship gives

$$\int_0^{L_y}\int_0^{L_x} \frac{\Delta\Phi_k \Delta\Phi_l}{\|\Phi_k\|\|\Phi_l\|}\ dxdy = \frac{\rho h}{D}\omega_k^2 \delta_{k,l}; \tag{2.64a}$$

$$\int_0^{L_y}\int_0^{L_x} \frac{\Delta\Psi_k \Delta\Psi_l}{\|\Psi_k\|\|\Psi_l\|}\ dxdy = \zeta_k^4 \delta_{k,l}. \tag{2.64b}$$

The expressions for η_k, η_l in Eq. (2.62c) are obtained from Eq. (2.50). Putting these results all together, and remembering the expression for $\Gamma^s_{p,q,r}$ in Eq. (2.61), one obtains

$$T = \frac{\rho h}{2} S_w^2 \sum_{k=1}^{N_\Phi} \dot{q}_k^2(t); \tag{2.65a}$$

$$U_l = \frac{\rho h}{2} S_w^2 \sum_{k=1}^{N_\Phi} \omega_k^2 q_k^2(t); \tag{2.65b}$$

$$U_{nl} = \frac{Eh}{4} \frac{S_w^4}{S_F^2} \sum_{p,q,r,s=1}^{N_\Phi} \Gamma^s_{p,q,r} q_p(t) q_q(t) q_r(t) q_s(t); \tag{2.65c}$$

These are the time-dependent energy expressions for a von Kármán plate in terms of the modes. Note that the last expression can be written in terms of the components η as

$$U_{nl} = \frac{1}{2Eh} \sum_{k=1}^{N_\Psi} \zeta_k^4 \eta_k^2(t). \tag{2.66}$$

This last expression will become useful to prove energy conservation of the stable scheme presented in sec. 2.7. Energy conservation reads

$$\frac{d}{dt}(T + U_l + U_{nl}) = 0. \tag{2.67}$$

2.7. Time integration schemes

In the previous sections the original Partial Differential System was discretised onto the space formed by the eigenmodes of the system. This allowed to reduce the problem to a series of coupled Ordinary Differential Equations depending on the time variable. Thus, it is necessary to develop a numerical scheme in order to perform integration over time. In this section, two numerical time integration schemes are presented. The first is a classical integration scheme, *i.e.* the Störmer-Verlet scheme. Properties of this scheme can be found in the book by Hairer *et al.* [45]. The second scheme is an energy-conserving, stable scheme developed by Bilbao [7], and used before by this author [27].

The aim of a numerical time-integration scheme is to approximate the solution to the differential equation

$$\ddot{\mathbf{q}} = \mathbf{f}(\mathbf{q}, t),$$

where $\mathbf{q}$ is the vector of the state variables (for instance, the modal coordinates), and $\mathbf{f}$ is the function describing the dynamics (which is a nonlinear function in the case of the von Kármán plate). In order to do so, a discretisation of the time variable is introduced, depending on a *sampling rate* F_s or, equivalently, a time step $k = 1/F_s$. Hence, the solution can be calculated at discrete instants, separated by the distance k; the discrete instant at which the solution is calculated can be denoted by the index n, and the discrete solution denoted by $\mathbf{q}(n)$. The goal of a scheme is to introduce discrete mapping λ_k which pushes the solution from the step n to the step $n+1$, such that

$$\lambda_k : \mathbf{q}(n) \longrightarrow \mathbf{q}(n+1).$$

A list of discrete operators is now introduced. A more exhaustive list will be presented in Chapter 3 dealing with Finite Difference schemes. The most obvious operator is the identity operator, denoted by

$$1\mathbf{q}(n) = \mathbf{q}(n). \tag{2.68}$$

The backward and forward shift operators are, respectively,

$$e_{t-}\mathbf{q}(n) = \mathbf{q}(n-1); \qquad e_{t+}\mathbf{q}(n) = \mathbf{q}(n+1). \tag{2.69}$$

Backward, centered, forward approximations to first time derivatives are defined as

$$\delta_{t-} \equiv \frac{1}{k}(1 - e_{t-}); \qquad \delta_{t\cdot} \equiv \frac{1}{2k}(e_{t+} - e_{t-}); \qquad \delta_{t+} \equiv \frac{1}{k}(e_{t+} - 1). \tag{2.70}$$

An approximation to the second time derivative can be constructed by combining the previous operators. In such a way, a particular form employed here is given by

$$\delta_{tt} \equiv \delta_{t+}\delta_{t-} = \frac{1}{k^2}(e_{t+} - 2 + e_{t-}) \tag{2.71}$$

Backward, centered, forward averaging operators are introduced as

$$\mu_{t-} \equiv \frac{1}{2}(1 + e_{t-}); \qquad \mu_{t\cdot} \equiv \frac{1}{2}(e_{t+} + e_{t-}); \qquad \mu_{t+} \equiv \frac{1}{2}(e_{t+} + 1). \tag{2.72}$$

The accuracy of each operator can be calculated applying the operator to a generic well-behaved function $u(t)$ (defined over the continuous time variable t) and by expanding the result in Taylor series about t. As an example, consider the backward discrete time derivative operator; applying it to the function u gives

$$\delta_{t-}u(t) = \frac{1}{k}(u(t) - u(t-k)).$$

Now define $\tau = t - k$ and expand $u(\tau)$ around the point $\tau = t$

$$u(\tau) = u(t) - k\left(\frac{du}{dt}\right) + k^2\left(\frac{d^2u}{dt^2}\right) + O(k^3).$$

Hence

$$\delta_{t-}u(t) = \frac{1}{k}(u(t) - u(\tau)) = \frac{du}{dt} + O(k). \tag{2.73}$$

It is seen that the operator δ_{t-} approximates the first time derivative to the order of k, the timestep. In a similar manner, one can show that the the centered operators are $O(k^2)$ accurate, whereas the backward and forward operators are $O(k)$ accurate. The approximation to the second time derivative is also $O(k^2)$ accurate.

2.7.1. Störmer-Verlet scheme. Consider the von Kármán modal equations without forcing and loss terms, Eq. (2.52). A Störmer-Verlet scheme is obtained by considering

$$\delta_{tt}\mathbf{q}(n) = \mathbf{f}(\mathbf{q}(n)) \tag{2.74}$$

(Note that in this case the function $\mathbf{f}$ does not depend explicitly on t). Such a scheme is second-order, symmetric and symplectic [45]. When adding and forcing terms are introduced in the von Kármán system as in Eq. (2.57), one has to choose an approximation to the first time derivative. Here the choice is to use a centered derivative as it is second-order accurate. The discrete counterpart of Eq. (2.57) is now written as

$$\delta_{tt}\mathbf{q}(n) = -\mathbf{K}\mathbf{q}(n) - \mathbf{C}\delta_{t\cdot}\mathbf{q}(n) - \mathbf{s}(n) + \mathbf{p}(n). \tag{2.75}$$

In the equation above, the matrices $\mathbf{K}$, $\mathbf{C}$ denote the normalised stiffness and damping matrices (independent of the step n). In practice, if N_Φ denoted the length of the vectors, then these matrices are $N_\Phi \times N_\Phi$; the two matrices are diagonal, and their elements are

$$K_{m,m} = \omega_m^2; \tag{2.76a}$$

$$C_{m,m} = 2\chi_m\omega_m. \tag{2.76b}$$

The vector $\mathbf{s}$ is the vector of the nonlinear terms, acting as a coupling. This is, simply

$$s_m(n) = \frac{ES_w^2}{\rho}\sum_{j,k,l=1}^{N_\Phi}\Gamma^m_{j,k,l}q_j(n)q_k(n)q_l(n). \tag{2.77}$$

Finally, $\mathbf{p}$ is the vector containing the forcing terms, *i.*e.

$$p_m(n) = \frac{\Phi_m(\mathbf{x}_0)}{\|\Phi_m\|\rho h S_w}P(n). \tag{2.78}$$

Developing the discrete operators gives the following algebraic system, to be solved for the variable $\mathbf{q}(n+1)$

$$\left(\frac{\mathbb{I}}{k^2} + \frac{\mathbf{C}}{2k}\right)\mathbf{q}(n+1) = \left(\frac{2\mathbb{I}}{k^2} - \mathbf{K}\right)\mathbf{q}(n) + \left(\frac{\mathbf{C}}{2k} - \frac{\mathbb{I}}{k^2}\right)\mathbf{q}(n-1) - \mathbf{s}(n) + \mathbf{p}(n), \tag{2.79}$$

where $\mathbb{I}$ is the identity matrix. This scheme is explicit, and the algebraic linear system can solved easily in MATLAB by means of the operator \ (backslash). If the nonlinear terms of scheme (2.79) are set to zero, along with the damping and forcing terms, a discrete energy conservation law can be stated in the following form

$$\delta_{t+}\left\{\sum_{s=1}^{N_\Phi} S_w^2\frac{\rho h}{2}\left[\left(\delta_{t-}q_s(n)\right)^2 + \omega_s^2 q_s(n)\left(e_{t-}q_s(n)\right)\right]\right\} = 0, \tag{2.80}$$

or

$$\delta_{t+}\sum_{s=1}^{N_\Phi}(\tau_s(n) + \upsilon_s^l(n)) \tag{2.81}$$

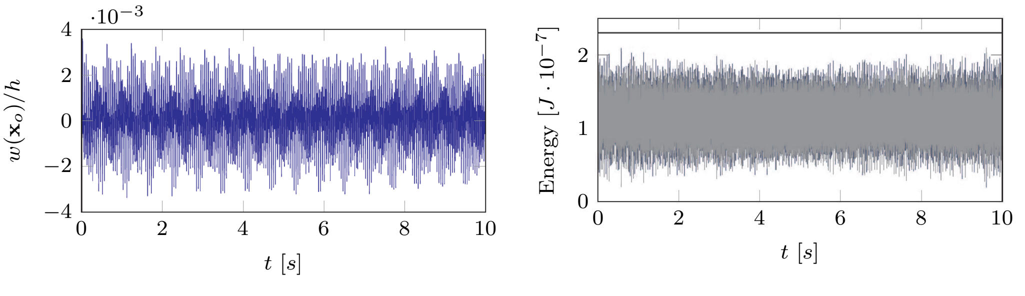

(a) **(b)**

FIGURE 4. Time simulations of a linear steel plate of dimensions $L_x \times L_y = 0.4 \times 0.6\text{m}^2$ and thickness $h = 1\text{mm}$. The plate is excited at input location $\mathbf{x}_i = [0.3L_x \;\; 0.2L_y]$ with a discrete dirac delta of length 1 sample and amplitude 1; the output is taken at $\mathbf{x}_o = [0.7L_x \;\; 0.3L_y]$. The number of transverse modes is $N_\Phi = 20$: the highest eigenfrequency of the system is $\omega_{20} = 1893.7\text{rad/s}$; hence the stability condition Eq. (2.82) gives the limiting sampling frequency $F_s = 947\text{Hz}$. **(a)** Time series sampled at 5kHz, showing linear behaviour ($w \ll h$); **(b)** total energy (black thick line), kinetic (grey) and linear potential (navy).

which corresponds to Eq. (2.67) (where the nonlinear energy is zero). In the equation above, $\tau_s(n)$, $v_s^l(n)$ can be though of as, respectively, the discrete kinetic and linear potential energies.

Conservation of discrete energy allows to derive a stability condition for the scheme applied to the linear plate equation. Let ω_s denote the largest eigenfrequency of the system, then the scheme is stable when

$$k < \frac{2}{\omega_s}. \tag{2.82}$$

When this condition is enforced, then the discrete energies are positive definite. This condition (along with the mathematical proof) will be extended to the nonlinear system in the next subsection. Fig 4 shows that when the system is a linear regime, then energy is conserved.

If one wishes to solve Eq. (2.58), a modification of the damping matrix is needed. The only part that may pose problems is the term proportional to the Laplacian of the velocity. However, for simply supported boundary conditions on the transverse modes, the solution is harmonic, and so $\Delta\dot{w} \propto \dot{w}$. Given the modal expansion (2.46a) and the simply supported boundary conditions, one can easily find the modal projection onto the m^{th} coordinate; this is

$$\left\langle \Phi_m, S_w \sum_{n=1}^{N_\Phi} \frac{\Delta\Phi_n}{\|\Phi_n\|} \right\rangle = -S_w \left[\left(\frac{m_1\pi}{L_x}\right)^2 + \left(\frac{m_2\pi}{L_y}\right)^2 \right] \|\Phi_m\| \Phi_m, \tag{2.83}$$

where m_1, m_2 replace the generic indices m, n of Eq. (2.31). Thus, the damping matrix now reads

$$C_{m,m} = \frac{2\sigma_0}{\rho h} + \left[\left(\frac{m_1\pi}{L_x}\right)^2 + \left(\frac{m_2\pi}{L_y}\right)^2\right]\frac{2\sigma_1}{\rho h}. \tag{2.84}$$

The damping matrix is still diagonal constant over time, and the frequency dependence is expressed through the modal indices m_1, m_2.

The Störmer-Verlet scheme will be used extensively in Chapter 6 to obtain gong-like sounds. In fact, although stability for such a scheme cannot be proved, the implementation of such a scheme is really easy, and leads to fast computations. However, if one wishes to perform a study of the plate in a strongly nonlinear regime, stability becomes a priority. This is why, in the next section, a stable scheme will be presented.

2.7.2. A stable, energy-conserving scheme. In this section, a stable scheme is presented. A stability condition will stem directly from the conservation of a discrete quantity which will act as the counterpart of the total energy of the plate. The scheme is constructed as follows

$$\delta_{tt}q_s(n) + K_{s,s}q_s(n) = \frac{S_F}{\rho h}\sum_{k=1}^{N_\Phi}\sum_{l=1}^{N_\Psi} E^s_{k,l}q_k(n)[\mu_{t\cdot}\eta_l(n)] - C_{s,s}\delta_{t\cdot}q_s(n) + p_s(n); \tag{2.85a}$$

$$\mu_{t-}\eta_l(n) = -\frac{Eh}{2\zeta_l^4}\frac{S_w^2}{S_F}\sum_{i,j=1}^{N_\Phi} H^l_{i,j}q_i(n)[e_{t-}q_j(n)]. \tag{2.85b}$$

In the scheme above, the stiffness and damping matrices $\mathbf{K}$, $\mathbf{C}$ are the same as in the previous subsection. Rearranging all the terms gives

$$\left(\frac{1}{k^2} + \frac{C_{s,s}}{2k}\right)q_s(n+1) + \frac{ES_w^2}{\rho}\sum_{i,j,k=1}^{N_\Phi}\Gamma^s_{k,i,j}q_k(n)q_j(n)q_i(n+1) =$$

(2.86a)

$$\left(\frac{2}{k^2} - K_{s,s}\right)q_s(n) + \left(\frac{C_{s,s}}{2k} - \frac{1}{k^2}\right)q_s(n-1) + \frac{S_F}{\rho h}\sum_{k=1}^{N_\Phi}\sum_{l=1}^{N_\Psi}H^l_{k,s}\left(\frac{\eta_l(n-1) - \eta_l(n)}{2}\right)q_k(n) + p_s(n);$$

$$\eta_l(n+1) = -\eta_l(n) - \frac{Eh}{\zeta_l^4}\frac{S_w^2}{S_F}\sum_{i,j=1}^{N_\Phi}H^l_{i,j}q_i(n+1)q_j(n). \tag{2.86b}$$

This scheme is implicit, therefore more computationally demanding than Störmer-Verlet. However, for such a scheme there exist an energy conservation law, in a discrete sense. Energy conservation is obtained by multiplying Eq. (2.85a) (without losses and forcing) by $\delta_{t\cdot}\, q_s(n)\ \rho h$ and by summing over the index s. In addition, Eq. (2.85b) is multiplied by δ_{t+}. This gives

(2.87a)

$$\rho h\sum_{s=1}^{N_\Phi}\left(\delta_{t\cdot}q_s(n)\right)\delta_{tt}\,q_s(n)+\rho h\sum_{s=1}^{N_\Phi}\left(\delta_{t\cdot}q_s(n)\right)K_{s,s}q_s(n)=S_F\sum_{k,s=1}^{N_\Phi}\sum_{l=1}^{N_\Psi}E^s_{k,l}\,\left(\delta_{t\cdot}q_s(n)\right)q_k(n)(\mu_{t\cdot}\,\eta_l(n))$$

(2.87b)

$$\mu_{t-}\left(\delta_{t+}\eta_l(n)\right)=-\frac{EhS_w^2}{2\zeta_l^4 S_F}\sum_{k,s=1}^{N_\Phi}\frac{1}{k}H^l_{k,s}\left(q_k(n+1)q_s(n)-q_k(n)q_s(n-1)\right)$$

Now, owing to the symmetry property of the H tensor when the indices k,s are swapped, the right hand side of Eq. (2.87b) can be written as

$$\begin{aligned}\frac{1}{k}H^l_{k,s}\left(q_k(n+1)q_s(n)-q_k(n)q_s(n-1)\right)&=\frac{1}{k}H^l_{k,s}\left(\underbrace{q_s(n+1)q_k(n)}_{\text{indices are swapped owing to symmetry of }H}-q_k(n)q_s(n-1)\right)\\&=2H^l_{k,s}q_k(n)\delta_{t\cdot}q_s(n).\end{aligned}$$

Hence Eq.(2.87b) may be rewritten as

$$-\frac{\zeta_l^4 S_F}{EhS_w^2}\mu_{t-}\left(\delta_{t+}\eta_l(n)\right)=\sum_{k,s=1}^{N_\Phi}H^l_{k,s}q_k(n)\delta_{t\cdot}q_s(n)\tag{2.89}$$

Owing to the triple self-adjointness property, one may write $E^s_{k,l}=H^l_{k,s}$ and insert the left hand side of Eq. (2.89) into the right hand side of Eq. (2.87a). This gives

$$\begin{aligned}S_F\sum_{k,s=1}^{N_\Phi}\sum_{l=1}^{N_\Psi}(\delta_{t\cdot}q_s(n))q_k(n)(\mu_{t\cdot}\eta_l(n)))&=-\frac{1}{S_w^2Eh}\sum_{l=1}^{N_\Psi}[\mu_{t-}(\delta_{t+}\eta_l(n))](\mu_{t\cdot}\eta_l(n))\\&=-\frac{\delta_{t+}}{2EhS_w^2}\sum_{l=1}^{N_\Psi}(\mu_{t-}(\eta_l(n)\eta_l(n)))\zeta_l^4.\end{aligned}\tag{2.90}$$

The left hand side of Eq. (2.87a) can be rewritten as

(2.91)

$$\rho h\sum_{s=1}^{N_\Phi}\left(\delta_{t\cdot}q_s(n)\right)\delta_{tt}\,q_s(n)+\rho h\sum_{s=1}^{N_\Phi}\left(\delta_{t\cdot}q_s(n)\right)\omega_s^2q_s(n)=\frac{\rho h}{2}\delta_{t+}\sum_{s=1}^{N_\Phi}\left(\left(\delta_{t-}q_s(n)\right)^2+\omega_s^2q_s(n)\left(e_{t-}q_s(n)\right)\right)$$

Putting together Eq. (2.90) and (2.91) gives

$$\delta_{t+}\left\{\sum_{s=1}^{N_\Phi}S_w^2\frac{\rho h}{2}\left[\left(\delta_{t-}q_s(n)\right)^2+\omega_s^2q_s(n)\left(e_{t-}q_s(n)\right)\right]+\frac{1}{2Eh}\sum_{l=1}^{N_\Psi}\left(\mu_{t-}\left(\eta_l(n)\eta_l(n)\right)\right)\zeta_l^4\right\}=0,\tag{2.92}$$

which is a discrete counterpart to Eq. (2.67).

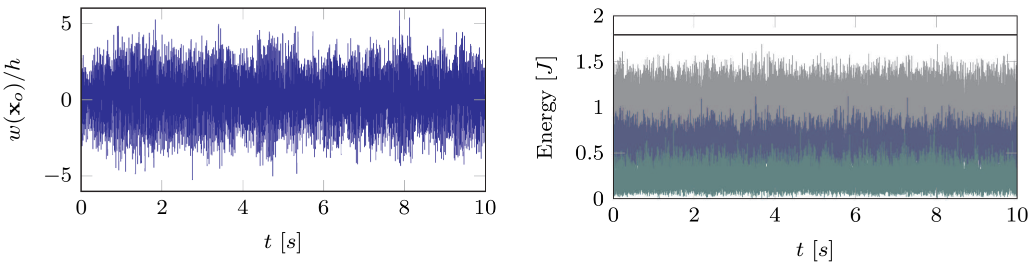

(a) **(b)**

FIGURE 5. Time simulations of a steel plate of dimensions $L_x \times L_y = 0.4 \times 0.6\text{m}^2$ and thickness $h = 1\text{mm}$. The plate is excited at input location $\mathbf{x}_i = [0.3L_x \;\; 0.2L_y]$ with a discrete dirac delta of length 1 sample and amplitude 5000; the output is taken at $\mathbf{x}_o = [0.7L_x \;\; 0.3L_y]$. The number of in-plane modes is $N_\Psi = 32$, the number of transverse modes is $N_\Phi = 20$: the highest eigenfrequency of the system is $\omega_{20} = 1893.7\text{rad/s}$; hence the stability condition Eq. (2.82) gives the limiting sampling frequency $F_s = 947\text{Hz}$. **(a)** Time series sampled at 10kHz; **(b)** total energy (black thick line), kinetic (grey), linear potential (navy), nonlinear potential (dark green).

For this equation to make sense, the discrete energy must be a positive definite quantity. A proof of this is now offered. Let the conservation of discrete energy be written as

$$\delta_{t+}\sum_{s=1}^{N_\Phi}(\tau_s(n) + \upsilon_s^l(n)) + \delta_{t+}\sum_{l=1}^{N_\Psi}\upsilon_l^{nl}(n) = 0, \tag{2.93}$$

where $\tau_s(n)$, $\upsilon_s^l(n)$, $\upsilon_l^{nl}(n)$ are, respectively, the discrete kinetic, linear and nonlinear potential energy expressions at the step n. The equation above means that, given a certain amount of energy ϵ at the time $n = 0$, then one has

$$\epsilon(n) = \epsilon(0) \equiv \epsilon. \tag{2.94}$$

Now, it is easy to see that $\upsilon_l^{nl}(n)$ is a positive definite quantity. In fact

$$\upsilon_l^{nl}(n) = \frac{\zeta_l^4}{4Eh}\left(\eta_l(n)\eta_l(n) + \eta_l(n-1)\eta_l(n-1)\right), \tag{2.95}$$

and hence $\upsilon_l^{nl}(n)$ is the sum of squared quantities (thus surely positive definite). The next step is to prove that $\tau_s(n) + \upsilon_s^l(n)$ is also positive definite. This quantity is the contribution to the linear energy of the transverse mode s at the time n. One may write

$$\epsilon_s^l(n) = \tau_s(n) + \upsilon_s^l(n), \tag{2.96}$$

where $\epsilon_s^l(n)$ is interpreted as the linear discrete energy coming from the mode s at the time n. The idea is to prove that $\epsilon_s^l(n) > 0 \; \forall n$. Now, developing the operators in the definition of $\epsilon_s^l(n)$ gives

$$\epsilon_s^l(n) = \frac{\rho h}{2} S_w^2 \left(\frac{q_s(n)q_s(n) + q_s(n-1)q_s(n-1) - 2q_s(n)q_s(n-1)}{k^2} + \omega_s^2 \, q_s(n) \, q_s(n-1) \right). \tag{2.97}$$

This last expression can be written as the equation of a conic in the $x - y$ space, where $x = q_s(n)$ and $y = q_s(n-1)$. This gives

$$x^2 + y^2 + 2\alpha xy = \frac{2k^2 \epsilon_s^l(n)}{\rho h S_w^2}$$
$$\alpha = \frac{k^2 \omega_s^2}{2} - 1.$$

A closed conic (ellispe or circle) is obtained when $|\alpha| < 1$, in which case $\frac{2k^2\epsilon_s^l(n)}{\rho h S_w^2} > 0$ and

$$|x|, |y| \leq \sqrt{\frac{2k^2 \epsilon_s^l(n)}{\rho h (1-\alpha^2) S_w^2}} \tag{2.98}$$

This last equation is the bound on the solution size. Note that the stability condition $|\alpha| < 1$ is obtained when

$$k < \frac{2}{\omega_s}. \tag{2.99}$$

Fig. 5 shows energy conservation for a plate activated impulsively in a strong nonlinear regime; Fig. 6 shows that failing to respect the stability condition leads to unstable solutions. In addition, when the stability condition is not fulfilled the linear energies are not positive definite (see Fig. 7), although the total sum $\epsilon(n)$ is still constant over time.

2.7.3. Vectorisation. The numerical scheme presented in the previous section are written in terms of tensors. The tensors are often summed over their indices, and thus a convenient way of handling this has to be devised in a numerical code. The schemes above have been implemented in MATLAB. On one hand, this is a reasonable choice as MATLAB is able to handle tensors very comfortably. On the other hand, it is important to avoid all nested loops when doing sums, and work with a "vectorised" code. In such a code, the sum over a particular tensor is not written using a `for` loop, but using a convenient matrix multiplication. As it will be seen in Chapter 6, the number of modes needed to simulate a large plates in a strongly nonlinear regime is of the order of $N_\Phi \approx 500$, and thus it is important that the code manages memory and calculation in the smartest way possible. Examples of how to do that are now presented.

The norm of the Airy stress eigenfunctions Ψ_k is now considered. These functions are sought as the eigenfunctions of a Kirchhoff clamped plate, because of the particular form of the boundary conditions Eq. (2.56). Borrowing from section 2.4, one may then write

$$\tilde{\Psi}(x,y) = \sum_{m,n=0}^{N_\Psi - 1} \tilde{a}_{mn} X_m(x) Y_n(y),$$

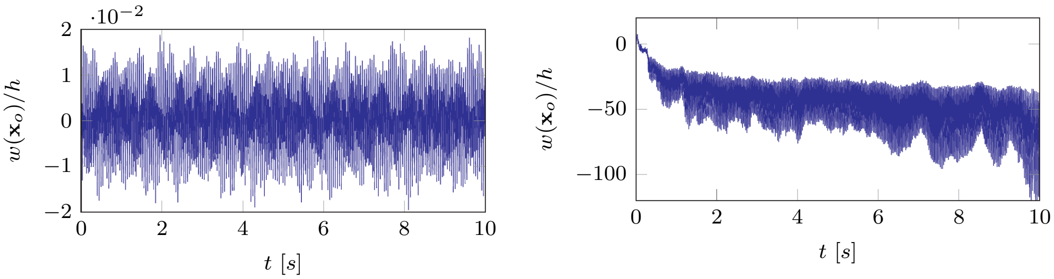

(a) **(b)**

FIGURE 6. Time simulations of a steel plate of dimensions $L_x \times L_y = 0.4 \times 0.6\text{m}^2$ and thickness $h = 1\text{mm}$. The plate is excited at input location $\mathbf{x}_i = [0.3L_x \quad 0.2L_y]$ with a discrete dirac delta of length 1 sample and amplitude 10; the output is taken at $\mathbf{x}_o = [0.7L_x \quad 0.3L_y]$. The number of in-plane modes is $N_\Psi = 32$, the number of transverse modes is $N_\Phi = 20$: the highest eigenfrequency of the system is $\omega_{20} = 1893.7\text{rad/s}$; hence the stability condition Eq. (2.99) gives the limiting sampling frequency $F_s = 947\text{Hz}$. **(a)** simulation at 1kHz (above stability limit); **(b)** simulation at 0.5kHz (below stability limit) showing unstable behaviour.

where $\tilde{\Psi}(x, y)$ is one particular eigenfunction. The norm of such a function is then

$$\|\tilde{\Psi}\|^2 = \sum_{m,n,p,q=0}^{N_\Psi - 1} \tilde{a}_{mn}\tilde{a}_{pq} \int_0^{L_x} X_m X_p \, dx \int_0^{L_y} Y_n Y_q \, dy. \tag{2.100}$$

It is seen that the calculation of this norm involves a quadruple sum over the indices m, n, p, q. When calculating these sums in a code, a possible way is to create four nested `for` loops over each one of the indices and summing up the partial results. This is not very convenient in an environment such as MATLAB, which is notoriously slow when it comes to nested loops. However, the sum can be replaced by a convenient matrix manipulations.

The idea is to create two column vectors, $\hat{\mathbf{s}}$, $\hat{\mathbf{a}}$ of length N_Ψ^4, so that

- $\hat{\mathbf{s}}$ is the vector containing the values of the integral product $\int_0^{L_x} X_m X_p \, dx \int_0^{L_y} Y_n Y_q \, dy$, ordered in some manner;
- $\hat{\mathbf{a}}$ is the vector containing the values of $\tilde{a}_{mn}\tilde{a}_{pq}$ ordered in the same manner as $\hat{\mathbf{s}}$.

Obviously the order of the indices m, n, p, q in $\hat{\mathbf{s}}$, $\hat{\mathbf{a}}$ is arbitrary, because the indices are summed; however, the two vectors must be ordered in the same way. Once the column vectors are created, then one has immediately

$$\|\tilde{\Psi}\|^2 = (\hat{\mathbf{a}})^T \hat{\mathbf{s}}. \tag{2.101}$$

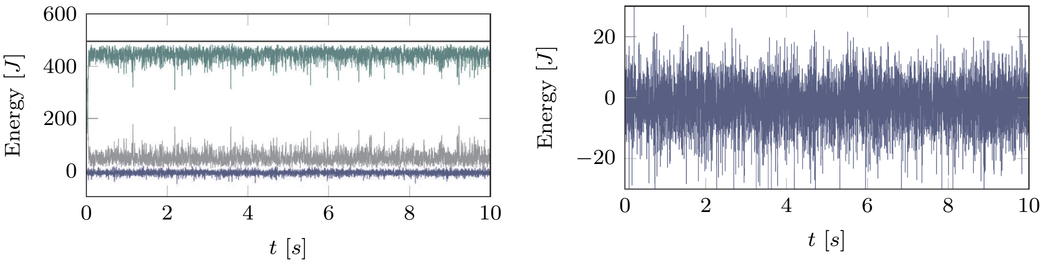

(a) **(b)**

FIGURE 7. Time simulations of a steel plate of dimensions $L_x \times L_y = 0.4 \times 0.6\text{m}^2$ and thickness $h = 1\text{mm}$. The plate is excited at input location $\mathbf{x}_i = [0.3L_x \quad 0.2L_y]$ with a discrete dirac delta of length 1 sample and amplitude 5000; the output is taken at $\mathbf{x}_o = [0.7L_x \quad 0.3L_y]$. The number of in-plane modes is $N_\Psi = 32$, the number of transverse modes is $N_\Phi = 20$: the highest eigenfrequency of the system is $\omega_{20} = 1893.7\text{rad/s}$; hence the stability condition Eq. (2.99) gives the limiting sampling frequency $F_s = 947\text{Hz}$. The figures are obtained using a sampling rate $F_s = 0.5kHz$ (below the stability limit). **(a)** Total energy (black thick line), kinetic (grey), linear potential (navy), nonlinear potential (dark green); **(b)** linear potential energy showing non physical behaviour (it is not positive definite).

A way for obtaining this is now explained, in view of an easy implementation in MATLAB. Let the matrix $\mathbf{G}^x$ be defined as

$$G^x_{m,p} = \int_0^{L_x} X_m X_p \; dx.$$

This matrix is clearly $N_\Psi \times N_\Psi$. Let the vector $\mathbf{g}$ be defined as

$$g^x_{pm} = G^x_{m,p}.$$

In practice, $\mathbf{g}$ is a column vector of length N_Ψ^2 obtained by stacking up together the columns of $\mathbf{G}$. This is easily accomplished in MATLAB using the function `reshape`. The vector $\mathbf{g}$ is then used to create the matrix $\hat{\mathbf{G}}$ in the following way

$$\hat{\mathbf{G}}^x = [\underbrace{\mathbf{g}^x \quad \mathbf{g}^x \quad \mathbf{g}^x \quad ... \quad \mathbf{g}^x}_{N_\Psi^2 \text{ times}}]$$

In practice, $\hat{\mathbf{G}}$ is a $N_\Psi^2 \times N_\Psi^2$ matrix. In MATLAB, this can be done easily using the function `repmat`. Owing to the definition of $\hat{\mathbf{G}}$, a matrix $\hat{\mathbf{D}}$ of dimensions $N_\Psi^2 \times N_\Psi^2$ is obtained as

$$\hat{\mathbf{D}} = \hat{\mathbf{G}}^x \circ (\hat{\mathbf{G}}^y)^T,$$

where the symbol $\circ$ denotes the Hadamard (or pointwise) product between two matrices[1], and T denotes the transpose. (The matrix $\hat{\mathbf{G}}^y$ is obtained exactly as $\hat{\mathbf{G}}^x$ by replacing the functions X_m, X_p with Y_n, Y_q and by integrating over y). The vector $\hat{\mathbf{s}}$ is obtained as

$$\hat{s}_{qnpm} = \hat{D}_{mq,pn}. \tag{2.102}$$

In MATLAB this operation is accomplished by first transforming $\hat{\mathbf{D}}$ into a fourth order tensor using `reshape`, by then permuting dimensions using `permute`, and finally by using `rehsape` again to obtain a column vector.

The vector $\hat{\mathbf{a}}$ is obtained easily by constructing the matrix $\hat{\mathbf{A}}$ as

$$\hat{\mathbf{A}} = [\underbrace{\tilde{\mathbf{a}} \quad \tilde{\mathbf{a}} \quad \tilde{\mathbf{a}} \quad \ldots \quad \tilde{\mathbf{a}}}_{N_\Psi^2 \text{ times}}]$$

where $\tilde{\mathbf{a}}$ is the vector of expansion coefficients coming from the algebraic eigenvalue problem. Then construct the matrix $\hat{\mathbf{B}} = \hat{\mathbf{A}}^T \circ \hat{\mathbf{A}}$. Hence

$$\hat{a}_{qnpm} = \hat{B}_{qn,pm}. \tag{2.103}$$

In MATLAB, a correct implementation of Eq. (2.101) allows to calculate 100 norms in about 2s, whereas about 20min are needed when using four nested `for` loops and Eq. (2.101).

Using similar matrix manipulations, one can calculate the expression for the tensor $\Gamma^s_{p,q,r}$ of (2.61) and avoid nested loops. Once the off-line calculation for $\Gamma^s_{p,q,r}$ is completed, one may save the tensor as use it at the input for schemes (2.79) and (2.85). Note, however, that such a tensor requires a lot of physical memory to be stored. If, for instance, $N_\Phi = 150$, then the tensor of coupling coefficients contains $150^4 = 506250000$ entries, and occupies about 4Gb of memory. On the other hand, the tensor H with $N_\Phi = 150$ and, for example, $N_\Psi = 100$ occupies only 18Mb. In order to maximise the number of transverse modes that one can keep in a code, it is then necessary to replace $\Gamma^s_{p,q,r}$ by Eq. (2.61) in both schemes (2.79) and (2.85).

---

[1] In practice, $(\mathbf{A} \circ \mathbf{B})_{i,j} = A_{i,j}B_{i,j}$.

CHAPTER 3

Numerical Methods II: Finite Difference Schemes

In this chapter, a quick review of Finite Difference techniques is offered. Finite Difference schemes are used primarily to solve PDEs: for that, the spatial domain upon which a problem is defined is restricted to a set of grid points at which the solution is computed. Time is discretised in a similar way, by means of a *sampling frequency*. Needless to say, a great deal of literature exists. For a general introduction, see the book by Mitchell and Griffiths, [64].

Such methods have a very long history and can be traced back to the seminal work of Courant, Friedrichs and Lewy in 1928 [22] (in German; for an English version see [23]), who treated the cases of elliptic and hyperbolic problems of classical physics (including the vibrating string) in terms of discrete approximations. A lot of early work has successively been devoted to electromagnetics-related problems [81, 82, 96], dealing with potential theory and propagation.

The realm of musical acoustics, and in particular sound synthesis, has served as a great field of application of Finite Difference techniques. The first work in this sense can be traced back to the work of Ruiz on string vibrations [79], although it was not until the work by Chaigne that sophisticated models started to be considered [15, 16, 17]. Nonlinear plate vibrations have been treated extensively by Bilbao [7] and, more recently, by Torin [85]. Bilbao is also the author of a book [8] in which Finite Difference schemes are systematically adopted in the realm of sound synthesis. The contents of this Chapter, and the notation, are largely borrowed from that reference.

3.1. Finite Difference Operators

In this section grid functions will be used. A grid function is any function defined over a discrete grid. For the moment, for simplicity, let the grid be 1D. Given that a constant grid size will be used, of step h, the grid can be identified with the set of the integer numbers, $\mathbb{Z}$, or a subset of it. For 1D systems such as a bar or a string, the subset can selected as $\mathbb{U}_N = [0, 1, ..., N-1]$ and the boundaries of this interval correspond to the ends of the bar or string. Time is discretised in a similar manner as space, hence a sampling frequency F_s (with corresponding timestep $k = 1/F_s$) is introduced. A grid function is identified in the following section as

$$w_l^n \equiv w(hl, kn),$$

meaning that the continuous function $w(x,t)$ has been approximated by the grid function w_l^n evaluated at the time kn and grid point hl. A list of temporal difference operators was offered in sec. 2.7, along with their accuracies. It was seen that centered discrete operators are second-order accurate, whereas forward or backward operators are first-order accurate. Spatial operator in 1D are derived straightforwardly from the temporal operators. Hence

- Backward and forward shift operators:

$$e_{x-}w_l^n = w_{l-1}^n; \qquad e_{x+}w_l^n = w_{l+1}^n. \tag{3.1}$$

- Backward, centered, forward spatial difference operators:

$$\delta_{x-} \equiv \frac{1}{h}(1 - e_{x-}); \qquad \delta_{x\cdot} \equiv \frac{1}{2h}(e_{x+} - e_{x-}); \qquad \delta_{x+} \equiv \frac{1}{h}(e_{x+} - 1). \tag{3.2}$$

- Backward, centered, forward averaging operators:

$$\mu_{x-} \equiv \frac{1}{2}(1 + e_{x-}); \qquad \mu_{x\cdot} \equiv \frac{1}{2}(e_{x+} + e_{x-}); \qquad \mu_{x+} \equiv \frac{1}{2}(e_{x+} + 1). \tag{3.3}$$

Approximations to the second and fourth space derivatives can be obtained by considering

$$\delta_{xx} \equiv \delta_{x+}\delta_{x-} = \frac{1}{h^2}(e_{x+} - 2 + e_{x-}); \qquad \delta_{xxxx} \equiv \delta_{xx}\delta_{xx} = \frac{1}{h^4}(e_{x+}e_{x+} - 4e_{x+} + 6 - 4e_{x-} + e_{x-}e_{x-}). \tag{3.4}$$

Note that, owing to Taylor series arguments,

$$\delta_{xxxx} = \frac{\partial^4}{\partial x^4} + O(h^2), \tag{3.5}$$

and thus this operator is second order accurate.

When one wants to approximate a function depending on two space variables, a 2D grid is needed. In this case, the grid function can be indicated by

$$w_{l,m}^n \equiv w(h_x l, h_y m, kn),$$

meaning that the function $w(x, y, t)$ has been approximated by the grid function $w_{l,m}^n$ depending on the spatial steps h_x, h_y and the timestep k. It is assumed that the grid is cartesian, which is the case of interest here given that the rectangular geometry of the plate leads naturally to this kind of discrete approximation. Hence, for an infinite system, $(l, m) \in \mathbb{Z}^2$; for the case of a plate, which is a bounded system, $(l, m) \in \mathbb{U}_{N_x,N_y}^2 = \{(l, m) \in \mathbb{Z}^2, 0 \leq l \leq N_x - 1, 0 \leq m \leq N_y - 1\}$.

Spatial shift operators may be defined as

$$e_{x+}w_{l,m}^n = w_{l+1,m}^n; \quad e_{x-}w_{l,m}^n = w_{l-1,m}^n; \quad e_{y+}w_{l,m}^n = w_{l,m+1}^n; \quad e_{y-}w_{l,m}^n = w_{l,m-1}^n. \tag{3.6}$$

Owing to these definitions, one may construct the forward, backward, centered difference operators in the x and y directions in an analogous manner as (3.2). Hence

$$\delta_{x-} \equiv \frac{1}{h_x}(1 - e_{x-}); \qquad \delta_{x\cdot} \equiv \frac{1}{2h_x}(e_{x+} - e_{x-}); \qquad \delta_{x+} \equiv \frac{1}{h_x}(e_{x+} - 1) \tag{3.7}$$

$$\delta_{y-} \equiv \frac{1}{h_y}(1 - e_{y-}); \qquad \delta_{y\cdot} \equiv \frac{1}{2h_y}(e_{y+} - e_{y-}); \qquad \delta_{y+} \equiv \frac{1}{h_y}(e_{y+} - 1). \tag{3.8}$$

In an analogous way as Eq. (3.4), one may approximate second derivatives in the x and y directions, as well as introducing averaging operators. In view of an application to the plate equations, one may wish to approximate the Laplacian and double Laplacian operators. This can be done quite straightforwardly as

$$\delta_{\Delta} = \delta_{xx} + \delta_{yy} = \Delta + O(h^2); \qquad \delta_{\Delta\Delta} = \delta_{\Delta}\delta_{\Delta} = \Delta\Delta + O(h^2). \tag{3.9}$$

See [8] for more options.
The idea of a discrete inner product between two grid functions can be given by analogy with Eq. (2.6). Hence the symbol

$$< \alpha, \beta >_{\mathbb{U}^2_{N_x,N_y}} = \sum_{(l,m)\in\mathbb{U}^2_{N_x,N_y}} h^2 \alpha_{l,m}\beta_{l,m} \tag{3.10}$$

denotes the "inner product" (a Riemann sum) over the domain of definition of the discrete problem.

3.1.1. Matrix Interpretation and Boundary Conditions.

In view of practical implementations in a code, the spatial operators are here given an interpretation in terms of matrix multiplication. Consider the state vector $\mathbf{w}^n$, and assume for the moment the vector to be defined over all $\mathbb{Z}$. Consider, for example, the operator δ_{x-} defined in Eq. (3.2); one may define a new vector $\mathbf{u}^n$ by considering $u^n_l \equiv \delta_{x-} w^n_l = \frac{1}{h}(w^n_l - w^n_{l-1})$. In a matrix form, one may write

$$\mathbf{u}^n = \mathbf{D}_{x-}\mathbf{w}^n,$$

where

$$\mathbf{D}_{x-} = \frac{1}{h}\begin{pmatrix} \ddots & & & & & \mathbf{0} \\ \ddots & 1 & & & & \\ & -1 & 1 & & & \\ & & -1 & 1 & & \\ & & & -1 & 1 & \\ \mathbf{0} & & & & \ddots & \ddots \end{pmatrix}.$$

Now, the matrix above is obviously infinite as the state vector $\mathbf{w}^n$ is unbounded. In this matrix, the entries on the main diagonal are all 1, and the entries on the diagonal underneath the main diagonal are all -1. Similarly, one may define matrices corresponding to the other difference operators of Eqs. (3.2) and (3.4). These are

$$\mathbf{D}_{x+} = \frac{1}{h}\begin{pmatrix} \ddots & \ddots & & & & \mathbf{0} \\ & -1 & 1 & & & \\ & & -1 & 1 & & \\ & & & -1 & 1 & \\ & & & & -1 & \ddots \\ \mathbf{0} & & & & & \ddots \end{pmatrix}; \tag{3.11}$$

$$\mathbf{D}_{xx} = \frac{1}{h^2}\begin{pmatrix} \ddots & \ddots & & & & \mathbf{0} \\ \ddots & -2 & 1 & & & \\ & 1 & -2 & 1 & & \\ & & 1 & -2 & 1 & \\ & & & 1 & -2 & \ddots \\ \mathbf{0} & & & & \ddots & \ddots \end{pmatrix}; \quad \mathbf{D}_{xxxx} = \frac{1}{h^4}\begin{pmatrix} \ddots & \ddots & \ddots & \ddots & & & & \mathbf{0} \\ \ddots & 1 & 6 & 1 & -4 & & & \\ & -4 & 1 & 6 & 1 & -4 & & \\ & & -4 & 1 & 6 & 1 & -4 & \\ & & & -4 & 1 & 6 & 1 & \ddots \\ & & & & \ddots & \ddots & \ddots & \ddots \\ \mathbf{0} & & & & & & \ddots & \ddots \end{pmatrix}. \tag{3.12}$$

The cases of practical interest are those where the state vector $\mathbf{w}^n$ takes values over a bounded interval, for example $\mathbb{U}_N$ (defined above). In this case, the form of each matrix changes according to the boundary conditions supplied with the problem. As an example of such, consider the simple conditions

$$\underbrace{w_0 = w_{N-1} = 0}_{\text{Dirichelet conditions}}, \quad \underbrace{\delta_{x\cdot} w_0 = \delta_{x\cdot} w_{N-1} = 0}_{\text{Neumann conditions}}, \tag{3.13}$$

and consider the operator $\mathbf{D}_{xx}$. For the Dirichelet-type conditions one has

$$\mathbf{D}_{xx}\begin{pmatrix} w_1 \\ w_2 \\ ... \\ w_{N-3} \\ w_{N-2} \end{pmatrix} = \frac{1}{h^2}\begin{pmatrix} -2 & 1 & & & & \mathbf{0} \\ 1 & -2 & 1 & & & \\ & \ddots & \ddots & \ddots & & \\ & & & 1 & -2 & 1 \\ \mathbf{0} & & & & 1 & -2 \end{pmatrix}\begin{pmatrix} w_1 \\ w_2 \\ ... \\ w_{N-3} \\ w_{N-2} \end{pmatrix}.$$

Note that the points u_0, u_{N-1} have not been considered as they are constantly zero.
For Neumann-type conditions one has

$$\mathbf{D}_{xx}\begin{pmatrix} w_0 \\ w_1 \\ ... \\ w_{N-2} \\ w_{N-1} \end{pmatrix} = \frac{1}{h^2}\begin{pmatrix} -2 & 2 & & & & \mathbf{0} \\ 1 & -2 & 1 & & & \\ & \ddots & \ddots & \ddots & & \\ & & & 1 & -2 & 1 \\ \mathbf{0} & & & & 2 & -2 \end{pmatrix}\begin{pmatrix} w_0 \\ w_1 \\ ... \\ w_{N-2} \\ w_{N-1} \end{pmatrix}.$$

When the grid functions are two dimensional, they are themselves naturally written as matrices. In this way, the two dimensional spatial operators such as those of Eq. (3.9) can be though of third-order tensors. However, the matrix describing a given grid function can be transformed into a vector by, say, stacking up its columns; similarly the third-order tensor associated with a given difference operator becomes a standard two-dimensional matrix. Implementation of boundary conditions can then be done in an analogous way as in 1D (see [8]).

3.2. Linear plate vibrations

Linear plate vibrations without damping and forcing terms may be simulated by discretising the Kirchhoff equation in the following way

$$\rho h \delta_{tt} w = -D \delta_{\Delta\Delta} w. \tag{3.14}$$

This is not, obviously, the only option. It is, indeed, quite a straightforward one. Despite its simplicity, such a scheme is energy conserving in a discrete sense. To prove numerical energy conservation, one could take an inner product of the form (3.10) of Eq.(3.14) and $\delta_{t\cdot}w$, so to get

$$\delta_{t+}\left\{ \frac{\rho h}{2}\left\langle \delta_{t-}w, \delta_{t-}w \right\rangle_{\mathbb{U}_{N_x,N_y}} + \frac{D}{2}\left\langle \delta_{\Delta}w, e_{t-}\delta_{\Delta}w \right\rangle_{\mathbb{U}_{N_x,N_y}} \right\} = \mathfrak{b}, \tag{3.15}$$

where $\mathfrak{b}$ is a boundary term. At the edge $x = 0$ such term vanishes under the following numerical boundary conditions

Simply-Supported	Clamped	Free
$w = \delta_{xx} w = 0.$	$w = \delta_{x-} w = 0.$	$(\delta_{xx} + \nu\delta_{yy})w =$ $\delta_{x-}(\delta_{xx} + (2-\nu)\delta_{yy})w = 0;$ $\delta_{x-y-}w_{0,0} = 0.$ (condition at corner)

The conserved, discrete energy can be proven to be a non-negative scalar under particular circumstances (see [8]); in that case, scheme (3.14) is stable.
Note that the same scheme can be used to calculate the eigenvalues and vectors of the Kirchhoff plate. In fact, it is sufficient to consider the eigenvalue equation

$$\omega^2 \Phi = \frac{D}{\rho h} \delta_{\Delta\Delta} \Phi \tag{3.16}$$

and to calculate eigenvalues and vectors of the matrix $\mathbf{D}_{\Delta\Delta}$. One has

$$\frac{\omega_m^2 \rho h}{D} = \mathrm{eig}(\mathbf{D}_{\Delta\Delta})_m; \qquad \Phi_m = \mathrm{eigenvector}(\mathbf{D}_{\Delta\Delta})_m. \tag{3.17}$$

The results can be compared with those coming from the Rayleigh-Ritz method, presented in Chapter 2. This is done in the next subsection.

3.2.1. Eigenfunctions and frequencies of the Kirchhoff plate.

In this section, the Kirchhoff plate equation is solved using the Finite Difference scheme (3.16). As a first case, consider Table 1 presenting the results for the completely simply-supported plate. Four different aspect ratios are considered: $\eta = 1.0, 1.5, 2.0, 2.5$; for all cases $L_x = 1$m. The "grid density" r_g can be recovered by dividing the number of grid points $N_x \times N_y$ by the surface size $L_x \times L_y$. Hence, for $\eta = 1.0$ one has, for the values proposed in the table, $r_g = 8100, 12100, 16129$ points/m^2. Note that, for larger aspect ratios, the number of grid points in the y direction increases so to keep the grid density constant for all aspect ratios.

					Mode					
	1	**2**	**3**	**4**	**5**	**25**	**50**	**75**	**100**	$N_x \times N_y$
η=1.0	2.000	4.998	4.998	7.997	9.992	39.87	72.58	105.3	142.9	90×90
	2.000	4.999	4.999	7.998	9.994	39.91	72.72	105.5	143.6	110×110
	2.000	4.999	4.999	7.998	9.996	39.93	72.79	105.6	143.9	127×127
	2.000	5.000	5.000	8.000	10.00	40.00	73.00	106.0	145.0	Analytical
η=1.5	1.444	2.777	4.443	4.998	5.776	25.73	49.20	70.69	93.00	90×135
	1.444	2.777	4.443	4.999	5.776	25.74	49.28	70.83	93.15	110×165
	1.444	2.778	4.444	4.999	5.777	25.75	49.32	70.90	93.22	127×190
	1.444	2.778	4.444	5.000	5.778	25.78	49.44	71.11	93.44	Analytical
η=2.0	1.250	2.000	3.249	4.248	4.998	19.97	36.87	52.76	71.74	90×179
	1.250	2.000	3.250	4.249	4.999	19.98	36.91	52.84	71.82	110×219
	1.250	2.000	3.250	4.249	4.999	19.99	36.93	52.88	71.87	127×254
	1.250	2.000	3.250	4.250	5.000	20.00	37.00	53.00	72.00	Analytical
η=2.5	1.160	1.640	2.440	3.559	4.158	16.61	28.93	43.70	56.59	90×225
	1.160	1.640	2.440	3.559	4.159	16.62	28.96	43.75	56.67	110×275
	1.160	1.640	2.440	3.560	4.159	16.63	28.97	43.77	56.71	127×317
	1.160	1.640	2.440	3.560	4.160	16.64	29.00	43.84	56.84	Analytical

TABLE 1. Eigenfrequencies ζ_i^2/π^2 for the SS-SS-SS-SS plate, under different aspect ratios $\eta = L_y/L_x$ ($L_x = 1$m) and different values of grid points $N_x \times N_y$. Analytical values are also given.

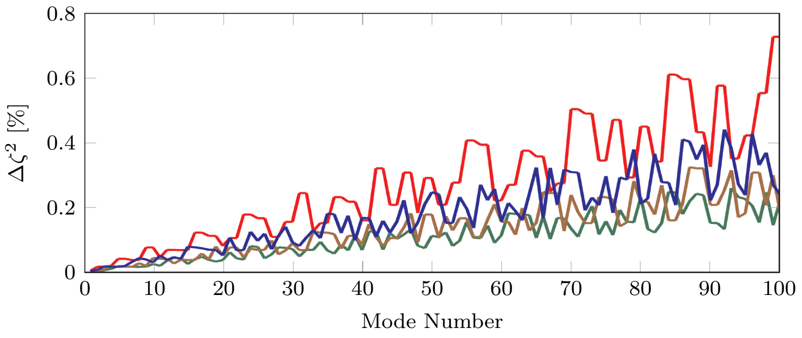

FIGURE 1. Relative error of the eigenfrequencies of the SS-SS-SS-SS plate calculated using the FD scheme using a grid density $r_g = 16129$point/m^2 and compared to exact values from Eq. (2.31). Error plotted for different aspect ratios $\eta = L_y/L_x$. Red: $\eta = 1.0$, blue: $\eta = 1.5$, brown: $\eta = 2.0$, green: $\eta = 2.5$.

	Mode									
	1	**2**	**3**	**4**	**5**	**25**	**50**	**75**	**100**	$N_x \times N_y$
	3.567	7.274	7.274	10.73	13.04	45.30	79.45	113.08	151.8	90×90
η=1.0	3.581	7.303	7.303	10.80	13.09	45.52	79.89	113.72	153.1	110×110
	3.590	7.321	7.321	10.80	13.12	45.65	80.14	114.10	153.8	127×127
	2.681	4.151	6.557	6.630	7.925	29.97	55.23	77.26	99.15	90×135
η=1.5	2.691	4.164	6.582	6.650	7.954	30.11	55.53	77.58	99.59	110×165
	2.697	4.172	6.598	6.662	7.971	30.19	55.70	77.77	99.85	127×190
	2.439	3.167	4.467	6.328	6.343	22.37	41.51	58.68	76.24	90×179
η=2.0	2.448	3.178	4.479	6.344	6.368	22.43	41.67	58.98	76.57	110×219
	2.454	3.184	4.487	6.354	6.384	22.46	41.77	59.15	76.76	127×254
	2.345	2.760	3.531	4.664	6.153	18.95	33.27	47.35	60.34	90×225
η=2.5	2.354	2.774	3.542	4.675	6.167	19.00	33.35	47.49	60.64	110×275
	2.360	2.780	3.548	4.680	6.176	19.03	33.40	47.56	60.81	127×317

TABLE 2. Eigenfrequencies ζ_i^2/π^2 for the C-C-C-C plate, under different aspect ratios $\eta = L_y/L_x$ ($L_x = 1$m) and different values of grid points $N_x \times N_y$.

The values calculated using the FD scheme can be compared to the analytical values (here called ζ_t^2) of Eq. (2.31). The relative error can be defined as

$$\Delta\zeta^2 = \frac{\zeta_t^2 - \zeta_{FD}^2}{\zeta_t^2}; \tag{3.18}$$

note that there is no need to introduce the absolute value notation as the FD results converge from below. Fig. 1 reproduces $\Delta\zeta^2$ for the first 100 modes and the four aspect ratios. The square plate is the one presenting the largest deviation, which however remains quite small ($\Delta\zeta^2 \lesssim 0.7\%$); for the other aspect ratios, the error remains bounded below 0.4%.

For the cases of the completely clamped and free plates there is no analytical solutions. The values of the eigenfrequencies calculated using the FD code are presented in Table 2 (clamped plate) and Table 3 (free plate). The grid densities are the same as the simply-supported case. Note that convergence is again from below.

Instead of calculating a relative error, one may construct a table to show upper and lower bounds for the eigenfrequencies of the clamped and free plates. In fact, the convergence of the Rayleigh-Ritz method is from above, and FD converges from below. Table 4 presents such bounds for the clamped plate, and Table 5 considers the free plate. Note that, in most cases, the modal approach and the FD scheme yield the same results up to the second significant digit, meaning that the "true" eigenfrequencies are bounded within an error of the order of 1%.

	Mode									
$\nu = 0.3$	**1**	**2**	**3**	**4**	**5**	**25**	**50**	**75**	**100**	$N_x \times N_y$
η=1.0	1.326	1.945	2.407	3.431	3.431	21.18	49.92	76.39	105.7	90×90
	1.333	1.952	2.416	3.448	3.448	21.30	50.20	76.90	106.4	110×110
	1.337	1.956	2.422	3.459	3.459	21.37	50.37	77.19	106.8	127×127
η=1.5	0.8834	0.9511	2.040	2.200	2.555	14.19	32.38	51.61	70.25	90×135
	0.8873	0.9535	2.049	2.209	2.563	14.24	32.50	51.85	70.66	110×165
	0.8896	0.9549	2.054	2.214	2.567	14.27	32.56	51.99	70.89	127×190
η=2.0	0.5382	0.6586	1.451	1.494	2.182	11.32	24.27	38.35	52.38	90×179
	0.5392	0.6612	1.457	1.497	2.191	11.34	24.38	38.47	52.56	110×219
	0.5398	0.6628	1.460	1.499	2.196	11.36	24.45	38.54	52.67	127×254
η=2.5	0.3451	0.5239	0.9589	1.126	1.870	8.837	19.72	29.62	41.62	90×225
	0.3456	0.5259	0.9603	1.130	1.873	8.852	19.80	29.75	41.74	110×275
	0.3459	0.5270	0.9612	1.132	1.875	8.861	19.86	29.83	41.81	127×317

TABLE 3. Eigenfrequencies ζ_i^2/π^2 for the F-F-F-F plate, for $\nu = 0.3$, under different aspect ratios $\eta = L_y/L_x$ ($L_x = 1$m) and different values of grid points $N_x \times N_y$.

	Mode									
$\nu = 0.3$	**1**	**2**	**3**	**4**	**5**	**25**	**50**	**75**	**100**	Bounds
η=1.0	3.646	7.436	7.436	10.96	13.33	46.43	81.60	116.2	156.7	Upper
	3.590	7.321	7.321	10.80	13.12	45.65	80.14	114.1	153.8	Lower
η=1.5	2.736	4.225	6.700	6.740	8.086	30.69	56.69	78.89	101.4	Upper
	2.697	4.172	6.598	6.662	7.971	30.19	55.70	77.77	99.85	Lower
η=2.0	2.490	3.225	4.536	6.417	6.483	22.69	42.49	60.17	77.64	Upper
	2.454	3.184	4.487	6.354	6.384	22.46	41.77	59.15	76.76	Lower
η=2.5	2.396	2.817	3.589	4.729	6.231	19.20	33.69	47.99	61.83	Upper
	2.360	2.780	3.548	4.680	6.176	19.03	33.40	47.56	60.81	Lower

TABLE 4. Upper and lower bounds for the eigenfrequencies ζ_i^2/π^2 of the C-C-C-C plate, under different aspect ratios $\eta = L_y/L_x$ Lower bounds are taken from Table 2; upper bounds are taken from running the modal scheme presented in section 2.4 with $N_\Phi = 25$.

	Mode									
$\nu = 0.3$	**1**	**2**	**3**	**4**	**5**	**25**	**50**	**75**	**100**	Bounds
η=1.0	1.365	1.988	2.467	3.534	3.534	21.86	51.49	79.16	109.6	Upper
	1.337	1.956	2.422	3.459	3.459	21.37	50.37	77.19	106.8	Lower
η=1.5	0.9063	0.9667	2.090	2.254	2.605	14.50	33.11	52.92	72.46	Upper
	0.8896	0.9549	2.054	2.214	2.567	14.27	32.56	51.99	70.89	Lower
η=2.0	0.5464	0.6752	1.483	1.513	2.235	11.52	24.93	39.10	53.83	Upper
	0.5398	0.6628	1.460	1.499	2.196	11.36	24.45	38.54	52.67	Lower
η=2.5	0.3517	0.5375	0.9690	1.149	1.891	8.941	20.22	30.43	42.55	Upper
	0.3459	0.5270	0.9612	1.132	1.875	8.861	19.86	29.83	41.81	Lower

TABLE 5. Upper and lower bounds for the eigenfrequencies ζ_i^2/π^2 of the F-F-F-F plate, for $\nu = 0.3$, under different aspect ratios $\eta = L_y/L_x$ Lower bounds are taken from Table 3; upper bounds are taken from running the modal scheme presented in section 2.5 with $N_\Phi = 17$.

3.3. Finite Difference schemes for the von Kármán equations

In this section two resolution schemes are presented for the von Kármán equations in terms of Finite Differences approximations. The first scheme is a semi-explicit scheme and the second one is an implicit, energy-conserving scheme. Both schemes are presented in the book by Bilbao [8], to which the reader is referred for a more detailed discussion. The conservative scheme presented here is but one of a family of schemes depending on two parameters. The choice presented here is a particularly useful one in terms of ease of implementation, and stability properties. See [7] for a complete discussion. When discretising the von Kármán system, an important first step is the discretisation of the von Kármán operator, presented in Eq. (1.38). For the schemes presented here, the discrete counterpart will be denoted by $\mathfrak{l}$, acting on two generic grid functions α, β, defined as

$$\mathfrak{l}(\alpha,\beta) = \delta_{xx}\alpha\delta_{yy}\beta + \delta_{yy}\alpha\delta_{xx}\beta - 2\mu_{x-}\mu_{y-}(\delta_{x+y+}\alpha\delta_{x+y+}\beta). \tag{3.19}$$

This choice will prove useful for showing energy conservation of the implicit scheme. In addition, the triple self-adjointness property Eq. (1.49) finds a discrete counterpart when the von Kármán operator is approximated as in Eq. (3.19). Hence

$$< \alpha, \mathfrak{l}(\beta,\gamma) >_{\mathbb{U}_{N_x,N_y}} = < \mathfrak{l}(\alpha,\beta), \gamma >_{\mathbb{U}_{N_x,N_y}} + \mathfrak{j}, \tag{3.20}$$

where the symbol $< \cdot,\cdot >_{\mathbb{U}_{N_x,N_y}}$ denotes a discrete inner product over the plate discrete domain $\mathbb{U}_{N_x,N_y}$, and $\mathfrak{j}$ is a boundary integral.

3.3.1. A semi-explicit scheme. Referring to the von Kármán Eq. (2.58), one may approximate the continuous system as

$$D\delta_{\Delta\Delta}w + \rho h\delta_{tt}w = \mathfrak{l}(w,F) - 2\sigma_0\delta_{t\cdot}w + 2\sigma_1\delta_{\Delta}\delta_{t-}w + f_{in}P; \tag{3.21a}$$

$$\delta_{\Delta\Delta}F = -\frac{Eh}{2}\mathfrak{l}(w,w). \tag{3.21b}$$

Note that f_{in} denotes a distribution corresponding to the spatial part of the input mechanism, and P is its temporal component. The parameters σ_0 and σ_1 are the same as those found in Eq. (2.58), leading to the dissipation laws in the frequency domain described in Eq. (2.59). In this case, Eq. (3.21b) needs a linear system solver, whereas Eq. (3.21a) may be updated explicitly. Stability of such a scheme is not guaranteed at high excitation amplitudes, although it will be used in Chapter 6 to produce gong-like sounds.

3.3.2. An implicit, energy conserving scheme. In Chapter 5, the plate will be excited to high amplitudes in order to produce a cascade of energy and study the statistical properties of such turbulent system. For that, scheme (3.21) is not a good candidate as the instability issue would make impossible to simulate such a large cascade of energy. Hence, a stable scheme is needed. The stable scheme is now presented, and its properties briefly described. See [7] for more details.
The scheme is

$$D\delta_{\Delta\Delta}w + \rho h\delta_{tt}w = \mathfrak{l}(w,\mu_{t\cdot}F) - 2\sigma_0\delta_{t\cdot}w + 2\sigma_1\delta_{\Delta}\delta_{t-}w + f_{in}P; \tag{3.22a}$$

$$\mu_{t-}\delta_{\Delta\Delta}F = -\frac{Eh}{2}\mathfrak{l}(w,e_{t-}w). \tag{3.22b}$$

When run in absence of damping and forcing terms, such a scheme is energy conserving, and energy conservation leads directly to a stability condition. Derivation of an energy-conserving property is done in [7], and reads

$$\delta_{t+}\left\{\frac{\rho h}{2}\left\langle\delta_{t-}w,\delta_{t-}w\right\rangle_{\mathbb{U}_{N_x,N_y}} + \frac{D}{2}\left\langle\delta_{\Delta}w,e_{t-}\delta_{\Delta}w\right\rangle_{\mathbb{U}_{N_x,N_y}} + \frac{1}{2Eh}\left\langle\delta_{\Delta}F,\delta_{\Delta}F\right\rangle_{\mathbb{U}_{N_x,N_y}}\right\} = \mathfrak{b}, \tag{3.23}$$

where $\mathfrak{b}$ is a boundary term that vanishes under special combinations of boundary conditions on w, F. For the edge at $x = 0$, a set of such conditions may be extracted as

$$w = (\delta_{xx} + \nu\delta_{yy})w = 0, \qquad F = \delta_{x-}F = 0, \tag{3.24}$$

which correspond formally to Eq. (2.56) identifying a simply supported, in-plane movable edge.
Energy conservation leads naturally to a stability condition, and to bounds on the solution size (see [7, 88]), and thus it will be used to simulate a wave turbulence state in Chapter 5, where the plate attains large amplitudes of vibration. Such condition can be expressed as a bound on the timestep k, as a function of the spatial steps h_x, h_y, and reads

$$k \le \frac{h_x^2\ h_y^2}{2(h_x^2+h_y^2)}\sqrt{\frac{\rho h}{D}}. \tag{3.25}$$

Note that the step h_y can always be expressed as a function of h_x by considering $h_y = L_y/L_x h_x$. Hence, the condition above is basically a link between the grid size and the sampling rate. In other words, one can fix the sampling rate and get the grid steps in order to satisfy the relation above as close as possible to equality, as Bilbao suggests in [8].

Although this relation is given here for the implicit scheme (3.22), in Chapter 6 it will be used for scheme (3.21) as well. This choice is justified on a pragmatic basis: in most cases occurring in Chapter 6, such a condition gives a convergent solution and is thus systematically adopted.

Part 2

Part II: Applications

CHAPTER 4

Nonlinear Modal Interaction

In this chapter the Nonlinear Normal Modes of the von Kármán plate are calculated. This chapter corresponds to a paper published in Acta Mechanica [31]. Sections 2 and 3 have been covered in great detail in Chapter 2. Section 4 gives the numerical values of a few coupling coefficients, and an heurstic rule to identify the null ones. Section 5 is the core of this Chapter, presenting the periodic solutions of the nonlinear system. See also [29]. Bibliographic references as well as appendices are included in this chapter, and not at the end of the manuscript.

Acta Mech 225, 213–232 (2014)
DOI 10.1007/s00707-013-0931-1

**Michele Ducceschi · Cyril Touzé · Stefan Bilbao ·
Craig J. Webb**

Nonlinear dynamics of rectangular plates: investigation of modal interaction in free and forced vibrations

Received: 26 April 2013 / Revised: 13 July 2013 / Published online: 25 August 2013

Abstract Nonlinear vibrations of thin rectangular plates are considered, using the von Kármán equations in order to take into account the effect of geometric nonlinearities. Solutions are derived through an expansion over the linear eigenmodes of the system for both the transverse displacement and the Airy stress function, resulting in a series of coupled oscillators with cubic nonlinearities, where the coupling coefficients are functions of the linear eigenmodes. A general strategy for the calculation of these coefficients is outlined, and the particular case of a simply supported plate with movable edges is thoroughly investigated. To this extent, a numerical method based on a new series expansion is derived to compute the Airy stress function modes, for which an analytical solution is not available. It is shown that this strategy allows the calculation of the nonlinear coupling coefficients with arbitrary precision, and several numerical examples are provided. Symmetry properties are derived to speed up the calculation process and to allow a substantial reduction in memory requirements. Finally, analysis by continuation allows an investigation of the nonlinear dynamics of the first two modes both in the free and forced regimes. Modal interactions through internal resonances are highlighted, and their activation in the forced case is discussed, allowing to compare the nonlinear normal modes (NNMs) of the undamped system with the observable periodic orbits of the forced and damped structure.

1 Introduction

Plates elements are commonly found in a variety of contexts in structural mechanics. An understanding of their vibrational properties is crucial in many contexts, e.g. fluid-structure interaction problems, plate and panel flutter in aeronautics [13], energy harvesting of fluttering flexible plates [18], piezoelectric and laminated plates [15,21], as well as their coupling with electro-magnetic and thermal fields [22]. When the plates are thin, vibration amplitudes can easily attain the same order of magnitude as the thickness. In this case, the nonlinear geometric effects cannot be neglected, resulting in a rich variety of dynamics [2,38]. Examples can be given ranging from weakly to strongly nonlinear cases: nonlinear vibrations of plates with moderate nonlinearity [2,45], fluid–structure interaction problems [25] and the transition from periodic to chaotic vibrations [4,37,50]. Aside from typical engineering problems, the chaotic dynamics exhibited by thin plates excited at large amplitudes finds application in the field of musical acoustics, as it accounts for the bright and shimmering sound of gongs and cymbals [6,7,12,29]. It was pointed out recently, from the theoretical, numerical and experimental viewpoints that the complex dynamics of thin plates vibrating at large amplitudes

---

M. Ducceschi · C. Touzé ( )
Unité de Mecanique, ENSTA-ParisTech, 828 Boulevard des Maréchaux, Palaiseau, France
E-mail: cyril.touze@ensta.fr

S. Bilbao · C. J. Webb
James Clerk Maxwell Building, University of Edinburgh, Edinburgh, Scotland

displays the characteristics of wave turbulence systems, and thus, it should be studied within this framework [9,20,34,35,49].

A widely used model in nonlinear plate modelling is due to von Kármán [54]. This model takes into account a quadratic correction to the longitudinal strain, as compared to the classical linear plate equation by Kirchhoff [16,33,38,46]. The type of nonlinearity introduced is thus purely geometrical. The von Kármán equations are particularly appealing because they describe a large range of phenomena while retaining a relatively compact form, introducing a single bilinear operator in the classic linear equations by Kirchhoff.

Pioneering analytical work in the analysis of rectangular thin plate vibrations with geometrical nonlinearities was carried out in the 1950s by Chu and Herrmann [17], demonstrating for the first time the hardening-type nonlinearity that has been confirmed by numerous experiments; see, e.g. [1,28]. Restricting the attention to the case of rectangular plates, the work by Yamaki [55] confirms analytically the hardening-type nonlinearity for forced plates. The case of 1:1 internal resonance for rectangular plates (where two eigenmodes have nearly equal eigenfrequencies) has been studied by Chang et al. [14] and by Anlas and Elbeyli [3]. Parametrically excited nearly square plates, also displaying 1:1 internal resonance, have also been considered by Yang and Sethna [56]. All these works focus on the moderately nonlinear dynamics of rectangular plates where only a few modes (typically one or two) interact together. In these cases, the von Kármán plate equations are projected onto the linear modes, and the coupling coefficients are computed with ad-hoc assumptions that appear difficult to generalise. Finite element methods have also been employed—see, e.g. the work by Ribeiro et al. [42–44], and Boumediene et al. [10] to investigate the nonlinear forced response in the vicinity of a eigenfrequency. Recently, numerical simulations of more complex dynamical solutions, involving a very large number of modes in the permanent regime, have been conducted, in order to simulate the wave turbulence regime and to reproduce the typical sounds of cymbals and gongs. For that, Bilbao developed an energy-conserving scheme for finite difference approximation of the von Kármán system [5], which allows the study of the transition to turbulence [49] and the simulation of realistic sounds of percussive plates and shells [6,7]. Spectral methods with a very large number of degrees of freedom have also been employed in [20] to compare theoretical and numerical wave turbulence spectra.

This work aims at extending the possibilities of the modal approach to simulate numerically the nonlinear regime of rectangular plates. Instead of introducing ad-hoc assumptions, a general model is here presented; this model retains a vast number of interacting modes, making possible the investigation of the global dynamics of the plate while making it very precise. Within this framework, the advantages of the modal approach are retained (accuracy of linear and nonlinear coefficients, flexibility in setting modal damping terms in order to calibrate simulation with experiment, ...), and its limitations are overcome: there is no restriction with respect to the amount of modes that one wants to keep. In this work, the possibility of simulating dynamical solutions with a large number (say a few hundred) of modes is detailed. The case under study is that of a simply supported plate with in-plane movable edges. For this particular choice, the transverse modes are readily obtained from a double sine series [26]; the in-plane modes, however, are not available in closed form. Interestingly, it was shown in [46] that the problem of finding the in-plane modes for the chosen boundary conditions corresponds mathematically to the problem of finding the modes of a fully clamped Kirchhoff plate. To this extent, a general strategy proposed in [31] is here adapted to find the clamped plate modes. To validate the results, the resonant response of the plate in the vicinity of the first two modes is numerically investigated, for vibration amplitudes up to three to four times the thickness. Secondly, a thorough comparison of the modal approach with the finite difference method developed in [5,6] is also given. Calculation of the free response allows the study of the first two nonlinear normal modes of the plate and to highlight the complicated dynamics displayed at large amplitudes. Modal couplings, resonant and nonresonant, are investigated. Finally, the forced response is also computed, and the link between the backbone curve and the forced response is investigated, showing the role of internal resonance and damping.

2 Model description

Plates whose flexural vibrations are comparable to the thickness are most efficiently described by the von Kármán equations [17,33,39,46]. In the course of this paper, a rectangular plate of dimensions L_x, L_y and thickness h (with $h \ll L_x, L_y$) is considered. The plate material is homogeneous, of volume density ρ, Young's modulus E and Poisson's ratio ν. Its flexural rigidity is then defined as $D = Eh^3/12(1-\nu^2)$. The von Kármán system then reads

$$D\Delta\Delta w + \rho h\ddot{w} + c\dot{w} = L(w, F) + \delta(\mathbf{x} - \mathbf{x_0}) f \cos(\Omega t), \tag{1.1}$$

$$\Delta\Delta F = -\frac{Eh}{2} L(w, w), \tag{1.2}$$

where Δ is the Laplacian operator, $w = w(x, y, t)$ is the transverse displacement, and $F = F(x, y, t)$ is the Airy stress function. The equations present a viscous damping term $c\dot{w}$ and a sinusoidal forcing term $\delta(\mathbf{x} - \mathbf{x_0}) f \cos(\Omega t)$ applied at the point $\mathbf{x_0}$ on the plate. The damping will take the form of modal viscous damping once the equations are discretised along the normal modes. The bilinear operator $L(\cdot, \cdot)$ is known as von Kármán operator [46] and, in Cartesian coordinates, it has the form of

$$L(\alpha, \beta) = \alpha_{,xx}\beta_{,yy} + \alpha_{,yy}\beta_{,xx} - 2\alpha_{,xy}\beta_{,xy}, \tag{2}$$

where $_{,s}$ denotes differentiation with respect to the variable s. This operator, although itself bilinear, is the source of the nonlinear terms in the equations. All the quantities are taken in their natural units, so that Eq. (1.1) and Eq. (1.2) have the dimensions, respectively, of kg m^{-1} s^{-2} and kg m^{-2} s^{-2}. The term $L(w, w)$ in Eq. (1.2) is quadratic in w and its derivatives, so once the solution for F is injected into (1.1), a cubic nonlinearity will appear, leading to a Duffing-type set of coupled ordinary differential equations (ODEs).

2.1 Linear modes

The strategy adopted here to solve the von Kármán system makes use of the linear modes for the displacement w and Airy stress function F. This strategy is particularly useful for investigating the free and forced vibrations of the system, in the sense that it allows for the reduction of the dynamics of the problem from an infinite number of degrees of freedom to a finite one. The eigenmodes for the displacement w will be denoted by the symbol $\Phi_k(x, y)$, and thus $w(x, y, t)$ is written as

$$w(x, y, t) = S_w \sum_{k=1}^{N_w} \frac{\Phi_k(x, y)}{\|\Phi_k\|} q_k(t), \tag{3.1}$$

where Φ_k is such that

$$\Delta\Delta\Phi_k(x, y) = \frac{\rho h}{D}\omega_k^2 \Phi_k(x, y). \tag{3.2}$$

Note that the sum in Eq. (3.1) is terminated at N_w in practice. The linear modes can be defined up to a constant of normalisation that can be chosen arbitrarily. For the sake of generality, S_w here denotes the constant of normalisation of the function $\bar{\Phi} = S_w \frac{\Phi_k(x,y)}{\|\Phi_k\|}$. The norm is obtained from a scalar product (α, β) between two functions $\alpha(x, y)$ and $\beta(x, y)$, defined as

$$< \alpha, \beta >= \int_S \alpha\, \beta\, dS \quad \longrightarrow \quad \|\Phi_k\|^2 =< \Phi_k, \Phi_k >. \tag{4}$$

Eq. (3.2) is the eigenvalue problem definition, and it is a Kirchhoff-like equation for linear plates.

The Airy stress function is expanded along an analogue series:

$$F(x, y, t) = S_F \sum_{k=1}^{N_F} \frac{\Psi_k(x, y)}{\|\Psi_k\|} \eta_k(t), \tag{5.1}$$

$$\Delta\Delta\Psi_k(x, y) = \zeta_k^4 \Psi_k(x, y). \tag{5.2}$$

Boundary conditions for w and F will be specified in the next subsection. The linear modes so defined are orthogonal with respect to the scalar product and are therefore a suitable function basis [26]. Orthogonality between two functions $\Lambda_m(x, y)$, $\Lambda_n(x, y)$ is expressed as

$$< \Lambda_m, \Lambda_n >= \delta_{m,n} \|\Lambda_m\|^2, \tag{6}$$

where $\delta_{m,n}$ is the Kronecker delta.

Once the linear modal shapes are known, system (1.1) may then be reduced to a set of ordinary differential equations, each referring to the kth modal coordinate $q_k(t)$, $k = 1, \ldots, N_w$. N_w represents the order of the system of ODEs.

2.2 Reduction to a set of ODEs

The introduction of the expansion series (3.1) and (5.1) allows for the decomposition of the original von Kármán problem onto a set of coupled, nonlinear ordinary differential equations (ODEs). As a starting point, Eq. (5.1) is substituted into Eq. (1.2) to obtain

$$\eta_k = -\frac{Eh}{2\zeta_k^4}\frac{S_w^2}{S_F}\sum_{p,q} q_p q_q \frac{\int_S \Psi_k L(\Phi_p,\Phi_q)\mathrm{d}S}{\|\Psi_k\|\|\Phi_p\|\|\Phi_q\|}. \tag{7}$$

Integration is performed over the area of the plate, and the orthogonality relation is used. Injecting Eqs. (3) and (7) into Eq. (1.1) gives

$$\begin{aligned}&\rho h S_w \sum_k \frac{\omega_k^2 \Phi_k}{\|\Phi_k\|} q_k + \rho h S_w \sum_k \frac{\Phi_k}{\|\Phi_k\|}\ddot{q}_k + c S_w \sum_k \frac{\Phi_k}{\|\Phi_k\|}\dot{q}_k \\ &= -\frac{EhS_w^3}{2}\sum_{n,p,q,r}\frac{1}{\zeta_n^4}\frac{L(\Phi_p,\Psi_n)}{\|\Psi_p\|\|\Phi_n\|}\frac{\int_S \Psi_n L(\Phi_q,\Phi_r)\mathrm{d}S}{\|\Phi_q\|\|\Phi_r\|\|\Psi_n\|} q_p q_q q_r + \delta(\mathbf{x}-\mathbf{x_0}) f\cos(\Omega t).\end{aligned} \tag{8}$$

Then, the equation is multiplied on both sides by Φ_s and integrated over the surface of the plate. The result is

$$\ddot{q}_s + \omega_s^2 q_s + 2\chi_s\omega_s\dot{q}_s = -\frac{ES_w^2}{2\rho}\sum_{p,q,r}^{n}\frac{H_{q,r}^n E_{p,n}^s}{\zeta_n^4} q_p q_q q_r + \frac{\Phi_s(\mathbf{x_0})}{\|\Phi_s\|\rho h S_w} f\cos(\Omega t), \tag{9}$$

where a modal viscous damping is introduced in the equation, scaled by $\chi_s = c/(2\rho h\omega_s)$ (a dimensionless parameter). A practical advantage of the modal description is that χ_s can be estimated experimentally for a large number of modes [11], and so the modal approach allows the simulation of complex frequency dependent damping mechanisms with practically no extra effort.

Two third order tensors, $H_{q,r}^n$ and $E_{p,n}^s$, appear in Eq. (9). These are defined as

$$H_{p,q}^n = \frac{\int_S \Psi_n L(\Phi_p,\Phi_q)\mathrm{d}S}{\|\Psi_n\|\|\Phi_p\|\|\Phi_q\|}, \qquad E_{r,n}^s = \frac{\int_S \Phi_s L(\Phi_r,\Psi_n)\mathrm{d}S}{\|\Phi_r\|\|\Phi_s\|\|\Psi_n\|}. \tag{10}$$

It is seen that the ODEs are cubic with respect to the variables q_s, so a fourth-order tensor Γ can conveniently be introduced in the equations, as

$$\Gamma_{p,q,r}^s = \sum_{n=1}^{N_F}\frac{H_{p,q}^n E_{r,n}^s}{2\zeta_n^4}. \tag{11}$$

Once the tensor Γ is known, one is left with a set of coupled ODEs that can be integrated in the time variable using standard integration schemes. Alternatively, continuation methods can be employed to derive a complete bifurcation analysis of the nonlinear dynamics.

2.3 Boundary conditions

To recover the von Kármán equations, one may define the potential and kinetic energies of a bent plate, in the following way:

$$V = \sum_{i,k=1}^{3}\frac{h}{2}\int_S \sigma_{ik}u_{ik}\mathrm{d}S, \tag{12.1}$$

$$T = \frac{\rho h}{2}\int_S \dot{w}^2\mathrm{d}S, \tag{12.2}$$

$$U = \sum_{i,k=1}^{2}\frac{h}{2}\int_S \tilde{\sigma}_{ik}\tilde{u}_{ik}\mathrm{d}S \tag{12.3}$$

where V, T are the potential and kinetic energies for pure bending, and U is the potential energy for the stretching in the in-plane direction. Note that two strain tensors (u_{ik} and $\tilde{u}_{ik}$) and two stress tensors (σ_{ik} and $\tilde{\sigma}_{ik}$) are introduced, in order to account for the pure bending and in-plane energies; note also that the indices of the in-plane tensors can take only two values. Suppose that the displacement vector is $\mathbf{u} = (u_x, u_y, w)$ defined in a Cartesian set of coordinates $\mathbf{x} = (x, y, z)$. The symmetric strain tensor u_{ik} is linear and can be given in terms of the vertical displacement w as follows [23]:

$$u_{xx} = -z\partial^2 w/\partial x^2; \quad u_{yy} = -z\partial^2 w/\partial y^2; \quad u_{xy} = -z\partial^2 w/\partial x\partial y; \quad u_{zz} = \frac{\nu}{1-\nu} z(\partial^2 w/\partial x^2 + \partial^2 w/\partial y^2), \tag{13}$$

and zero for all the other components. The stress–strain relationships are also linear, as the material is assumed to be, and read

$$\sigma_{ik} = \sum_{l=1}^{3} \frac{E}{1+\nu}\left(u_{ik} + \frac{\nu}{1-2\nu}\, u_{ll}\, \delta_{ik}\right). \tag{14}$$

The symmetric, two-dimensional strain tensor $\tilde{u}_{ik}$ is nonlinear and given by

$$\tilde{u}_{ik} = \left[\frac{1}{2}\left(\frac{\partial u_i}{\partial x_k} + \frac{\partial u_k}{\partial x_i}\right) + \frac{1}{2}\frac{\partial w}{\partial x_i}\frac{\partial w}{\partial x_k}\right], \tag{15}$$

and the stress–strain relationships for the in-plane stretching are given as

$$\tilde{\sigma}_{xx} = \frac{E}{1-\nu^2}(\tilde{u}_{xx} + \nu\tilde{u}_{yy}); \quad \tilde{\sigma}_{yy} = \frac{E}{1-\nu^2}(\tilde{u}_{yy} + \nu\tilde{u}_{xx}); \quad \tilde{\sigma}_{xy} = \frac{E}{1+\nu}\tilde{u}_{xy} \tag{16}$$

and zero for all the other components. The Airy stress function F is introduced as

$$\tilde{\sigma}_{xx} = \partial^2 F/\partial y^2; \quad \tilde{\sigma}_{yy} = \partial^2 F/\partial x^2; \quad \tilde{\sigma}_{xy} = -\partial^2 F/\partial x\partial y. \tag{17}$$

Note that the only nonlinear term that appears in the definitions of the energies is the quadratic factor in $\tilde{u}_{ik}$. It is possible to make use of Hamilton's principle, stated in the form

$$\int_{t_0}^{t_1} \delta(T - V - U)\, dt = 0, \tag{18}$$

to recover the equations of motion (1.1) plus the boundary conditions. These can be categorised as follows [46] (here $_{,n}$, $_{,t}$ denote differentiation along the normal and tangent directions, respectively):

- In-plane direction
  - free edge: $F_{,nt} = F_{,tt} = 0$
  - immovable edge ($w = 0$ along the boundary): $F_{,nn} - \nu F_{,tt} = F_{,nnn} + (2+\nu)F_{,nnt} = 0$
- Edge rotation
  - rotationally free: $w_{,nn} + \nu w_{,tt} = 0$
  - rotationally immovable $w_{,n} = 0$
- Edge vertical translation
  - free: $w_{,nnn} + (2-\nu)w_{,ntt} - \frac{1}{D}(F_{,tt}w_{,n} - F_{,nt}w_t) = 0$
  - immovable $w = 0$.

A corner condition arises as well, and it is

$$w_{,xy} = 0 \qquad \text{at corners.} \tag{19}$$

This constraint has to be imposed as an extra condition only when the edge is transversely free. It is evident that the boundary conditions must be fulfilled by all the linear modes Φ_k, Ψ_k that appear in the expansions (2.1), (5.1). For the transverse function, simply supported boundary conditions are considered for the remainder of the paper. These describe a fixed, rotationally free edge and permit a simplified analysis because a solution is readily available:

$$\Phi_k = \sin\left(\frac{k_1\pi x}{L_x}\right)\sin\left(\frac{k_2\pi y}{L_y}\right); \qquad \omega_k^2 = \frac{D}{\rho h}\left[\left(\frac{k_1\pi}{L_x}\right)^2 + \left(\frac{k_2\pi}{L_y}\right)^2\right]^2. \tag{20}$$

For the in-plane direction, a free edge is considered. However, a different form of the boundary conditions will be used, i.e. $F = F_{,n} = 0$. It is evident that the assumed conditions are sufficient to satisfy the proper conditions $F_{,nt} = F_{,tt} = 0$. Note that, mathematically speaking, the assumed conditions on F turn the stress function problem into a transversely clamped plate problem.

The selected boundary conditions are also known as *simply supported with movable edges* [1].

3 A solution for the clamped plate

As shown in the previous section, the eigenvalue problem for F with the chosen boundary conditions is equivalent to that of a clamped Kirchhoff plate. To this extent, the Galerkin method is employed, as an analytical solution for the problem is not available.

The starting point of the Galerkin method is to express the eigenfunction Ψ_k of Eqs. (5) as a series of this form:

$$\Psi_k(x, y) = \sum_{n=0}^{N_c} a_n^k \Lambda_n(x, y) \tag{21}$$

where $\Lambda_n(x, y)$ are the expansion functions depending on some index n, and a_n^k are the expansion coefficients: these depend on the index n and of course on the index k. The total number of expansion functions is N_c, and obviously, the accuracy of the solution improves as this parameter is increased. The Λ's must be carefully selected from the set of all comparison functions [48]; this is to say that they need to satisfy the boundary conditions associated with the problem that they are at least p times differentiable (where p is the order of the PDE), and they form a complete set over the domain of the problem. Completeness is quite a rather involved property to prove; however, one generally resorts to variations of sine or cosine Fourier series, for which completeness follows directly from the Fourier theorem.

For this work, the expansion functions were selected according to a general method proposed in [31], where it is shown how a Kirchhoff plate problem can be solved by means of a double modified Fourier cosine series, i.e.

$$\Lambda_n(x, y) = X_{n_1}(x)Y_{n_2}(y) = \left(\cos\left(\frac{n_1\pi x}{L_x}\right) + p_{n_1}(x)\right)\left(\cos\left(\frac{n_2\pi y}{L_y}\right) + p_{n_2}(y)\right), \tag{22}$$

where $p_{n_1}(x)$, $p_{n_2}(y)$ are fourth-order polynomials in the variables x and y, and depending as well on the integers n_1, n_2. Note that the order of the polynomials corresponds to the order of the PDE. The role of the polynomial is to account for possible discontinuities at the edges due to the boundary conditions. Li [31] is mainly concerned with a general solution strategy, where the plate is equipped with linear and rotational springs at the edges to simulate the effect of different boundary conditions. In [31], the polynomials of Eq. (22) do not appear explicitly, as they are obtained through matrix inversion in order to comply with the general form of the boundary conditions. In turn, these matrices present the values of all the springs, and the general expression of the Λ's is rather involved. However, given that the focus here is on the clamped plate only, the analytical limit of all the springs having infinite stiffness is taken, so that an explicit form for (22) can indeed be recovered, and this is:

$$X_{n_1}(x) = \cos\left(\frac{n_1\pi x}{L_x}\right) + \frac{15(1+(-1)^{n_1})}{L_x^4}x^4 - \frac{4(8+7(-1)^{n_1})}{L_x^3}x^3 + \frac{6(3+2(-1)^{n_1})}{L_x^2}x^2 - 1, \tag{23}$$

and similarly for $Y_{n_2}(y)$. Note that for the clamped plate satisfaction of the boundary conditions is essential for a fast converging solution. This is because the conditions at the edges for the clamped plate are *geometrical*, as they prescribe the vanishing of the displacement and of the slope. Thus, an expansion function that does not satisfy these conditions could lead to slow converging solutions, if not to wrong results.

Table 1 Convergence of clamped plate frequencies, $\zeta_k^2 L_x L_y$, $\xi = 2/3$

k	N_c					
	25	100	144	255	400	484
1	40.509	40.508	40.508	40.508	40.508	40.508
2	62.563	62.556	62.556	62.556	62.556	62.556
3	99.193	99.187	99.187	99.186	99.186	99.186
4	99.790	99.787	99.783	99.783	99.783	99.783
5	119.75	119.71	119.71	119.71	119.71	119.71
20	476.05	359.60	359.58	359.57	359.57	359.57
50	–	859.52	839.38	839.31	839.31	839.31
100	–	2,439.9	1,669.7	1,574.3	1,500.3	1,500.3

Table 2 Comparison of clamped plate frequencies, $\zeta_k^2 L_x L_y$, $\xi = 2/3$

k	Source		
	Galerkin ($N_c = 400$)	Leissa	FD (241×161)
1	40.51	40.51	40.05
2	62.56	62.58	61.93
3	99.19	98.25	98.00
10	208.0	207.9	205.5
20	359.6	–	355.32

It is seen that this expansion satisfies the clamped plate conditions, but not the differential equation. It is possible to show however that one particular choice for the expansion coefficients a_n^k will render the function Ψ_k an eigenfunction for the problem. The Galerkin method describes how to build up stiffness and mass matrices in order to calculate the coefficient vector a_n^k and the corresponding eigenfrequency ζ_k^4. For the problem (5.2), these matrices are

$$K_{ij} = \int_S [\Delta\ \Lambda_i\ \Delta\ \Lambda_j - L(\Lambda_i, \Lambda_j)]\mathrm{d}S, \qquad \text{Stiffness Matrix} \tag{24.1}$$

$$M_{ij} = \int_S \Lambda_i\ \Lambda_j\ \mathrm{d}S, \qquad \text{Mass Matrix} \tag{24.2}$$

where $L(\cdot, \cdot)$ is the von Kármán operator. Note that the integrals can be calculated analytically, because of the simple form of the expansion function. Explicit forms of the integrals are presented in "Appendix A". Then,

$$K\mathbf{a} = \zeta^4 M\mathbf{a}, \tag{25}$$

which is the required eigenvalue problem that leads to the expansion coefficients and the eigenvalues.

3.1 Numerical results for the clamped plate

In this section, the results obtained by Galerkin's method are compared to the classical results found in Leissa's tables [30]. A finite difference scheme (FD) developed by Bilbao [5] is as well used as a benchmark. A useful parameter in plate problems is the aspect ratio, here defined as Lx/Ly and denoted by the symbol ξ. Assume that two plates present the same aspect ratio: then, it is straightforward to show that the quantity $\zeta^2 L_x L_y$ is constant for the two plates, where ζ is defined in Eq. (5.2) (thus making $\zeta^2 L_x L_y$ a nondimensional parameter). As a first step, the rate of convergence of the eigenfrequencies is proposed in Table 1. The plate has an aspect ratio of $2/3$. N_c denotes the number of modes kept in the expansion (21). Note that convergence for the first 100 eigenfrequencies is obtained up to the fifth significant digit when $N_c = 400$. This corresponds to a calculation time of less than 10 s in MATLAB on a standard machine equipped with an Intel Core i5 CPU 650 @ 3.20 GHz, and a memory of 4 GB. In Table 2, the results obtained by Galerkin's method are compared to those found in Leissa as well as to the outcome of the FD scheme. For this, the plate parameters have been set as: $L_x = 0.4$ m, $L_y = 0.6$ m, $\rho = 7,860$ kg/m^3, $\nu = 0.3$, $h = 0.001$ m, $E = 2 \times 10^{11}$ Pa. The FD scheme employs 241×161 discretisation points, so that $\frac{\Delta x \Delta y}{S} = 2.6 \times 10^{-5}$. Even though Leissa's book represents

Table 3 Convergence of clamped plate frequencies, FD scheme, $\zeta_k^2 L_x L_y$, $\xi = 2/3$

k	Grid points					
	36×54	51×76	114×171	161×241	228×342	280×419
1	38.539	39.094	39.862	40.048	40.182	40.242
2	59.889	60.638	61.682	61.934	62.115	62.196
3	93.993	95.484	97.509	97.995	98.343	98.499
4	95.768	96.914	98.491	98.865	99.134	99.253
10	197.00	200.20	204.48	205.49	206.22	206.54

Table 4 Convergence of clamped plate frequencies, $\zeta_k^2 L_x L_y$, $\xi = 1$ (square plate)

k	N_c					
	25	100	144	255	400	484
1	35.986	35.985	35.985	35.985	35.985	35.985
2	73.398	73.394	73.394	73.394	73.394	73.394
3	73.398	73.394	73.394	73.394	73.394	73.394
4	108.24	108.22	108.22	108.22	108.22	108.22
5	131.60	131.58	131.58	131.58	131.58	131.58
20	376.42	371.37	371.35	371.35	371.34	371.34
50	–	805.89	805.42	805.35	805.34	805.34
100	–	2,217.0	1,588.7	1,546.2	1,546.1	1,546.1

Table 5 Comparison of clamped plate frequencies, $\zeta_k^2 L_x L_y$, $\xi = 1$ (square plate)

k	Source		
	Galerkin ($N_c = 400$)	Leissa	FD (161×161)
1	35.98	35.99	35.54
2	73.39	73.41	72.49
3	73.39	73.41	72.49
4	108.2	108.3	106.9
20	371.3	–	366.7

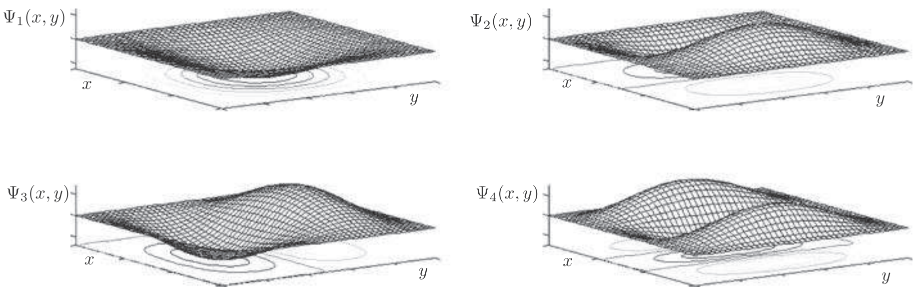

Fig. 1 First four modes for the clamped plate, $\xi = 2/3$

one of the main references in the area of plate eigenmodes and frequencies, its results are somehow outdated, being about 40 years old. Thus, discrepancies between the presented Galerkin's method and the numbers from Leissa's book are not at all concerning. On the other hand, it is known that FD schemes converge at a slower rate than a pure modal approach. This is a consequence of the fact that FD schemes rely on discrete grid meshes. Convergence for the first eigenfrequencies for the plate using the FD scheme is presented in Table 3. Note that the eigenfrequencies tend to converge to the same values as Galerkin's method. However, the calculation time in MATLAB for a mesh grid of 280 × 419 points is much slower (about 20 min). Table 4 presents the eigenfrequencies for the square plate, using Galerkin's method. It is possible to appreciate the same rate of convergence as for the previous case. Again, the results are compared with Leissa and to the FD scheme outcome (161 × 161 grid points) in Table 5. Plots of some clamped plate eigenmodes are presented in Fig. 1. These results show that the Galerkin method, with the carefully chosen expansion (23), is indeed a fast converging strategy for the calculation of the eigenfrequencies, as it allows for precisely computing hundreds of modes within seconds.

4 The nonlinear coupling coefficients

4.1 Symmetry properties

In this section, symmetry properties for the coupling coefficients Γ that appear in Eq. (11) are presented. First, it is obvious that

$$H^i_{p,q} = H^i_{q,p}, \tag{26}$$

because of the symmetry of the operator $L(\cdot,\cdot)$. Secondly, integrating by parts, the integral in the definition of E in Eq. (10) gives

$$\begin{aligned}\|\Psi_q\|\|\Phi_n\|\|\Phi_p\|E^n_{p,q} = &\oint\left[\Phi_n\Psi_{q,y}\Phi_{p,xx} - 2\Phi_n\Psi_{q,x}\Phi_{p,xy} - \Psi_q\frac{\partial}{\partial y}\left(\Phi_n\Phi_{p,xx}\right)\right]\mathbf{y}\cdot\mathbf{n}\,\mathrm{d}\Omega\, + \\ &+\oint\left[\Phi_n\Psi_{q,x}\Phi_{p,yy} + 2\Psi_q\frac{\partial}{\partial y}\left(\Phi_n\Phi_{p,xy}\right) - \Psi_q\frac{\partial}{\partial x}\left(\Phi_n\Phi_{p,yy}\right)\right]\mathbf{x}\cdot\mathbf{n}\,\mathrm{d}\Omega \\ &+\int\Psi_q L(\Phi_p,\Phi_n)\mathrm{d}S.\end{aligned} \tag{27}$$

It is easy to see that the selected boundary conditions make the surface integrals vanish, so that the following property holds:

$$E^n_{p,q} = H^q_{p,n}. \tag{28}$$

In this way, the tensor Γ may then be conveniently written as

$$\Gamma^s_{p,q,r} = \sum_{n=1}^{N_F}\frac{H^n_{p,q}H^n_{r,s}}{2\zeta_n^4}. \tag{29}$$

Note that the tensor H as defined in Eq. (10) is divided by the norms of the modes, so the value of Γ is independent of the particular choice for the constants S_w, S_F in Eqs. (3.2), (5.2). Basically, the symmetry properties for Γ mean the following sets of indices will produce the same numerical value:

$$(s,p,q,r),\ (r,p,q,s),\ (s,q,p,r),\ (r,q,p,s),\ (q,r,s,p),\ (p,r,s,q),\ (q,s,r,p),\ (p,s,r,q). \tag{30}$$

These symmetry properties can lead to large memory savings when the number of transverse and in-plane modes is a few hundred.

4.2 Null coupling coefficients

For the sake of numerical computation, it would be interesting to know *a priori* which coupling coefficients are null. In actual fact, empirical observations of the Γ tensor suggest that only a smaller fraction of coefficients is not zero. As an example, consider Table 6 where the nonzero values for the coefficients $\Gamma^1_{5,q,r}$ for a plate with $\xi = 2/3$ were collected (with $p, q = 1 \ldots 10$): the table presents only 24 nonzero coefficients out of a total of 100. These coefficients measure the amount of interaction between the different transverse modes. As a matter of fact, the modes can be classified according to the symmetry with respect to the x and y axis where the origin is placed at the centre of the plate. Four families exist, and they are: doubly symmetric (SS), antisymmetric-symmetric (AS and SA) and doubly antisymmetric (AA). For instance, the first mode is a doubly symmetric mode because it presents one maximum at the centre of the plate, and is thus symmetric with respect to the two orthogonal directions departing from the centre of the plate in the x and y directions, whereas mode 5 is AA. The first sixteen modes for the case under study may be classified in the following groups:

- SS: 1, 4, 8, 11, 12
- SA: 2, 7, 9, 14, 16
- AS: 3, 6, 13, 15
- AA: 5, 10

Table 6 Nonzero $\Gamma^1_{5,q,r}(L_xL_y)^3$, $\xi = 2/3$, for $q = 1:10$, $r = 1:10$

Value	q	r	Modal shape groups	Value	q	r	Modal shape groups
21.36	1	5	SS AA SS AA	27.55	6	2	SS AA AS SA
−21.75	1	10	SS AA SS AA	150.98	6	7	SS AA AS SA
48.46	2	3	SS AA SA AS	36.52	6	9	SS AA AS SA
7.55	2	6	SS AA SA AS	−72.47	7	3	SS AA SA AS
122.11	3	2	SS AA AS SA	119.51	7	6	SS AA SA AS
−169.47	3	7	SS AA AS SA	56.36	8	5	SS AA SS AA
−69.44	3	9	SS AA AS SA	−64.89	8	10	SS AA SS AA
56.71	4	5	SS AA SS AA	10.19	9	3	SS AA SA AS
9.8	4	10	SS AA SS AA	65.63	9	6	SS AA SA AS
3.1	5	1	SS AA AA SS	−51.96	10	1	SS AA AA SS
144.68	5	4	SS AA AA SS	97.76	10	4	SS AA AA SS
46.47	5	8	SS AA AA SS	30.75	10	8	SS AA AA SS

This list will become useful when interpreting the free vibration diagrams of the next section. Remarkably, the number of indices of the Γ coefficients (four) matches the number of modal shape sets. Table 6 presents the modal families to which the interacting modes belong; observation of alike tables permits to state the following heuristic rule:

> *the indices* (s, p, q, r) *will give a nonzero value for* $\Gamma^s_{p,q,r}$ *if and only if modes s,p,q,r come all from distinct modal shape groups or if they come from the same group two by two.*

For example, the combinations (SS, SS, AS, SA) and (SS, SS, SS, AS) will definitely give a zero value; on the other hand, the combinations (SS, SS, SS, SS), (SS, AA, SS, AA) and (SS, AS, SA, AA) will give a nonzero value. A rigorous mathematical proof is not carried out as it involves a rather lengthy development which is beyond the scope of the present work. However, it has been numerically checked for a large number of Γ's involving a few hundred modes, providing an exhaustive verification of this rule.

This rule, in combination with the previous remarks on symmetry, can be used to speed up the calculation of the Γ tensor (for example by pre-allocating the zero entries when using a sparse matrix description). In some way, this observation relates to the already noted property of von Kármán shells [47]. There, the coupling rules are actually more involved, but they can be somehow more directly proved mathematically.

4.3 A few words on the FD scheme

To validate the computational results for the Γ tensor, an FD scheme developed in [5] has been extensively used. In this sense, the role of the discretised L operator in Eq. (11) is central. For two discrete functions α, β defined over the plate grid, the form for the discrete counterpart $l(\alpha, \beta)$ has been selected as

$$l(\alpha, \beta) = \delta_{xx}\alpha\delta_{yy}\beta + \delta_{yy}\alpha\delta_{xx}\beta - 2\mu_{x-}\mu_{y-}(\delta_{x+y+}\alpha\delta_{x+y+}\beta). \tag{31}$$

The δ's are discrete derivative operators, and the μ's are averaging operators, as follows from

$$\delta_{xx} = \frac{1}{h_x^2}(e_{x+} - 2 + e_{x-}); \quad \delta_{x+} = \frac{1}{h_x}(e_{x+} - 1); \quad \mu_{x-} = \frac{1}{2}(e_{x-} + 1), \tag{32}$$

where e_{x+} (e_{x-}) is the positive (negative) shifting operator, and h_x is the step size along the x direction. Note that this particular choice for the l operator is due to the fact that it produces an energy-conserving scheme, as explained exhaustively in [5]. The eigenmodes are obtained by solving discrete counterparts of Eqs. (3.2) and (5.2), and thus, a discrete double Laplacian is needed. At interior points, it can be approximated by

$$\delta_{\Delta\boxplus}\delta_{\Delta\boxplus} = (\delta_{xx} + \delta_{yy})(\delta_{xx} + \delta_{yy}) = \Delta\Delta + O(h_x h_y). \tag{33}$$

Enforcing of boundary conditions (simply supported and clamped) is described in [6]. Once the modes are known, one makes use of (31) to get the values of the coupling coefficients in Eq. (11).

Table 7 Convergence of coupling coefficients, $\Gamma^{k}_{k,k,k}(L_x L_y)^3$, $\xi = 2/3$

k	N_F					
	100	144	225	400	484	625
1	20.033	20.034	20.034	20.034	20.034	20.034
20	7.5605×10^3	9.4893×10^3	9.4960×10^3	9.4970×10^3	9.4975×10^3	9.4977×10^3
50	1.3928×10^4	1.3929×10^4	1.3937×10^4	1.3937×10^4	1.3937×10^4	1.3937×10^4
100	1.4847×10^4	2.7360×10^4	1.2413×10^5	1.3334×10^5	2.2100×10^5	2.2108×10^5

Table 8 Convergence of coupling coefficients, FD scheme, $\Gamma^{k}_{k,k,k}(L_x L_y)^3$, $\xi = 2/3$, $N_F = 100$

k	Grid points					
	36×54	51×76	114×171	161×241	228×342	280×419
1	21.113	20.523	20.523	20.380	20.252	20.188
20	9.8904×10^3	9.7238×10^3	9.6364×10^3	9.5761×10^3	9.5218×10^3	9.4944×10^3
50	1.4542×10^4	1.4430×10^4	1.4319×10^4	1.4224×10^4	1.4124×10^4	1.4070×10^4
100	1.0864×10^4	8.2016×10^3	6.8281×10^3	5.9133×10^3	5.1224×10^3	4.7387×10^3

Table 9 Convergence of coupling coefficients, FD scheme, $\Gamma^{k}_{k,k,k}(L_x L_y)^3$, $\xi = 2/3 N_F = 225$

k	Grid points					
	36×54	51×76	114×171	161×241	228×342	280×419
1	21.114	20.728	20.523	20.381	20.253	20.189
20	9.9634×10^3	9.7935×10^3	9.7035×10^3	9.6413×10^3	9.5851×10^3	9.5567×10^3
50	1.4552×10^4	1.4440×10^4	1.4329×10^4	1.4234×10^4	1.4134×10^4	1.4080×10^4
100	2.0268×10^5	2.0223×10^5	2.0227×10^5	2.0246×10^5	2.0271×10^5	2.0286×10^5

4.4 Numerical results

In this subsection, some numerical results are presented. It is somehow useful to note that the Γ's depend only on the aspect ratio. In other words, the quantity

$$\Gamma^{s}_{p,q,r}(L_x L_y)^3 \tag{34}$$

is constant for all the plates sharing the same aspect ratio. Table 7 presents a convergence test for a plate of aspect ratio $\xi = 2/3$. The convergence in this case depends on two factors: the first is the amount of stress function modes retained in the definition of Γ [N_F in Eq. (11)]; the second is the accuracy on the Airy stress function modes and frequencies [quantified by the number N_c in Eq. (21)]. For clarity, in the following Tables, N_F is always the same as N_c. It is seen that a four-digit convergence up to the $\Gamma^{100}_{100,100,100}$ coefficient is obtained when $N_F = 484$, and thus, the convergence rate for these coefficients is slower than that of the stress functions eigenfrequencies alone. For the FD scheme, convergence depends on the number of modes retained and also on the grid size. Thus, Tables 8 and 9 present some values for $N_F = 100$ and $N_F = 200$, respectively. Note that, contrary to what happens for the eigenfrequencies, convergence for the coupling coefficients is from above for FD and from below for the modal approach. It is also evident that a sufficiently large number of stress modes has to be retained to calculate reasonable approximate values for the Γ's: failing to do so may result in completely erroneous estimates (see for instance the last row of Table 8 compared to the last row of Table 9).

5 Analysis of the periodic solutions

The nonlinear dynamics of the plate is now analysed in terms of periodic solutions. The periodic orbits of the conservative system, also called the nonlinear normal modes (NNMs) [53], are first computed thanks to a pseudo arc-length numerical continuation method implemented in the software AUTO [19]. The amplitude–frequency relationships (i.e. the backbone curves) are exhibited for the first two modes up to 3–4 times the thickness, displaying a complicated network of bifurcation branches generated by internal resonances and modal couplings. Secondly, the forced responses of the damped plate are computed and their relationship with the backbone curve illustrated.

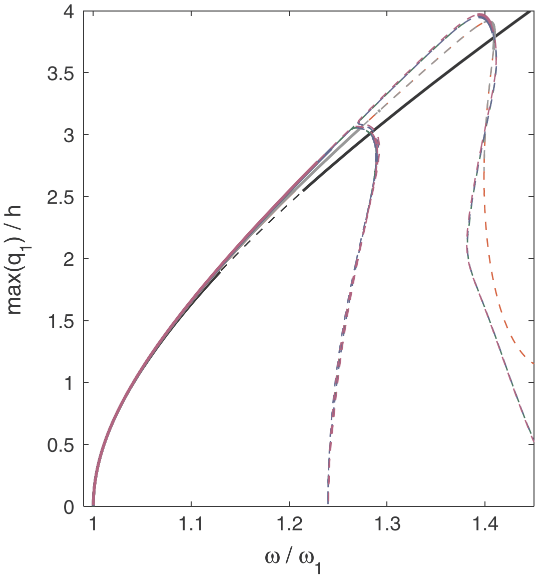

Fig. 2 Backbone curve (principal branch) convergence for mode 1: $N_w = 6$ (*black*), $N_w = 8$ (*red*), $N_w = 10$ (*grey*), $N_w = 14$ (*green*), $N_w = 16$ (*blue*), $N_w = 18$ (*purple*) (colour figure online)

5.1 Mode 1

5.1.1 Free vibrations

Figure 2 is an illustration of the backbone convergence, for mode 1. The backbone is the curve obtained by plotting the maxima of the periodic solutions, in the case of undamped, unforced vibrations, which can be stable (continuous lines) or unstable (dashed lines). Note that only the principal branch is represented, and thus, the figure does not take into account the secondary branches departing from the bifurcation points. The figure presents the six backbones obtained when $N_w = 6, 8, 10, 14, 16, 18$. It is evident that the period of the vibration decreases as the amplitude increases, and thus, the curves bend to the right in the diagram; this behaviour is known in the literature as hardening-type nonlinearity. The backbone curves obtained for $N_w = 14, 16, 18$ are almost exactly superimposed showing the convergence of the main solution branch for vibration amplitudes up to $4h$. Note also that the cases $N_w = 8, 10$ are exactly superimposed because modes 9 and 10 do not belong to SS (the family of mode 1); hence, the shape of the backbone does not change, although the stability intervals do not coincide. No stable solutions are detected by AUTO for vibrations larger than $4h$: this result is consistent with numerous experimental and numerical simulations of large amplitude vibrations of plates; higher vibration amplitudes give way to unstable solutions, in quasiperiodic or turbulent regimes [49,50]. The range of convergence of the backbone decreases when less modes N_w are considered; particularly for the case of $N_w = 6$, the backbone displays significant differences from the converged solution. In addition, unstable solutions in this case set in much earlier, leading to the conclusion that when $N_w = 6$ the backbone curve depicts an unrealistic scenario for amplitudes larger than $1.8h$. The principal branch for the cases $N_w = 14$, $N_w = 16$, $N_w = 18$ undergoes an internal resonance around $\omega/\omega_1 \approx 1.27$. This is a resonance between mode 1 and mode 11, and will be commented later. It is seen that the cases $N_w = 16$, $N_w = 18$ are perfectly superimposed, and thus, a total number of $N_w = 16$ modes is sufficient for full convergence; hence, this is the number of modes that will be considered in the remainder of the paper. Figure 3 shows the complete resonance scenario for mode 1, and in other words, it presents the backbone and the bifurcated branches. Figure 3 is basically a representation of the first NNM as a function of the frequency of vibration for the first mode. For clarity, only the most significant modal coordinates are represented. Branches are denoted by the symbol $\mathbf{B}_k^i$ where the index i refers to the branch number and k is the coordinate involved. Thus, $\mathbf{B}^1$ is the main (backbone) branch, and $\mathbf{B}^2$, $\mathbf{B}^3$, ... are secondary branches featuring a sudden loss of energy of q_1 in favour of other nonlinearly resonant modes. The appearance of internal resonance tongues due to the exchange of energy between modes at nonlinear frequencies of vibration has been previously observed for systems involving a few degrees of freedom, or for continuous systems with local nonlinearities [8,24,27,41]; in turn, these works

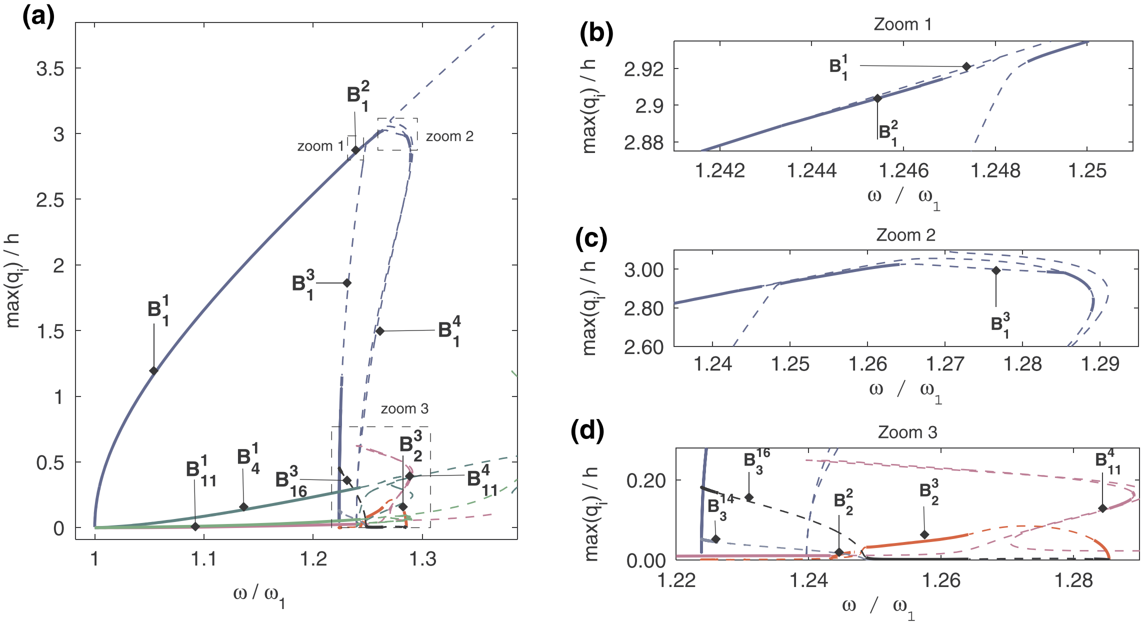

Fig. 3 **a** Free vibration diagram for mode 1, $N_w = 16$. **b**– **d** Bifurcated branches and internal resonances (colour figure online)

show that NNM branches may fold in the presence of internal resonances. In this paper, internal resonance foldings in the NNM branches are reported for a continuous structure with distributed geometric nonlinearity. The bifurcated branches are composed mainly by unstable states along intricate paths and are difficult to compute numerically when using continuation. Note, however, that the free NNM is a physical abstraction: when damping and forcing are introduced in the system, most of the complicated details disappear, as it will be shown in the next subsection.

Observing $\mathbf{B}^1$ before the first bifurcation point, it is easily seen that modes 4 ($\mathbf{B_4^1}$, green), 8 ($\mathbf{B_8^1}$, light green), 11 ($\mathbf{B_{11}^1}$, magenta) and 12 (not shown) bear a relatively important contribution. Here, a typical nonresonant coupling is at hand. As it can be deduced from Sect. 4.2, the only nonvanishing coefficients $\Gamma_{1,1,1}^p$ with $p = 1, \dots, 16$ are obtained for $p = 1, 4, 8, 11, 12$. These coefficients are of prime importance as they give rise to a term of the form $\Gamma_{1,1,1}^p q_1^3$ in the equation for q_p. Thus, when q_1 is large, modes 4,8,11 and 12 acquire nonnegligible energy through the nonresonant coupling terms $\Gamma_{1,1,1}^p$, which act on the modal equations as forcing terms. These coefficients have been referred to as *invariant-breaking* terms because they have the property of breaking the invariance of the linear normal modes through modal coupling [51,52]. The coupling in these cases is nonresonant because no commensurability relationship exists between the frequencies of vibration.

The first bifurcated branch is $\mathbf{B}^2$ and develops along a very narrow frequency interval between $1.2435 < \omega/\omega_1 < 1.248$. It is a very small branch, and it is visible in Fig.3b ($\mathbf{B_1^2}$) and Fig.3d ($\mathbf{B_2^2}$). The modes involved in this bifurcation are 1 and 2. It is evident that mode 2, so far quiescent, is activated by an internal resonance with mode 1. The order of the internal resonance can be obtained from a temporal simulation of the system comprising $N_w = 16$ modes, fed at the input by the maximum displacements and velocities for all the modal coordinates along $\mathbf{B^2}$. In this work, a fourth-order Runge–Kutta scheme is used for the time integration, giving at the output the oscillation in time for all the modes in the periodic regime. Figure 4a represents modes 1 and 2 in the time domain on the point at $\omega/\omega_1 = 1.246$ along the branch $\mathbf{B^2}$. The figure shows that the period of vibration for mode 2 is exactly half the period of mode 1, resulting in a 1:2 internal resonance. Note that starting the simulation on any other point of the same branch will lead to the same resonance ratio.

In the next section, it will be seen that the bifurcation giving rise to $\mathbf{B^2}$ is key to the dynamics of the driven damped oscillations: this branch tends to occupy larger portions of the phase space as the forcing and damping terms increase, modifying the local structure of the invariant NNM manifold.

Following the principal branch in Fig. 3b, one encounters a second bifurcation giving rise to $\mathbf{B^3}$. This is an interesting branch where again quiescent modes are activated by internal resonances. Figure 3d reveals that these are modes 2 ($\mathbf{B_2^3}$, red), 14 ($\mathbf{B_{14}^3}$, grey) and 16 ($\mathbf{B_{16}^3}$, black). Note that the branch $\mathbf{B^3}$ emerges at

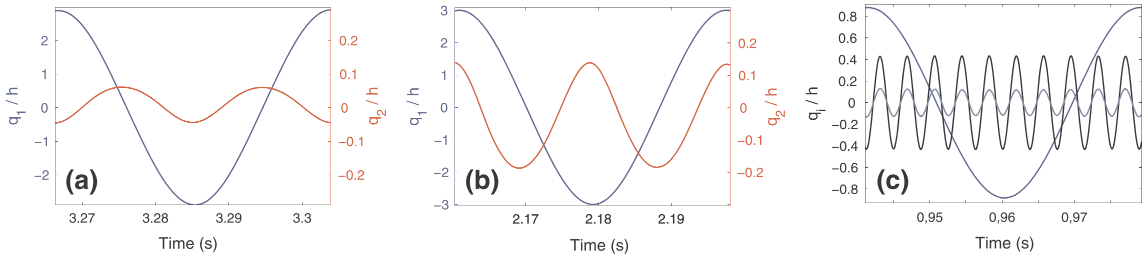

Fig. 4 **a** Modes 1 (*blue*) and 2 (*red*) along $\mathbf{B}^2$ displaying 1:2 internal resonance. **b** Modes 1 (*blue*) and 2 (*red*) along $\mathbf{B}^3$ displaying 1:2 internal resonance. **c** Modes 1 (*blue*), 14 (*grey*) and 16 (*black*) along $\mathbf{B}^3$ displaying 1:10 internal resonance (colour figure online)

$\omega/\omega_1 = 1.285$ and first develops to the left towards decreasing frequencies. The branch is characterised at first by a strong coupling between modes 1 and 2 (visible in Fig. 3d) and then by a coupling amongst modes 1,14 and 16. The order of the resonance can again be extrapolated from a Runge–Kutta time-domain scheme fed with the AUTO output. This gives Fig. 4b, c where it is seen that modes 1 and 2 undergo a second 1:2 internal resonance, whereas modes 1–14 and 1–16 display a 1:10 internal resonance. Thus, the dynamics of this branch is again dominated by even-order internal resonances. The last branch is $\mathbf{B^4}$. This is an improper labelling because this branch is actually the principal branch undergoing an internal resonance with mode 11 ($\mathbf{B^4_{11}}$, magenta). This branch is almost entirely unstable, and the Runge–Kutta time-domain simulation does not return stable periodic solutions. There is no doubt, however, that the branch is activated by internal resonance between modes 1 and 11, given the rapid growth of the latter in the bifurcation diagram at the expense of mode 1.

The analysis of the first NNM revealed some important aspects of the nonlinear system: in particular, it was shown that the bifurcated branches are generated by even-order internal resonances which, in turn, break the symmetry of the cubic nonlinearity possessed by the system. This symmetry-breaking bifurcation has already been observed for the simple Duffing equation [32,40], as well as in systems with material nonlinearity [36]. Physically speaking, the most important properties returned by the analysis of the free NNM are as follows: (i) the loss of stability of the periodic solutions for amplitudes above $3h$; (ii) the pitchfork bifurcation giving rise to $\mathbf{B^2}$ presenting a strong coupling between modes 1 and 2. The next subsection will treat in some detail a few examples of forced-damped vibrations, and it will be seen how the shape of the NNM gets modified by the damping and forcing terms.

5.1.2 Forced-damped vibrations

In this section, forced-damped vibrations are considered. The plate is forced with a sinusoid of maximum amplitude f and frequency Ω [see Eq. (9)] varied around the eigenfrequency of the first mode, ω_1. In turn, damping and forcing terms modify the shape of the invariant manifold corresponding to the NNM of the previous section. Internal resonances change too: some are basically unseen by the modified NNM, whereas others play a major role.

The first case under study presents a forcing amplitude of $f = 0.17$ N, and a damping coefficient $\chi_i = 0.001$ (same for all modes). The result is pictured in Fig. 5. In the figure, the forced branches are represented with the usual colouring scheme (blue for mode 1 and red for mode 2), whereas the black lines are the branches from the Hamiltonian dynamics. The point labelled **G** in Fig. 5 corresponds to a pitchfork symmetry-breaking bifurcation, driven by the underlying Hamiltonian dynamics and by the existence of the 1:2 internal resonance. The main branch becomes unstable in favour of stable periodic orbits where both modes 1 and 2 are activated in a 1:2 internal resonance. Hence, branch $\mathbf{B^2}$ reveals its importance as it has a major effect in the damped-driven case. One can also notice that, for this small amount of damping, the turning point **J** is located just before the resonant tongue along the original backbone curve.

In order to understand more deeply the role of the branch $\mathbf{B^2}$, two more cases of interest are portrayed in Figs. 6 and 7. Here, $f = 1.36$ N for both cases, and $\chi_i = 0.005$ for Fig. 6 and 0.001 for Fig. 7. The first important remark is the location of the pitchfork bifurcation along the main branch: $q_1/h = 1.899$ for Fig. 6 and $q_1/h = 1.824$ for Fig. 7. It is seen that the invariant manifold of the Hamiltonian dynamics is largely affected by the damping and forcing terms: the bifurcation **G** is located at very different points in the phase space when comparing free and forced-damped vibrations. The 1:2 internal resonance giving rise to $\mathbf{B^2}$ becomes

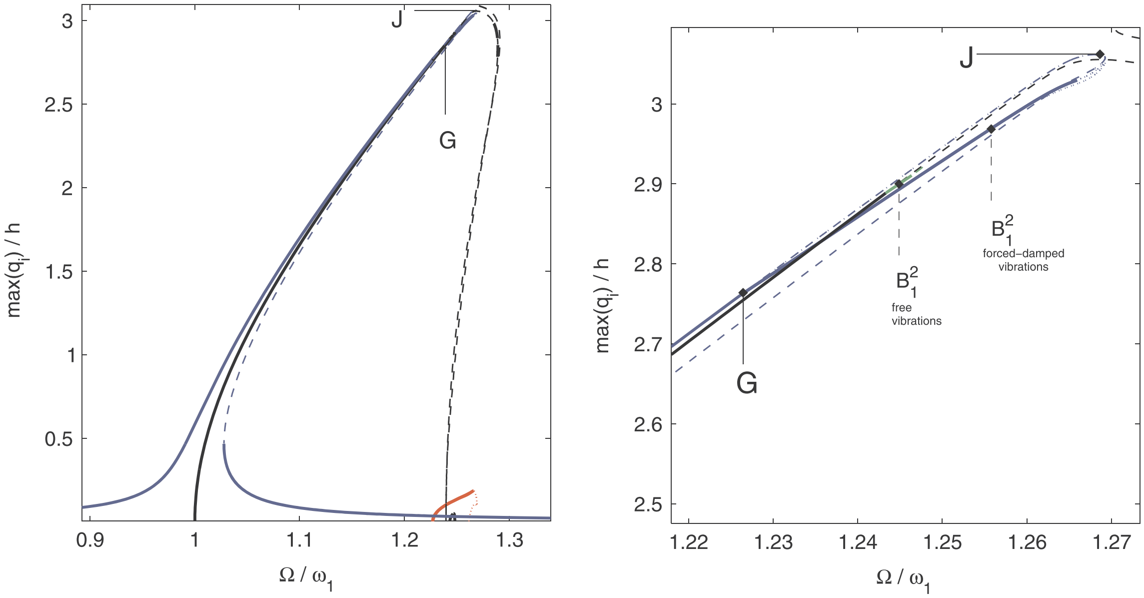

Fig. 5 Forced response for mode 1 with $f = 0.17$ N, $\chi = 0.001$. **G**: pitchfork bifurcation point leading to the coupled solution; **J** turning point. Mode 1: *blue*, mode 2: *red* (colour figure online)

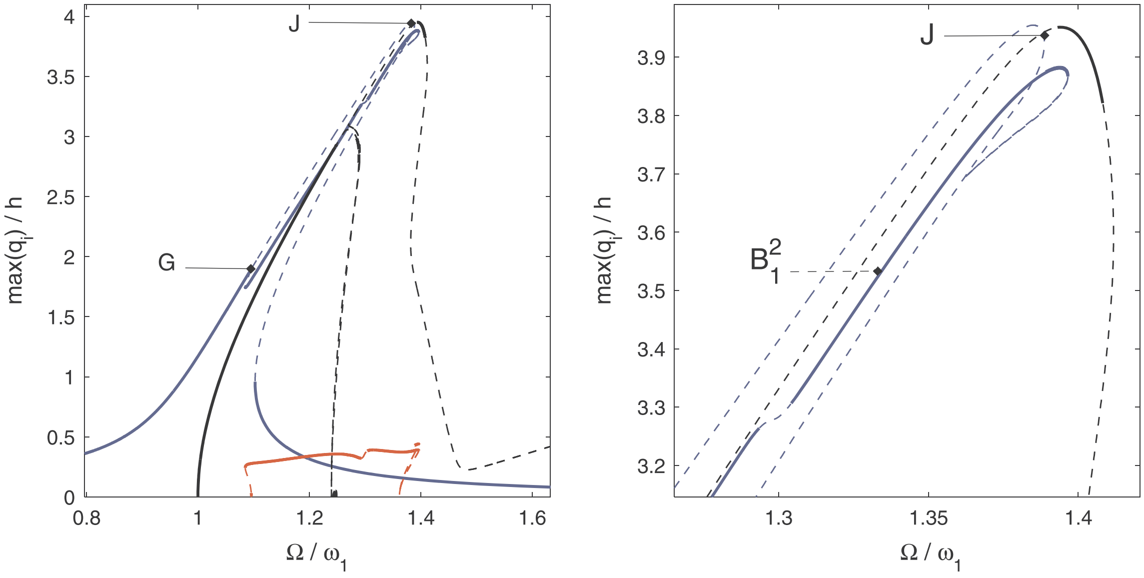

Fig. 6 Forced response for mode 1 with $f = 1.36$ N, $\chi = 0.005$. **G**: pitchfork bifurcation point leading to the coupled solution; **J** turning point. Mode 1: *blue*, mode 2: *red* (colour figure online)

in the latter case a dominant part of the dynamics, taking up a large portion of the phase space composed mainly of stable solutions. As a consequence, stable solutions are found on $\mathbf{B^2}$ at amplitudes larger then $3h$. In addition, there is no trace of the other bifurcations giving rise to $\mathbf{B^3}$, $\mathbf{B^4}$ in the Hamiltonian dynamics. This observation leads to the conclusion that the free and forced-damped analyses are complementary: on one hand, it is not straightforward to understand which bifurcations are key to the forced-damped vibrations when looking solely at the Hamiltonian dynamics; on the other hand, the forced-damped system is more easily interpreted by making use of the free vibrations diagrams. Hence, a complete scenario for the forced-damped vibrations cannot be obtained if a preliminary analysis of free vibrations is disregarded.

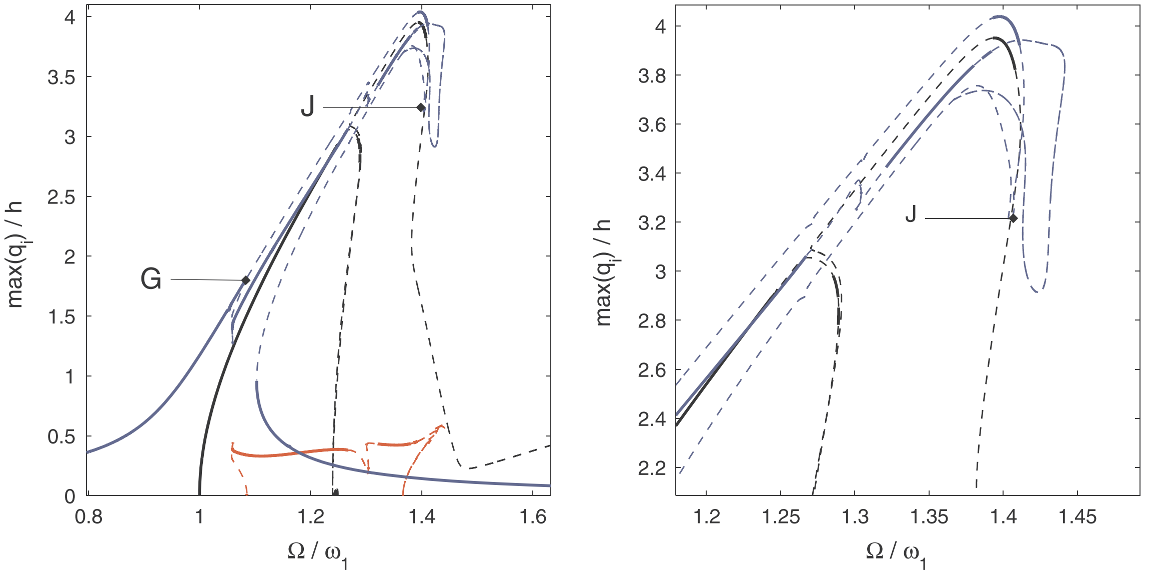

Fig. 7 Forced response for mode 1 with $f = 1.36$ N, $\chi = 0.001$. **G**: pitchfork bifurcation point leading to the coupled solution; **J** turning point. Mode 1: *blue*, mode 2: *red* (colour figure online)

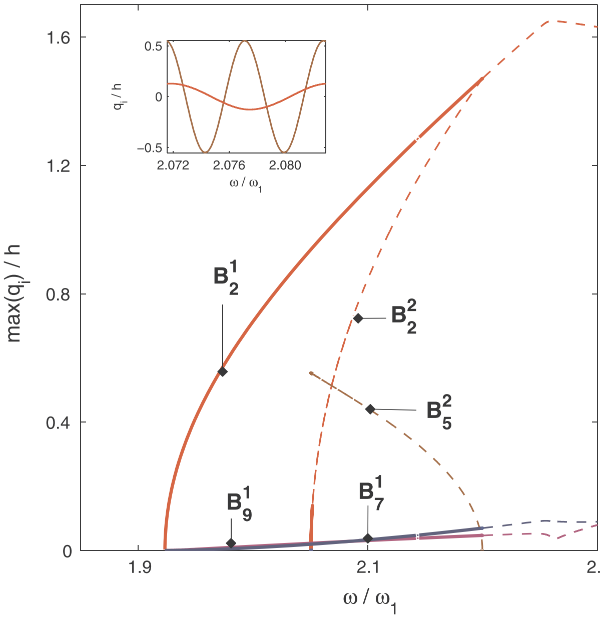

Fig. 8 Backbone for mode 2 obtained when $N_w = 16$. Modes 7 (*pink*) and 9 (*dark blue*) are activated by the nonresonant coupling within the SA family; mode 5 (*brown*) from the AA family is activated by 1:2 internal resonance (see *inset*) (colour figure online)

5.2 Mode 2

5.2.1 Free vibrations

Figure 8 shows the second NNM for $N_w = 16$. Convergence in this case is not shown for the sake of brevity; note, however, that the convergence study gave results comparable to those of mode 1. Thus, the same model including N_w=16 modes is kept for the remainder of the study. Once again, one can notice that no stable solutions are found beyond a certain amplitude limit, which is numerically found at $1.5h$ for mode 2. Actually, the principal branch loses its stability at the appearance of the coupled branch. As for mode 1, some modes are activated by nonresonant coupling, and these are the modes belonging to the same family as mode 2 (SA): the

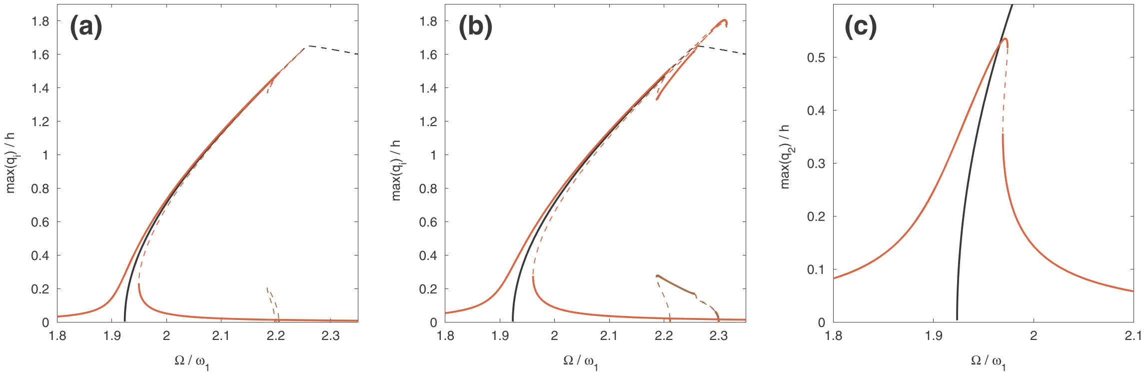

Fig. 9 Examples of forced-damped vibrations around the NNM for mode 2. **a** $f = 1.2$ N, $\chi = 0.001$; **b** $f = 2.0$ N, $\chi = 0.001$; **c** $f = 3.2$ N, $\chi = 0.01$. Mode 2: *red*, mode 5: *brown* (colour figure online)

Figure shows for clarity only modes 7 ($\mathbf{B_7^1}$, pink) and 9 ($\mathbf{B_9^1}$, dark blue). The most salient feature of the dynamics is the internal resonance between modes 2 and 5: a time integration was performed on $\mathbf{B^2}$ at $\omega/\omega_1 = 2.0515$, leading to the solution visible in the inset of Fig. 8 showing a 1:2 internal resonance. Interestingly, this branch is almost entirely unstable, except on the interval $2.051 \leq \omega/\omega_1 \leq 2.052$. As for mode 1, the Hamiltonian manifold will be modified when damping and forcing are introduced in the system.

5.2.2 Forced-damped vibrations

Examples of forced-damped solution are presented in Fig. 9. The cases (a) and (b) present the same damping coefficient, $\chi_i = 0.001$, and the forcing values are, respectively, $f = 1.2$ N, $f = 2.0$ N. Both forcing values are sufficient to reach amplitudes high enough to detect the internal resonance with mode 5. For case (a), the bifurcated branch remains almost completely unstable, as for the Hamiltonian dynamics. When the forcing is high enough, however, stable solutions appear along the interval $2.2 \leq \omega/\omega_1 \leq 2.3$. As a consequence, mode 2 possesses a secondary branch of stable periodic orbits of amplitude larger than $1.5h$, which was seen to be the limit of stability for the Hamiltonian manifold. As for mode 1, it is seen that the introduction of forcing and damping may lead to extended stable solutions on the coupled branches. Another case of interest is portrayed in Fig. 9c. Here, the maximum forcing is $f = 3.2$ N, and the damping coefficient is $\chi_i = 0.01$. In this case, the damping effects are so evident that the turning point is located away from the backbone. Distortion is a typical effect of damping: the forced response does not fit tightly along the backbone, and the turning point moves away from it.

In turn, the analysis of the forced responses for mode 1 and 2 revealed some interesting aspects of the global dynamics: (i) symmetry-breaking resonances are common and key to the dynamics of the dynamical response; (ii) stable solutions on the coupled branches may reach higher amplitudes than the Hamiltonian manifold, for particular combinations of damping and forcing factors.

6 Conclusions

The nonlinear dynamics of rectangular plates has been investigated. A robust numerical method has been developed to obtain accurate modal solutions for a very large number of modes. In this sense, a fast converging solution strategy has been derived for the calculation of the eigenmodes of a fully clamped plate (needed here to solve for the Airy stress function of a plate in a nonlinear regime). Formal symmetry properties and coupling rules have been illustrated to allow large computational and memory savings when calculating the coupling coefficients Γ's. Reference values for some of these coefficients, previously unavailable in the case of a rectangular geometry, have been presented.

Free and forced vibrations have then been taken under consideration for the first two modes. For the first time, the NNM branches of solution (conservative case) have been drawn out to very large amplitudes, showing the existence of internal resonance branches. An important feature, the nonexistence of periodic solutions beyond some vibration amplitude ($4h$ for mode 1, $1.8h$ for mode 2) has been found. A thorough comparison of the Hamiltonian dynamics with the forced-damped (observable) dynamics has been derived, in order to highlight: (i) the necessity of a preliminary analysis of the free vibrations, (ii) the main differences one can expect between the NNMs of the conservative systems and the observable periodic orbits of the forced-damped system. Simple features such as the shift of the turning point from the backbone for large values of the damping have been found. More interestingly, the importance of certain internal resonance tongues (those with the simpler ratio) has been underlined, whereas other are mostly undetected in the forced case. Finally, it has been found that some coupled branches may override the amplitude limit of existence of periodic solutions predicted by the backbone curve.

Even though the results presented here involve at most 16 modes, the numerical scheme developed is able to consider a few hundreds of them interacting together. The results shown here have been necessary to validate the model, which will be used to undertake further study of more involved dynamical problems (*i.e.* wave turbulence or sound synthesis of damped impacted plates for the reproduction of gong-like sounds).

Appendix A: Matrices for the clamped plate problem

To set up the eigenvalue problem, Eq. (25), one may proceed as follows. First, it is necessary to define the size of the square matrices $K_{ij},\ M_{ij}$. Suppose this size is $A^2 \times A^2$ (where A is an integer). Then, the indices $n_1,\ n_2$ for the expansion function (22) range from 0 to $A-1$. In this way, the total number of eigenvalues calculated will be A^2. Note that all the quantities that appear in the definition of the matrices are quadratic, so one needs really four indices to define the $_{ij}$ entry in each matrix. Suppose these indices are (m, n) and (p, q). Then,

$$K(i,j) = K(mn,pq) = \int_0^{L_x} X_m''(x)X_p''(x)\mathrm{d}x \int_0^{L_y} Y_n(y)Y_q(y)\mathrm{d}y + \int_0^{L_x} X_m(x)X_p(x)\mathrm{d}x \int_0^{L_y} Y_n''(y)Y_q''(y)\mathrm{d}y$$

$$+2\int_0^{L_x} X_m'(x)X_p'(x)\mathrm{d}x \int_0^{L_y} Y_n'(y)Y_q'(y)\mathrm{d}y,$$

$$M(i,j) = M(mn,pq) = \int_0^{L_x} X_m(x)X_p(x)\mathrm{d}x \int_0^{L_y} Y_n(y)Y_q(y)\mathrm{d}y.$$

The integrals are

$$\int_0^{L_x} X_m''(x)X_p''(x)\mathrm{d}x =$$

$$\begin{cases} 720/L_x^3; & \text{if } m=p=0 \\ (\pi^4 m^4 - 672(-1)^m - 768)/(2L_x^3); & \text{if } m=p\neq 0 \\ 0 & \text{if } m \text{ or } p=0 \text{ and } m\neq p \\ -24(7(-1)^m + 7(-1)^p + 8(-1)^m(-1)^p + 8)/L_x^3; & \text{otherwise,} \end{cases}$$

$$\int_0^{L_x} X_m(x)X_p(x)\mathrm{d}x =$$

$$\begin{cases} 10L_x/7; & \text{if } m=p=0 \\ 67L_x/70 - (-1)^m L_x/35 - 768L_x/(\pi^4 m^4) - 672(-1)^m L_x/(\pi^4 m^4); & \text{if } m=p\neq 0 \\ 3L_x((-1)^p+1)(\pi^4 p^4 - 1680))/(14\pi^4 p^4); & \text{if } m=0 \text{ and } p\neq 0 \\ 3L_x((-1)^m+1)(\pi^4 m^4 - 1680))/(14\pi^4 m^4); & \text{if } p=0 \text{ and } m\neq 0 \\ -(L_x(11760(-1)^m + 11760(-1)^p - 16\pi^4 m^4 + 13440(-1)^m(-1)^p + & \\ (-1)^m\pi^4 m^4 + (-1)^p\pi^4 m^4 - 16(-1)^m(-1)^p\pi^4 m^4 + 13440))/ & \\ (70\pi^4 m^4) - (L_x(13440m^4 + 11760(-1)^m m^4 + 11760(-1)^p m^4 & \\ +13440(-1)^m(-1)^p m^4))/(70\pi^4 m^4 p^4); & \text{otherwise,} \end{cases}$$

$$\int_0^{L_x} X'_m(x)X'_p(x)\mathrm{d}x =$$

$$\begin{cases} 120/(7L_x); & \text{if } m = p = 0 \\ (768\pi^2m^2 - 47040(-1)^m + 35\pi^4m^4 + 432(-1)^m\pi^2m^2 - 53760)/(70L_x\pi^2m^2); & \text{if } m = p \neq 0 \\ (60((-1)^p + 1)(\pi^2p^2 - 42))/(7L_x\pi^2p^2); & \text{if } m = 0 \text{ and } p \neq 0 \\ (60((-1)^m + 1)(\pi^2m^2 - 42))/(7L_x\pi^2m^2); & \text{if } p = 0 \text{ and } m \neq 0 \\ 192/(35L_x)(1 + (-1)^m(-1)^p) - 192/(m^2p^2L_x\pi^2)((p^2 + m^2)(1 + (-1)^m(-1)^p)) & \\ -168/(m^2p^2L_x\pi^2)((p^2 + m^2)((-1)^m + (-1)^p)) & \\ \quad +108/(35L_x)((-1)^m + (-1)^p); & \text{otherwise,} \end{cases}$$

and similarly for the integrals involving the functions Y.

References

1. Amabili, M.: Nonlinear vibrations of rectangular plates with different boundary conditions: theory and experiments. Comput. Struct. **82**, 2587–2605 (2004)
2. Amabili, M.: Nonlinear Vibrations and Stability of Shells and Plates. Cambridge University Press, Cambridge (2008)
3. Anlas, G., Elbeyli, O.: Nonlinear vibrations of a simply supported rectangular metallic plate subjected to transverse harmonic excitation in the presence of a one-to-one internal resonance. Nonlinear Dyn. **30**, 1–28 (2002)
4. Awrejcewicz, J., Krysko, V.A., Krysko, A.V.: Spatio-temporal chaos and solitons exhibited by von Kármán model. Int. J. Bifurc Chaos. **12**, 1465–1513 (2002)
5. Bilbao, S.: A family of conservative finite difference schemes for the dynamical von Kármán plate equations. Numer. Methods Partial Differ. Equ. **24**, 193–216 (2008)
6. Bilbao, S.: Numerical Sound Synthesis Finite Difference Schemes and Simulation in Musical Acoustics. Wiley, New York (2009)
7. Bilbao, S.: Percussion synthesis based on models of nonlinear shell vibration. IEEE Trans. Audio Speech Lang. Process. **18**, 872–880 (2010)
8. Blanc, F., Touzé, C., Mercier, J.-F., Ege, K., Bonnet Ben-Dhia, A.-S.: On the numerical computation of nonlinear normal modes for reduced-order modelling of conservative vibratory systems. Mech. Syst. Signal Process. **36**, 520–539 (2013)
9. Boudaoud, A., Cadot, O., Odille, B., Touzé, C.: Observation of wave turbulence in vibrating plates. Phys. Rev. Lett. **100**, 234504 (2008)
10. Boumediene, F., Duigou, L., Boutyour, E.H., Miloudi, A., Cadou, J.M.: Nonlinear forced vibration of damped plates by an asymptotic numerical method. Comput. Struct. **87**, 1508–1515 (2009)
11. Chaigne, A., Lambourg, C.: Time-domain simulation of damped impacted plates. I. Theory and experiments. J. Acoust. Soc. Am. **109**, 1422–1432 (2001)
12. Chaigne, A., Touzé, C., Thomas, O.: Nonlinear vibrations and chaos in gongs and cymbals. Acoust. Sci. Technol. **26**, 403–409 (2005)
13. Chang, S.I., Bajaj, A.K., Krousgrill, C.M.: Nonlinear oscillations of a fluttering plate. AIAA J. **4**, 1267–1275 (1966)
14. Chang, S.I., Bajaj, A.K., Krousgrill, C.M.: Non-linear vibrations and chaos in harmonically excited rectangular plates with one-to-one internal resonance. Nonlinear Dyn. **4**, 433–460 (1993)
15. Chen, W.Q., Ding, H.J.: On free vibration of a functionally graded piezoelectric rectangular plate. Acta Mechanica **153**, 207–216 (2002)
16. Chia, C.Y.: Nonlinear Analysis of Plates. Mc Graw Hill, New York (1980)
17. Chu, H.N., Herrmann, G.: Influence of large amplitudes on free flexural vibrations of rectangular elastic plates. J. Appl. Mech. **23** (1956)
18. Doaré, O., Michelin, S.: Piezoelectric coupling in energy-harvesting fluttering flexible plates: linear stability analysis and conversion efficiency. J. Fluids Struct. **27**, 1357–1375 (2011)
19. Doedel, E., Paffenroth, R.C., Champneys, A.R., Fairgrieve, T.F., Kuznetsov, Y.A., Oldeman, B.E., Sandstede, B., Wang, X.: Auto2000: Continuation and Bifurcation Software for Ordinary Differential Equations (with HomCont). Technical report, Concordia University, Canada (2002)
20. Düring, G., Josserand, C., Rica, S.: Weak turbulence for a vibrating plate: can one hear a Kolmogorov spectrum? Phys. Rev. Lett. **97**, 025503 (2006)
21. Fu, Y.M., Chia, C.Y.: Nonlinear bending and vibration of symmetrically laminated orthotropic elliptical plate with simply supported edge. Acta Mech. **74**, 155–170 (1988)
22. Gao, Y., Xu, B., Huh, H.: Electromagneto-thermo-mechanical behaviors of conductive circular plate subject to time-dependent magnetic fields. Acta Mech. **210**, 99–116 (2010)
23. Géradin, M., Rixen, D.: Mechanical Vibrations. Wiley, New York (1997)
24. Golinval, J.C., Stephan, C., Lubrina, P., Peeters, M., Kerschen, G.: Nonlinear normal modes of a full-scale aircraft. In: 29th International Modal Analysis Conference, Jacksonville, USA (2011)
25. Gordnier, R.E., Visbal, M.R.: Development of a three-dimensional viscous aeroelastic solver for nonlinear panel flutter. J. Fluids Struct. **16**, 497–527 (2002)
26. Hagedorn, P., DasGupta, A.: Vibrations and Waves in Continuous Mechanical Systems. Wiley, Chichester (2007)

27. Kerschen, G., Peeters, M., Golinval, J.C., Vakakis, A.F.: Nonlinear normal modes, part I: a useful framework for the structural dynamicist. Mech. Syst. Signal Process. **23**, 170–194 (2009)
28. Kung, G.C., Pao, Y.-H.: Nonlinear flexural vibrations of a clamped circular plate. J. Appl. Mech. **39**, 1050–1054 (1972)
29. Legge, K.A., Fletcher, N.H.: Nonlinearity, chaos, and the sound of shallow gongs. J. Acoust. Soc. Am. **86**, 2439–2443 (1989)
30. Leissa, A.: Vibration of Plates. Acoustical Society of America, New York (1993)
31. Li, W.L.: Vibration analysis of rectangular plates with general elastic support. J. Sound Vib. **273**, 619–635 (2003)
32. Luo, A.C.J, Huang, J.: Analytical solutions for asymmetric periodic motions to chaos in a hardening Duffing oscillator. Nonlinear Dyn. **72**, 417–438 (2013)
33. Meenen, J., Altenbach, H.: A consistent deduction of von Kármán-type plate theories from three-dimensional nonlinear continuum mechanics. Acta Mech. **147**, 1–17 (2001)
34. Mordant, N.: Are there waves in elastic wave turbulence? Phys. Rev. Lett. **100**, 234505 (2008)
35. Mordant, N.: Fourier analysis of wave turbulence in a thin elastic plate. Eur. Phys. J. B **76**, 537–545 (2010)
36. Moussa, M.O., Moumni, Z., Doaré, O., Touzé, C., Zaki, W.: Non-linear dynamic thermomechanical behaviour of shape memory alloys. J. Intell. Mater. Syst. Struct. **23**, 1593–1611 (2012)
37. Murphy, K.D., Virgin, L.N., Rizzi, S.A.: Characterizing the dynamic response of a thermally loaded, acoustically excited plate. J. Sound Vib. **196**, 635–658 (1996)
38. Nayfeh, A.H.: Nonlinear Oscillations. Wiley, New York (1995)
39. Nayfeh, A.H., Pai, P.F.: Linear and Nonlinear Structural Mechanics. Wiley, New York (2004)
40. Parlitz, U., Lauterborn, W.: Superstructure in the bifurcation set of the Duffing equation. Phys. Lett. A **107**, 351–355 (1985)
41. Peeters, M., Viguié, R., Sérandour, G., Kerschen, G., Golinval, J.-C.: Nonlinear normal modes, part II: toward a practical computation using numerical continuation techniques. Mech. Syst. Signal Process. **23**, 195–216 (2009)
42. Ribeiro, P.: Nonlinear vibrations of simply-supported plates by the p-version finite element method. Finite Elem. Anal. Des. **41**, 911–924 (2005)
43. Ribeiro, P., Petyt, M.: Geometrical non-linear, steady-state, forced, periodic vibration of plate, part I: model and convergence study. J. Sound Vib. **226**, 955–983 (1999)
44. Ribeiro, P., Petyt, M.: Geometrical non-linear, steady-state, forced, periodic vibration of plate, part II: stability study and analysis of multimodal response. J. Sound Vib. **226**, 985–1010 (1999)
45. Sathyamoorthy, M.: Nonlinear vibrations of plates: an update of recent research developments. Appl. Mech. Rev. **49**, S55–S62 (1996)
46. Thomas, O., Bilbao, S.: Geometrically nonlinear flexural vibrations of plates: In-plane boundary conditions and some symmetry properties. J. Sound Vib. **315**, 569–590 (2008)
47. Thomas, O., Touzé, C., Chaigne, A.: Non-linear vibrations of free-edge thin spherical shells: modal interaction rules and 1:1:2 internal resonance. Int. J. Solids Struct. **42**, 3339–3373 (2005)
48. Thomsen, J.J.: Vibrations and Stability. Springer, Berlin (2003)
49. Touzé, C., Bilbao, S., Cadot, O.: Transition scenario to turbulence in thin vibrating plates. J. Sound Vib. **331**, 412–433 (2011)
50. Touzé, C., Thomas, O., Amabili, M.: Transition to chaotic vibrations for harmonically forced perfect and imperfect circular plates. Int. J. Non-Linear Mech. **46**, 234–246 (2011)
51. Touzé, C., Thomas, O., Chaigne, A.: Hardening/softening behaviour in non-linear oscillations of structural systems using non-linear normal modes. J. Sound Vib. **273**, 77–101 (2004)
52. Touzé, C., Thomas, O., Huberdeau, A.: Asymptotic non-linear normal modes for large-amplitude vibrations of continuous structures. Comput. Struct. **82**, 2671–2682 (2004)
53. Vakakis, A.F.: Non-linear normal modes (nnms) and their applications in vibration theory: an overview. Mech. Syst. Signal Process. **11**, 3–22 (1997)
54. von Kármán, T.: Festigkeitsprobleme im Maschinenbau. Encyklopädie der Mathematischen Wissenschaften **4**, 311–385 (1910)
55. Yamaki, N.: Influence of large amplitudes on flexural vibrations of elastic plates. Zeitschrift für Angewandte Mathematik und Mechanik **41**, 501–510 (1961)
56. Yang, X.L., Sethna, P.R.: Local and global bifurcations in parametrically excited vibrations of nearly square plates. Int. J. Non-Linear Mech. **26**, 199–220 (1991)

CHAPTER 5

Plates in a Strongly Nonlinear Regime: Wave Turbulence

This chapter corresponds to a paper published on Physica D [28] and dealing with the aspects of Wave Turbulence in elastic plates. Section 2 gives the dynamical equations of von Kármán plates and the Finite Difference scheme to solve them, and thus it has been treated in great detail in Chapters 2 and 3. Section 4 is the core of the article, presenting the results and scaling properties of the turbulent plate. Bibliographic references as well as appendices are included in this chapter, and not at the end of the manuscript.

Physica D 280–281 (2014) 73–85

Contents lists available at ScienceDirect

Physica D

journal homepage: www.elsevier.com/locate/physd

Dynamics of the wave turbulence spectrum in vibrating plates: A numerical investigation using a conservative finite difference scheme

Michele Ducceschi [a], Olivier Cadot [a], Cyril Touzé [a,*], Stefan Bilbao [b]

[a] *Unité de Mécanique (UME), Ensta-ParisTech, 828, Boulevard des Maréchaux, 91762 Palaiseau Cedex, France*

[b] *Room 7306B, James Clerk Maxwell Building, King's Buildings, Mayfield Rd., Edinburgh EH9 3JZ, UK*

HIGHLIGHTS

- Non-stationary wave turbulence in a vibrating plate is numerically studied.
- Self-similar dynamics of the spectra are found with and without periodic external forcing.
- The self-similar solutions are in agreement with the kinetic equation.
- A realistic geometric imperfection is shown to have no effect on the global properties.

ARTICLE INFO

Article history:
Received 19 November 2013
Received in revised form
12 April 2014
Accepted 25 April 2014
Available online 10 May 2014
Communicated by M. Vergassola

Keywords:
Non-stationary wave turbulence
Elastic plate
Imperfections
Pointwise forcing
Finite difference
Conservative scheme

ABSTRACT

The dynamics of the local kinetic energy spectrum of an elastic plate vibrating in a wave turbulence (WT) regime is investigated with a finite difference, energy-conserving scheme. The numerical method allows the simulation of pointwise forcing together with realistic boundary conditions, a set-up which is close to experimental conditions. In the absence of damping, the framework of non-stationary wave turbulence is used. Numerical simulations show the presence of a front propagating to high frequencies, leaving a steady spectrum in its wake. Self-similar dynamics of the spectra are found with and without periodic external forcing. For the periodic forcing, the mean injected power is found to be constant, and the frequency at the cascade front evolves linearly with time resulting in a increase of the total energy. For the free turbulence, the energy contained in the cascade remains constant while the frequency front increases as $t^{1/3}$. These self-similar solutions are found to be in accordance with the kinetic equation derived from the von Kármán plate equations. The effect of the pointwise forcing is observable and introduces a steeper slope at low frequencies, as compared to the unforced case. The presence of a realistic geometric imperfection of the plate is found to have no effect on the global properties of the spectra dynamics. The steeper slope brought by the external forcing is shown to be still observable in a more realistic case where damping is added.

1. Introduction

Wave Turbulence (WT) describes a system of waves interacting nonlinearly away from thermodynamical equilibrium [1,2]. Although the system under study is composed of waves only, the term "turbulence" is used here in analogy with hydrodynamic turbulence, where the energy of the system is transferred through scales (referred to as a cascade) resulting in a large bandwidth energy spectrum. A particular property is that, for WT systems, the form of the spectrum can be derived analytically [3] and not just in terms of dimensional analysis as for the Kolmogorov 41 theory of hydrodynamics turbulence [4]. Using the assumption of weak nonlinearity, and an appropriate separation of timescales, a natural closure arises leading to an analytical expression for the equation for the second order moment (*e.g.* the kinetic energy spectrum). Solutions to this equation lead to two physically different scenarios: the first one represents the system at equilibrium, where the total energy of the system is equally spread among all the Fourier components of the system (known as the modes), and thus corresponding to a Rayleigh–Jeans type of spectrum. The second scenario is out-of-equilibrium and leads to the Kolmogorov–Zakharov spectrum that describes a flux of energy from the injection scale, where energy is input in the system, to the dissipation scale such as in hydrodynamics turbulence. In the latter scenario the modes re-

---

[*] Corresponding author. Tel.: +33 1 69 31 97 34; fax: +33 1 69 31 99 97.
E-mail address: cyril.touze@ensta-paristech.fr (C. Touzé).

http://dx.doi.org/10.1016/j.physd.2014.04.008
0167-2789/

ceive and give energy to adjacent modes, thus creating a cascade of energy through scales. WT formalism has been applied to many systems in a variety of contexts, ranging from quantum-mechanical to astrophysical systems, and includes many systems encountered in the ordinary world. An exhaustive list may be found in [1]; here some examples are recalled: capillary [5,6] and surface gravity waves [7–9], Alfvén waves [10,11], and Kelvin waves [12,13].

Flexural waves produced by large amplitude vibrations of elastic plates have been studied within the framework of the wave turbulence theory [14] applied to the von Kármán equation [15,16] for the transverse displacement w. The analytical Kolmogorov–Zakharov spectrum is then given by

$$P_v(f) = \frac{Ch}{(1-\nu^2)^{2/3}} \varepsilon_c^{1/3} \log^{1/3}\left(\frac{f_c^\star}{f}\right); \tag{1}$$

where ε_c is the constant flux of energy transferred through scales, P_v refers to the power spectrum of the transverse velocity $v = \dot{w}$, h is the thickness of the plate, ν Poisson's ratio of the material, and C a constant. Because the theory is fully inertial, $f_c^\star$ is the frequency at which energy is removed from the system. In experiments, this is ensured by the damping of the plate. At first order the spectrum is flat, but with a log-correction in the inertial range of frequencies. The WT theoretical result has been compared to experiments [17,18], showing discrepancies regarding the shape and scaling of the spectrum with the energy flux. Thus, recent work has focused on the investigation of the possible causes for such discrepancies. Experimentally, the wave-structure and dispersion relation was checked in [18], leading to the conclusion that the nonlinear vibrations of a plate are indeed due to a set of waves following the theoretical (linear) dispersion relation. The correct separation of timescales, necessary assumption for the WT theory, was verified in [19]. A first discrepancy effect was observed in [20], showing that the local forcing of the shaker is responsible for a steeper slope in the supposed inertial range of the energy spectra. More recently, damping has also been shown to be the cause for a steeper slope of the spectrum, indicating that the inertial range might not exist for thin plates used in experiments, rendering then meaningless any comparison with the WT theory [21]. From the numerical standpoint, it is worth mentioning that all the numerical methods used so far are spectral schemes [14,22,21,23–25]. Hence the forcing is in the Fourier space, a feature that is different from a pointwise excitation used in experimental conditions. All available numerical results recover the KZ spectrum of Eq. (1) when the damping is localized at high frequency only. However, when realistic damping is added, see *e.g.* [21,23], the same conclusions as for the experiment are met.

Other sources of discrepancies have not been addressed yet, such as the finite size effects or the possibility of three wave interactions (quadratic nonlinearities) in real plates. Because of the $w \rightarrow -w$ symmetry of the von Kármán equation, these nonlinearities are not taken into account in [14]. Indeed, geometrical imperfections are unavoidable in real plates, and they are known to break this symmetry and to produce quadratic nonlinearities [26,27]. In particular, it has been shown in [28,29] that imperfections play an important role in the transition scenario to turbulence and favor instabilities and the appearance of quasiperiodic vibrations.

The numerical method used in this work relies on a finite difference, time domain, energy-conserving scheme [30,29]. The main advantages are that: (i) the time-stepping integration method conserves energy up to machine accuracy, so that essential properties of the underlying continuous Hamiltonian systems are preserved by the discretization [31]; (ii) the external forcing is pointwise in space just as in the real experiments; (iii) realistic boundary conditions can be implemented instead of using periodic boundary conditions as considered by previous numerical investigations using spectral methods [14,22,25].

The aim of this article is to investigate numerically wave turbulence produced by the von Kármán plate equations. With a numerical scheme close to experimental conditions, unavoidable effects in real experiments such as pointwise forcing and geometric imperfections can be accounted for. In order to properly distinguish the different effects, most of the presented results are obtained in the absence of damping, where the framework of non-stationary wave turbulence should be used [32,33]. The theory predicts self-similar dynamics of the spectra with a front propagating to higher frequencies. Such propagation has been observed for surface gravity waves in experiments [34]. On the contrary, capillary turbulence [35,36] exhibits a decay that begins from the high frequency end of the spectral range. The discrepancy with the self-similar theory of wave turbulence is ascribed to the presence of finite damping at all frequencies of the wave system [35,37].

The article is organized as follows: the governing equations together with the numerical approach are described in Section 2. Section 3 presents the data analysis tools used to study the spectral dynamics. The main results are given in Section 4. Periodically forced turbulence for a perfect plate is first considered. A self-similar propagation of a steep front towards the high frequencies, leaving in its wake a steady spectrum, is observed. The frequency of the front is found to evolve linearly with time. The presence of realistic geometric imperfections is then taken into account and shown to have no influence on the spectral dynamics. In Section 4.2, the case of a free, undamped turbulence is exhibited. In that case, self-similar dynamics of the spectra are also observed, but now the front evolves with time as $t^{1/3}$. Self-similar solutions derived from the kinetic equation are found to display the same dependences, thus validating the numerical results that give in addition the shape of the self-similar function. The pointwise forcing is found to influence the shape of the universal spectrum left in the wake of the front, with a steeper slope for the forced case. Finally, the effect of the pointwise forcing, underlined in the undamped cases, is confirmed in Section 4.3, where a decaying turbulence with a simple frequency-independent damping law is addressed. Discussion and concluding remarks appear in Section 5.

2. Dynamical equations

2.1. Continuous time and space equations

The system under study is a rectangular elastic plate of thickness h, dimensions L_x, L_y, volume density ρ, Poisson's ratio ν and Young's modulus E. Its flexural rigidity is defined as $D = \frac{Eh^3}{12(1-\nu^2)}$. The dynamics of weakly nonlinear waves for the transverse displacement $w(\mathbf{x}, t)$ can be described by the von Kármán equations [15,16]. The general case of an imperfect plate is here considered. If $w_0(\mathbf{x})$ denotes the initial (static) imperfection, then the equations of motion read [26,38,27]

$$D\Delta\Delta w + \rho h \ddot{w} = L(w + w_0, F) + \mathcal{F}(\mathbf{x}, t) - R(\dot{w}, t), \tag{2a}$$

$$\Delta\Delta F = -\frac{Eh}{2} L(w + 2w_0, w), \tag{2b}$$

where Δ is the Laplacian operator, $\Delta a(\mathbf{x}) = a_{,xx} + a_{,yy}$, and $L(\cdot, \cdot)$ is the bilinear symmetric von Kármán operator, $L(a(\mathbf{x}), b(\mathbf{x})) = a_{,xx}\, b_{,yy} + a_{,yy}\, b_{,xx} - 2a_{,xy}\, b_{,xy}$. $F(\mathbf{x}, t)$ is an auxiliary function called the Airy stress function which encapsulates the behavior of the plate in the in-plane direction, $R(\mathbf{x}, t)$ is a loss factor of some kind which will be specified shortly and $\mathcal{F}(\mathbf{x}, t)$ is the external excitation load. In this work, the material parameters are chosen to correspond to a steel plate; thus $E = 2 \times 10^{11}$ Pa, $\rho = 7860$ kg/m^3, $\nu = 0.3$. The other geometrical and physical parameters will be reported case by case.

The dynamics of the plate is not complete until the boundary conditions are not selected. Physical boundary conditions can be derived by conducting an energy analysis based on the Lagrangian of the system [16,39,40]. For this work, the particular case of a transversely simply supported plate with movable in-plane edges is considered. In turn, the following conditions hold along the boundary ∂S

$$w = w_{,nn} = 0 \quad \forall \mathbf{x} \in \partial S, \tag{3a}$$

$$F = F_{,n} = 0 \quad \forall \mathbf{x} \in \partial S, \tag{3b}$$

where n is the direction normal to the boundary. This is an important difference with respect to previously presented numerical simulations, where periodic boundary conditions were employed.

The term $R(\mathbf{x}, t)$ represents losses. An artificial damping law may be used,

$$R(\dot{w}, t) = 2\sigma_0 \dot{w}, \tag{4}$$

that dissipates energy at equal rates at all scales. In the context of time-domain simulations of damped plates, the problem of an accurate representation of the damping law with an ad-hoc time operator is complex and has led numerous authors to various laws, the implementation of which still remains a numerical challenge; see *e.g.* [41]. Here the simplest time-domain operator has been chosen allowing us to explore numerically its effect on the dynamics of the cascade. The reader should however keep in mind that it is ad-hoc and does not correspond to a real case.

The forcing is pointwise and of the form:

$$\mathcal{F}(\mathbf{x}, t) = \delta(\mathbf{x} - \mathbf{x}_{\mathcal{F}}) A(t) \sin(2\pi f_p t). \tag{5}$$

The injection point has been chosen at $\mathbf{x}_{\mathcal{F}} = (0.42L_x, 0.57L_y)$ for all the simulations. The forcing frequency f_p is selected to be close to the fourth eigenfrequency of the system, in order to activate the cascade more easily [29]. $A(t)$ is chosen to be:

$$A(t) = \begin{cases} A_0\, t/t_0 & \text{for } 0 \le t \le t_0; \\ A_0 & \text{for } t_0 \le t \le t_1; \\ 0 & \text{for } t \ge t_1. \end{cases} \tag{6}$$

In the above definition, t_0 corresponds to the ramp time: the forcing ramps linearly from zero up to A_0 in t_0 seconds. Then, the forcing remains constant at A_0 for $t_1 - t_0$ seconds, where t_1 corresponds to the total length of the simulation in the case of periodic forcing.

The injected power is defined in this work as

$$\varepsilon(t) = \mathcal{F}(\mathbf{x}, t) \cdot \dot{w}(\mathbf{x}_p, t)/\rho S. \tag{7}$$

After division by the factor ρS, where $S = L_x L_y$ is the area of the plate, the injected power has the dimension of a velocity cubed.

2.2. Finite difference time domain scheme

In this section the numerical solution to system (2) together with boundary conditions (3) is presented. Although numerical simulations of von Kármán plates in the context of WT have been successfully developed in previous studies [14,22,25,23,24], here a time domain simulation in physical space is presented. Time and space are discretized so that the continuous variables (x, y, t) are approximated by their discrete counterparts $(l\delta x, m\delta y, n\delta t)$, where (l, m, n) are integer indices and $(\delta x, \delta y, \delta t)$ are the steps. Boundedness of the domain implies that $(l, m) \in [0, N_x] \times [0, N_y]$ so that the grid size is given by $(N_x + 1) \times (N_y + 1)$. The continuous variables $w(\mathbf{x}, t), F(\mathbf{x}, t)$ are then approximated by $w^n_{l,m}, F^n_{l,m}$ at the discrete time n for the grid point (l, m). Time shifting operators are introduced as

$$e_{t+} w^n_{l,m} = w^{n+1}_{l,m}, \qquad e_{t-} w^n_{l,m} = w^{n-1}_{l,m}. \tag{8}$$

Time derivatives can then be approximated by

$$\delta_{t\cdot} = \frac{1}{2h_t}(e_{t+} - e_{t-}), \qquad \delta_{t+} = \frac{1}{h_t}(e_{t+} - 1),$$
$$\delta_{t-} = \frac{1}{h_t}(1 - e_{t+}), \qquad \delta_{tt} = \delta_{t+}\delta_{t-}. \tag{9}$$

Time averaging operators are introduced as

$$\mu_{t+} = \frac{1}{2}(e_{t+} + 1), \qquad \mu_{t-} = \frac{1}{2}(1 + e_{t-}),$$
$$\mu_{t\cdot} = \frac{1}{2}(e_{t+} + e_{t-}), \qquad \mu_{tt} = \mu_{t+}\mu_{t-}. \tag{10}$$

Similar definitions hold for the space operators. Hence, the Laplacian Δ and the double Laplacian $\Delta\Delta$ are given by

$$\delta_{\Delta} = \delta_{xx} + \delta_{yy}, \qquad \delta_{\Delta\Delta} = \delta_{\Delta}\delta_{\Delta}. \tag{11}$$

The von Kármán operator at interior points $L(w, F)$ can then be discretized as

$$l(w, F) = \delta_{xx} w \delta_{yy} F + \delta_{yy} w \delta_{xx} F$$
$$\qquad - 2\mu_{x-}\mu_{y-}(\delta_{x+y+} w \delta_{x+y+} F). \tag{12}$$

Thus the discrete counterpart of (2) is

$$D\delta_{\Delta\Delta} w + \rho h \delta_{tt} w = l(w + w_0, \mu_{t\cdot} F) + P^n_{l,m} - R^n_{l,m}; \tag{13a}$$

$$\mu_{t-} D\delta_{\Delta\Delta} F = -\frac{Eh}{2} l(e_{t-}(w + 2w_0), w). \tag{13b}$$

The damping terms are

$$r_0(l, m, n) = 2\sigma_0 \delta_{t\cdot} w^n_{l,m}; \qquad r_1(l, m, n) = -2\sigma_1 \delta_{\Delta} w^n_{l,m}. \tag{14}$$

When $\sigma_0 = 0$, the scheme is energy conserving, where the discrete energy is positive definite and yields a stability condition, as proved in [30,42]. Implementation of boundary conditions is explained thoroughly in [42].

3. Data analysis

The work is focused on the turbulent response at one point of the plate chosen as $(0.3L_x, 0.2L_y)$. The kinetic energy spectrum is given by the velocity power spectrum which is calculated starting from a velocity discrete-time series. For the remainder of the paper, the symbol v_n will identify the discrete velocity at the output point, at the time $t = n\delta t$. Spectra analyses are performed on time windows of duration τ. The discrete-time velocity power spectrum is then defined as:

$$P_v(f) = \frac{(\delta t)^2}{\tau} \left| \sum_{n=1}^{N} v_n e^{-i2\pi f n} \right|^2 \tag{15}$$

where $N = \tau/\delta t$ is the total number of samples within the time window. For the typical case of a thickness $h = 1$ mm and surface 0.4×0.6 m^2, the sampling frequency is chosen as $1/\delta t = 400$ kHz and a time window of $\tau = 0.05$ s is selected for the analysis of the spectra. In order to obtain a better convergence of the shape of the spectra, a mean is taken over $M = 3$ consecutive spectra; in other words, the symbol $\langle P_v(f) \rangle$ will identify the mean take over 3 spectra covering a total time window $T = M\tau$. When the thickness of the plate changes, time window and sampling frequency change accordingly. So, for instance, for a thickness $h = 0.1$ mm, the time window is multiplied by a factor of 10, $\tau = 0.5$ s and the sampling frequency is divided by a factor of 10, $1/\delta t = 40$ kHz. The number M remains instead fixed. In the following, the brackets $\langle \cdots \rangle$ will denote an averaging on T which will generally depends on the time.

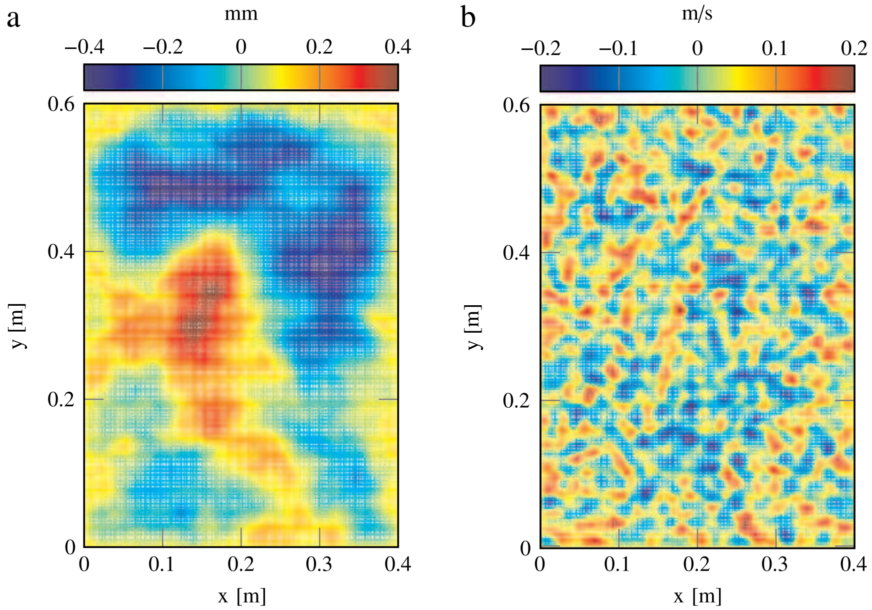

Fig. 1. (a) Displacement field in the turbulent regime for an undamped, perfectly flat plate of thickness $h = 0.1$ mm and dimensions $L_x \times L_y = 0.4 \times 0.6$ m^2. (b) Corresponding velocity field.

Table 1
Case studies.

	A_0 (N)	h (mm)	f_p (Hz)	S	Grid points
Case 1	10	1	75	0.4×0.6	102×153
Case 2	20	1	75	0.4×0.6	102×153
Case 3	30	1	75	0.4×0.6	102×153
Case 4	45	1	75	0.4×0.6	102×153
Case 5	70	1	75	0.4×0.6	102×153
Case 6	2.5	0.5	37.5	0.4×0.6	102×153
Case 7	5	0.5	37.5	0.4×0.6	102×153
Case 8	0.75	0.4	30	0.4×0.6	102×153
Case 9	1.5	0.4	30	0.4×0.6	102×153
Case 10	0.1	0.2	15	0.4×0.6	102×153
Case 11	0.02	0.1	7.5	0.4×0.6	144×216
Case 12	0.005	0.1	7.5	0.4×0.6	102×153
Case 13	1	0.5	20	1×2	114×227
Case 14	1.75	0.5	20	1×2	114×227
Case 15	2.5	0.5	20	1×2	114×227

The analysis for the injected power follows the same averaging rules. The injected power discrete time series is denoted by ε_n, from which the mean $\langle\varepsilon\rangle$ and the variance $\langle\varepsilon^2\rangle$ are calculated. The temporal average $\bar{\varepsilon}$ is defined as the mean over the total data.

A characteristic frequency f_c for the velocity power spectrum is here introduced as

$$f_c = \frac{\int \langle P_v(f)\rangle \, f \, df}{\int \langle P_v(f)\rangle \, df}, \tag{16}$$

with $P_v(f_c)$ also defining a characteristic spectral amplitude. Note that f_c should not be confused with the theoretical cut-off frequency $f_c^\star$ defined in Eq. (1). The characteristic frequency f_c will be used in the next section in order to quantify the self-similar dynamics of the spectra in the non-stationary cases.

4. Numerical results

This section presents the results obtained for the following cases:

(i) $R(\dot{w}, t) = 0$, $w_0(\mathbf{x}) = 0$ (perfectly flat, undamped plate);
(ii) $R(\dot{w}, t) = 0$, $w_0(\mathbf{x}) \neq 0$ (imperfect, undamped plate);
(iii) $R(\dot{w}, t) \neq 0$, $w_0(\mathbf{x}) = 0$ (perfectly flat, damped plate).

Simulations are also conducted by varying the dimensions S and the thickness h of the plate for different forcing amplitudes A_0 and frequencies f_p. The first part is devoted to periodically forced turbulence and the second to free turbulence (or decaying, when damping is added) after the forcing is stopped.

4.1. Periodically forced undamped turbulence

4.1.1. Perfect, undamped plates

Typical numerically obtained displacement and velocity fields are shown in Fig. 1 for illustration. The displacement field presents low frequency patterns; taking the velocity filters out these low frequencies resulting in a much more homogeneous field, meaning that velocity measurements at one point are relevant for the turbulent property of the whole plate as already mentioned in experiments having similar forcing schemes [17–19]. The anisotropy effects due to the local forcing have been evidenced and characterized experimentally by Miquel and Mordant [19].

A case study is first examined to serve as a master example of the type of analysis that has been conducted on all the simulations. It corresponds to case 1 in Table 1 considering a plate of thickness $h = 1$ mm, forced at $f_p = 75$ Hz with a forcing of amplitude $A_0 = 10$ N and a ramp time $t_0 = 0.5$ s (see Eq. (6), where t_1 is the whole duration of the simulation). The surface is $L_x \times L_y = 0.4 \times 0.6$ m^2 and the grid size is 102×153 points, corresponding to a sampling rate of 400 kHz for the time integration.

Fig. 2(a) shows the spectrogram (evolution of the frequency spectra with respect to time) of the velocity at the measurement point. It reveals the activated frequencies of the turbulent cascade as a function of time. The energy keeps flowing into the system, creating a never ending cascade where modes of higher frequency receive energy from the adjacent lower frequency modes. Fig. 2(b) shows the velocity power spectra at different stages of the dynamics. It is evident that for these simulations no stationary state exists: the spectra tend to occupy larger portions of the available frequency range as time goes by. It should be pointed out that the cascade front will develop up to half the sampling frequency of the computation (200 kHz in this case): when the cascade hits this limit, an artificial boundary reflects the energy back into the box, towards smaller frequencies. This is a peculiar,

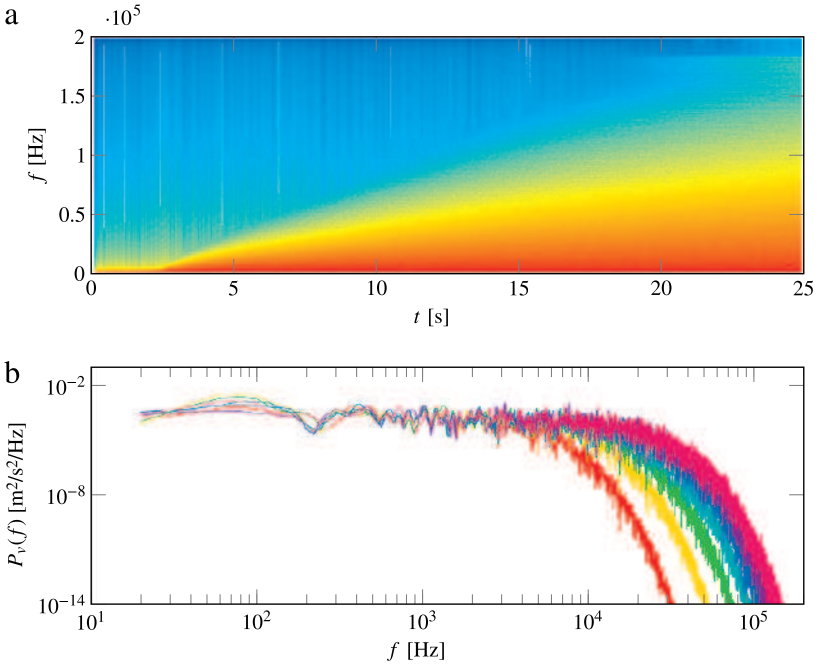

Fig. 2. (a) Spectrogram of the velocity for the perfect undamped plate of thickness $h = 1$ mm, forcing from 0 to 10 N in 0.5 s (case 1 from Table 1), and then kept constant. (b) Corresponding velocity power spectra computed every 2.5 s from 5 to 25 s.

unwanted numerical phenomenon that is not taken into account in the analysis. The simulation is stopped before the boundary reflection happens; in this way, the cascade can be regarded as developing within an infinite frequency domain. Fig. 3(a) shows that the evolution of the characteristic frequency $f_c(t)$ is linear, $f_c = c_f \cdot t$. The cascade front in Fig. 2 then develops to larger frequencies with a constant cascade velocity c_f. The spectral amplitude at the characteristic frequency $\langle P_v(f_c)\rangle$ in Fig. 3(b) is seen to be fairly constant over time. The power velocity spectra, rescaled using both the characteristic frequency f_c and amplitude $P_v(f_c)$, are displayed in Fig. 4. They all satisfactorily superimpose, indicating that the dynamics of the energy spectrum is self-similar. This allows us to write for the spectra

$$\langle P_v(f)\rangle = \langle P_v(f_c)\rangle\, \phi_P\left(\frac{f}{f_c}\right), \tag{17}$$

where their shapes are given by the unique function $\phi_P\,(f/f_c)$ (the subscript $_P$ stands for periodically forced turbulence).

The injected power during the self-similar dynamics is shown in Fig. 5(a): the fluctuations increase with time while the average stays constant. More precisely, Fig. 5(b) shows that $\langle\varepsilon^2\rangle = Dt$, and $\langle\varepsilon\rangle = \bar{\varepsilon}$. Hence, the self-similar dynamics originate with the injection of a stationary energy flux characterized by $\bar{\varepsilon}$. Meanwhile, the fluctuations of the injection flux grow following a diffusion-type behavior characterized by the coefficient D.

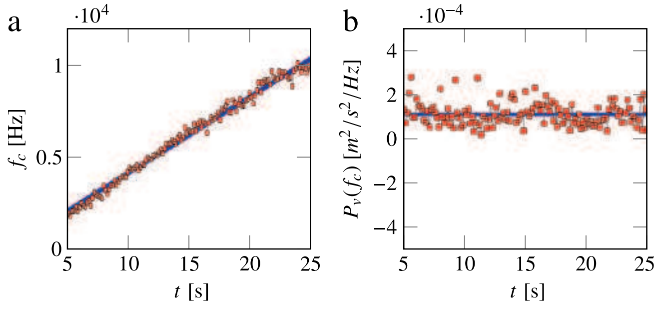

Fig. 3. (a) Time evolution of the characteristic frequency f_c, (b) corresponding spectral amplitude of the spectra shown in Fig. 2(b) (case 1 in Table 1). The characteristic frequency evolves as $f_c = c_f t$ with $c_f = 412.05$ s^{-2} and the mean amplitude is $\langle P_v(f_c)\rangle = 1.11\cdot 10^{-4}$ m^2/s^2/Hz.

The analysis described above is now applied to 15 different cases, summarized in Table 1. For all cases, the self-similar dynamics display a constant injected power $\bar{\varepsilon}$, a linear growth of the variance of injected power $\langle\varepsilon^2\rangle$, a linear increase of f_c over time and constant $\langle P_v(f_c)\rangle$ has been observed. It is worth noting that the forcing values cover about four decades; this results in a large range for the mean injected power $\bar{\varepsilon}$. The thickness values cover one decade also. For each one of the cases, the cascade velocity c_f, the spectral amplitude at the characteristic frequency $\langle P_v(f_c)\rangle$, the diffusion coefficient D are calculated. These quantities are plotted in Fig. 6 as functions of combinations of $\bar{\varepsilon}$ and h having the same dimensions. It can be seen that for all cases a linear relationship is found, confirming the consistency of the dimensional argument. The constants of proportionalities are found from best linear fits:

$$\langle P_v(f_c)\rangle = 2.51 h(\bar{\varepsilon})^{1/3}, \tag{18a}$$

$$c_f = 0.20\frac{(\bar{\varepsilon})^{2/3}}{h^2}, \tag{18b}$$

$$D = 2.07\cdot 10^4\,\frac{(\bar{\varepsilon})^{7/3}}{h}. \tag{18c}$$

In conclusion, the main result arising from the numerical simulations of the periodically forced undamped plate is a self-similar evolution of the power spectra. It is characterized by the progression towards higher frequencies of a steep cascade front, which leaves a steady self-similar spectrum in its wake. The self-similar progression is found to be linear with time and has been characterized by nondimensional numbers. The spectral amplitude at f_c is found to have a dependence on $(\bar{\varepsilon})^{1/3}$ (see Fig. 6) and the self-similar spectrum can be expressed as

$$P_v(f) = 0.42 h(\bar{\varepsilon})^{\frac{1}{3}}\,\Phi_P\left(\frac{f}{f_c}\right), \tag{19}$$

where $\bar{\varepsilon}$ is the mean injected power. In the absence of damping, the mean injected power can be confounded with the energy flux

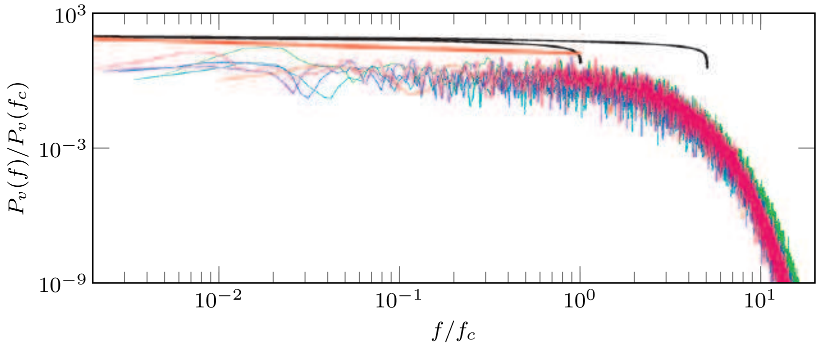

Fig. 4. Spectra of Fig. 2(b) but normalized using the characteristic frequency f_c and amplitude $P_v(f_c)$. Continuous red line shows a power law $f^{-\frac{1}{4}}$. Continuous black lines show the log correction $\log^{1/3}\left(\frac{f_c^\star}{f}\right)$ of the KZ spectrum, see Eq. (1), with $f_c^\star = f_c$ and $f_c^\star = 5f_c$. (For interpretation of the references to color in this figure legend, the reader is referred to the web version of this article.)

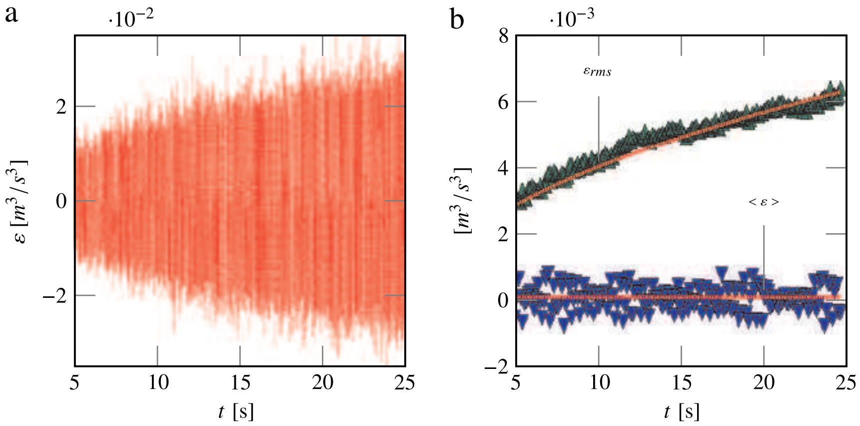

Fig. 5. Time evolution of the injected power for the perfect undamped plate (case 1 in Table 1). (a) Time series, (b) $\langle\varepsilon\rangle$ and $\varepsilon_{rms} = \sqrt{\langle\varepsilon^2\rangle}$. Continuous lines are best fits that give $\bar{\varepsilon} = 9.65 \cdot 10^{-5}$ m^3/s^3, and $D = 1.6 \cdot 10^{-6}$ m^6/s^7 (see the text).

transfer ε_c through scales. The progression of the cascade front towards higher frequencies is given by $f_c(t) = c_f t \propto \frac{\bar{\varepsilon}^{\frac{2}{3}}}{h^2} t$ (from Eq. (18b)). The function Φ_P displayed in Fig. 4 increases as frequencies decrease towards the forcing frequency f_p. A best-fit approximation of the slope of Φ_P indicates that it follows a power-law for low frequencies with a small exponent close to $-1/4$; see Fig. 4.

The self-similar solutions for the kinetic equation derived from the von Kármán plate equations are given in Appendix A. Considering a self-similar solution for the wave spectrum $n(k, t)$ of the form:

$$n(k,t) = t^{-q} f_1(kt^{-p}) = t^{-q} f_1(\xi), \tag{20}$$

one finds for the power frequency spectrum $P_v(\omega, t)$:

$$P_v(\omega,t) \sim f_1\left(\sqrt{\frac{\omega}{t}}\right) = g_1\left(\frac{\omega}{t}\right). \tag{21}$$

This relationship clearly evidenced that the frequency of the front must evolve linearly with time, which is retrieved by the numerical simulation. The function g_1 can be identified with the function Φ_P found numerically.

Let us now compare the self-similar spectrum with the KZ solution. As the theoretical cut-off frequency $f_c^\star$ cannot be related to a given physical quantity in our numerical framework, the KZ spectrum is built from Eq. (1) by selecting $f_c^\star = f_c$ and $f_c^\star = 5f_c$, and reported in Fig. 4. As one is interested in the power-law behavior in the low-frequency range, one can observe that selecting $f_c^\star = f_c$ or $f_c^\star = 5f_c$ has little influence on the slope comparison. It appears that even though the log-correction of the KZ spectrum cannot be discarded, the slope of the self-similar numerical solution appears to be a bit steeper.

Table 2
Case studies for the imperfect plate.

	A_0 (N)	h (mm)	f_p (Hz)	Z (mm)
Case 1	7	0.5	8.5	1
Case 2	3	0.5	8.5	1
Case 3	0.02	0.1	10.5	0.5
Case 4	0.01	0.1	10.5	0.5
Case 5	0.03	0.1	13	1
Case 6	0.02	0.1	8.5	0.1
Case 7	0.02	0.1	13	1
Case 8	0.01	0.1	8.5	0.1
Case 9	100	1	127	10
Case 10	70	1	127	10
Case 11	90	1	103	5
Case 12	60	1	103	5

The injected power fluctuation is found to increase as a diffusive law during the self-similar dynamics. A comprehensive interpretation of this behavior may be given by the model of injected power proposed in [43,44] for this system. In this work, the velocity $\dot{w}(\mathbf{x}_{\mathcal{F}}, t)$ at the forcing point is assumed to result from a turbulent feedback v described by the velocity spectrum, and a linear response of the deterministic forcing $\mathcal{F}(\mathbf{x}, t)$, say:

$$\dot{w}(\mathbf{x}_{\mathcal{F}}, t) = v + \mathcal{L}\mathcal{F}, \tag{22}$$

with $\mathcal{L}$ a linear operator. The feedback turbulent velocity is assumed to be statistically independent of the forcing. Thus, using Eq. (22) and the periodic forcing in Eq. (5) with $A(t) = A_0$, the mean

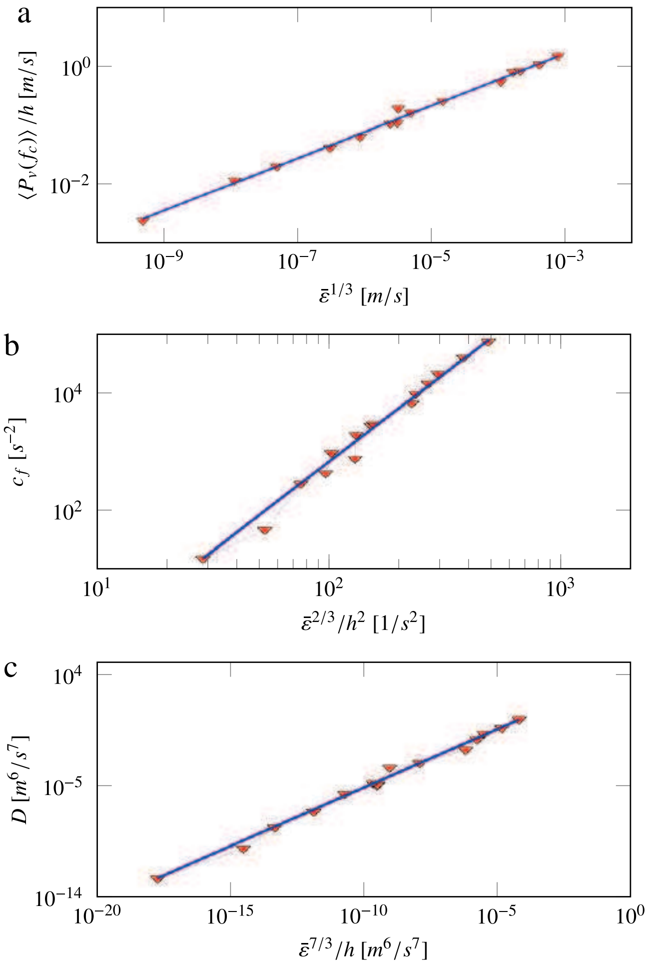

Fig. 6. Results of simulations for the perfect, undamped plate with a periodic forcing, for all the 15 cases reported in Table 1. (a) Spectral amplitude $\langle P_v(f_c)\rangle/h$, (b) cascade velocity c_f and (c) diffusion coefficient D.

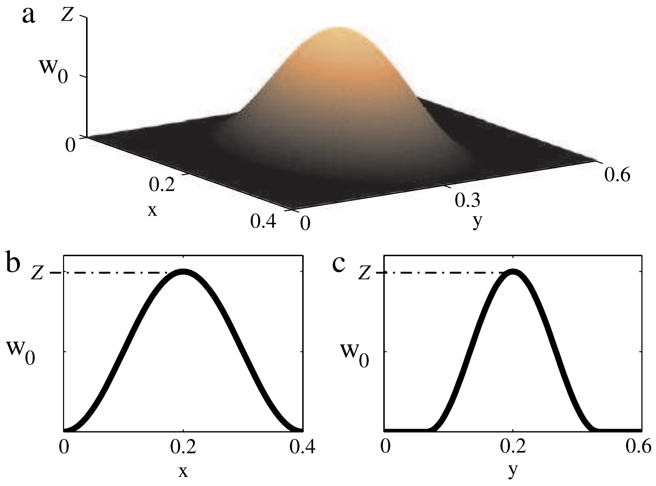

Fig. 7. Plate of dimensions 0.4×0.6 m^2 with imperfection in the form of a raised cosine. (a) 3D view, (b) and (c) x and y axes views.

of the squared injected power becomes:

$$\langle(\mathcal{F}\dot{w})^2\rangle = \frac{A_0^2}{2}\langle v^2\rangle + \langle(\mathcal{L}\mathcal{F})^2\mathcal{F}^2\rangle. \tag{23}$$

After a sufficiently long time, the stationary forcing term will be negligible compared with the quadratic term that keeps increasing with time as the cascade propagates. Using Parseval's identity:

$$\langle v^2\rangle = \int_0^\infty P_v(f)df \tag{24}$$

and the expression of the self-similar time-dependent spectrum in Eq. (19), Eq. (23) becomes:

$$\langle(\mathcal{F}\dot{w})^2\rangle \sim \frac{A_0^2}{2}\langle v^2\rangle \propto A_0^2\frac{\bar{\varepsilon}t}{h}, \tag{25}$$

then

$$\langle\varepsilon^2\rangle \propto A_0^2\frac{\bar{\varepsilon}t}{h(\rho S)^2} \tag{26}$$

which gives the expected diffusive behavior. Hence, the injected power fluctuation is the consequence of a direct feedback of the propagation of the kinetic energy spectrum during the self-similar dynamics.

4.1.2. Imperfect, undamped plates

The effect of the presence of a plate imperfection on the turbulent dynamics is now investigated. Results are presented following the same procedure as for the perfect plate.

The static deformation $w_0(\mathbf{x})$ appearing in Eq. (2) is chosen in the form of a raised cosine

$$w_0(\mathbf{x}) = \frac{Z}{2}\left[1 + \cos\left(\frac{\pi\sqrt{(x-x_0)^2+(y-y_0)^2}}{L}\right)\right], \tag{27}$$

when $(x - x_0)^2 + (y - y_0)^2 \leq L^2$, and zero otherwise. Here Z is the static (vertical) deflection, L is the width and $\mathbf{x}_0$ is the center of the deformation. The plate area is 0.4×0.6 m^2 and the width is here selected to be 0.2 m, and $\mathbf{x}_0$ is the center of the plate; see Fig. 7. Z is then a free parameter that changes case by case. This form of imperfection has been selected as it is close to what can be observed in experiments, where large plates are generally affected by a pattern of large wavelength. Our goal is thus to quantify the effect of a selected realistic geometric imperfection in order to assess its potential effect on the turbulence spectra. For the perfect plate with $w_0(\mathbf{x}) = 0$, the internal restoring force is symmetric so that only cubic nonlinearities are present in the von Kármán equations. However when an imperfection is considered, quadratic nonlinearity appears in the model equations and so three-wave processes are present in the dynamics.

A case study (case 11 in Table 2) is first examined. It corresponds to a plate with a thickness $h = 1$ mm, and a deformation $Z = 5$ mm as defined in Eq. (27). As the eigenfrequencies increase with the imperfection (see *e.g.* [29,27]), the excitation frequency is now shifted so as to remain in the vicinity of the fourth eigenfrequency, so that now $f_p = 103$ Hz, and the forcing amplitude is selected as $A_0 = 90$ N.

During the dynamics, it is observed that the velocity power spectra evolve almost identically to the case of the perfect plate, so that the spectrogram and power spectra of the imperfect plate are similar to those shown in Fig. 2. The characteristic frequency increases linearly with time while the characteristic amplitude remains fairly constant as shown in Fig. 8. The normalized spectra in Fig. 9 are superimposed according to a curve $\phi_P(f/f_c) = \langle P_v(f)\rangle/\langle P_v(f_c)\rangle$ indicating self-similar dynamics. The self-similar dynamics is also produced during a mean constant injection flux with diffusive-type fluctuations, as seen in Fig. 10.

A total of 12 simulations are considered for imperfect plates. The parameters are listed in Table 2. Note that the magnitude of the imperfection considered is large ($Z \geq h$), and of the order of what can be expected in real experiments. In particular, it has been shown in [45,27,46] that an imperfection of the order of the

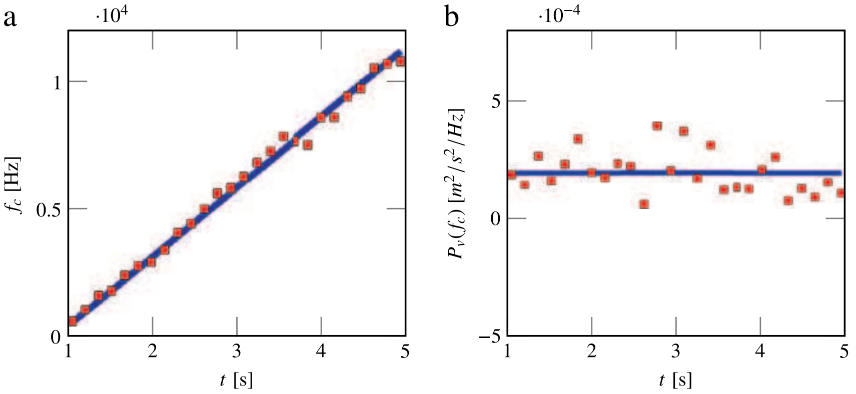

Fig. 8. Imperfect, undamped plate, case 11 of Table 2. (a) Time evolution of the characteristic frequency, (b) corresponding spectral amplitude. Continuous lines are best fit $f_c = c_f t$ with $c_f = 226$ s^{-2} (a), and the mean amplitude $\langle P_v(f_c)\rangle = 2.66 \cdot 10^{-4}$ m^2/s^2/Hz.

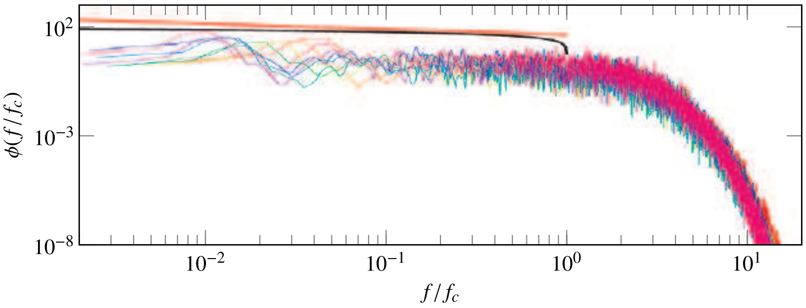

Fig. 9. Normalized velocity spectra using the characteristic frequency f_c and amplitude $P_v(f_c)$ (case 11 in Table 2). Continuous black line shows the log correction $\log^{1/3}\left(\frac{f_c^\star}{f}\right)$ of the KZ spectrum, see Eq. (1), with $f_c^\star = f_c$. Dashed red line shows a power law $f^{-\frac{1}{4}}$. (For interpretation of the references to color in this figure legend, the reader is referred to the web version of this article.)

thickness h is able to change the type of nonlinearity of the low frequency modes. For each one of the cases, the cascade velocity c_f, the spectral amplitude at the characteristic frequency $P_v(f_c)$ and the coefficient D are plotted as functions of combinations of $\bar{\varepsilon}$ and h. It can be seen that for all cases a linear relationship is found (Fig. 11):

$$\langle P_v(f_c)\rangle = 2.30h\bar{\varepsilon}^{1/3} \tag{28a}$$

$$c_f = 0.19\frac{\bar{\varepsilon}^{2/3}}{h^2} \tag{28b}$$

$$D = 1.86 \cdot 10^4\frac{\bar{\varepsilon}^{7/3}}{h}. \tag{28c}$$

The scaling laws are identical to the perfect case, although the data are a bit more scattered in Fig. 11 than in Fig. 6. The obtained values for the proportional constants are also very close. The quadratic nonlinearity introduced by an imperfection is then hardly discernable in the turbulent cascade dynamics which indicates that the vibration amplitudes are sufficiently important so that the cubic term dominates the quadratic one; hence only the cubic nonlinearity seems to drive the main characteristics. In conclusion, the geometric imperfection retained in this study, and which has been selected as it provides insight into realistic imperfections one may encounter in experimental situations, has no effect on the main characteristics of the turbulent spectra. Hence it appears that plate imperfections should not be considered as a potential cause for explaining the discrepancies observed between theory derived for perfect plates and real experiments with unavoidable imperfections.

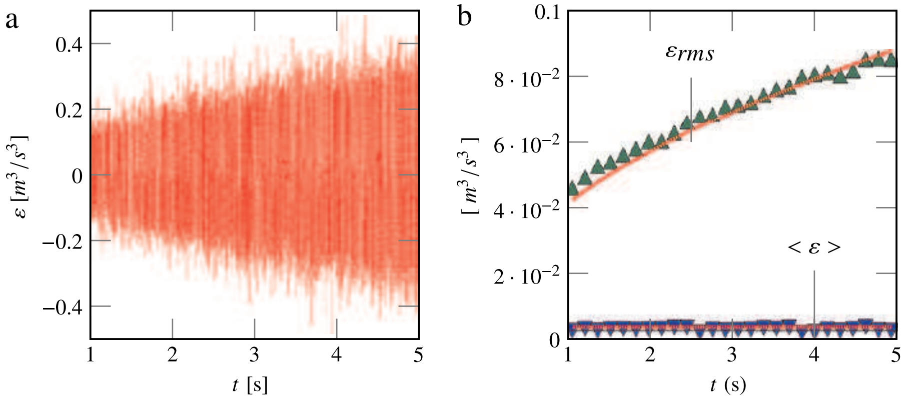

Fig. 10. Time evolution of the injected power for the imperfect undamped plate (case 11 in Table 2). (a) Time series, (b) $\langle\varepsilon\rangle$ and $\varepsilon_{rms} = \sqrt{\langle\varepsilon^2\rangle}$. Continuous lines are best fits: $\bar{\varepsilon} = 1.15 \cdot 10^{-5}$ m^3/s^3, and $D = 0.0015$ m^6/s^7 (see the text).

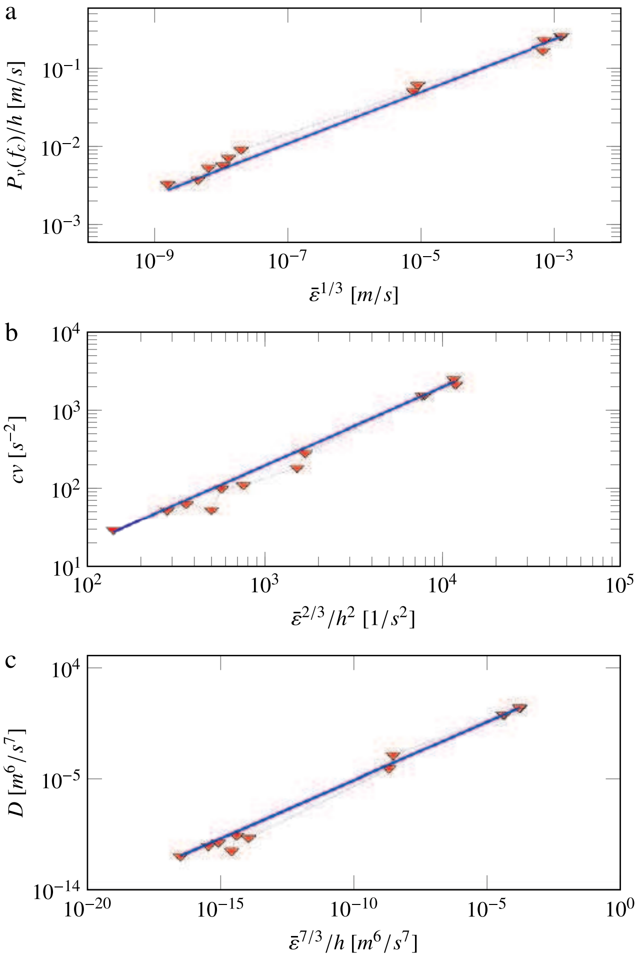

Fig. 11. Results of simulations for the imperfect, undamped plate with a periodic forcing, for the 12 cases reported in Table 2. (a) Spectral amplitude $\langle P_v(f_c)\rangle/h$, (b) cascade velocity c_f and (c) coefficient D.

In the remainder of the paper, the plate imperfections are no longer considered. The next section is devoted to the study of free (unforced) turbulence in order to highlight the effect of the pointwise forcing.

4.2. Free undamped turbulence

We now consider the case where the perfect, undamped plate, given an initial turbulent spectrum energy, is left free to vibrate in the absence of forcing and develops a cascade. The plate dimensions are $L_x \times L_y = 0.4 \times 0.6$ m^2, and the thickness is selected as $h = 0.1$ mm. The sampling rate is chosen as 40 kHz resulting in a grid size of 102 × 153 points. The excitation frequency is in the vicinity of the fourth eigenmode at 7.5 Hz. The forcing amplitude reaches $A_0 = 0.1$ N linearly after a duration $t_0 = 0.1$ s and is then abruptly stopped. The response of the system is shown over a long time duration in the spectrogram of Fig. 12(a). Even after stopping the external excitation, the number of excited modes keeps increasing slowly. Because of the slowness of this dynamics, the data analysis has been exceptionally changed with respect to the standard procedure explained in Section 3. Here the time window is $\tau = 0.1$ s and the number of spectra over which the average is taken is $M = 100$, resulting in a time $T = M\tau = 10$ s.

The velocity power spectra of the free decaying turbulence are shown at different stages of the dynamics in Fig. 12(b). The shape of the spectra changes abruptly just after the forcing is stopped. There is an evidence of a flattening in the low-frequency part of

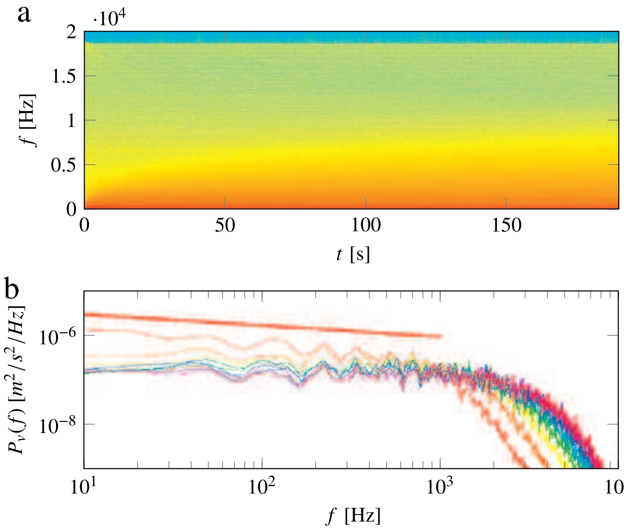

Fig. 12. (a) Spectrogram of the velocity of the perfect, undamped plate for which the forcing is stopped after 0.1 s. The plate is of thickness $h = 0.1$ mm and the sampling rate 40 kHz. (b) Corresponding velocity power spectra averaged over 10 s, displayed for time intervals of 30 s. The first one (red) is computed from 0.1s (i.e. the end of the forcing) to 10.1 s. Straight red line corresponds to the power law $f^{-1/4}$. (For interpretation of the references to color in this figure legend, the reader is referred to the web version of this article.)

the spectra, indicating once again the effect of the external forcing has on the power-law slope. On the other hand, the cascade front still progresses towards high frequencies even without forcing. The corresponding characteristic frequency evolution is shown in Fig. 13(a) and follows a clear 1/3 power law, significantly different from the linear dependence found for the case with external forcing. The energy conservation during the dynamics justifies the $-1/3$ power law best fit for the spectra amplitude in Fig. 13(b). More precisely, the characteristic frequency is found to behave as $f_c = at^{1/3}$ with $a = 331.5$ s$^{-\frac{4}{3}}$, whereas the spectral amplitude reads $P_v(f_c) = bt^{-1/3}$ with $b = 1.1 \cdot 10^{-7}$ m^2 s$^{-\frac{2}{3}}$. In order to express these dependences with nondimensional numbers, one can introduce the conserved quantities of the system, *i.e.* the total energy $\xi = \frac{h}{2}\int P_v(f)df$ of the turbulent fluctuations – once the forcing stopped the system is conservative – and the plate thickness h. The energy ξ may locally fluctuate since it is actually the energy of the whole plate that is conserved. However, for the point considered, it is found to keep reasonably constant at $\xi \approx 2 \cdot 10^{-8}$ m^3/s^2 during the self-similar dynamics, as shown in Fig. 14. Using the relationships derived from the best fits obtained in Fig. 13 together with a dimensional analysis, one can reexpress the dependences as

$$f_c(t) = 0.45\frac{\xi^{\frac{2}{3}}}{h^2}t^{\frac{1}{3}} \qquad P_v(f_c) = 0.41h\xi^{\frac{1}{3}}t^{-\frac{1}{3}}. \tag{29}$$

The two constants now appearing in Eq. (29) should be universal, as are the nondimensional numbers derived from the analyses in previous sections.

The normalized spectra using both the characteristic frequency and corresponding spectra amplitude are shown in Fig. 15 for times larger than 10 s (i.e. after the low frequency spectra flattening). They all superimpose showing that the dynamics becomes self-similar with a spectrum universal shape Φ_F such that $P_v(f) = P_v(f_c)\Phi_F\left(\frac{f}{f_c}\right)$.

The progression of the cascade front towards higher frequencies must be accomplished by the presence of an energy flux ε_c. It can be estimated from the energy $d\xi_c$ of the activated modes between f_c and $f_c + df_c$ as the cascade propagates during the time interval

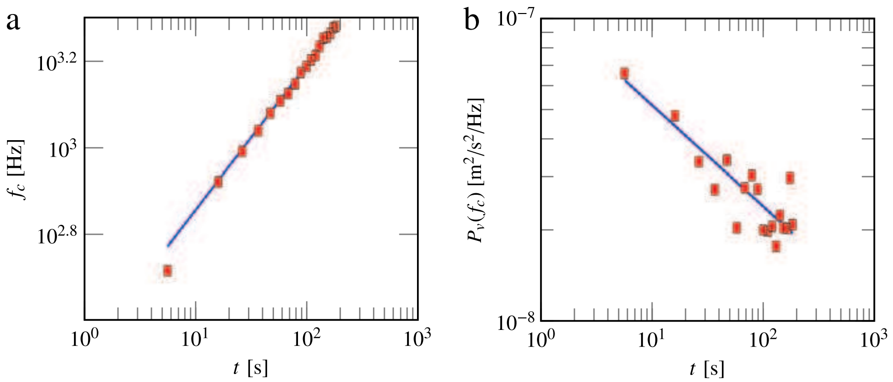

Fig. 13. Undamped free turbulence. (a) Time evolution of the characteristic frequency f_c and (b) corresponding spectral amplitude. Continuous lines are best fits $f_c = at^{1/3}$ with $a = 331.5\ \mathrm{s}^{-\frac{4}{3}}$ (a), and $P_v(f_c) = bt^{-1/3}$ with $b = 1.1 \cdot 10^{-7}\ \mathrm{m}^2\ \mathrm{s}^{-\frac{2}{3}}$ (b).

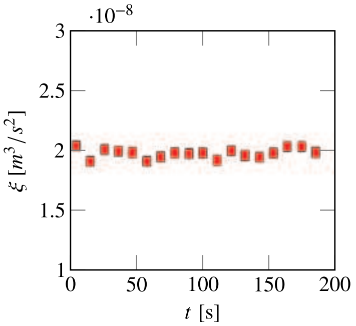

Fig. 14. Time evolution of the kinetic energy $\xi = \frac{h}{2}\int P_v(f)df$ for the free undamped turbulence.

dt, $\varepsilon_c = \frac{d\xi_c}{dt} = \frac{h}{2}P_v(f_c)\frac{df_c}{dt}$. Using both evolutions in Eq. (29), the estimation gives:

$$\varepsilon_c = 0.03\xi t^{-1}. \tag{30}$$

The spectrum in the self-similar dynamics of free turbulence can thus be expressed as:

$$P_v(f) = 13.34h\varepsilon_c^{\frac{1}{3}}\Phi_F\left(\frac{f}{f_c}\right). \tag{31}$$

As for the first case with periodic forcing, the dependence of the frequency front in $t^{1/3}$ can be derived from the theoretical kinetic equation governing the dynamics of the wave spectrum for vibrating plates. Following the calculations presented in Appendix A, and considering now that, for the self-similar solution of the form given by Eq. (20), the total energy of the system is conserved, one finds that the power frequency spectrum should fulfill the relationship:

$$P_v(\omega, t) \sim t^{-1/3}f_2\left(\sqrt{\frac{\omega}{t^{1/3}}}\right) = t^{-1/3}g_2\left(\frac{\omega}{t^{1/3}}\right). \tag{32}$$

This theoretical results clearly exhibits the fact that the frequency front should evolve as $t^{1/3}$ while the total energy as $t^{-1/3}$. In this case of free turbulence, the function g_2 can now be directly identified from the numerical solution Φ_F.

Let us now compare the self-similar solution with the theoretical KZ spectrum for vibrating plates. Because of the spectral flattening highlighted in Fig. 12(b), one can observe that the function Φ_F is now very close to the log-correction of the theoretical KZ spectrum for vibrating plates, as displayed in Fig. 15, and shown here for $f_c^\star = f_c$. The similarity between the self-similar spectrum of decaying turbulence with the stationary KZ spectrum has already been mentioned for surface gravity waves [34] and capillary waves [35,37,36]. The comparison between the self-similar spectra of periodically forced turbulence (Fig. 4) and free turbulence (Fig. 15) shows a steeper slope when forcing is present. This result should be retrieved in a more realistic case where damping is also considered and should corroborate the experimental results shown in [20]. The aim of the last section is thus to verify this numerically in the case of a decaying turbulence.

4.3. Damped turbulence

The effect of the forcing is now studied in a damped case. The plate dimensions are $L_x \times L_y = 0.4 \times 0.6\ \mathrm{m}^2$, the grid size is 102×153 and $h = 1$ mm. The damping introduced in Eq. (4) is selected as $\sigma_0 = 0.5\ \mathrm{s}^{-1}$. The forcing frequency is $f_p = 75$ Hz, with a forcing amplitude of $A_0 = 140$ N and a ramp time $t_0 = 0.5$ s. The forcing remains periodic from 0.5 to 3.5 s ($t_1 = 4$ s in Eq. (6)) and then abruptly stopped at $t = 4$ s.

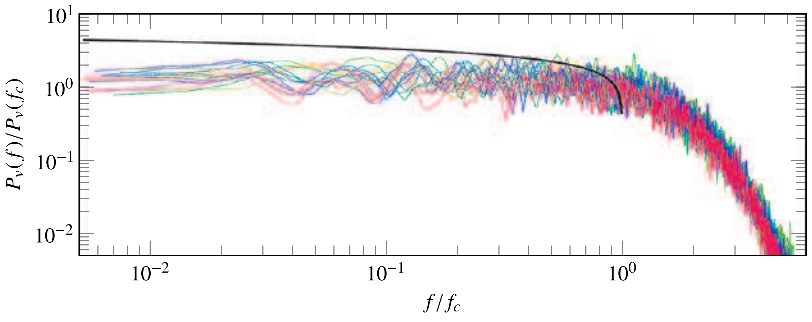

Fig. 15. Free undamped turbulence. Normalized velocity power spectra of Fig. 12(b) for $t > 10$ s during the self-similar dynamics. Black line shows the log correction $\log^{1/3}\left(\frac{f_c^\star}{f}\right)$ of the KZ spectrum, Eq. (1), with $f_c^\star = f_c$.

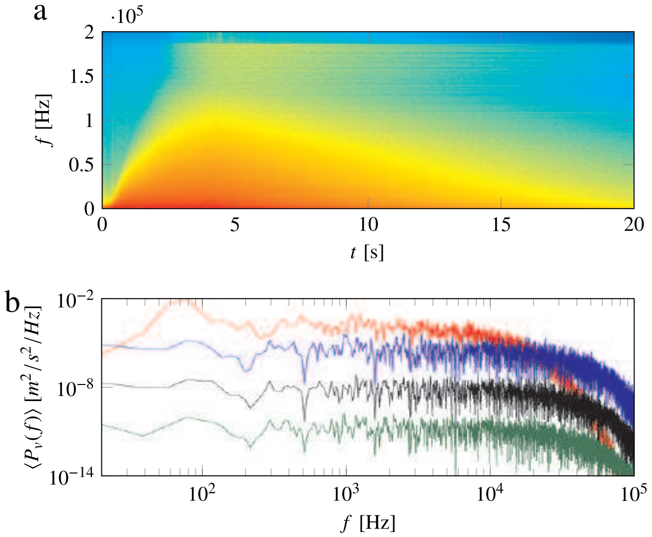

Fig. 16. (a) Spectrogram of the velocity for the perfect damped plate. (b) Corresponding velocity power spectra averaged over $T = 0.15$ s computed every 5 s from 5 to 20 s.

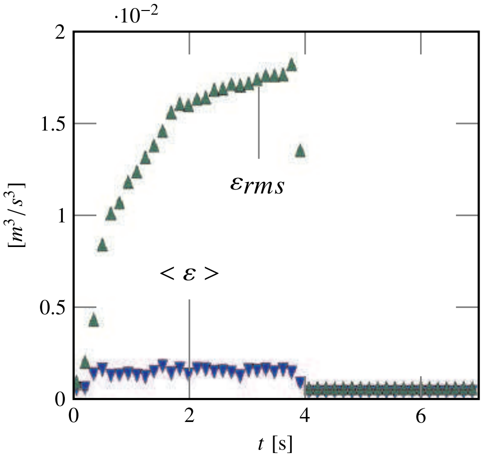

Fig. 17. Time evolution of the injected power, $\langle \varepsilon \rangle$ and $\varepsilon_{rms} = \sqrt{\langle \varepsilon^2 \rangle}$ for the decaying turbulence experiment shown in Fig. 16.

The response of the damped system is shown over 20 s of duration in the spectrogram in Fig. 16(a). The spectra reach a nearly steady state just before $t = 4$ s that corresponds to the time at which the forcing is stopped. Meanwhile, the injected power remains fairly constant in Fig. 17, $\langle \varepsilon \rangle (t) \simeq \bar{\varepsilon}$, and the characteristic frequency grows, just as for the undamped case studied in Section 4.1. The main difference is that the characteristic frequency (Fig. 18) will saturate to a constant value once the statistical steady state of turbulent energy will be reached. In other words, the cascade velocity front decreases towards zero when approaching the steady state.

As the cascade progresses to higher frequencies, more and more modes are activated, which results in an increase of the dissipation flux ε_d since each mode has a linear energy loss parameterized by σ_0 that should be compensated by the incoming flux. Hence, less and less energy flux ε_c is available to propagate the cascade front velocity, since $\langle \varepsilon_c \rangle (t) = \bar{\varepsilon} - \langle \varepsilon_d \rangle (t)$. Once the forcing is stopped at $t = 4$ s, the characteristic frequency overshoots as shown in Fig. 18 and then sharply saturates. The drastic increase of the characteristic frequency is provoked by the flattening of the spectral shape at low frequencies as observed in Fig. 16(b).

The effect of the pointwise forcing evidenced in previous sections is here retrieved for the damped dynamics. The numerical experiment shown here shares similarities with the experimental result of [20], where the spectral flattening was also observed in the decaying turbulence regime. Once the forcing stopped, the spectrum simply decreases exponentially as $e^{-2\sigma_0 t}$ as expected by a pure damping linear dynamics; see Fig. 18(b). Actually one can observe that the nonlinear dynamics are still present but very weak since the nonlinear propagation depends on the vanishing turbulent energy $\xi(t)$. Note that selecting other damping laws should lead to different behaviors in the decaying regime, resulting from the competition between the nonlinear propagation effect with the energy losses, both of which having different frequency-dependences associated to different timescales. Here the damping law is frequency independent so that the results lend themselves to an easy physical interpretation.

5. Discussion and concluding remarks

The nonlinear dynamics of turbulent vibrating plates has been studied numerically with a finite-difference, energy-conserving scheme including a pointwise forcing together with realistic boundary conditions. The most important results have been obtained in the absence of damping, in the framework of non-stationary wave turbulence. Self-similar solutions for the energy spectrum have been exhibited for a wide range of parameter variations. The simulations display the presence of a front propagating to high frequencies. With pointwise forcing, this propagation is linear with time, whereas for free turbulence the dependence is in $t^{1/3}$. These self-similar behaviors can be directly retrieved from the kinetic equation by analyzing the admissible self-similar solutions. From the numerical solutions, one is thus able to get a numerical value for the self-similar functions in non-stationary wave turbulence for plates, for the two cases studied in this paper, with and without external forcing. Comparing the shape of these numerically obtained functions, one observes that they share similarities with the theoretical KZ spectrum computed by [14], albeit exhibiting interesting differences. In the case of a pointwise forcing, a steeper slope is observed as compared to the free undamped turbulence. Note also that the power 1/3 dependence on the energy flux is numerically retrieved.

This observation is robust to adding the damping in the simulations and thus recovers experimental results shown in [20]. It can thus be concluded that the local pointwise forcing has a measurable effect on the slope in the low-frequency range. This effect has been related in [20] to an anisotropy induced by the presence of the shaker. A direct extension of the results presented herein should thus to compute spatial spectra in order to verify numerically that the same argument holds.

For the first time, our numerical set-up allows for an investigation of the effect of a geometrical imperfection on the turbulent dynamics. The results, obtained in a non-stationary framework, clearly indicates that perfect and imperfect plates present identical characteristics in the WT regime. This emphasizes the fact that in this regime the cubic nonlinear terms dominate the quadratic ones, which thus have no measurable effect on the spectral characteristics of the WT. Note however that this is not true for the regimes of transition to turbulence that involve weaker excitation amplitudes [28,29]. Note also that only a simple, low-frequency pattern has been introduced as a geometric imperfection, in order to present numerical results close to what can be expected in real-life situations. The conclusions, based on numerical experiments, are only valid for those cases. Extensions of the present work could consider more complex geometric imperfections, with smaller wavelengths, in order to continue the quantification of the transition between perfect and imperfect plates' turbulent dynamics.

Finally, dimensional arguments have been used in order to properly quantify the results in non-stationary cases. As no

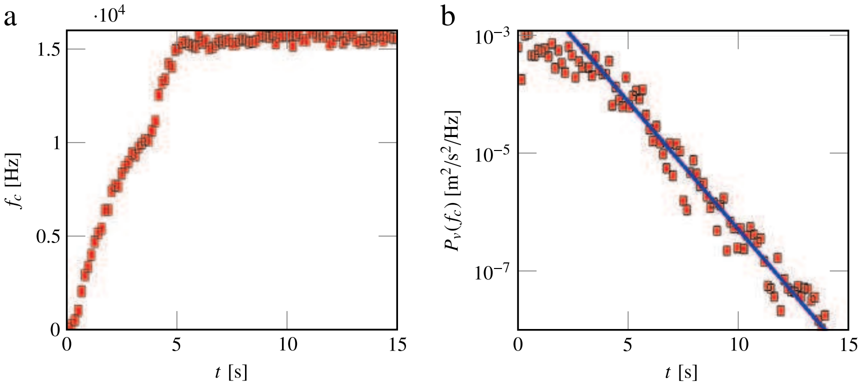

Fig. 18. (a) Time evolution of the characteristic frequency f_c and (b) corresponding spectral amplitude decreasing as $\langle P_v(f_c)\rangle = 0.012e^{-2\sigma_0 t}$ of the spectra shown in Fig. 16, with $\sigma_0 = 0.5$ s^{-1} (blue thick line).

theoretical prediction for the non-stationary evolution of systems with log-corrected spectra exist at the present time, we believe the results shown here could be used so as to ascertain a theoretical development that may predict the observations reported in this contribution.

Acknowledgments

S. Bilbao was supported by the European Research Council, under Grant number StG-2011-279068-NESS. The authors want to thank Christophe Josserand for a fruitful discussion on the collision integral.

Appendix. Self-similar solutions for non-stationary wave turbulence in plates

This appendix is devoted to the derivation of self-similar solutions from the kinetic equation describing the wave turbulence in the von Kármán plate equations. Following the theoretical calculations reported by Düring et al. [14], the 4-waves kinetic equation has the general expression given by Zakharov et al. [2], and reads

$$\frac{\partial n(\mathbf{k},t)}{\partial t} = I(\mathbf{k}), \tag{A.1}$$

with $n(\mathbf{k},t) \equiv n_{\mathbf{k}}$ the wave spectrum and $I(\mathbf{k})$ the collision integral, the expression of which can be found in [14]:

$$I(\mathbf{k}) = 12\pi \int |J_{k123}|^2 f_{k123}\delta(\mathbf{k} + s_1\mathbf{k}_1 + s_2\mathbf{k}_2 + s_3\mathbf{k}_3) \times \delta(\omega_k + s_1\omega_1 + s_2\omega_2 + s_3\omega_3)d\mathbf{k}_1 d\mathbf{k}_2 d\mathbf{k}_3, \tag{A.2}$$

where J_{k123} stands for the interaction term and f_{k123} is such that

$$f_{k123} = \sum_{s_1,s_2,s_3} n_{\mathbf{k}} n_{\mathbf{k}_1} n_{\mathbf{k}_2} n_{\mathbf{k}_3} \left(\frac{1}{n_{\mathbf{k}}} + \frac{s_1}{n_{\mathbf{k}_1}} + \frac{s_2}{n_{\mathbf{k}_2}} + \frac{s_3}{n_{\mathbf{k}_3}}\right). \tag{A.3}$$

Following [2], let us introduce a self-similar solution for the non-stationary evolution, depending only on the wavevector modulus, as

$$n(\mathbf{k},t) = t^{-q} f(kt^{-p}) = t^{-q} f(\eta). \tag{A.4}$$

Plugging this ansatz in the kinetic equation (A.1), and taking into account the expression of $|J_{k123}|^2$ found in [14], one gets

$$-t^{-q-1}\left[qf(\eta) + p\eta f'(\eta)\right] = I(\eta)t^{-3q+2p}, \tag{A.5}$$

so that a solution of the form (A.4) is possible only if the condition $-q-1 = -3q+2p$ is satisfied. It can be rewritten as

$$2(q-p) = 1. \tag{A.6}$$

Let us introduce the total energy of the distribution

$$\xi = \int \omega\, n_{\mathbf{k}}\, d\mathbf{k} \tag{A.7}$$

and consider the two cases numerically studied:

Case 1: The plate is forced by a sinusoidal pointwise forcing of constant amplitude and excitation frequency. In this case the total energy increases linearly with time so that $\xi \sim t$.

Case 2: The plate is left free to vibrate, given an amount of energy as the initial condition. In this case the total energy is constant so that $\xi \sim t^0$.

Substituting (A.4) into (A.7) one obtains a second relationship between p and q, which reads, depending on the case considered

$$4p - q = \begin{cases} 1 & \text{for case 1} \\ 0 & \text{for case 2.} \end{cases} \tag{A.8}$$

Solving for (p,q) in both cases give

$$\text{case 1}: \ p = 1/2, \qquad q = 1, \tag{A.9}$$

$$\text{case 2}: \ p = 1/6, \qquad q = 2/3. \tag{A.10}$$

The last step consists in expressing the self-similar solution for $P_v(\omega)$ the power spectrum of the transverse velocity $v = \dot{w}$ used in the analysis, which is related to the power spectrum of the displacement $P_w(\omega)$ by a proportionality relationship $P_v(\omega) \propto \omega^2 P_w(\omega)$. Using the space–frequency relationship $P_w(\omega)d\omega \propto P_w(k)kdk$, together with the dispersion relation, one finds $P_w(\omega) \propto P_w(k)$, such that $P_v(\omega) \propto k^4 P_w(k)$. Finally, using the relationship $P_w(k) \propto \frac{n_k}{\omega}$ given in [14], one obtains finally $P_v(\omega,t) \propto k^2 n(k,t)$, so that the self-similar solutions for $P_v(\omega,t)$ finally reads for the general case with $n_{\mathbf{k}}$ given by Eq. (A.4):

$$P_v(\omega,t) \sim t^{2p-q} f(\omega^{1/2} t^{-p}). \tag{A.11}$$

Specifying now the solutions for (p,q) found for the two cases under study, one obtains for case 1:

$$P_v(\omega,t) \sim f_1\left(\sqrt{\frac{\omega}{t}}\right) = g_1\left(\frac{\omega}{t}\right), \tag{A.12}$$

and for case 2:

$$P_v(\omega,t) \sim t^{-1/3} f_2\left(\sqrt{\frac{\omega}{t^{1/3}}}\right) = t^{-1/3} g_2\left(\frac{\omega}{t^{1/3}}\right), \tag{A.13}$$

where $g_{1,2}$ (or $f_{1,2}$) have been indexed with respect to case 1 and case 2, and are functions to be defined.

References

[1] S. Nazarenko, Wave Turbulence, Springer-Verlag, Berlin, Heidelberg, 2011.

[2] V. Zakharov, V. L'vov, G. Falkovich, Kolmogorov Spectra of Turbulence 1: Wave Turbulence, in: Series in Nonlinear Dynamics, Springer, 1992.

[3] A. Newell, S. Nazarenko, L. Biven, Wave turbulence and intermittency, Physica D 152–153 (2001).

[4] U. Frisch, Turbulence, Cambridge University Press, Cambridge, 1995.

[5] V.E. Zakharov, N.N. Filonenko, Energy spectrum for stochastic oscillations of surface of a liquid, J. Appl. Mech. Tech. Phys. 8 (1967) 37.

[6] A.N. Pushkarev, V.E. Zakharov, Turbulence of capillary waves, Phys. Rev. Lett. 76 (1996) 3320–3323.

[7] V.E. Zakharov, N.N. Filonenko, Energy spectrum for stochastic oscillations of surface of a liquid, Sov. Phys. Dokl. 11 (1967) 881–883.

[8] M. Onorato, A.R. Osborne, M. Serio, D. Resio, A. Pushkarev, V.E. Zakharov, C. Brandini, Freely decaying weak turbulence for sea surface gravity waves, Phys. Rev. Lett. 89 (2002) 144501.

[9] E. Falcon, C. Laroche, S. Fauve, Observation of gravity—capillary wave turbulence, Phys. Rev. Lett. 98 (2007) 094503.

[10] S. Galtier, S. Nazarenko, A. Newell, A. Pouquet, A weak turbulence theory for incompressible magnetohydrodynamics, J. Plasma Phys. 63 (2000) 447–488.

[11] S. Galtier, S. Nazarenko, A. Newell, A. Pouquet, Anisotropic turbulence of shear-Alfvèn waves, Astrophys. J. Lett. 564 (2002) L49–L52.

[12] W. Vinen, Classical character of turbulence in a quantum liquid, Phys. Rev. B 61 (2000) 1410–1420.

[13] W. Vinen, Decay of superfluid turbulence at a very low temperature: the radiation of sound from a Kelvin wave on a quantized vortex, Phys. Rev. B 64 (2001) 134520.

[14] G. Düring, C. Josserand, S. Rica, Weak turbulence for a vibrating plate: can one hear a Kolmogorov spectrum? Phys. Rev. Lett. 97 (2006) 025503.

[15] T. von Kármán, Festigkeitsprobleme im Maschinenbau, Encyklopadie Math. Wiss. 4 (1910) 311–385.

[16] O. Thomas, S. Bilbao, Geometrically nonlinear flexural vibrations of plates: in-plane boundary conditions and some symmetry properties, J. Sound Vib. 315 (2008) 569–590.

[17] A. Boudaoud, O. Cadot, B. Odille, C. Touzé, Observation of wave turbulence in vibrating plates, Phys. Rev. Lett. 100 (2008) 234504.

[18] N. Mordant, Are there waves in elastic wave turbulence? Phys. Rev. Lett. 100 (2008) 234505.

[19] B. Miquel, N. Mordant, Nonlinear dynamics of flexural wave turbulence, Phys. Rev. E 84 (2011) 066607.

[20] B. Miquel, N. Mordant, Nonstationary wave turbulence in an elastic plate, Phys. Rev. Lett. 107 (2011) 034501.

[21] T. Humbert, O. Cadot, G. Düring, C. Josserand, S. Rica, C. Touzé, Wave turbulence in vibrating plates: the effect of damping, Europhys. Lett. 102 (2013) 30002.

[22] N. Yokoyama, M. Takaoka, Weak and strong wave turbulence spectra for elastic thin plate, Phys. Rev. Lett. 110 (2013) 105501.

[23] B. Miquel, A. Alexakis, N. Mordant, Role of dissipation in flexural wave turbulence: from experimental spectrum to Kolmogorov–Zakharov spectrum, Phys. Rev. E (2014) submitted for publication.

[24] B. Miquel, Études expérimentales et numériques de la turbulence d'ondes de flexion (Ph.D. thesis), Université Pierre et Marie curie, Paris, 2013.

[25] B. Miquel, A. Alexakis, C. Josserand, N. Mordant, Transition from wave turbulence to dynamical crumpling in vibrated elastic plates, Phys. Rev. Lett. 111 (2013) 054302.

[26] Z. Celep, Free flexural vibration of initially imperfect thin plates with large elastic amplitudes, ZAMM Z. Angew. Math. Mech. 56 (1976) 423–428.

[27] C. Camier, C. Touzé, O. Thomas, Non-linear vibrations of imperfect free-edge circular plates and shells, Eur. J. Mech. A Solids 28 (2009) 500–515.

[28] C. Touzé, O. Thomas, M. Amabili, Transition to chaotic vibrations for harmonically forced perfect and imperfect circular plates, Internat. J. Non-Linear Mech. 46 (2011) 234–246.

[29] C. Touzé, S. Bilbao, O. Cadot, Transition scenario to turbulence in thin vibrating plates, J. Sound Vib. 331 (2012) 412–433.

[30] S. Bilbao, A family of conservative finite difference schemes for the dynamical von Kármán plate equations, Numer. Methods Partial Differential Equations 24 (2008) 193–216.

[31] E. Hairer, C. Lubich, G. Wanner, Geometric Numerical Integration, Structure-Preserving Schemes for Ordinary Differential Equations, Springer, 2006.

[32] G. Falkovich, A. Shafarenko, Nonstationary wave turbulence, J. Nonlinear Sci. 1 (1991) 457–480.

[33] C. Connaughton, A. Newell, Y. Pomeau, Non-stationary spectra of local wave turbulence, Physica D 184 (2003) 64–85.

[34] R. Bedard, S. Lukaschuk, S. Nazarenko, Non-stationary regimes of surface gravity wave turbulence, JETP Lett. 97 (2013) 459–465.

[35] G.V. Kolmakov, A.A. Levchenko, M.Y. Brazhnikov, L.P. Mezhov-Deglin, A.N. Silchenko, P.V.E. McClintock, Quasiadiabatic decay of capillary turbulence on the charged surface of liquid hydrogen, Phys. Rev. Lett. 93 (2004) 074501.

[36] L. Deike, M. Berhanu, E. Falcon, Decay of capillary wave turbulence, Phys. Rev. E 85 (2012) 066311.

[37] G. Kolmakov, Decay of capillary turbulence on the surface of a viscous liquid, JETP Lett. 83 (2006) 58–63.

[38] G.L. Ostiguy, S. Sassi, Effects of initial geometric imperfections on dynamic behaviour of rectangular plates, Nonlinear Dynam. 3 (1992) 165–181.

[39] L.D. Landau, L.P. Pitaevskii, E.M. Lifshitz, A.M. Kosevich, Theory of Elasticity, third ed., Butterworth–Heinemann, 1986.

[40] M. Ducceschi, C. Touzé, S. Bilbao, C. Webb, Nonlinear dynamics of rectangular plates: investigation of modal interaction in free and forced vibrations, Acta Mech. 225 (2014) 213–232.

[41] A. Chaigne, C. Lambourg, Time-domain simulation of damped impacted plates. I: theory and experiments, J. Acoust. Soc. Am. 109 (2001) 1422–1432.

[42] S. Bilbao, Numerical Sound Synthesis: Finite Difference Schemes and Simulation in Musical Acoustics, Wiley, 2009.

[43] O. Cadot, A. Boudaoud, C. Touzé, Statistics of power injection in a plate set into chaotic vibration, Eur. Phys. J. B 66 (2008) 399–407.

[44] O. Cadot, C. Touzé, A. Boudaoud, Linear versus nonlinear response of a forced wave turbulence system, Phys. Rev. E 82 (2010) 046211.

[45] C. Touzé, O. Thomas, Non-linear behaviour of free-edge shallow spherical shells: effect of the geometry, Internat. J. Non-Linear Mech. 41 (2006) 678–692.

[46] C. Touzé, C. Camier, G. Favraud, O. Thomas, Effect of imperfections and damping on the type of non-linearity of circular plates and shallow spherical shells, Math. Probl. Eng. 2008 (2008) Article ID 678307.

CHAPTER 6

Sound Synthesis of Gongs

In the previous chapters, the von Kármán equations were shown to be an appealing system to study because they give rise to a vast range of nonlinear phenomena despite the apparent simplicity of the system under consideration (a vibrating thin plate). An attractive possibility of numerical modelling of thin plates resides in the synthesis of gong-like sounds.

The aim of this chapter is to present some simulation results coming from running the modal code. For the first time, a modal approach is used in reproducing the weakly and strongly nonlinear vibrations of thin plates. The chapter presents at the beginning a discussion on how to implement an excitation mechanism to set the plate into motion, and convenient ways of extracting the output.

A quick discussion on loss is then offered, to show that the modal approach is very flexible in terms of the damping law that one wants to implement. Successively, a discussion on the number of modes to be retained in the simulation is offered, and finally a comparison with a Finite Difference scheme is given. See also [30].

6.1. Simulation Parameters

In this section the setup for the simulations is presented. The excitation, output and damping factor choices are explained and examples given.

6.1.1. Plate excitation. In order to produce a gong-like sound, a plate must be excited in a way that approximates how one may actually set a gong into motion. The most obvious way is to strike a plate. For that, one may think of the excitation mechanism $P(\mathbf{x},t)$ to be in the form of

$$P(\mathbf{x},t) = f(\mathbf{x})p(t), \tag{6.1}$$

where $f(\mathbf{x})$ is some kind of spacial distribution and $p(t)$ is a temporal forcing. The spacial distribution can be safely chosen to be a Dirac delta, $f(\mathbf{x}) = \delta(\mathbf{x}-\mathbf{x}_i)$, where $\mathbf{x}_i$ is the input location. This is largely sufficient, in many cases, for striking. When the ratio between mallet size and area of the plate gets larger, however, one may choose a different form for $f(\mathbf{x})$; for example a 2D *raised cosine* distribution [8]. Such a function, here denoted by $f_r(\mathbf{x})$, is

$$f_r(\mathbf{x}) = \begin{cases} \frac{H}{2}\left[1+\cos\left(\pi\sqrt{(x-x_i)^2+(y-y_i)^2}/r\right)\right] & \text{if } (x-x_i)^2+(y-y_i)^2 \le r^2; \\ 0 & \text{if } (x-x_i)^2+(y-y_i)^2 > r^2. \end{cases} \tag{6.2}$$

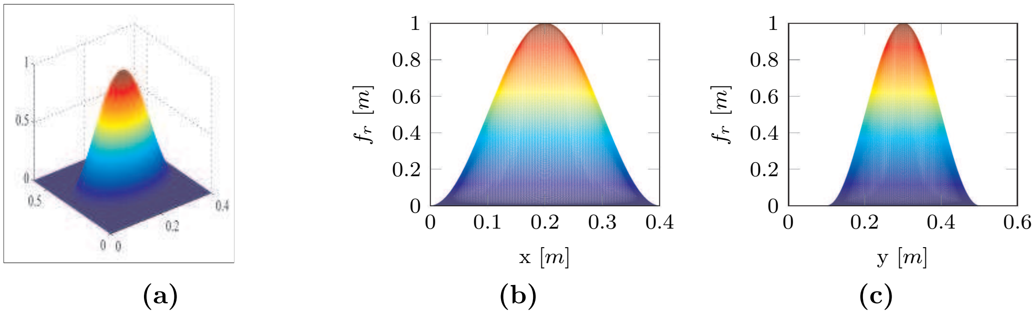

FIGURE 1. 2D raised cosine distribution, Eq. (6.2), with amplitude $H = 1$m and width $r = 0.2$m, centered around the point $\mathbf{x}_i = [0.2\text{m} \quad 0.3\text{m}]$. **(a)**: 3D view; **(b)**: x-section; **(c)**: y-section

Such a function depends on 2 parameters, a radius r and an amplitude H; an example of such a function is given in Fig. 1.

Turning the attention to the temporal excitation, one may wish to represent it as interaction between the surface of the plate and a mallet. Let $w_H(t)$ be the position of the mallet at the time t. Then the force acting on the plate due to the mallet interaction is given by Newton's second law

$$p(t) = -m_H w_{H,tt},$$

where m_H is the mass of the mallet. This force is usually represented as a "one-sided" nonlinearity, i.e. a nonlinear function of which acts when its argument is positive and is zero otherwise. Hence

$$-m_H w_{H,tt} = k_H^{\alpha+1}\left([w_H - \langle f_r, w\rangle]^+\right)^{\alpha},$$

where k_H a stiffness parameter and

$$([w_H - \langle f_r, w\rangle]^+)^{\alpha} = \begin{cases} 0 & \text{if } w_H - \langle f_r, w\rangle \le 0; \\ (w_H - \langle f_r, w\rangle)^{\alpha} & \text{if } w_H - \langle f_r, w\rangle > 0. \end{cases}$$

Such a contact model has been used by Rhaouti *et al.* for membranes [75], as well as by Lambourg *et al.* for anisotropic plates [55]. The most attractive feature of such a nonlinear model is that the contact duration depends on the velocity of the striking mallet, leading to brighter sounds when the velocity is increased [8].

Given the short contact duration of the mallet and the plate (usually of the order of a few milliseconds), one may wish to make use of a simplified model for $p(t)$. This form is again in the form of a raised cosine, this time in the form of

$$p(t) = \begin{cases} \frac{p_m}{2}\left[1 + \cos\left(\pi(t - t_0)/T_{wid}\right)\right] & \text{if } |t - t_0| \le T_{wid}; \\ 0 & \text{if } |t - t_0| > T_{wid}. \end{cases} \quad (6.3)$$

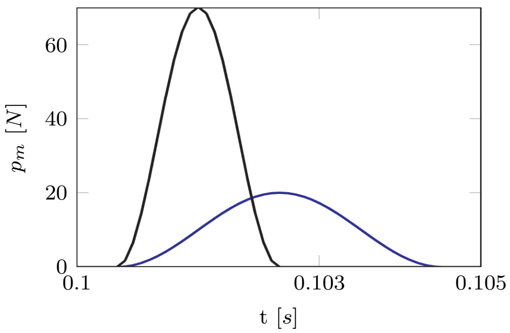

FIGURE 2. Time-dependent raised cosine to simulate the impact of a timpani mallet (blue) or a drumstick (black). T_wid is selected as 2ms for the mallet and 1ms for the stick; p_m is 20N for the mallet and 70N for the stick.

In this case, the contact distribution is symmetrical about the time t_0, and T_{wid} represents half of the contact duration. When activating the plate using a raised cosine distribution, one is free to select the contact duration and the amplitude of the distribution. Typically, one may select $T_{wid} \approx 1-3$ms and $p_m \approx 10-50$N for a timpani mallet (softer strike, longer contact); $T_{wid} \approx 0.25-1$ms and $p_m \approx 40-100$N for a drumstick (harder strike, shorter contact). Fig. 2 depicts two examples of such distribution.

Note that the examples presented in the next sections will be derived using a raised cosine as input conditions on one point of the plate; hence, for the remainder of this work

$$P(\mathbf{x},t) = \delta(\mathbf{x}-\mathbf{x}_i)p(t),$$

where $p(t)$ is as in Eq. (6.3).

Striking is not the only way that one may set a plate into motion. Very interesting effects can be obtained by bowing the plate at one edge. In this case, the function $f(\mathbf{x})$ is a Dirac delta at an input point $\mathbf{x}_i$ of a free edge. The temporal function can be looked for as

$$p(v_{rel}) = -p_b\phi(v_{rel}), \tag{6.4}$$

where $v_{rel} = w(\mathbf{x}_i,t)_{,t} - v_{bow}$ is the relative velocity of the bow and the input point on the plate, and $\phi(v_{rel})$ is, in general, an antisymmetric function of the velocity presenting a steep slope near zero (see [8] for details and examples). The attractive feature of such an input is that the variety of sounds that can be produced is very large, ranging from quasi-harmonic tones to noisy samples. However, examples of that will not be considered in this work.

In a scheme such the Störmer-Verlet or the energy conserving scheme of sec. 2.7, initial conditions can be inserted directly on $\mathbf{q}(0)$, $\mathbf{q}(1)$ (or, equivalently, in a displacement/velocity fashion, by considering an approximation to the velocity at the initial time, $\mathbf{v} = \delta_{t+}\mathbf{q}(0)$ such that $\mathbf{q}(1) = k\mathbf{v} + \mathbf{q}(0)$). An interesting effect might be obtained by considering a random excitation, *i.e.* by inputting random noise at the initial instant. This gives rise to a broadband excitation which resembles a strike, and that can be used as an alternative to the input strategies described before. Note, however, that not only such an excitation cannot be justified on a physical basis, but also that it cannot be controlled (it is a random sequence). Hence, implementing such initial conditions should really be regarded as a helpful shortcut while prototyping a code; this choice should however be discarded in refined models.

6.1.2. Output. When listening to a vibrating plate, the ears are sensitive to changes in the air pressure due to the waves produced on the surface of the plate and transmitted in the surrounding medium. The problem may be further compounded by the presence of walls and refractive objects in a closed space. Thus, a complete model of a sounding plate is achievable only when the surrounding environment is somehow taken under consideration in the simulations. Needless to say, for such simulations the computational requirements in terms of memory and time are enormous, even for small-sized rooms. Recently, the use of graphic cards and parallel computing has allowed the simulation of large scale environments and complex geometries; see, for instance, the work by the NESS project [9, 93, 10, 85], and the work by Chabassier on the piano [13, 14].

As a first approximation, however, one may extract the output directly on the surface of the plate, by recording the displacement of a particular point or by moving the output point around the surface of the plate (creating an interesting "phaser" effect). For the present work, the output is always taken at a point of the plate. Once the displacement waveform is extracted, it is possible to obtain the velocity and acceleration of the point by considering for instance the forward time derivative approximation in Eq. (2.70). These are high-pass filters that render the sound brighter, should one want to get rid of the low-frequency component of the displacement waveform. An example are presented in Fig. 3. In the figure, the time series of the displacement, velocity and acceleration are shown (normalised to have a maximum amplitude of 1, so to be played as audio samples). It is evident that the velocity and acceleration tend to privilege the high-frequency range of the output, and thus they are preferable over the displacement when trying to reproduce a bright, shimmering sound such that of a gong. This said, the low-frequency part of the spectrum is also important because it gives an idea of the dimensions of the gong that is being simulated. Hence, in many cases the velocity time series should be preferred over the acceleration. Notice, however, that the choice cannot be made in terms of pure physical arguments, and choosing amongst displacement, velocity and acceleration really becomes a question of taste.

6.1.3. Damping. Another factor that influences the perception of sound is damping. A distinct advantage of the modal approach is that one is able to tune the damping coefficients at will with practically no extra effort. This is indeed the most attractive feature of the modal approach applied to sound synthesis of gongs. A question remains to what damping law one should use for this problem. The question of damping in plates is an open one, and it has to do with the fact that the perceived "loss" is the contribution of a number of independent factors and underlying physical mechanisms.

Generally speaking, one may try to categorise loss in terms of

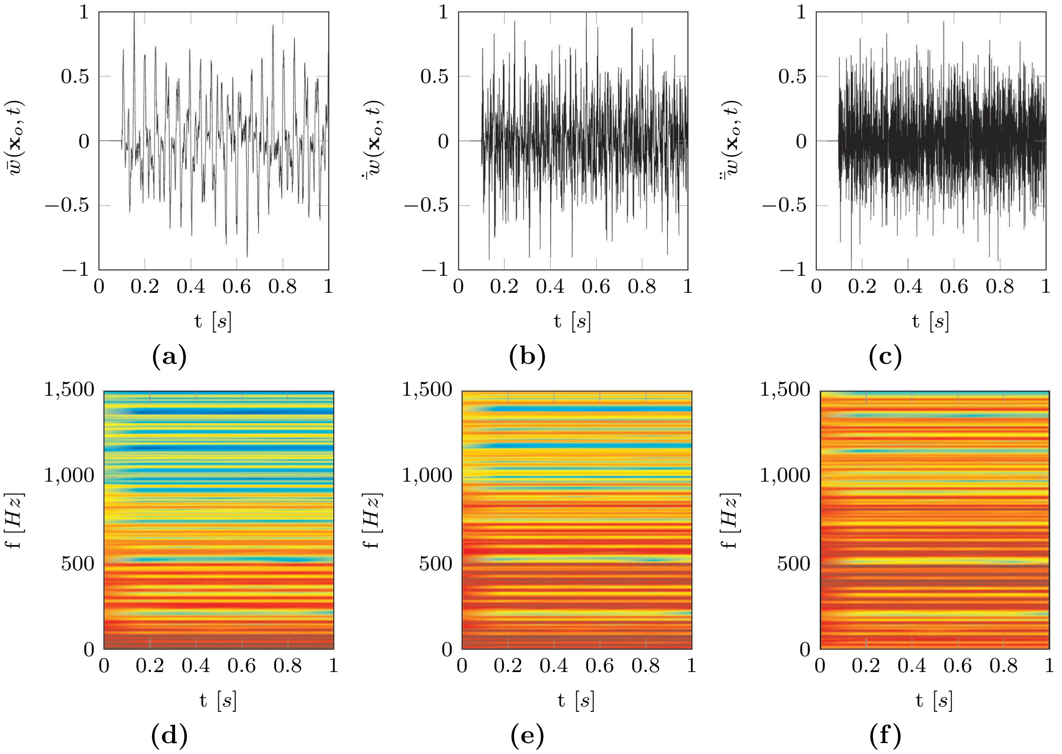

(a) **(b)** **(c)**

(d) **(e)** **(f)**

FIGURE 3. Time domain simulation of a steel plate of thickness 0.001 and dimensions $0.4 \times 0.6\text{m}^2$. The plate presents $N_\Phi = 50$ transverse modes and $N_\Psi = 12$ in-plane modes. The plate is activated using raised cosine of amplitude $p_m = 100\text{N}$ and $T_{wid} = 0.001\text{s}$, applied at the point $[0.3L_x \quad 0.3L_y]$. The output is recorded at $[0.7L_x \quad 0.3L_y]$. **(a)**: time series of normalised displacement at output point; **(b)**: time series of normalised velocity at output point; **(c)**: time series of normalised acceleration at output point; **(d)**: displacement spectrogram at output point; **(e)**: velocity spectrogram at output point; **(f)**: acceleration spectrogram at output point.

- *thermoelastic effects*: the vibrational energy is in this case transformed into heat generated by the friction between the molecules when the plate is deformed;
- *visoelastic effects*: the vibrational energy is lost to viscosity;
- *radiation damping*: the continuity equation between the air and the surface of the plate allows to define a "coincidence frequency" after which the flexural waves developing on the plate are passed into the surrounding medium (air). This happens when the speed of the flexural waves corresponds to the speed of the sound in air, denoted by c. The coincidence

frequency can be given as

$$f_r = \frac{c^2}{2\pi}\sqrt{\frac{12\rho(1-\nu^2)}{Eh^2}}; \tag{6.5}$$

- *edge damping*: losses due to clamps and supports of the vibrating plate.

Lambourg [54] tried to quantify experimentally the modal damping factors. He obtained results analogous to those presented in Fig. 4. In Fig. 4(a), one can appreciate that, after the coincidence frequency, the damping ratios increase sensibly. This means that the radiation damping is prominent in the frequency range past that frequency. On the other hand, at smaller frequencies the viscoelastic and thermoelastic effects dominate, and the modal damping ratios present variations around a supposedly mean value (Fig. 4(b)).

Arcas [5] points out that, for a thin plate with simply-supported boundary conditions, the contribution of the thermoelastic effect can be given as

$$\gamma_{th}(f) = \frac{4\pi^2 f^2 RC}{2(4\pi^2 f^2 h^2 + C/h^2)}, \tag{6.6}$$

where R, C, are constants depending on the thermal properties of the material (temperature, conductivity, ...). For steel, $C \approx 1.8 \cdot 10^2$ [rad/m^2/s] and $R \approx 9.7 \cdot 10^3$ (nondimensional constant).

In view of an application to wave turbulence, Humbert experimented with a thin steel plate ($h \approx$ 0.5mm) for which the coincidence frequency can be estimated to be $f_r \approx$20kHz [47]. In the audible range for such a plate, then, the viscoelastic and thermoelastic effects dominate, and Humbert measures a power-law dependence for the loss mechanism, as in

$$\gamma_h(f) = 0.05 f^{0.6} \quad [s^{-1}]. \tag{6.7}$$

An estimate of the loss mechanism in plates is beyond the scope of the present Thesis. However, the modal code was developed precisely because of the lack of a numerical models able to simulate a general damping law. In a Finite Difference environment, even a (seemingly) simple law such as (6.7) becomes a numerical challenge, but in the modal code, one just needs to set the damping coefficients in Eq. (2.57) as

$$\chi_s(f_s) = \frac{0.05}{4\pi}\,(f_s)^{-0.4}. \tag{6.8}$$

In this way, the discrete set of points given by $2\chi_s\omega_s$ will belong to the continuous curve $\gamma_h(f)$ of Eq. (6.7), see Fig. 6. Hence, very complicated damping laws can be fitted in the modal code, which is not possible in a Finite Difference scheme.

In his book [8], Bilbao proposes two damping laws for his finite difference scheme; these laws are summarised in Eq. (2.58) and they are global laws proportional to, respectively, the velocity field and the Laplacian of the velocity field. The coefficients σ_0, σ_1 can be chosen according to the plate reverberation time, which is is the typical time after which the Sound Pressure Level drops by 60dB (see [5]).

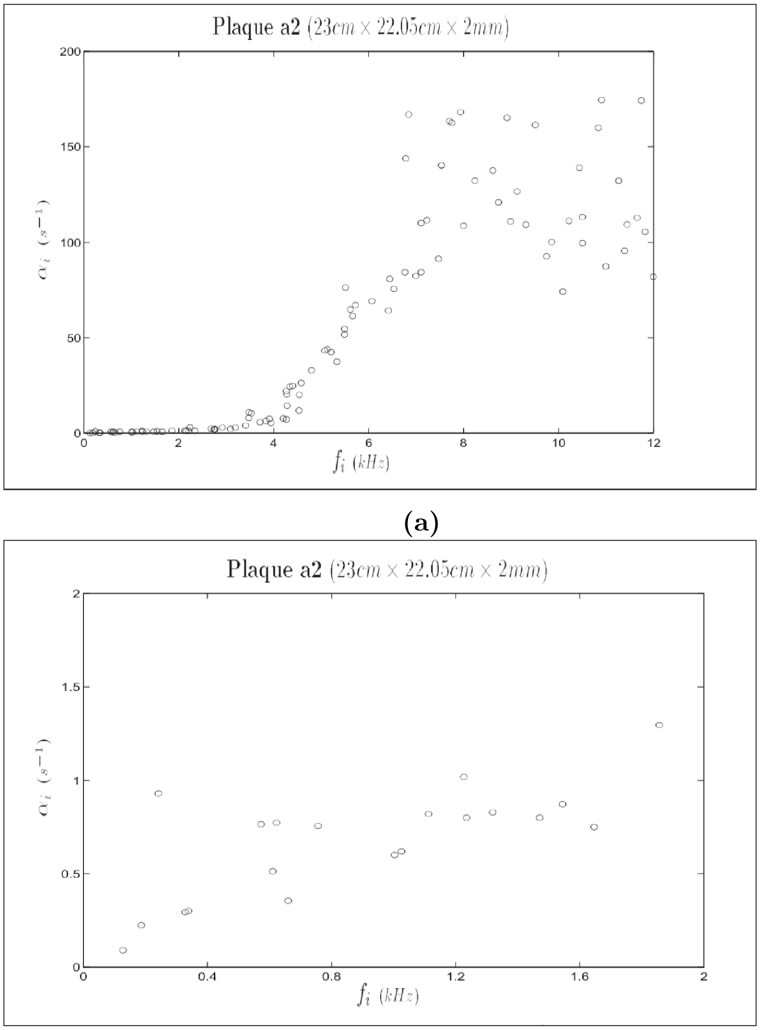

(a)

(b)

FIGURE 4. Damping ratios measured by Lambourg for a plate of dimensions $L_x \times L_y \times h = 0.23\text{m} \times 0.2205\text{m} \times 2\text{mm}$ vibrating in a linear regime. Figures are taken from reference [54].

For plates, one may choose them as

$$\sigma_0 \sim 0.38\rho h \quad [s^{-1}]; \qquad \sigma_1 \sim 1.5 \cdot 10^{-4} \rho h L_x L_y \quad [s^{-1}]. \tag{6.9}$$

Such parameters give realistic decay times for plates of different sizes, see Fig. 5 for examples, where it is seen that the waveforms fall to zero about 10s after activation.

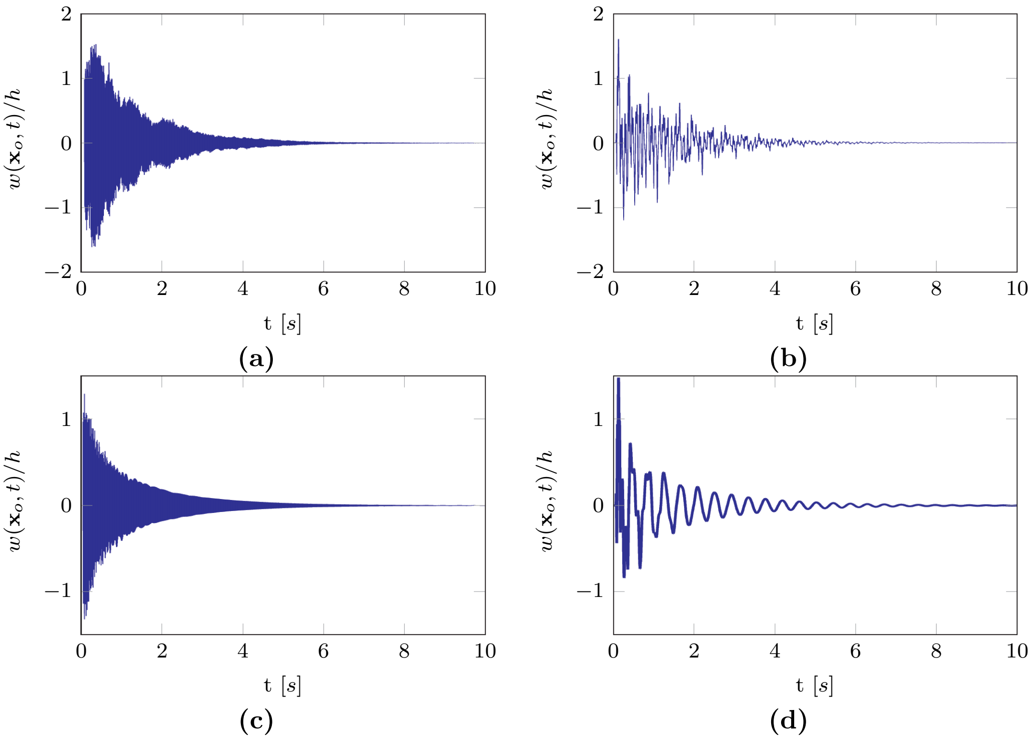

FIGURE 5. Time domain simulation of two steel square plates of thickness 0.5mm. The plates present $N_\Phi = 20$ transverse modes and $N_\Psi = 12$ in-plane modes. The plates are activated using raised cosine of amplitude $p_m = 150$N and $T_{wid} = 0.1$ms, applied at the point $[0.3L_x \;\; 0.3L_y]$. The output is recorded at $[0.7L_x \;\; 0.3L_y]$. The dimensions of the plates are [0.1m 0.1m] (**(a)** and **(c)**) and [1m 1m] (**(b)** and **(d)**). Figures **(a)** and **(b)** were obtained by setting $\sigma_0 = 0.38\rho h \;\; [s^{-1}]$ and $\sigma_1 = 0$; Figures **(c)** and **(d)** were obtained by setting $\sigma_0 = 0$ and $\sigma_1 = 0.015\rho h L_x L_y \;\; [s^{-1}]$, as suggested in Eq. (6.9).

6.1.4. Number of in-plane and transverse modes. When using a modal approach, a question arises as to how many modes one should retain. This is an important point because the memory and calculation requirements grow significantly as the number of modes is increased. Note that the sampling rate at which the scheme is run has also a large influence on the calculation time. All the simulations presented in this chapter can be obtained by running the Störmer-Verlet scheme, as in Eq. (2.79). Although the stability of such a scheme cannot be guaranteed in a nonlinear regime, for impulsive loading (like a strike) on a damped plate a sensible choice for the sampling rate is twice as much the limit of stability for the associated linear system, Eq. (2.82). Hence, for the following it is intended that $F_s = 2F_s^{lim} = f^{lim}$, where f^{lim} is the largest eigenfrequency (measured in Hz)

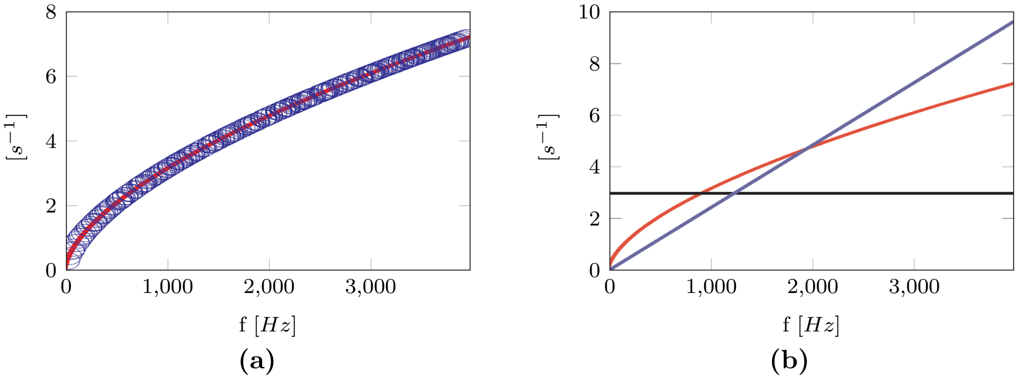

FIGURE 6. **(a)**: Damping law proposed by Humbert, Eq. (6.7) (red thick line) and damping coefficients χ_s set in order to belong to the curve (blue circles),as in Eq. (6.8); **(b)**: damping laws for a steel plate of dimensions $[0.403m \;\; 0.618m]$; the blue and black line are obtained by setting σ_0, σ_1 as suggested in Eq. (6.9).

of the system. Note that the energy diagrams shown in this section are obtained by running the conservative scheme, (2.85) (for which the discrete energy counterparts exist). However, when the calculation times are presented, these refer to the Störmer-Verlet scheme.

Consider first the number of in-plane modes, N_Ψ. A criterion to select this number might be given by considering the convergence of the coupling coefficients, as explained in Chapter 4: one selects as many in-plane modes as the required accuracy. As an order of magnitude, this would correspond to setting $N_\Psi \approx 500$ to obtain a convergence up to the fourth significant digit for the coupling coefficient $\Gamma^{50}_{50,50,50}$. For coupling coefficients of higher modes, N_Ψ increases drastically for such a convergence limit. In view of an application to sound synthesis, then, one must look out for a compromise amongst precision, memory requirements and calculation time. As pointed out in section 2.7.3, the modal code is written in terms of the H tensor, in order to maximise the number of transverse modes that one can keep in a simulation. This means that, in the time integration scheme, at each time step one must sum over the index defining the in-plane function; hence, increasing N_Ψ corresponds to increasing the computational time, as well as occupying memory that could possibly be allocated for more transverse modes. Ideally, one wants to keep enough in-plane modes in order to generate a nonlinear dynamics with a cascade of energy, but at the same time N_Ψ must be kept at a minimum in order to maximise the efficiency of the scheme.

As usual in this cases, direct experimentation with different parameters can help to shed some light on the problem. Three cases are here considered, namely a plate activated in a (almost) linear regime, a weakly nonlinear regime, and a strongly nonlinear regime. The question of the number of transverse modes is first addressed, followed by a discussion of the number of in-plane modes. Before running a massive simulation, it is useful to run a simulation with, say, $N_\Phi \sim 10$, $N_\Psi \sim 10$ and to look at the displacement waveform. This parameters are obviously too small for sound synthesis. However,

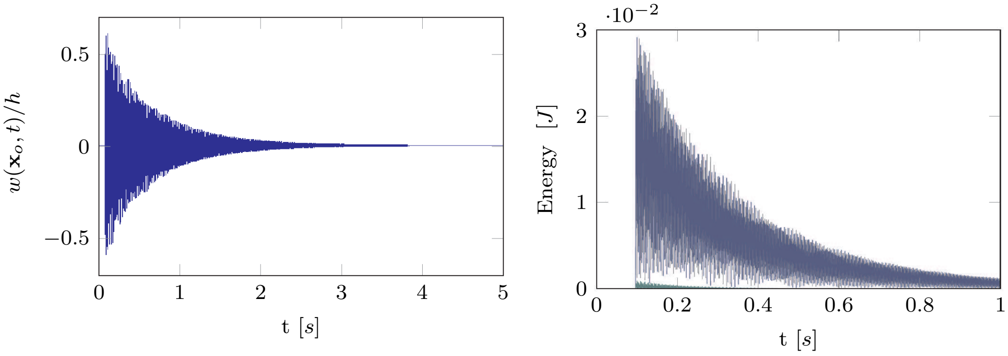

(a) **(b)**

FIGURE 7. **(a)**: Time domain simulation of a steel plate of dimensions $L_x \times L_y = 0.203\text{m} \times 0.118\text{m}$ and thickness $h = 1\text{mm}$, activated with a raised cosine of amplitude $p_m = 100N$ and duration $T_{wid} = 0.8\text{ms}$; the total number of transverse modes is $N_\Phi = 100$, and the total number of in-plane modes is $N_\Psi = 12$. Damping coefficients selected as in Eq. (6.8). **(b)**: Kinetic energy (grey), linear potential energy (navy) and nonlinear potential energy (green), showing that the plate is vibrating in a linear regime.

they suffice to understand the order of magnitude of the displacement and the decay characteristic for a plate of typical size $L_x \times L_y \times h \approx 0.5\text{m} \times 0.5\text{m} \times 1\text{mm}$; hence this serves a preliminary test that allows to understand how to set the forcing parameters and the damping.

If the displacement is smaller than the thickness, then the plate is vibrating in a linear regime. Once that the forcing and damping parameters are set, one may increase N_Φ (obviously there is no need to change N_Ψ because the dynamics is linear; to save memory and time one may as well set this parameter to zero). A plate vibrating in a linear regime produces a bell-like sound; pitch glides and crashes are not reproduced. The harmonics in the higher range, however, produce a nice effect when the damping ratios are set to appropriate values. In this case, it can be appreciated that $N_\Phi \sim 100$ suffices to catch the most salient features of the sound. For such a simulation, the calculation time in MATLAB (using a fully vectorised code) is of the order of 10s per second of simulation, on a plate of dimensions $L_x \times L_y \times h = 0.203\text{m} \times 0.118\text{m} \times 1\text{mm}$. See Fig. 7 where the displacement and the corresponding energies are plotted versus time.

A plate vibrates in a weakly nonlinear regime when $w(\mathbf{x}_o, t) \sim h$. For a plate of dimensions $L_x \times L_y = 0.203\text{m} \times 0.118\text{m}$ and thickness $h = 0.5\text{mm}$, this can be achieved by forcing the plate with a raised cosine of amplitude p_m=15N and half width $T_{wid} = 2\text{ms}$. In this case, a small cascade of energy is produced, resulting in a slight crashing effect and moderate pitch glides. In Fig. 8, the number of stress function is chosen as $N_\Psi = 12$, and the number of transverse modes is $N_\Phi = 120$. With these settings, the calculation time is about 12s per second of simulation.

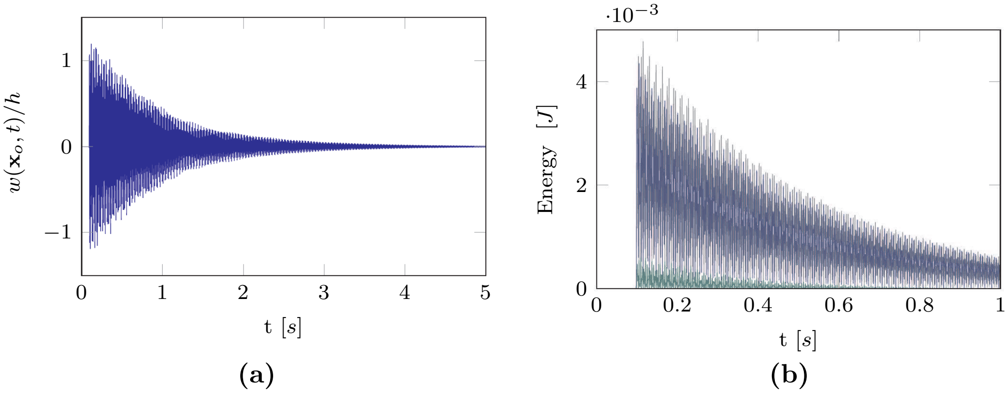

(a) **(b)**

FIGURE 8. **(a)**: Time domain simulation of a steel plate of dimensions $L_x \times L_y = 0.203\text{m} \times 0.118\text{m}$ and thickness $h = 0.5\text{mm}$, activated with a raised cosine of amplitude $p_m = 15$ and duration $T_{wid} = 2\text{ms}$; the total number of transverse modes is $N_\Phi = 120$, and the total number of in-plane modes is $N_\Psi = 12$. Damping coefficients selected as in Eq. (6.8). **(b)**: Kinetic energy (grey), linear potential energy (navy) and nonlinear potential energy (green), showing that the plate is vibrating in a weakly nonlinear regime.

Finally, a strong nonlinear regime is activated. The dimensions are chosen as $L_x \times L_y = 0.203\text{m} \times 0.218\text{m}$, $h = 0.5\text{mm}$. The plate is forced at $p_m = 100\text{N}$ and $T_{wid} = 2.5\text{ms}$ (see Fig.9). For such a simulation, $N_\Psi = 12$, and $N_\Phi = 450$ are chosen. Given the dimensions of the plate, the sound resembles that of a small gong or a small crash cymbal. With these settings, about 80s per second of simulation are needed.

For all the previous simulations, the number N_Ψ has been kept to a bare minimum in order to improve the computation time. For the linear case, increasing this parameter would be a waste of memory and time as the in-plane modes are not activated in a linear regime. For a weakly nonlinear regime, increasing the number of in-plane modes does not lead to a sensible increment of the quality of the simulation. Hence, one may safely assume that the ratio $N_\Phi/N_\Psi = 10$ suffices to simulate a plate vibrating in such a regime. When the strong nonlinear regime is activated, increasing N_Ψ to 90 seems to improve the sound (in terms of a less artificial sounding cascade). However, the improvement is really minimal, the simulation with $N_\Psi = 12$ being already sufficiently good. In any case, one may set the ratio $N_\Phi/N_\Psi = 5$ for a strong nonlinear regime.

The reader should take these parameters with caution. As pointed out before, such parameters are too small to guarantee an accurate calculation of the coupling coefficients. However, from a sound synthesis point of view, the role of the nonlinear couplings is to create a cascade of energy and to change the periods of vibration of the eigenmodes, corresponding to, respectively, a crashing sound and pitch glides (which are extremely inharmonic effects). Hence, in this sense, the accuracy of the

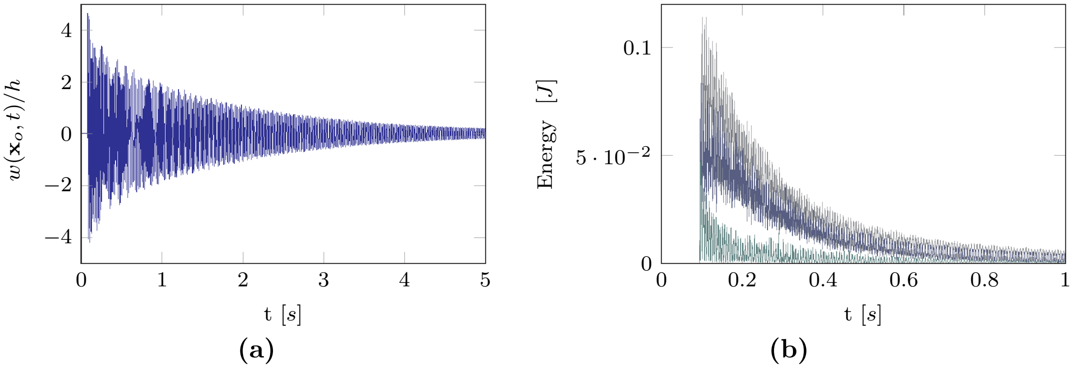

FIGURE 9. **(a)**: Time domain simulation of a steel plate of dimensions $L_x \times L_y =$ 0.203m $\times$ 0.218m and thickness $h = 0.5$mm, activated with a raised cosine of amplitude $p_m = 100$N and duration $T_{wid} = 2.5$ms; the total number of transverse modes is $N_\Phi = 450$, and the total number of in-plane modes is $N_\Psi = 12$. Damping coefficients selected as in Eq. (6.8). **(b)**: Kinetic energy (grey), linear potential energy (navy) and nonlinear potential energy (green), showing that the plate is vibrating in strongly nonlinear regime.

nonlinear mechanism is not of extreme importance because it only bears information regrading the perceived "naturalness" of such features. In turn, the number of the in-plane modes should be set according to the taste of the performer, rather than on an objective prescription.

The question remains on how to choose the number of transverse modes. An answer might come in this case by analysing the spectrogram of the simulation. Fig. 10(a) depicts the displacement spectrogram of the strongly nonlinear regime obtained running a Finite Difference code. It is evident that, for such a simulation, the energy cascade and the damping act on the system with opposite effects: the cascade would tend to activate more and more frequencies, while damping removes energy from the system so that, at some point, the eigenmodes start losing energy. At the peak of the cascade activity, it is plausible to identify a "peak frequency" which can be defined as the highest frequency activated by the cascade. When running the modal code, it is important that the number of transverse mode reaches the peak frequency (or at least close to that). If the peak frequency is correctly identified, then adding more transverse modes will not improve the quality of the simulation, despite the evident modal cutoff. Fig 10(b) shows that, in this case, $N_\Phi = 250$ is not a large enough number. In Fig 10(c) the number of transverse modes is increased to 450, past the peak frequency.

As a concluding remark, it was seen that, for fairly thin plates, $N_\Phi = 450$, $N_\Psi = 90$ are large enough parameters to give rise to very rich sounds. An estimate of how "thin" this plate is can be conducted by introducing the nondimensional parameter α, obtained by dividing the typical size of the surface of the plate (for instance $\sqrt{L_x L_y}$) by the plate thickness. For the strongly nonlinear simulation presented in this section one has $\alpha = \sqrt{L_x L_y}/h \sim 420$. On a machine equipped with MATLAB 64bit

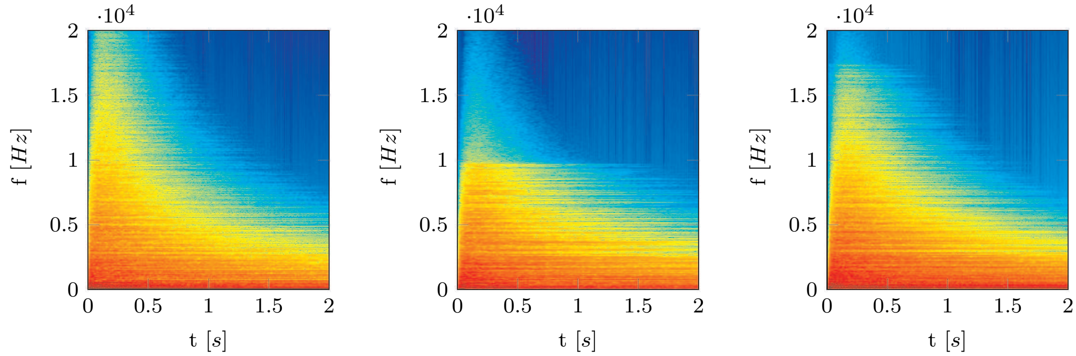

(a) **(b)** **(c)**

FIGURE 10. Displacement spectrograms of a a steel plate of dimensions $L_x \times L_y = 0.203\text{m} \times 0.218\text{m}$ and thickness $h = 0.5\text{mm}$, activated in a strongly nonlinear regime with a raised cosine of amplitude $p_m = 100\text{N}$ and duration $T_{wid} = 2.5\text{ms}$. **(a)**: Finite Difference scheme with sampling rate 100kHz and grid size 35×37 points.**(b)**: $N_\Phi = 120$, $N_\Psi = 18$. **(c)**: $N_\Phi = 450$, $N_\Psi = 18$.

and 8G of RAM, the physical limit for the present code is $N_\Phi \sim 650$, $N_\Psi \sim 162$, which suffices largely to simulate a plate of $\alpha \sim 700$. An example is given by a plate of about 0.5m per side, 0.8mm thick ($\alpha = 625$). With carefully chosen parameters, a time domain simulation of such a plate resembles closely the sound of a thunder plate, especially when run on powerful speakers able to simulate the vast dynamic range of this plate. Note that the calculation time under such conditions is about 30min per second of simulation.

6.2. Comparison between the modal approach and the Finite Difference scheme

In this section, the finite difference scheme and the modal method are compared when run using the same forcing and damping parameters. Again, the comparison will consider the cases of plates vibrating in linear, weakly nonlinear and strongly nonlinear regimes. The damping has been tuned by selecting an appropriate value for σ_1, because it gives a more natural decay queue. The three cases are summarised as follows

Linear regime

- dimensions: $L_x \times L_y \times h = 0.2\text{m} \times 0.1\text{m} \times 1\text{mm}$
- forcing parameters: $p_m = 100\text{N}$, $T_{wid} = 0.8\text{ms}$
- damping factor: $\sigma_1 = 0.002\text{s}^{-1}$
- FD grid: 24×11; sampling rate: 100kHz
- Number of modes: $N_\Phi = 100$, $N_\Psi = 12$

Weakly nonlinear regime

- dimensions: $L_x \times L_y \times h = 0.2\text{m}\times 0.1\text{m}\times 0.5\text{mm}$
- forcing parameters: $p_m = 35\text{N}$, $T_{wid} = 0.4\text{ms}$
- damping factor: $\sigma_1 = 0.0005\text{s}^{-1}$

- FD grid: 35×16; sampling rate: 100kHz
- Number of modes: $N_\Phi = 120$, $N_\Psi = 12$

Strongly nonlinear regime

- dimensions: $L_x \times L_y \times h = 0.3\text{m}\times 0.3\text{m}\times 0.5\text{mm}$
- forcing parameters: $p_m = 50\text{N}$, $T_{wid} = 3\text{ms}$
- damping factor: $\sigma_1 = 0.0008\text{s}^{-1}$
- FD grid: 35×16; sampling rate: 100kHz
- Number of modes: $N_\Phi = 250$, $N_\Psi = 50$

Note that, for the Finite Difference code, the grid size is chosen according the sampling rate, as in Eq. (3.25).

The linear case is sketched in Fig. 11. When listening to the samples, the Finite Difference scheme returns an overall less high-pitched sound: this happens because the eigenfrequencies of the Finite Difference system converge from below (see remarks in Chapter 3), and, in a linear regime, they are basically the only activated frequencies. Calculation times for the current settings can be given as 90s per second for the Finite Differences and 10s per second for the modes.

The weakly nonlinear case is summarised in Fig 12. In this case, the waveforms and spectrograms are very similar. Note the modal truncation in Fig.12(d). Indeed, it looks quite crude when compared to the spectrogram obtained running the Finite Difference scheme. However, the modes past the truncation are activated in a linear way, and thus they do not contribute to the overall "quality" of the sound. Calculation times for these settings can be given as 90s per second for the Finite Difference scheme, and 12s per second for the modes.

The last case presented here is summarised in Fig. 13. In this case, the waveforms and spectrograms are quite different. Note that the nondimensional size of the plate is in this case $\alpha = 600$, and thus, in the modal approach, the number of modes retained is not sufficient. In fact, the nonlinear cascade flows well beyond the limit imposed by the last mode (see Fig. 13(c)). In this case, the simulation coming from the Finite Difference scheme is somehow better, because it includes the effect of high-frequency modes being activated by the nonlinear cascade. The modal approach, on the other hand, returns a reasonable simulation, although the number of transverse modes should be increased. Calculation times for these settings can be given as 90s per second for the Finite Difference scheme, and 50s per second for the modes.

6.3. Final Remarks

In this chapter sound synthesis results were shown. It was seen that, under a careful selection of parameters, the dynamics of flat plates can simulate, to a first approximation, the sound of a gong or a cymbal. The modal approach was shown to be particularly useful because of the possibility of adding arbitrary damping ratios on each one of the modes. When compared to the Finite Difference scheme, the modal approach gives comparable results in the time and frequency domains. Despite the modal truncation (which looks quite crude on the spectrograms) the number of modes retained in the simulations need not be extremely large, especially for the linear and weakly nonlinear cases. For strongly nonlinear vibrations, the number of modes to be retained depends on how "thin" the

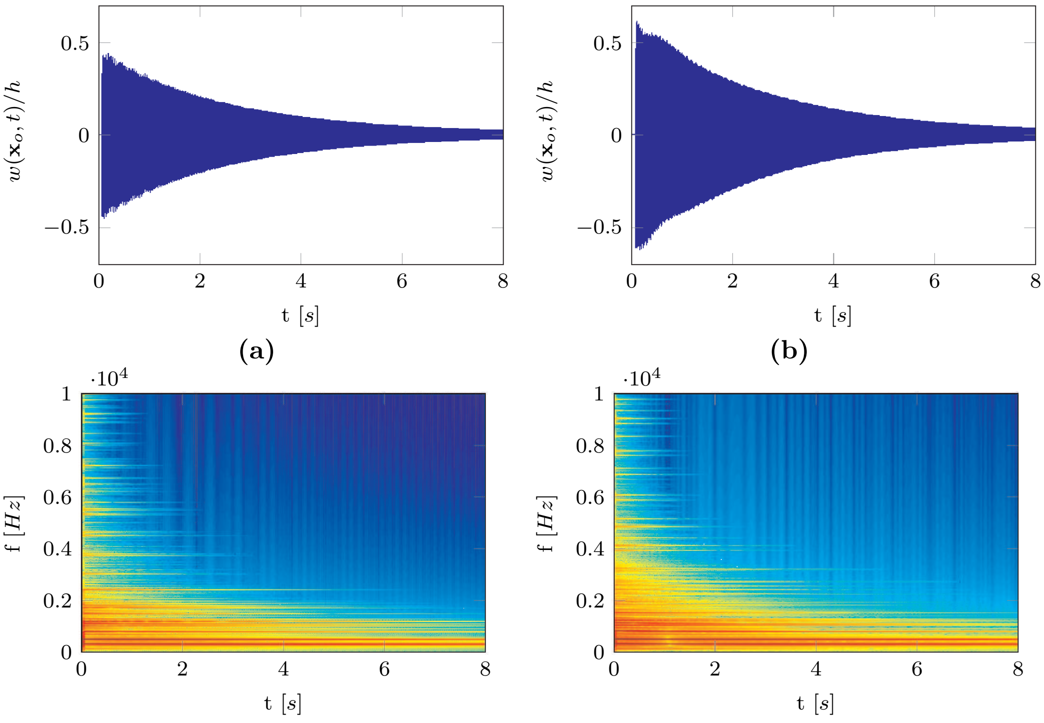

(a) **(b)**

(d) **(e)**

FIGURE 11. Comparison between Finite Difference and modes for a steel plate vibrating in a linear regime. Time domain representation of the displacement for Finite Differences (**(a)**) and modes (**(b)**); velocity spectrograms for Finite Differences (**(c)**) and modes (**(d)**).

plate is. A study in this sense was conducted and it was seen that, for plates of nondimensional size $\alpha = 420$, 450 transverse modes suffice to catch the dynamics of strongly nonlinear vibrations (at least in a sound synthesis perspective). For plates of larger α, however, this number must be increased. The number of Airy stress function modes can be set to 1/5 of the number of transverse modes for strongly nonlinear vibrations, and to 1/10 for weakly nonlinear vibrations.

As compared to the Finite Difference scheme, the modal approach really becomes an alternative. The ”quality” of the sounds cannot be completely justified on an objective basis. For sure, the modal approach offers possibilities that are unaccessible to a Finite Difference code (especially in terms of loss implementation), and thus it should be regarded as an alternative scheme to do sound synthesis. Sound synthesis of gongs in weakly and strongly nonlinear regimes using a modal approach has never been performed before this work (to the knowledge of the author), and thus this should be regarded as one of the major results of this thesis.

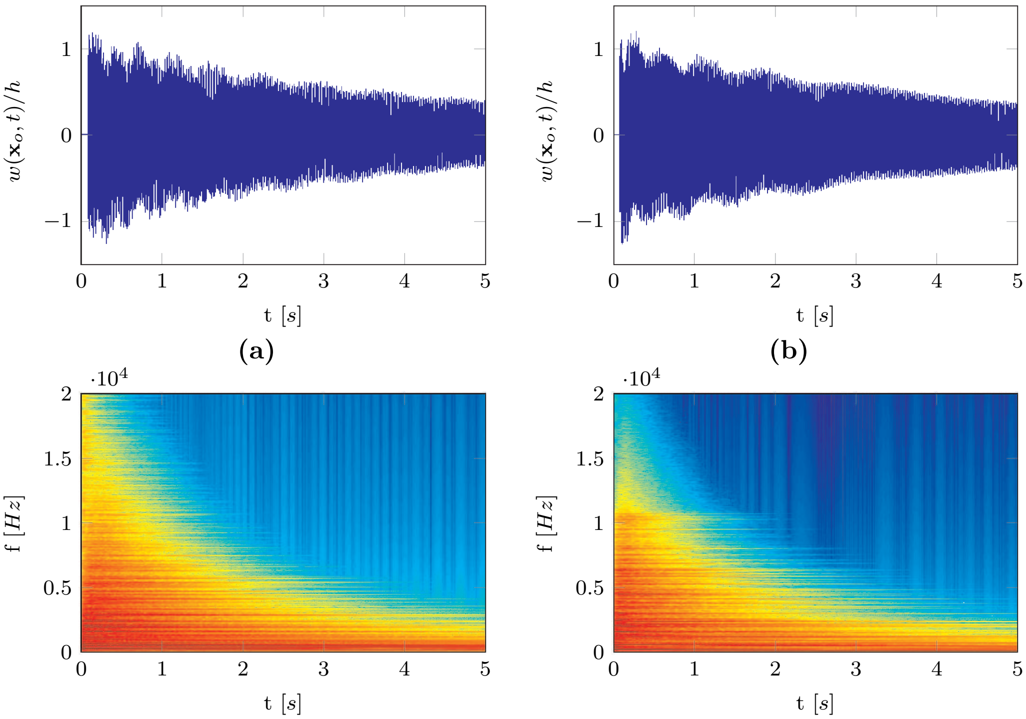

(a) **(b)**

(d) **(e)**

FIGURE 12. Comparison between Finite Difference and modes for a steel plate vibrating in a weakly nonlinear regime. Time domain representation of the displacement for Finite Differences ((**a**)) and modes ((**b**)); velocity spectrograms for Finite Differences ((**c**)) and modes ((**d**)).

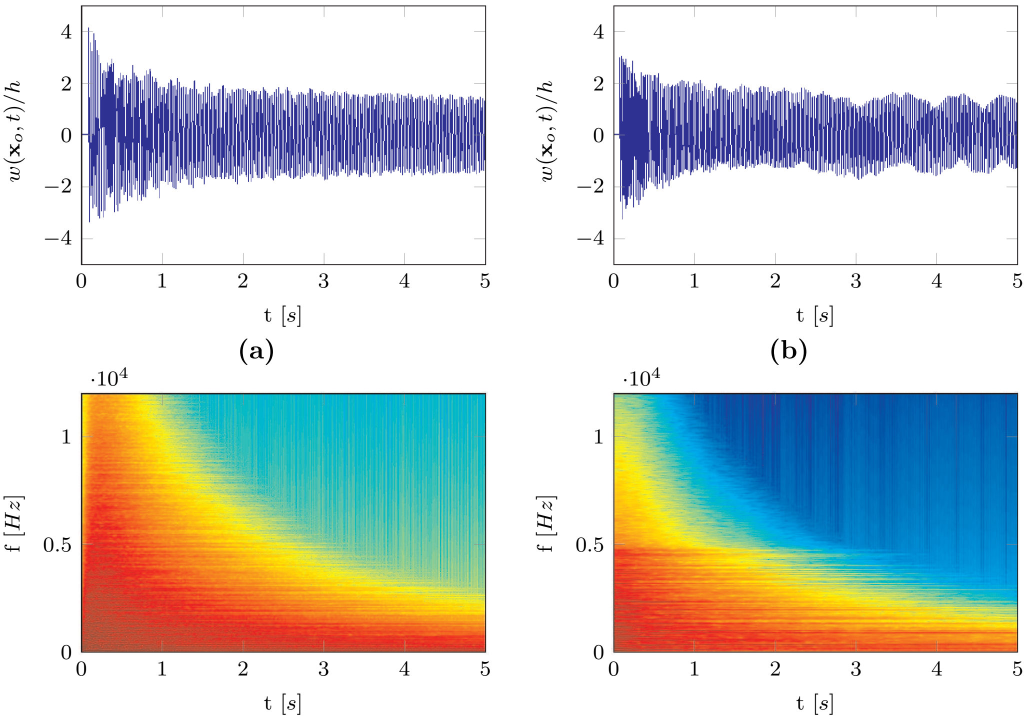

(a) **(b)**

(d) **(e)**

Figure 13. Comparison between Finite Difference and modes for a steel plate vibrating in a strongly nonlinear regime. Time domain representation of the displacement for Finite Differences ((**a**)) and modes ((**b**)); velocity spectrograms for Finite Differences ((**c**)) and modes ((**d**)).

Conclusions and Perspectives

Conclusions

This thesis presented a solid numerical method to simulate the dynamics of von Kármán rectangular plates. The method is based on modal projection and thus a great deal of work was spent in order to find robust strategies to calculate the eigenmodes of the plate equations under various boundary conditions. Particularly, the fully clamped linear plate equation was solved with great precision, and a solid eigenvalue routine was developed using the Rayleigh-Ritz method in order to compute hundreds of modes with great precision.

The case of the completely linear free plate was also solved using a simple expansion function series and the Rayleigh-Ritz method. Not only this solution is in agreement with previously published results, but it is also simpler and allows to look for high-frequency eigenmodes. The same expansion function series was used to treat the more practical problem of a plate with free edges supported at its centre.

The solution to the clamped plate problem allowed to treat in some detail the case of a simply supported von Kármán plate with in-plane movable edges, because the boundary conditions for the stress function are formally identical to those of a linear clamped plate. For such a problem, the von Kármán equations were discretised on the linear eigenspaces, reducing the original system of Partial Differential Equations to a system of coupled Ordinary Differential Equations. The coupling coefficients were calculated with great precision and a stable, energy conserving time-integration scheme was developed for the system of Ordinary Differential Equations. Symmetry properties and useful vectorisation strategies allowed to construct a numerical code, written in MATLAB, able to simulate the dynamics of von Kármán plates with hundreds of interacting modes.

The scheme was used primarily to perform sound synthesis of gong-like sounds. For the first time, a modal approach was used to reproduce the dynamics of plates ranging from a linear regime to a strongly nonlinear regime. From a sound synthesis perspective, the modal approach should be regarded as an alternative to other numerical schemes, namely Finite Difference schemes. Although it is difficult to quantify objectively the quality of the reproduced sounds, the modal scheme allows to implement a very rich damping mechanism and thus it is, in this sense, more versatile than a Finite Difference scheme.

The modal scheme was also used to calculate the Nonlinear Normal Modes of the von Kármán plate. The scheme allowed for the first time to draw bifurcation branches to very high amplitudes showing a very rich dynamics, particularily because of the presence of many internal resonances. The

Hamiltonian dynamics was seen to be strongly modified by the introduction of damping and forcing terms.

Finally, simulations obtained by running an energy conserving Finite Difference scheme allowed to investigate the case of a plate in a strongly nonlinear regime displaying a cascade of energy, and thus studied within the framework of Wave Turbulence. The case of an unstationary, undamped turbulence was treated for the first time in the case of plates. A self-similar dynamics was recovered, and scaling laws proposed. The case of a stationary, undamped turbulence was recovered by stopping the forcing, and it was seen that the shape of the spectra is highly affected by forcing. In particular, the spectra flatten in the absence of forcing. Geometrical imperfections were also added to the simulated plate, and it was seen that they do not introduce significant changes in the scaling properties of the system.

Perspectives

This work has prototyped a modal scheme for sound synthesis of gong-like sounds. Its capabilities have not been exploited in full. Particularily, it is advisable to port the scheme to another programming language than MATLAB, notably C. In this way, the scheme could benefit from improved calculation times and memory requirements.

A useful extension of this work could be represented by developing a scheme for circular plates. In this case, analytical solutions for the eigenmodes exist for all boundary conditions in the form of combinations of Bessel functions. Thus, it should be possible to calculate the nonlinear coupling coefficients for different combinations of boundary conditions, including the important case of a plate with a free transversely and in-plane edge. Once that the coupling coefficients are calcualated, one may use the temporal scheme developed for this work is order to solve the system of Ordinary Differential Equations. The case of a spherical shallow shell could be treated thereafter. Such geometries are indeed very close to those of a gong or cymbal.

This work has proved that modal synthesis is possible even for strongly nonlinear regimes, and thus it could represent a valid alternative when approaching the problems of the circular plate or the spherical cap, which are notoriously difficult to treat in the context of Finite Difference schemes.

APPENDIX A

Matrices for the clamped plate eigenvalue problem

The stiffness and mass matrices for the clamped plate problem are set up as follows:

$$K(i,j) = K(mn,pq) =$$

$$\int_0^{L_x} X_m''(x)X_p''(x)dx \int_0^{L_y} Y_n(y)Y_q(y)dy + \int_0^{L_x} X_m(x)X_p(x)dx \int_0^{L_y} Y_n''(y)Y_q''(y)dy + 2\int_0^{L_x} X_m'(x)X_p'(x)dx \int_0^{L_y} Y_n'(y)Y_q'(y)dy$$

$$M(i,j) = M(mn,pq) = \int_0^{L_x} X_m(x)X_p(x)dx \int_0^{L_y} Y_n(y)Y_q(y)dy$$

The integrals are

$$\int_0^{L_x} X_m''(x)X_p''(x)dx =$$

$$\begin{cases} 720/L_x^3; & \text{if } m = p = 0 \\ (\pi^4 m^4 - 672(-1)^m - 768)/(2L_x^3); & \text{if } m = p \neq 0 \\ 0 & \text{if } m \text{ or } p = 0 \text{ and } m \neq p \\ -24(7(-1)^m + 7(-1)^p + 8(-1)^m(-1)^p + 8)/L_x^3; & \text{otherwise} \end{cases}$$

$$\int_0^{L_x} X_m(x)X_p(x)dx =$$

$$\begin{cases} 10L_x/7; & \text{if } m=p=0 \\ 67L_x/70-(-1)^m L_x/35-768L_x/(\pi^4m^4)-672(-1)^m L_x/(\pi^4m^4); & \text{if } m=p\neq 0 \\ 3L_x((-1)^p+1)(\pi^4p^4-1680))/(14\pi^4p^4); & \text{if } m=0 \text{ and } p\neq 0 \\ 3L_x((-1)^m+1)(\pi^4m^4-1680))/(14\pi^4m^4); & \text{if } p=0 \text{ and } m\neq 0 \\ -(L_x(11760(-1)^m+11760(-1)^p-16\pi^4m^4+13440(-1)^m(-1)^p+ & \\ (-1)^m\pi^4m^4+(-1)^p\pi^4m^4-16(-1)^m(-1)^p\pi^4m^4+13440))/(70\pi^4m^4) & \\ -(L_x(13440m^4+11760(-1)^m m^4+11760(-1)^p m^4+13440(-1)^m(-1)^p m^4))/(70\pi^4m^4p^4); & \text{otherwise} \end{cases}$$

$$\int_0^{L_x} X_m''(x)X_p(x)dx =$$

$$\begin{cases} -120/(7L); & \text{if } m=p=0 \\ -(768\pi^2m^2-47040(-1)^m+35\pi^4m^4+432(-1)^m\pi^2m^2-53760)/(70L_x\pi^2m^2); & \text{if } m=p\neq 0 \\ -(60((-1)^p+1)(\pi^2p^2-42))/(7L_x\pi^2p^2); & \text{if } m=0 \text{ and } p\neq 0 \\ -(60((-1)^m+1)(\pi^2m^2-42))/(7L_x\pi^2m^2); & \text{if } p=0 \text{ and } m\neq 0 \\ (24(m^2+p^2)(7(-1)^m+7(-1)^p+8(-1)^m(-1)^p+8))/(L_x\pi^2m^2p^2) & \\ -((108(-1)^m+108(-1)^p+192(-1)^m(-1)^p+192))/(35L_x); & \text{otherwise} \end{cases}$$

and similarly for the integrals involving the functions Y.

APPENDIX B

Matrices for the free plate eigenvalue problem

The stiffness and mass matrices for the completely free plate are set up as follows:

$$K(i,j) = K(mn,pq) =$$

$$\begin{aligned}
&\int_0^{L_x} X''_m(x)X''_p(x)dx \int_0^{L_y} Y_n(y)Y_q(y)dy + \int_0^{L_x} X_m(x)X_p(x)dx \int_0^{L_y} Y''_n(y)Y''_q(y)dy + \\
&\int_0^{L_x} X''_m(x)X_p(x)dx \int_0^{L_y} Y_n(y)Y''_q(y)dy + \int_0^{L_x} X_m(x)X''_p(x)dx \int_0^{L_y} Y''_n(y)Y_q(y)dy - \\
&(1-\nu)\left[\int_0^{L_x} X''_m(x)X_p(x)dx \int_0^{L_y} Y_n(y)Y''_q(y)dy + \int_0^{L_x} X_m(x)X''_p(x)dx \int_0^{L_y} Y''_n(y)Y_q(y)dy\right. \\
&\left.-2\int_0^{L_x} X'_m(x)X'_p(x)dx \int_0^{L_y} Y'_n(y)Y'_q(y)dy\right]
\end{aligned}$$

$$M(i,j) = M(mn,pq) = \int_0^{L_x} X_m(x)X_p(x)dx \int_0^{L_y} Y_n(y)Y_q(y)dy$$

The integrals are

$$\int_0^{L_x} X''_m(x)X''_p(x)dx =$$

$$\begin{cases}
(144L_x)/(L_x^2-12)^2; & \text{if } m=p=0 \\
(36((-1)^m+1)^2(L_x^2+\pi^2m^2)^2)/(L_x^3(L_x^2-12)^2)+(\pi^3m^3(2pim))/(4L_x^3); & \text{if } m=p\neq 0 \\
(72((-1)^p+1)(L_x^2+\pi^2p^2))/(L_x(L_x^2-12)^2); & \text{if } m=0 \text{ and } p\neq 0 \\
(72((-1)^m+1)(L_x^2+\pi^2m^2))/(L_x(L_x^2-12)^2); & \text{if } p=0 \text{ and } m\neq 0 \\
(36((-1)^m+1)((-1)^p+1)(L_x^2+\pi^2m^2)(L_x^2+\pi^2p^2))/(L_x^3(L_x^2-12)^2); & \text{otherwise}
\end{cases}$$

$$\int_0^{L_x} X_m(x)X_p(x)dx =$$

$$\begin{cases}
(6L_x(L_x^4-20L_x^2+120))/(5(L_x^2-12)^2); & \text{if } m=p=0 \\[1em]
L_x/2+L_x^3((4(L_x^2+\pi^2m^2)^2(2L_x^2+6(-1)^m+(-1)^mL_x^2-6)^2)/(3L_x^6(L_x^2-12)^2)+ & \\
(2(3(-1)^m+3)(L_x^2+\pi^2m^2)^2(L_x^2+6(-1)^m-6))/(3L_x^4(L_x^2-12)^2))+ & \\
((L_x^2+\pi^2m^2)^2(L_x^2+6(-1)^m-6)^2)/(L_x^3(L_x^2-12)^2)+ & \\
(9L_x((-1)^m+1)^2(L_x^2+\pi^2m^2)^2)/(5(L_x^2-12)^2)- & \\
((2L_x^2+2\pi^2m^2)(L_x^2+\pi^2m^2)(L_x^2+6(-1)^m-6)(2L_x^2+6(-1)^m+(-1)^mL_x^2-6))/(L_x^3(L_x^2-12)^2)- & \\
((2L_x^2+2\pi^2m^2)(3(-1)^m+3)(L_x^2+\pi^2m^2)(2L_x^2+6(-1)^m+(-1)^mL_x^2-6))/(2L_x(L_x^2-12)^2)- & \\
(2(2L_x^2+2\pi^2m^2)(2L_x^2+6(-1)^m+(-1)^mL_x^2-6))/(L_x\pi^2m^2(L_x^2-12))+ & \\
(2\cos(\pi m)(2L_x^2+2\pi^2m^2)(2L_x^2+6(-1)^m+(-1)^mL_x^2-6))/(L_x\pi^2m^2(L_x^2-12))- & \\
(4L_x\cos(\pi m)(3(-1)^m+3)(L_x^2+\pi^2m^2))/(\pi^2m^2(L_x^2-12)); & \text{if } m=p\neq 0 \\[1em]
(L_x^3((-1)^p+1)(\pi^2L_x^2p^2-60L_x^2+\pi^4p^4+720))/(10\pi^2p^2(L_x^2-12)^2); & \text{if } m=0 \text{ and } p\neq 0 \\[1em]
(L_x^3((-1)^m+1)(\pi^2L_x^2m^2-60L_x^2+\pi^4m^4+720))/(10\pi^2m^2(L_x^2-12)^2); & \text{if } p=0 \text{ and } m\neq 0 \\[1em]
((3(-1)^m+3)(L_x^2+\pi^2m^2)(L_x^2+\pi^2p^2)(L_x^2+6(-1)^p-6))/(3L_x(L_x^2-12)^2)+ & \\
((3(-1)^p+3)(L_x^2+\pi^2m^2)(L_x^2+\pi^2p^2)(L_x^2+6(-1)^m-6))/(3L_x(L_x^2-12)^2)- & \\
((2L_x^2+2\pi^2m^2)(L_x^2+\pi^2p^2)(L_x^2+6(-1)^p-6)(2L_x^2+6(-1)^m+(-1)^mL_x^2-6))/(2L_x^3(L_x^2-12)^2)- & \\
((2L_x^2+2\pi^2p^2)(L_x^2+\pi^2m^2)(L_x^2+6(-1)^m-6)(2L_x^2+6(-1)^p+(-1)^pL_x^2-6))/(2L_x^3(L_x^2-12)^2)- & \\
((2L_x^2+2\pi^2m^2)(3(-1)^p+3)(L_x^2+\pi^2p^2)(2L_x^2+6(-1)^m+(-1)^mL_x^2-6))/(4L_x(L_x^2-12)^2)- & \\
((2L_x^2+2\pi^2p^2)(3(-1)^m+3)(L_x^2+\pi^2m^2)(2L_x^2+6(-1)^p+(-1)^pL_x^2-6))/(4L_x(L_x^2-12)^2)+ & \\
((L_x^2+\pi^2m^2)(L_x^2+\pi^2p^2)(L_x^2+6(-1)^m-6)(L_x^2+6(-1)^p-6))/(L_x^3(L_x^2-12)^2)+ & \\
((2L_x^2+2\pi^2m^2)(2L_x^2+2\pi^2p^2)(2L_x^2+6(-1)^m+ & \\
(-1)^mL_x^2-6)(2L_x^2+6(-1)^p+(-1)^pL_x^2-6))/(3L_x^3(L_x^2-12)^2)+ & \\
(L_x(3(-1)^m+3)(3(-1)^p+3)(L_x^2+\pi^2m^2)(L_x^2+\pi^2p^2))/(5(L_x^2-12)^2)- & \\
(2L_x\cos(\pi m)(3(-1)^p+3)(L_x^2+\pi^2p^2))/(\pi^2m^2(L_x^2-12))- & \\
(2L_x\cos(\pi p)(3(-1)^m+3)(L_x^2+\pi^2m^2))/(\pi^2p^2(L_x^2-12))- & \\
(2\sin((\pi p)/2)^2(2L_x^2+2\pi^2m^2)(2L_x^2+6(-1)^m+(-1)^mL_x^2-6))/(L_x\pi^2p^2(L_x^2-12))- & \\
(2\sin((\pi m)/2)^2(2L_x^2+2\pi^2p^2)(2L_x^2+6(-1)^p+(-1)^pL_x^2-6))/(L_x\pi^2m^2(L_x^2-12)); & \text{otherwise}
\end{cases}$$

$$\int_0^{L_x} X''_m(x)X_p(x)dx =$$

$$\begin{cases}
-(12L_x)/(L_x^2-12); & \text{if } m=p=0\\[1em]
(4L_x^4-12L_x^2-12L_x^2+4L_x^4+24(-1)^pL_x^2+4(-1)^pL_x^4-12\pi^2p^2- & \\
12\pi^2p^2+10L_x^2\pi^2p^2-(L_x^4\pi^2p^2)/2+24(-1)^p\pi^2p^2+ & \\
4(-1)^pL_x^2\pi^2p^2- & \\
(\pi L_x^4p\sin(2\pi p))/4+4L_x^2\pi^2p^2)/(L_x^3(L_x^2-12)); & \text{if } m=p\neq 0\\[1em]
0; & \text{if } m=0 \text{ and } p\neq 0\\[1em]
-(6\pi^2m^2((-1)^m+1))/(L_x(L_x^2-12)); & \text{if } p=0 \text{ and } m\neq 0\\[1em]
(2(L_x^2+\pi^2p^2)(12(-1)^p\sin((\pi m)/2)^2+3(-1)^mL_x^2- & \\
12\sin((\pi m)/2)^2+4L_x^2\sin((\pi m)/2)^2+ & \\
3(-1)^m(-1)^pL_x^2+2(-1)^pL_x^2sin((\pi m)/2)^2))/(L_x^3(L_x^2-12)); & \text{otherwise}
\end{cases}$$

$$\int_0^{L_x} X'_m(x)X'_p(x)dx =$$

$$\begin{cases}
(12L_x^3)/(L_x^2-12)^2; & \text{if } m=p=0\\[1em]
(\pi^2m^2)/(2L_x)-(2(2L_x^2+2\pi^2m^2)(2L_x^2+6(-1)^m+(-1)^mL_x^2-6))/(L_x^3(L_x^2-12))+ & \\
(12((-1)^m+1)^2(L_x^2+\pi^2m^2)^2)/(L_x(L_x^2-12)^2)- & \\
+(4(L_x^2+\pi^2m^2)^2(2L_x^2+6(-1)^m+(-1)^mL_x^2-6)^2)/(L_x^5(L_x^2-12)^2)- & \\
(4(-1)^m(3(-1)^m+3)(L_x^2+\pi^2m^2))/(L_x(L_x^2-12))+ & \\
(2(-1)^m(2L_x^2+2\pi^2m^2)(2L_x^2+6(-1)^m+(-1)^mL_x^2-6))/(L_x^3(L_x^2-12))- & \\
(2(2L_x^2+2\pi^2m^2)(3(-1)^m+3)(L_x^2+\pi^2m^2)(2L_x^2+6(-1)^m+(-1)^mL_x^2-6))/(L_x^3(L_x^2-12)^2); & \text{if } m=p\neq 0\\[1em]
(6L_x((-1)^p+1)(\pi^2p^2+12))/(L_x^2-12)^2; & \text{if } m=0 \text{ and } p\neq 0\\[1em]
(6L_x((-1)^m+1)(\pi^2m^2+12))/(L_x^2-12)^2; & \text{if } p=0 \text{ and } m\neq 0\\[1em]
(4(3(-1)^m+3)(3(-1)^p+3)(L_x^2+\pi^2m^2)(L_x^2+\pi^2p^2))/(3L_x(L_x^2-12)^2)- & \\
(2\sin((\pi m)/2)^2(2L_x^2+2\pi^2p^2)(2L_x^2+6(-1)^p+ & \\
(-1)^pL_x^2-6))/(L_x^3(L_x^2-12))-(2(-1)^p(3(-1)^m+3)(L_x^2+\pi^2m^2))/(L_x(L_x^2-12))- & \\
(2(-1)^m(3(-1)^p+3)(L_x^2+\pi^2p^2))/(L_x(L_x^2-12))- & \\
(2\sin((\pi p)/2)^2(2L_x^2+2\pi^2m^2)(2L_x^2+6(-1)^m+(-1)^mL_x^2-6))/(L_x^3(L_x^2-12))- & \\
((2L_x^2+2\pi^2m^2)(3(-1)^p+3)(L_x^2+\pi^2p^2)(2L_x^2+6(-1)^m+(-1)^mL_x^2-6))/(L_x^3(L_x^2-12)^2)- & \\
((2L_x^2+2\pi^2p^2)(3(-1)^m+3)(L_x^2+\pi^2m^2)(2L_x^2+6(-1)^p+(-1)^pL_x^2-6))/(L_x^3(L_x^2-12)^2)+ & \\
((2L_x^2+2\pi^2m^2)(2L_x^2+2\pi^2p^2)(2L_x^2+6(-1)^m+(-1)^mL_x^2-6)\times & \\
(2L_x^2+6(-1)^p+(-1)^pL_x^2-6))/(L_x^5(L_x^2-12)^2); & \text{otherwise}
\end{cases}$$

and similarly for the integrals involving the functions Y.

Acknowledgements

This manuscript marks the end of my doctorate studies. This path has not been long, not short either, surely difficult though, impossible to walk on my legs only: many are the people to whom I am thankful for their support.

Firstly, I would like to thank my main supervisor, Cyril Touzé. Cyril's contribution was fundamental for obtaining my PhD grant, having completed all by himself the tedious administrative work for my project (I could not speak a word of French at the time). I remember very well our first meeting at the RER station in Villebon: I was tense, silent and a little frightened, I had just arrived in France and every single thing was new to me. Cyril showed up with a copy of my Masters thesis under his arm, smiling, and with plenty of comments. He introduced me to the other colleagues and, once we completed some (preliminary) administrative work, we started discussing immediately. That was the first of many other meetings to come which became a fundamental part of the development of my project. Punctuality, clarity, honesty and a great scientific competence are the values that I most admired about Cyril, and that have been of great support and comfort during these years. I hope that Cyril benefitted from our joint work as much as I did.

I am very thankful to my second supervisor, Oliver Cadot. I learnt a lot from him, especially regarding Wave Turbulence and data analysis. Thanks to Olivier's interpretation, and his scientific perspicacity, the nonlinear physics hidden behind that awful lot of data resulted much clearer and pragmatic than I though at the start. As for Cyril, my hope is that Oliver benefitted from our joint work as much as I did.

A special thanks is for Antoine Chaigne, head of the Unité de Mécanique (UME) at the time of my PhD. Thanks to him I was able to work in a peaceful and stimulating environment which contributed to my growth as a researcher. For the same reason I would like to thank my colleagues and the personnel at UME (I do not think i can name them all, but I can try, in an absolutely random oreder): Corinne, Olivier D., Thierry, Nico, Romain M., Thomas H., Mélodie, Régine, Sylvie-Anne, Thomas A., Vladimir, Romain P., and all the other PhD students.

Outside UME, I would like to thank Oliver Thomas and Cristophe Josserand for their precious scientific contributions and fruitful discussions.

Outside France, up to remote Scotland, I am enormously thankful to Stefan Bilbao. Stefan was the course director during my Masters degree at Edinburgh University: I owe him my comeback in academia and a renewed passion for science and, particularly, physical modelling. Also, it is thanks to his academic recommendation that I was able to pursue a PhD in France. My academic debt with Stefan is enormous and I hope I can pay him back soon. I would also like to thank other members of the NESS project at Edinburgh: Alberto, Craig and Brian above all.

There are many people that contributed to this work although not in its scientific aspects: Fay is surely one of them. Thanks to her I learnt to brew the perfect cup of tea for relaxing moments during the long, wintery evenings when this manuscript was being written. She also introduced me to the fantastic world of Adventure Time. Her support and encouragement have been priceless and I hope I can soon return the favour.

A last word of gratitude, and a very special one, is for my extended family: grannies, aunties, uncles, cousins. This work is entirely dedicated to my sister Benedetta and my parents Luisa and Ezio, without whom none of this would make sense.

Palaiseau, Septembre 2014

Bibliography

For the bibliographic references pertaining to nonlinear modal dynamics and Wave Turbulence see Chapters 4 and 5.

1. F. Alijani and M. Amabili, *Theory and experiments for nonlinear vibrations of imperfect rectangular plates with free edges*, Journal of Sound and Vibration **332** (2013), no. 14, 3564 – 3588.
2. M. Amabili, *Nonlinear vibrations of rectangular plates with different boundary conditions: theory and experiments*, Computers and Structures **82** (2004), no. 31-32, 2587–2605.
3. M. Amabili and R. Garziera, *A technique for the systematic choice of admissible functions in the Rayleigh-Ritz method*, Journal of Sound and Vibration **224** (1999), no. 3, 519 – 539.
4. G. Anlas and O. Elbeyli, *Nonlinear vibrations of a simply supported rectangular metallic plate subjected to transverse harmonic excitation in the presence of a one-to-one internal resonance*, Nonlinear Dynamics **30** (2002), no. 1, 1–28.
5. K. Arcas, *Simulation numérique d'un réverbérateur à plaque*, Ph.D. thesis, École Polytechnique, 2009.
6. R.B. Bhat, *Natural frequencies of rectangular plates using characteristic orthogonal polynomials in Rayleigh-Ritz method*, Journal of Sound and Vibration **102** (1985), no. 4, 493 – 499.
7. S. Bilbao, *A family of conservative finite difference schemes for the dynamical von Kármán plate equations*, Numerical Methods for Partial Differential Equations **24** (2008), no. 1, 193–216.
8. S. Bilbao, *Numerical sound synthesis*, Wiley, 2008.
9. S. Bilbao, *Modeling of complex geometries and boundary conditions in finite difference/finite volume time domain room acoustics simulation*, IEEE Transactions on Audio Speech and Language Processing **21** (2013), no. 7, 1524 – 1533.
10. S. Bilbao, B. Hamilton, A. Torin, C. Webb, A. Gray P. Graham, K. Kavoussanakis, and J. Perry, *Large scale physical modeling synthesis*, Proceedings of the Stockholm Musical Acoustics Conference/Sound and Music Computing Conference (Stockholm, Sweden), July/August 2013.
11. A. Boudaoud, O. Cadot, B. Odille, and C. Touzé, *Observation of wave turbulence in vibrating plates*, Phys. Rev. Lett. **100** (2008), 234504.
12. T.E. Carmichael, *The vibration of a rectangular plate with edges elastically restrained against rotation*, The Quarterly Journal of Mechanics and Applied Mathematics **12** (1959), no. 1, 29–42.
13. J. Chabassier, *Modélisation et simulation numérique d'un piano par modéles physiques*, Ph.D. thesis, Ecole Polytechnique, 2012.

14. J. Chabassier, P. Joly, and A. Chaigne, *Modeling and simulation of a grand piano*, Journal of the Acoustical Society of America **134** (2013), 648.
15. A. Chaigne, *On the use of finite differences for musical synthesis. application to plucked string instruments*, Journal d'Acoustique **5** (1992), no. 2, 181–211.
16. A. Chaigne and A. Askenfelt, *Numerical simulations of struckstrings I. a physical model for a struck string using a finite difference method*, Journal of the Acoustical Society of America **95** (1994), no. 2, 1112–1118.
17. ———, *Numerical simulations of struckstrings II. comparison with measurements and systematic exploration of some hammer-string parameters*, Journal of the Acoustical Society of America **95** (1994), no. 3, 1631–1640.
18. S.I. Chang, A.K. Bajaj, and C.M. Krousgrill, *Nonlinear oscillations of a fluttering plate.*, AIAA Journal **4** (1966), 1267–1275.
19. ———, *Non-linear vibrations and chaos in harmonically excited rectangular plates with one-to-one internal resonance*, Nonlinear Dynamics **4** (1993), 433–460 (English).
20. W. Q. Chen and H. J. Ding, *On free vibration of a functionally graded piezoelectric rectangular plate*, Acta Mechanica **153** (2002), no. 3-4, 207–216.
21. H.N. Chu and G. Herrmann, *Influence of large amplitudes on free flexural vibrations of rectangular elastic plates*, Journal of Applied Mechanics **23** (1956), 532–540.
22. R. Courant, K. Friedrichs, and H. Lewy, *Über die partiellen differenzengleichungen der mathematischen physik*, Mathematische Annalen **100** (1928), 32–74.
23. ———, *On the partial difference equations of mathematical physics*, IBM J. Res. Develop. **11** (1967), 215–234.
24. S. M. Dickinson and E. K. H. Li, *The vibration of rectangular plates treated using simply supported plate functions in the Rayleigh-Ritz method*, The Journal of the Acoustical Society of America **69** (1981), no. S1, S87–S87.
25. Z. Ding, *Natural frequencies of rectangular plates using a set of static beam functions in Rayleigh-Ritz method*, Journal of Sound and Vibration **189** (1996), no. 1, 81 – 87.
26. O. Doaré and S. Michelin, *Piezoelectric coupling in energy-harvesting fluttering flexible plates: linear stability analysis and conversion efficiency*, Journal of Fluids and Structures **27** (2011), 1357–1375.
27. M. Ducceschi, *Rectangular, thin plate vibration: A modal approach*, Master's thesis, The University of Edinburgh, 2010.
28. M. Ducceschi, O. Cadot, C. Touzé, and S. Bilbao, *Dynamics of the wave turbulence spectrum in vibrating plates: A numerical investigation using a conservative finite difference scheme*, Physica D: Nonlinear Phenomena **280 - 281** (2014), no. 0, 73 – 85.
29. M. Ducceschi, C. Touzé, and S. Bilbao, *Nonlinear plate vibrations: A modal approach with application to cymbals and gongs*, Proceedings of Acoustics 2012 (Nantes), April 2012.

30. ______, *Sound synthesis of gongs obtained from nonlinear thin plates vibrations: comparison between a modal approach and a finite difference scheme*, Proceedings of the Stockholm Musical Acoustics Conference/Sound and Music Computing Conference (Stockholm, Sweden), July/August 2013.
31. M. Ducceschi, C. Touzé, S. Bilbao, and C.J. Webb, *Nonlinear dynamics of rectangular plates: investigation of modal interaction in free and forced vibrations*, Acta Mechanica **225** (2014), no. 1, 213 – 232.
32. G. Düring, C. Josserand, and S. Rica, *Weak turbulence for a vibrating plate: Can one hear a Kolmogorov spectrum?*, Phys. Rev. Lett. **97** (2006), 025503.
33. G. Eckel, F. Iovino, and R. Caussé, *Sound synthesis by physical modeling with Modalys*, Proceedings of the International Symposium on Musical Acoustics (Dourdan, France), 1195.
34. J. Farlow, *Partial differential equations for scientists and engineers*, Dover Publications, 1993.
35. C.P. Filipich and M.B. Rosales, *Arbitrary precision frequency of a free rectangular thin plate*, Journal of Sound and Vibration **230** (2000), no. 3, 521 – 539.
36. Y. M. Fu and C. Y. Chia, *Nonlinear bending and vibration of symmetrically laminated orthotropic elliptical plate with simply supported edge*, Acta Mechanica **74** (1988), no. 1-4, 155–170.
37. M. Géradin and D. Rixen, *Mechanical vibrations, second edition*, Wiley, 1997.
38. J.H. Ginsberg, *Mechanical and structural vibrations*, Wiley, 2001.
39. R.P. Goel, *Vibration of a beam carrying concentrated mass*, Journal of Applied Mathematics **40** (1973), 821 – 822.
40. D.J. Gorman, *Free vibration analysis of the completely free rectangular plate by the method of superposition*, Journal of Sound and Vibration **57** (1978), no. 3, 437 – 447.
41. D.J. Gorman and S.D. Yu, *A review of the superposition method for computing free vibration eigenvalues of elastic structures*, Computers and Structures **104105** (2012), no. 0, 27 – 37.
42. K.F. Graff, *Wave motion in elastic solids*, Dover Publications, 1975.
43. R.O. Grossi and P.A.A. Laura, *Transverse vibrations of orthotropic rectangular plates with thickness varying in two directions and with edges elastically restrained against rotation*, Fibre Science and Technology **14** (1981), no. 4, 311 – 317.
44. P. Hagedorn and A. DasGupta, *Vibrations and waves in continuous mechanical systems*, Wiley, 2007.
45. E. Hairer, C. Lubich, and G. Wanner, *Geometric numerical integration, structure-preserving schemes for ordinary differential equations*, Springer, 2006.
46. R.W. Hamming, *Numerical methods for scientists and engineers, second edition*, Dover Publications, 1973.
47. T. Humbert, O. Cadot, G. Düring, C. Josserand, S. Rica, and C. Touzé, *Wave turbulence in vibrating plates: the effect of damping*, European Physical Journal **102** (2013), 30002.
48. S. Hurlebaus, L. Gaul, and J.T.-S. Wang, *An exact series solution for calculating the eigenfrequencies of orthotropic plates with completely free boundary*, Journal of Sound and Vibration **244**

(2001), no. 5, 747 – 759.

49. S. Iguchi, *Die eigenschwingungen und klangfiguren der vierseitig freien rechteckigen platte*, Ingenieur-Archiv **21** (1953), no. 5-6, 303–322.
50. J.D. Jackson, *Classical electrodynamics, third edition*, Wiley, 1998.
51. C.S. Kim, P.G. Young, and S.M. Dickinson, *On the flexural vibration of rectangular plates approached by using simple polynomials in the Rayleigh-Ritz method*, Journal of Sound and Vibration **143** (1990), no. 3, 379 – 394.
52. A.N. Kounandis, *Dynamics response of cantilevers with attached masses*, Journal of Engineering Mechanics Division **101** (1975), no. EMS, 695–706.
53. G. C. Kung and Y.-H. Pao, *Nonlinear flexural vibrations of a clamped circular plate*, Journal of Applied Mechanics **39** (1972), no. 4, 1050–1054.
54. C. Lambourg, *Modèle temporel pour la simulation numerique de plaques vibrantes. application a la synthèse sonore*, Ph.D. thesis, Université du Maine, 1997.
55. C. Lambourg, A. Chaigne, and D. Matignon, *Time-domain simulation of damped impacted plates II: Numerical model and results*, Journal of the Acoustical Society of America **109** (2001), no. 4, 1433 – 1447.
56. L.D. Landau and E.M. Lifschitz, *Theory of elasticity, third edition*, Elsevier Butterworth Heinemann, 1986.
57. A.W. Leissa, *Vibration of plates*, Acoustical Society of America, 1993.
58. W.L. Li, *Free vibrations of beams with general boundary conditions*, Journal of Sound and Vibration **237** (2000), no. 4, 709 – 725.
59. ———, *Vibration analysis of rectangular plates with general elastic boundary supports*, Journal of Sound and Vibration **273** (2004), no. 3, 619 – 635.
60. M.J. Maurizi, R.E. Rossi, and J.A. Reyes, *Vibration frequencies for a uniform beam with one end spring-hinged and subjected to a translational restraint at the other end*, Journal of Sound and Vibration **48** (1976), no. 4, 565 – 568.
61. L. Meirovitch, *Computational methods in structural dynamics*, Sijthoff and Noordhoff, 1980.
62. ———, *Fundamentals of vibration*, Waveland Press, 2001.
63. B. Miquel, A. Alexakis, and N. Mordant, *Role of dissipation in flexural wave turbulence: from experimental spectrum to Kolmogorov-Zakharov spectrum*, Phys. Rev. E (submitted) (2008).
64. A.R. Mitchell and D.F.. Griffiths, *The finite difference method in partial differential equations*, Wiley, New York, 1980.
65. Y. Mochida, *Bounded eigenvalues of fully clamped and completely free rectangular plates*, Master's thesis, The University of Waikato, 2007.
66. Y. Mochida and S. Ilanko, *Transient vibration analysis of a completely free plate using modes obtained by Gorman's superposition method*, Journal of Sound and Vibration **329** (2010), no. 10, 1890 – 1900.

67. N. Mordant, *Are there waves in elastic wave turbulence?*, Phys Rev Lett **100** (2008), no. 23, 234505.
68. D. Morrison and J.-M. Adrien, *Mosaic: a framework for modal synthesis*, Computer Music Journal **17** (1993), no. 1, 45–56.
69. A.H. Nayfeh and P.F. Pai, *Linear and nonlinear structural mechanics*, Wiley-VCH, 2004.
70. S. Nazarenko, *Wave turbulence*, Springer-Verlag, Berlin Heidelberg, 2011.
71. O.Thomas, C. Touzé, and A. Chaigne, *Asymmetric non-linear forced vibrations of free-edge circular plates, part II: experiments*, Journal of Sound and Vibration **265** (2003), no. 5, 1075–1101.
72. M. Peeters, *Theoretical and experimental modal analysis of nonlinear vibrating stuctures using Nonlinear Normal Modes*, Ph.D. thesis, University of Liège, 2010.
73. A. Srikantha Phani and J. Woodhouse, *Viscous damping identification in linear vibration*, Journal of Sound and Vibration **303** (2007), no. 35, 475 – 500.
74. C.K. Rao and S. Mirza, *A note on vibrations of generally restrained beams*, Journal of Sound and Vibration **130** (1989), no. 3, 453 – 465.
75. L. Rhaouti, A. Chaigne, and P. Joly, *Time-domain modeling and numerical simulation of a kettledrum*, Journal of the Acoustical Society of America **105** (1999), no. 6, 3545 – 3562.
76. W. Ritz, *Theorie der transversalschwingungen einer quadratischen platte mit freien rändern*, Annalen der Physik **333** (1909), no. 4, 737–786.
77. R.M. Rosenberg, *The normal modes of a nonlinear n-degree-of-freedom systems*, Journal of Applied Mechanics **30** (1962), 7–14.
78. ———, *Of nonlinear vibrations of systems with many degrees of freedom*, Advances in Applied Mechanics **9** (1966), 115–242.
79. P. Ruiz, *A technique for simulating the vibrations of strings with a digital computer*, Master's thesis, University of Illisnois, 1969.
80. I.C. Seo, J.M. Lee, A.K. Bajaj, and C.M. Krousgrill, *Subharmonic responses in harmonically excited rectangular plates with one-to-one internal resonance*, Chaos, Solitons and Fractals **8** (1997), no. 4, 479–498.
81. A. Taflove, *Computational electrodynamics*, Artech House, 1995.
82. ———, *Advances in computational electrodynamics*, Artech House, 1998.
83. O Thomas and S Bilbao, *Geometrically nonlinear flexural vibrations of plates: In-plane boundary conditions and some symmetry properties*, Journal of Sound and Vibration **315** (2008), no. 3, 569–590.
84. G.P. Tolstov, *Fourier series*, Englewood Cliffs, 1965.
85. A. Torin and S. Bilbao, *A 3d multi-plate environment for sound synthesis*, Proceedings of the 16th International Digital Audio Effects Conference (Maynooth, Ireland), September 2013.
86. C. Touzé and M. Amabili, *Nonlinear normal modes for damped geometrically nonlinear systems: Application to reduced-order modelling of harmonically forced structures*, Journal of Sound and Vibration **298** (2006), no. 45, 958 – 981.

87. C. Touzé, M. Amabili, and O. Thomas, *Reduced-order models for large-amplitude vibrations of shells including in-plane inertia*, Computer Methods in Applied Mechanics and Engineering **197** (2008), no. 2124, 2030 – 2045.
88. C. Touzé, S. Bilbao, and O. Cadot, *Transition scenario to turbulence in thin vibrating plates*, Journal of Sound and Vibration **331** (2012), no. 2, 412 – 433.
89. C. Touzé, O. Thomas, and A. Huberdeau, *Asymptotic non-linear normal modes for large-amplitude vibrations of continuous structures*, Computers and Structures **82** (2004), no. 3132, 2671 – 2682.
90. A.F. Vakakis, *Non-linear normal modes (NNMs) and their applications in vibration theory: an overview*, Mechanical Systems and Signal Processing **11** (1997), no. 1, 3 – 22.
91. T. von Kármán, *Festigkeitsprobleme im maschinenbau*, Encyklopadie der Mathematischen Wissenschaften **4** (1910), 311–385 (German).
92. J.T.-S. Wang and C.-C. Lin, *Dynamic analysis of generally supported beams using Fourier series*, Journal of Sound and Vibration **196** (1996), no. 3, 285 – 293.
93. C.J. Webb, *Computing virtual acoustics using the 3D Finite Difference time domain method and Kepler architecture gpus*, Proceedings of the Stockholm Musical Acoustics Conference/Sound and Music Computing Conference (Stockholm, Sweden), July/August 2013.
94. J. Woodhouse, *Linear damping models for structural vibration*, Journal of Sound and Vibration **215** (1998), no. 3, 547 – 569.
95. N. Yamaki, *Influence of large amplitudes on flexural vibrations of elastic plates*, Zeitschrift für Angewandte Mathematik und Mechanik **41** (1961), no. 12, 501–510.
96. K. Yee, *Numerical solutions of intial boundary value problems involving maxwell's equations in isotropic media*, IEEE Transactions of Antennas and Propagation **14** (1966), 302–307.
97. N. Yokoyama and M. Takaoka, *Weak and strong wave turbulence spectra for elastic thin plate*, Phys. Rev. Lett. **110** (2013), 105501.
98. V.E. Zakharov, V.S. L'vov, and G. Falkovich, *Kolmogorov spectra of turbulence 1: Wave turbulence*, Series in Nonlinear Dynamics, Springer, 1992.